Scaling relations between super-massive black holes, galaxies and dark matter halos

Adam Larkin

PhD

Department of Physics, University of Keele.

June 2017

Abstract

The observed correlations between the masses of supermassive black holes (SMBH), $M_{\rm BH}$, with a gravitational influence on parsec scales, and properties of the host galaxy, measured on kiloparsec scales, strongly suggest that the SMBH and galaxy co-evolve. These correlations are likely to be a reflection of a more fundamental connection between $M_{\rm BH}$ and the depth of the potential wells that *just* fail to prevent gas blow-out, due to feedback from rapid accretion during a quasar-phase. The potential wells in question were dominated by dark matter, and a general method is lacking to connect the stellar properties at $z = 0$ to properties of their dark matter halos, both at $z = 0$ and higher redshifts. The work presented here develops a method to make these connections self-consistently.

Models of two-component spherical galaxies are used to establish scaling relations linking properties of spheroids at $z = 0$ (stellar masses, effective radii and velocity dispersions) to properties of the dark matter halo (virial masses and circular speeds), also at $z = 0$. These models are constrained by combining results from the literature connecting the masses and radii of dark matter halos to each other and stellar masses, with data samples for large, early-type galaxies. The $z = 0$ properties are then connected to dark matter properties at $z > 0$ by accounting for the halo redshift evolution. A critical SMBH mass prediction, with dependence on the maximum circular-speed in a protogalactic dark matter halo ($M_{\rm BH} \propto V_{\rm d,pk}^4$), is considered. Combining this with the scaling relations between $z = 0$ properties and halo properties at $z > 0$ transforms this theoretical relation into predictions for the observable SMBH correlations.

A new prediction is also derived, extending on the $M_{\rm BH} \propto V_{\rm d,pk}^4$ relation expected from momentum-driven outflows, allowing for the presence of stars and gas not tracing the dark matter. This new prediction is also compared to the observed correlations at $z = 0$.

Acknowledgements

The majority of the results presented in Chapters 2 and 3 in this thesis are based on the published work from Larkin & McLaughlin (2016). From Chapter 2, results in Sections 2.1 through to 2.2.7 inclusive are from the Larkin & McLaughlin (2016) paper, usually with a more detailed discussion here. Section 2.2.8 is not published, but is an extension of the work that *is* published from the rest of the Chapter. From Chapter 3, Sections 3.1, 3.2 and 3.3.2 are adapted from Larkin & McLaughlin (2016). The rest of Chapter 3 is again an extension of this published work.

At times it has been hellish, but then again nobody does a PhD because it is easy. You have to be slightly bonkers to start such a journey, and just try to avoid descending into complete madness. Here's to the people who have kept me sane these last four years. First of all, many thanks to Dean McLaughlin. You have shown the patience of a saint whilst guiding me to this point. Many hours of hard work and, no doubt, frustration on your part have hopefully paid off — my hat's off to you.

Secondly, to my fiancée, Sophie, who has been an absolute rock throughout the last four years. Her continued encouragement and emotional & financial support has pulled me through, especially in the last few months. Without doubt, I could not have completed this without her. Thanks also to my parents and brother, whose love and support have been invaluable. They have continued to push me along towards the finish line, and for that I am most grateful.

Extended family and close friends have also played their part. My former flatmate Grant, who I have shared many laughs with over the last few years, has helped to keep me motivated, simply by taking my mind off work for a few hours, normally involving drinking, pizza, peep show and Fifa. Also, my fellow PhD students from LJ 2.01 have provided a daily source of laughs and encouragement, so many thanks to you guys too.

Adam Larkin

June 2017

Contents

List of Figures

List of Tables

1 Introduction

Ever since galaxies were first observed, a key question for many astronomers has been how do they form and evolve. Initially, the research field of galaxy formation was mainly driven by the long-standing desire to explain the formation and evolution of the Universe. However, it has since become an area of much interest in its own right.

The discovery of quasars was a major breakthrough for astronomers (Schmidt 1963). Originally described as "quasi-stellar" due to their star-like appearance, their high redshifts identified them as being incredibly luminous objects. Quasars are high redshift members of the family of galaxies with active galactic nuclei, more commonly known as AGN. A large fraction of the luminosity of an active galaxy is produced in the central regions (i.e., the nucleus), hence the name. All observed AGN share several common properties; they are all very compact (in some cases, < 1 pc), extremely energetic and have similar variability time scales (typically of order 1 day). This led to the idea that a similar mechanism was the source of the large luminosities in all of these objects.

It became widely accepted that the power source in AGN is primarily gravitational. Salpeter (1964) was the first to suggest that Super-Massive Black Holes (SMBHs) were present in these objects. The idea that quasars are powered by the conversion of gravitational energy into radiation when matter accretes onto an SMBH soon became established (Lynden-Bell 1969; Lynden-Bell & Rees 1971). This quasar-phase is now understood to account for the majority of SMBH growth ($\geq$ 70%–80%: Soltan 1982; Yu & Tremaine 2002). It has also been shown, from observations and simulations, that there is a peak in quasar number, quasar activity and SMBH accretion rate densities in the Universe, at redshifts $z \sim 2$–4 (Richards et al. 2006; Hopkins et al. 2007; Delvecchio et al. 2014; also Sijacki et al. 2007, 2015; Di Matteo 2008).

Normal, quiescent galaxies at $z = 0$ have evolved through cosmic time, most likely from some more active stage (quasar activity, powered by SMBH accretion). It is now generally accepted that early-type galaxies and galaxy bulges host SMBHs at

their centres, with masses $M_{\rm BH} \sim 10^6$–$10^{10} M_\odot$. Observations show that these black hole masses correlate with various galaxy properties. These include $M_{\rm BH}$ correlating with bulge luminosities, $L_{\rm bulge}$, in various band passes (Magorrian et al. 1998; Marconi & Hunt 2003; Gültekin et al. 2009; McConnell & Ma 2013; Kormendy & Ho 2013), bulge mass (stellar or dynamical), $M_{\rm bulge}$ (Magorrian et al 1998; Marconi & Hunt 2003; Häring & Rix 2004; McConnell & Ma 2013; Kormendy & Ho 2013), and stellar velocity dispersion of the host bulge, σ (Ferrarese & Merritt 2000; Gebhardt et al. 2000; Ferrarese & Ford 2005; Gültekin et al. 2009; McConnell & Ma 2013; Kormendy & Ho 2013). There is also evidence for a bivariate dependence of $M_{\rm BH}$ on a combination of σ and $M_{\rm bulge}$ or stellar effective radius, R_e (Hopkins et al. 2007a; Hopkins et al. 2007b).

These connections between the SMBH, with a sphere of influence radius of tens of parsecs, and global properties of the host galaxy on kiloparsec scales strongly suggest that the evolution of the SMBH and galaxy are closely related. This idea was suggested, in part, due to the relatively small intrinsic scatter in the observed correlations, with typical values of 0.2–0.4 dex (Ferrarese & Ford 2005; Hopkins et al. 2007a; Kormendy & Ho 2013). However, the intrinsic scatter has always been calculated around best-fits, normally assumed to be single power-laws (linear in log–log space), with generally no physical justification. A prediction based on a physical model will not necessarily lead to linear model curves for the SMBH relations. How the data scatters around such model curves could shed some light on whether any one of the observed correlations are more fundamental than the others, or if they reflect a more significant connection. The initial challenge for this is to know the "correct" trends, based on a physical model, for $M_{\rm BH}$ versus galaxy properties at $z = 0$, around which the scatter should be calculated.

The co-evolution between the black hole and galaxy likely involved some form of self-regulated feedback. As mentioned above, most of the SMBH mass is grown in a quasar phase, when the black hole accretes at, or near, the Eddington rate. This results in significant momentum and energy being deposited back into the gas supply, and can lead to a blow-out, halting further SMBH growth. In this context, one would then expect a connection between the black hole mass, and the depth of the potential well which the SMBH feedback had to overcome to expel the gas. The observed correlations

in $z = 0$ galaxies will therefore reflect this fundamental connection.

However, it is not clear in detail how the stellar properties in normal galaxies at $z = 0$ relate to the protogalactic potential wells when any putative blow-out occurred and the main phase of accretion-driven SMBH growth came to an end. For most systems, this was presumably around $z \sim 2$–4, when quasar activity in the Universe was at a peak. The potential wells in question are dominated by dark matter, and a general method is lacking to connect stellar $\sigma_{\rm ap}$ or $M_{*,\rm tot}$ in spheroids to the properties of their dark matter halos, not only at $z = 0$, but at higher redshift as well. Moreover, it is not necessarily obvious what specific property (or properties) of dark matter halos provides the key measure of potential-well depth in the context of a condition for accretion-driven blow-out. Different simulations of galaxy and SMBH co-evolution with different recipes for quasar-mode feedback appear equally able (with appropriate tuning of their free parameters) to reproduce the observed SMBH correlations.

Under the assumption that accretion feedback is momentum-conserving and takes the form of a spherical shell driven outwards by an SMBH wind with momentum flux $dp_{\rm wind}/dt = L_{\rm Edd}/c$, McQuillin & McLaughlin (2012) derive a minimum SMBH mass sufficient to expel an initially static and virialised gaseous medium from any protogalaxy consisting of dark matter and gas only. This critical mass is approximately

$$\begin{aligned} M_{\rm BH} &\simeq \frac{f_0 \kappa}{\pi G^2} \frac{V_{\rm d,pk}^4}{4} \\ &\simeq 1.14 \times 10^8 \, M_\odot \left(\frac{f_0}{0.2} \right) \left(\frac{V_{\rm d,pk}}{200 \, {\rm km \, s^{-1}}} \right)^4 , \end{aligned} \tag{1.1}$$

where κ is the Thomson-scattering opacity and f_0 is the (spatially constant) gas-to-dark matter mass fraction in the protogalaxy. The velocity scale $V_{\rm d,pk}$ refers to the peak-value of the circular speed $V_d^2(r) = GM_d(r)/r$ in a dark matter halo with mass profile $M_d(r)$. Equation (1.1) holds for any form of the mass profile, so long as the associated circular-speed curve has a single, global maximum — as all realistic descriptions of the halos formed in cosmological N-body simulations do.

The goals of this thesis are two-fold: (1) to develop a general method for self-consistently comparing theoretical predictions between SMBH mass and properties of

the dark matter halo that measure the depth of the potential well, established at $z > 0$ via quasar-mode feedback, to the observed $M_{\rm BH}$–bulge property correlations observed at $z = 0$; (2) to derive a new critical SMBH mass required to clear gas out of a protogalaxy after quasar-mode accretion. Ultimately, model predictions for the SMBH correlations are obtained based on the physical model introduced above from McQuillin & McLaughlin (2012). There is inevitable intrinsic scatter around these model predictions, and this is important and contains physical information. However, the main focus here is establishing the "correct" trends for the SMBH correlations, around which the intrinsic scatter should be calculated, and not to characterise the scatter itself.

First of all, it is necessary to consider stellar and dark matter properties of $z = 0$ galaxies. This is the focus of Chapter 2, where simple models of two-component spherical galaxies are considered. In §2.1, results from cosmological simulations that connect the radii and masses of dark matter halos to each other and to total stellar masses are brought together, along with details of stellar and dark matter distributions. Combining these with data from the literature for early-type galaxies, average trends between various galaxy properties at $z = 0$ are obtained in §2.2. Properties that are considered include: total stellar masses, $M_{*,\rm tot}$; stellar effective radii, R_e; virial radii, $r_{\rm vir}$; halo virial masses, $M_{\rm d,vir}$; peak halo circular speeds, $V_{\rm d,pk}$; stellar mass fractions, $f_*(r)$; stellar velocity dispersions, $\sigma_{\rm ap}(R_e)$ and total (stars and dark matter) circular speeds, $V_c(r)$. The focal point is on stellar masses in the range $10^{10} M_\odot \lesssim M_{*,\rm tot} \lesssim 10^{12} M_\odot$, encompassing the SMBH data.

The next step involves relating the dark matter halo properties at $z = 0$, such as halo mass, $M_{\rm d,vir}$, and the maximum of the circular speed, $V_{\rm d,pk}$, to the corresponding properties at $z > 0$. Chapter 3 considers this in detail, making use of the halo progenitor evolution with redshift in §3.1. §3.2 considers how both $M_{\rm d,vir}$ and $V_{\rm d,pk}$ at $z > 0$ relate to the stellar properties at $z = 0$, with particular emphasis on stellar velocity dispersions and total stellar masses. Folding in a theoretical relation between $M_{\rm BH}$ and $V_{\rm d,pk}$ at $z > 0$, §3.3 details how to compare such a prediction to the observed correlations. Relations between SMBH mass and stellar velocity dispersion, total stellar

mass, total halo mass and combinations of velocity dispersion and effective radius, are all discussed in detail.

All current predictions for a critical SMBH mass required for gas blow-out make several simplifying assumptions (cf. §1.4.7). After establishing a general method for comparing such predictions to the observed $M_{\rm BH}$–bulge property correlations, it makes sense to derive new predictions with some of the assumptions relaxed. This is the main focus in Chapter 4, where a spherical three-component protogalaxy is considered. This allows for the presence of stars in the protogalaxy that contribute to the gravity containing the outflow, as well as a non-virialised gas. Neither of these have been considered before in detail. The full mathematical derivation of the new prediction is given in §4.1. This is then compared to previous results in §4.2, along with pulling together results from cosmological simulations and data that relate masses and radii of the three different components to each other. This enables the models to be constrained, which is useful for the examples used to illustrate the new result in §4.3. The focus of these examples is to show how different assumptions about the gas distribution are likely to influence the critical SMBH mass. The new prediction is also folded in with the general method devised in Chapters 2 and 3, so that it can be compared to the $M_{\rm BH}$–$\sigma_{\rm ap}(R_e)$ relation. Throughout Chapter 4, the new prediction is compared to equation (1.1).

Before getting into the details of this new work, a review of the current literature is given. Chapters 2 and 3 in particular bring together several different parts of the literature, as outlined above, so a comprehensive overview of all of this is essential. This is the purpose for the remainder of Chapter 1. §1.1 discusses the key ideas behind galaxy formation, including galaxy classifications, formation processes, cosmological parameters, dark matter distributions, halo concentrations and halo progenitors. §1.2 focuses on baryons in galaxies, with particular emphasis on the stars. Stellar distributions, mass ratios, scaling relations of stellar properties and population synthesis models are all discussed. The observational evidence of SMBHs and the correlations between $M_{\rm BH}$ and galaxy properties are reviewed in §1.3. Finally, §1.4 reviews the key physical concepts behind the theoretical models used to explain how the $M_{\rm BH}$–bulge relations are established.

1.1 Galaxy Formation

1.1.1 Galaxy classifications

Broadly speaking, there are three different types of galaxies; elliptical, spiral and irregular. Spirals and ellipticals are often further divided into subgroups, known as the Hubble (1926) sequence, shown in Figure 1.1 (also known as the tuning fork diagram). Elliptical galaxies are denoted En, with $n \equiv 10[1 - (b/a)]$ representing the degree of ellipticity (higher $n \longrightarrow$ flatter galaxy). In this expression, b/a is the ratio of minor-to-major axis length. The spirals are then split into two branches; those with (SB) and without (S) bar-like structures in their central regions. The lower case letters indicate how tightly wound the spiral arms appear to be and the bulge-to-disk luminosity ratio, B/D. Moving from left to right in Figure 1.1, B/D decreases. Lenticular galaxies, denoted S0, are very similar to ellipticals in appearance, but also have an extended disk-like structure. Hubble initially proposed this as an evolutionary sequence, with ellipticals flattening out and evolving into spirals. This is now known to be incorrect.

The Hubble sequence classifies galaxies purely based on their appearance. This morphological classification system can also be used to split galaxies into two categories: early-types and late-types. The early-types, consisting of elliptical and lenticular galaxies, generally contain little gas and dust, have no spiral arms and show little or no signs of star formation. On the other hand, late-type galaxies (spiral and irregular) show significant star formation, are generally made up of younger stars and have clear disk-like features.

The physical mechanisms of forming the central components may be different for early- and late-type galaxies. For example, Kormendy & Kennicutt (2004) argue that spirals could be classified by splitting into two groups; those with classical bulges and those with pseudo-bulges. They define classical bulges as being ellipticals living at the centre of disks. They define a pseudo-bulge based on the following characteristics:

- if the apparent flattening of the bulge is similar to that of the outer disk;

- if it has a Sérsic index (cf. §1.2.1) $n \lesssim 2$;
- if it is rotation-dominated, requiring $V_{\rm max}/\sigma > 1$, where $V_{\rm max}$ is the maximum rotation velocity and σ is the stellar velocity dispersion.

If any of these are evident, Kormendy & Kennicutt (2004) identify the central component as a pseudo-bulge. The more of the characteristics that apply, the more secure the classification becomes. More recently, Kormendy (2012) and Fisher & Drory (2015) have provided further classification criteria. These include constraints on the velocity dispersion, σ, and the bulge-to-total luminosity ratio, B/T: if $\sigma > 130\,{\rm km\,s^{-1}}$ (Fisher & Drory 2015) and/or $B/T \gtrsim 0.5$ (Kormendy 2012), then the bulge is definitely classical, otherwise it *could* be a pseudo-bulge. Classifying the galaxies in this way has implications for the black hole–bulge scaling relations discussed in §1.3.

Kormendy & Kennicutt (2004) suggest that classical bulges and pseudo-bulges have different formation histories. They say that pseudo-bulges are a product of the slow, secular evolution of galaxy disks, whereas classical bulges form in the same way as ellipticals, via major galaxy mergers. Despite these justifications from Kormendy & Kenicutt for classifying spirals in this way, it has been argued that many of the selection criteria do not require an alternative formation mechanism to be explained (Graham & Scott 2013; Graham & Scott 2015). From a kinematical view point, mergers between galaxies can form bulges with larger than average $V_{\rm max}/\sigma$ values (Bekki 2010; Keselman & Nusser 2012). It is also possible for bars to spin-up bulges, through exchange of angular momentum between the bar and the spheroid (Saha, Martinez-Valpuesta & Gerhard 2012). Both of these suggest that galaxy rotation might not necessarily indicate how the central component formed, as suggested by Kormendy & Kennicutt (2004).

Furthermore, the presence of inner spiral arms in the central regions does not necessarily require the presence of a pseudo-bulge (Eliche-Moral, Gonzalez-Garcia & Balcells 2011; dosAnjos & daSilva 2013). There is no doubt that bulges exist that exhibit various properties outlined above. However, it is unclear whether or not such bulges are formed in a different way or not.

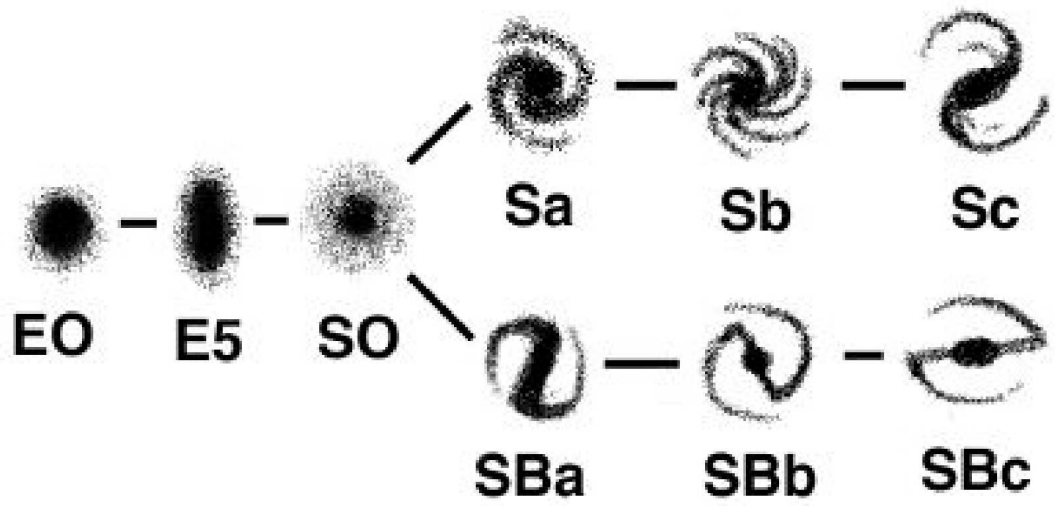

Figure 1.1: The Hubble (1926) sequence for classifying galaxies, also known as the tuning fork diagram. Elliptical galaxies are denoted by En, where $n \equiv 10[1 - (b/a)]$, represents the degree of ellipticity. The spirals are then split into two branches; the lower branch are spirals with bars (SB) and the upper branch are galaxies without bar-like structure (S). The lower case letters indicate how tightly wound the spiral arms are. Lenticular galaxies, similar in appearance to ellipticals, are denoted S0. Image source: pics-about-space.com/hubble-s-tuning-fork-diagram

1.1.2 Initial structure formation and feedback

Zwicky (1933) was the first to realise that galaxies and galaxy clusters were surrounded by large amounts of non-luminous matter, when he compared the mass-to-light ratio of the Coma cluster to the mass-to-light ratios in luminous parts of individual galaxies. These non-luminous components are now referred to as dark matter halos. As the name suggests, dark matter does not emit or interact with electromagnetic radiation. Although it cannot be observed directly, the gravitational effects on baryonic matter can be detected.

It is widely accepted that dark matter constitutes approximately 85% of all matter in the Universe (Planck Collaboration 2014). Astronomers generally favour the idea of Cold Dark Matter (CDM) — the dark matter particles move slowly compared to the speed of light — as simulations of galaxy formation with this form of dark matter generally show good agreement with observations, although hot dark matter is able to form structure too. The most recent observational results (Planck Collaboration 2014) yield cosmological parameters where the energy density of the Universe is shared between dark energy, $\Omega_\Lambda, 0 = 0.68$, dark matter, $\Omega_d, 0 = 0.271$ and baryonic matter, $\Omega_b, 0 = 0.049$, with a Hubble parameter of $H_0 = 67.1\,\mathrm{km\,s^{-1}\,Mpc^{-1}}$.

The large scale structures observed in the Universe all initially formed in the same way. In such a scenario, the early smooth Universe contains random density fluctuations (Harrison 1970; Zel'dovich 1972). These initial perturbations are evidenced by images of the cosmic microwave background (Smoot, Bennett & Kogut 1992). By resolving the structures of the density fluctuations, it was found that the CMB maps were consistent with predictions from Harrison (1970) and Zel'dovich (1972), that the distribution of the perturbations is Gaussian. These results have since been confirmed and refined by subsequent observations from the WMAP (Bennett, Halpern & Hinshaw 2003; Hinshaw, Nolta & Bennett 2007) and the *Planck* Collaboration (2014).

Once these perturbations become non-linear, their evolution is significantly more complicated. Empirical methods determining the statistical distribution of matter in the non-linear regime (Peacock & Dodds 1996; Heitmann et al. 2009), together with N-

body simulations (Klypin & Shandarin 1983; Springel, Di Matteo & Hernquist 2005), show a network of halos strung along walls and filaments forms, creating a cosmic web. To connect the initial density fluctuations to the non-linear structure observed in the Universe today, non-linear evolution needs to be considered.

Gunn & Gott (1972) and Gunn (1977) consider a simple, spherical model describing the growth and collapse of an initial perturbation. Gunn & Gott (1972) demonstrate that material surrounding a density perturbation in the early Universe can be bound to the perturbation and will fall into it. Gunn (1977) extends this by considering the equilibrium spatial distribution of the in-fallen material. Gunn demonstrates that dissipationless collapse (that is, the collapse of non-interacting particles) results in a quasi-equilibrium system, therefore linking the initial perturbation directly to an equilibrium state. This simple argument is more commonly referred to as the spherical top-hat collapse model.

The favoured theory for initial structure formation from density perturbations in the early Universe involves CDM (Peebles 1982; Bond, Szalay & Turner 1982; Blumenthal, Pagels & Primack 1982; Blumenthal et al. 1984). If it is cold, the dark matter component of the initial perturbation will have no pressure support, and therefore must undergo gravitational collapse, and hence the perturbations will grow. The collapsed objects lead to potential wells dominated by dark matter (the initial dark matter halos). A dark matter halo is supported against its own self-gravity by random motions of the constituent particles. In a hierarchical Universe, the first halos form from the initial, small-scale density fluctuations. Larger halos then form from the merging of these early generation halos. This is known as bottom-up formation: the smallest objects form first, and these merge to form the largest objects at later times.

Press & Schechter (1974) associated the dark matter halos with peaks in a Gaussian density field of dark matter in the early Universe. By using statistics of random Gaussian fields, they were able to derive a halo mass distribution. This distribution is such that the number of halos per unit volume in the mass range M to $M + dM$ is

$\delta M(dn/dM)$, where:

$$\frac{dn}{dM}(M,t) = \left(\frac{2}{\pi}\right)^{1/2} \frac{\rho_0}{M^2}\frac{\delta_c(t)}{\sigma(M)}\left[\frac{d\ln\sigma}{d\ln M}\right] \exp\left[-\frac{\delta_c^2(t)}{2\sigma^2(M)}\right]. \tag{1.2}$$

Here, ρ_0 is the mean density of the Universe, $\sigma(M)$ quantifies the variance in the density field, smoothed using a top-hat filter that contains, on average, a mass M, and $\delta_c(t)$ is the critical overdensity for a spherical top-hat collapse at time t. An extension of the Press-Schechter theory allows for a statistical description of the formation of dark matter halos (Lacey & Cole 1993). Specifically, the sequence of merging events, and the halo masses involved in those events, can be extracted. This relates the distribution of halo masses at two different redshifts, z_1 and z_2, that is then interpreted as a merger rate.

At the same time that initial dark matter halos are forming and merging, gaseous baryons fall into the halos. Unlike dark matter, baryons can emit radiation and cool down, settling toward the centre of the dark matter halos. As they do so, they form cool dense clouds, ultimately leading to star formation and hence small galaxies. This is the two-stage theory proposed by White & Rees (1978), containing many of the basic ideas behind modern galaxy formation theory. White & Rees (1978) realised that star formation (and hence galaxy formation) could not proceed with 100% efficiency in all dark matter halos. Observations provide evidence of this, in particular the total mass density in stars, $\Omega_{*,0} = (2.3 \pm 0.34) \times 10^{-3}$ (Cole et al. 2001), is much less than the total baryonic mass density of the Universe, with $\Omega_{*,0}/\Omega_{b,0} \simeq 0.047$.

More evidence is provided by the disagreement between the distribution of galaxy luminosities and the distribution of halo masses (Benson et al. 2003). There are many results from observations (Hudson et al. 1998; Guzik & Seljak 2002; Sheldon et al. 2004; Madelbaum et al. 2006) and simulations (Moster et al. 2010; Moster, Naab & White 2013; Behroozi, Conroy & Wechsler 2010; Behroozi, Wechsler & Conroy 2013) which indicate that star formation efficiency depends strongly upon halo mass. This is usually quantified by considering the global ratio of stellar-to-dark matter mass in central galaxies as a function of dark matter halo mass. Figure 1.2, taken from Berhoozi et al. (2013), compares several derivations from the literature of this function

at $z \approx 0$. Clearly there is good agreement over the non-monotonic shape, with a peak in $M_*/M_d \simeq 0.01$–0.05 at $M_{\rm d} \simeq 3 \times 10^{11} M_\odot$–$10^{12} M_\odot$. This implies that in both low- and high-mass halos, star formation is extremely inefficient.

Clearly a process is required that suppresses the formation of stars in both the smallest and largest galaxies. Such a process therefore needs to reheat the gas to prevent it from cooling. One way of doing this is for an ongoing physical process to inject significant quantities of energy and/or momentum into the gas, known as feedback. There are various flavours of feedback that span a range of processes including; reionization at very high redshifts, supernova explosions and input from active galactic nuclei (AGN). White & Rees (1978) invoked supernova feedback in dwarfs to explain the low efficiency of star formation in dwarf galaxies.

Supernovae can heat gas to temperatures $T \gtrsim 10^6\,{\rm K}$, at which it can escape from halos with circular speeds $\lesssim 100\,{\rm km\,s^{-1}}$ (Dekel & Silk 1986), corresponding to halo masses $M_{\rm d} \lesssim 10^{11} M_\odot$. Such feedback is therefore able to heat the gas to the extent that it escapes from the galaxy, suppressing star formation, in low-mass systems. As mass increases, the depth of the potential well increases, and less gas will escape. This will lead to more stars being formed, and hence a larger value of M_*/M_d. However, for massive galaxies, star formation is again inefficient and hence M_*/M_d is peaked. Supernova feedback has little effect on the formation for the largest systems, so this cannot explain the low efficiencies.

One popular idea for a feedback process in the most massive galaxies involves AGN, and more specifically their high redshift counterparts, quasars. The idea is that during the peak of quasar activity, at redshifts $z \sim 2$–4 (Richards et al. 2006; Hopkins, Richards & Hernquist 2007), powerful feedback from a central Super Massive Black Hole (SMBH) clears the gas out of a galaxy, preventing any further star formation. This ties in with the SMBH – bulge correlations and black hole feedback ideas that are discussed in §1.3. Most of the SMBH mass in large galaxies is grown during this quasar phase of Eddington (cf. §1.4.1) rate accretion (Soltan 1982; Yu & Tremaine 2002), at these high redshifts. Such accretion can lead to gas blow-out, halting further accretion onto the SMBH. This SMBH feedback is able to suppress star formation

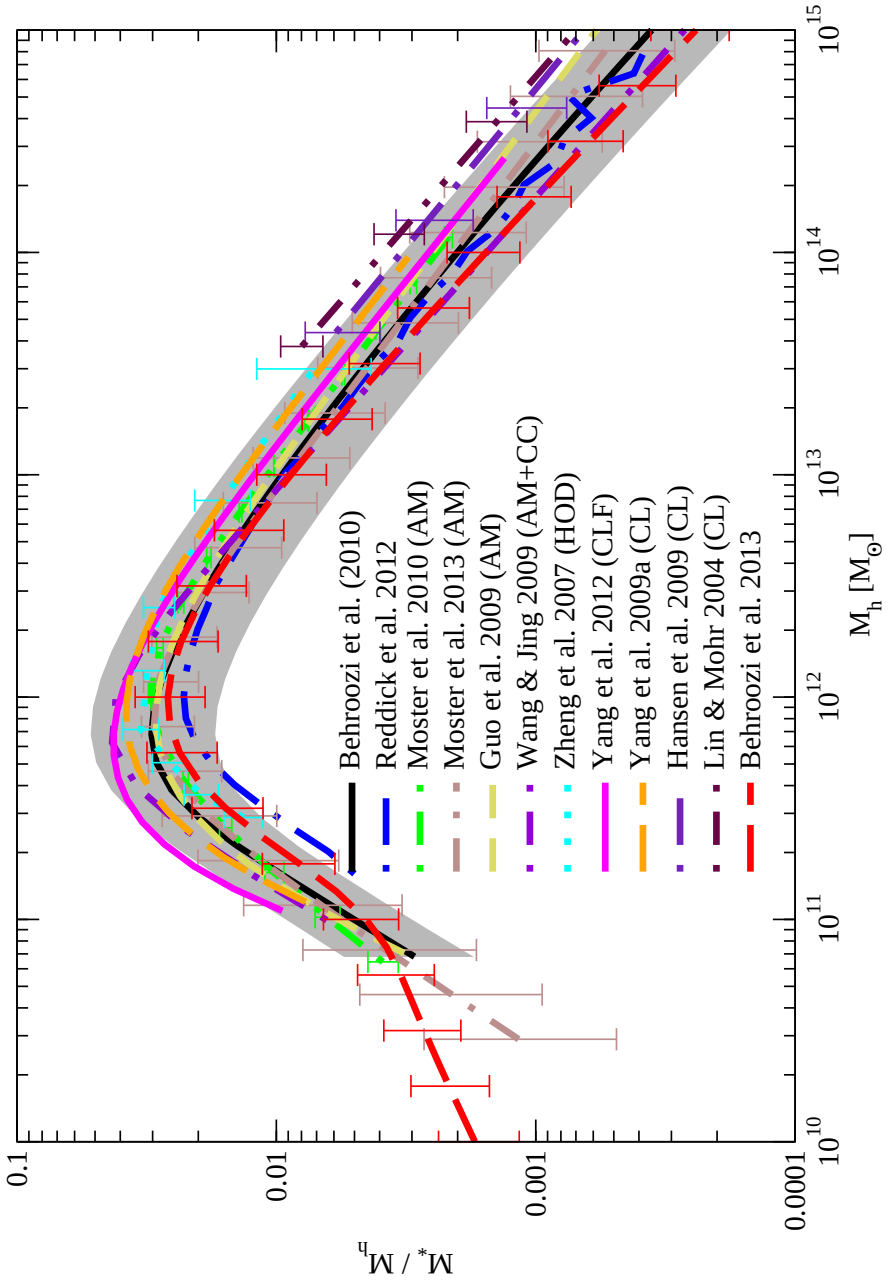

Figure 1.2: The global stellar-to-dark matter mass ratio as a function of dark matter halo mass. This Figure is taken from Behroozi et al. (2013), showing the results from several authors. There are different methods used to obtain M_*/M_d, including abundance matching, clustering constraints, halo occupation distribution modelling, conditional luminosity function and various results on galaxy clusters.

in the largest galaxies and entire clusters $10^{13}M_{\odot} \lesssim M_{\rm d} \lesssim 10^{15}M_{\odot}$. Simulations of galaxy formation using different recipes for this so called quasar-mode feedback appear equally able to reproduce observed correlations and consistently yield $z = 0$ galaxies with $M_{*,\rm tot} \lesssim 10^{12}M)_{\odot}$. The quasar-phase of galaxy formation is therefore essential for limiting the stellar masses of early-type galaxies that are observed at $z = 0$.

The main point in the context of the work presented here is that dark matter halos dominate the gravity ($M_*/M_d \ll 1$ for all halo masses). Hence, they are key to the containment (or not) of black hole feedback and determining the SMBH mass. Understanding the various properties of the dark matter halos is therefore essential to interpreting the present-day correlations between SMBH mass and stars.

Many simulations have investigated properties of CDM halos, using both analytical and N-body methods. These properties include halo density profiles (cf. §1.1.4; Dubinski & Carlberg 1991; Navarro et al. 1996, 1997; Dehnen & McLaughlin 2005), halo concentrations (cf. §1.1.5; Bullock et al. 2001; Zhao et al. 2009; Dutton & Maccio 2014) and merger histories (cf. §1.1.6; Lacey & cole 1993; van den Bosch 2002; Zhao et al. 2009; Giocoli et al. 2012; van den Bosch et al. 2014).

1.1.3 Virial radii and cosmological parameters

The virial radius, $r_{\rm vir}$, is often used to define the total extent of a dark matter halo. A spherical dark matter halo is said to be in virial equilibrium for $r \leq r_{\rm vir}$, where the virial theorem

$$2E_K = -E_P, \tag{1.3}$$

relating the kinetic energy, E_K, and the gravitational potential energy, E_P, is applicable. Given that $E_K \propto V^2$ and $E_P \propto M/R$, and folding in the Hubble law, $V = H_0R$, where H_0 is the Hubble constant, leads to the scaling $H_0^2 \propto M/R^3 \propto \rho$. This can be used to determine the virial radius by relating the density, $\rho_d(r)$, of the dark matter halo, to the critical density of the Universe, ρ_c — if $\rho_d(r)$ is $\Delta_{\rm vir}$ times ρ_c, the halo is

in virial equilibrium. For a halo at $z = 0$, this requires

$$\rho_d(r_{\rm vir}) \equiv \frac{3M_{\rm d,vir}}{4\pi r_{\rm vir}^3} = \Delta_{\rm vir}\rho_c = \Delta_{\rm vir}\frac{3H_0^2}{8\pi G}. \tag{1.4}$$

The constant of proportionality, $\Delta_{\rm vir}$, is referred to as the overdensity of a virialised sphere. For a matter dominated Universe ($\Omega_{\rm m} = 1$ with no cosmological constant), the overdensity can be found approximated analytically, with $\Delta_{\rm vir} \simeq 18\pi^2 \sim 178$ (Bertschinger 1987). This classic result is why the radius r_{200} is commonly referred to in the literature as a virial radius (cf. §1.1.5), although strictly speaking, r_{200} corresponds to an overdensity of $\Delta = 200$.

For a (Λ)CDM Universe, calculating $\Delta_{\rm vir}$ is somewhat more complicated, and depends on the cosmological parameters chosen. Bryan & Norman (1998) provide a fitting formula for the overdensity in a Universe dominated by a cosmological constant. Assuming a flat Universe, with a cosmological constant ($\Omega_{\rm m} + \Omega_\Lambda = 1$), the Bryan & Norman (1998) formalism gives $\Delta_{\rm vir}$ as a function of redshift:

$$\Delta_{\rm vir}(z) \equiv \frac{2\,GM(r_{\rm vir})}{H^2(z)\,r_{\rm vir}^3} = 18\pi^2 + 82[\Omega_{\rm m}(z) - 1] - 39[\Omega_{\rm m}(z) - 1]^2, \tag{1.5}$$

with

$$\Omega_{\rm m}(z) = \frac{\Omega_{\rm m,0}(1+z)^3}{[H(z)/H_0]^2} \quad \text{and} \quad \frac{H(z)}{H_0} = [\Omega_{\rm m,0}(1+z)^3 + \Omega_{\Lambda,0}]^{1/2}. \tag{1.6}$$

The cosmological parameters from the *Planck* 2013 results (Planck Collaboration 2014) are $h_0 = 0.67$ with $\Omega_{m,0} = 0.32$ (which includes a baryon density of $\Omega_{b,0} = 0.049$) and $\Omega_{\Lambda,0} = 0.68$. The virial overdensity from equation (1.5) is then $\Delta_{\rm vir}(0) \simeq 104$ at $z = 0$, increasing to higher redshift with an upper limit of $\Delta_{\rm vir}(z) < 18\pi^2 \simeq 178$.

1.1.4 Dark matter density distributions

Ostriker, Peebles & Yahil (1974) tabulated galaxy masses for local giant spirals as a function of radius, and found that the masses increase linearly with r up to tens and hundreds of kiloparsecs. Observations show that the total circular speed curves of

many galaxies remain flat out to large radii, beyond the extent of the luminous matter (Rubin, Ford & Thonnard 1980; Burstein 1982). By definition, the circular speed for a spherical distribution is $V_c^2(r) = GM(r)/r$, where $M(r)$ is the total gravitating mass enclosed within a radius r, so this observation is consistent with the findings of Ostriker et al. (1974).

Given the observation that $M(r) \propto r$ (approximately), a good zeroth-order approximation for describing galaxies including dark matter is the Singular Isothermal Sphere (SIS). The density and mass profiles for an SIS distribution are given by

$$\rho(r) = \frac{\sigma_0^2}{2\pi G r^2} \qquad \text{and} \qquad M(r) \equiv \int_0^r 4\pi u^2 \rho(u) du = \frac{2\sigma_0^2 r}{G}, \tag{1.7}$$

where σ_0 is the velocity dispersion of the halo. The circular speed profile of an SIS halo is therefore constant at all radii:

$$V_c^2(r) = \frac{GM(r)}{r} = 2\sigma_0^2. \tag{1.8}$$

For such a simple model, this shows remarkable agreement with observations of real halos (Rubin et al. 1980; Burstein 1982).

However, the SIS has $\rho(r) \propto r^{-2}$ everywhere, so the mass increases linearly with r out to infinitely large radii. In analytical calculations, a truncated SIS is used by observers, where outside some radius (e.g. the virial radius), the mass is taken to be zero. It is also true that the SIS is only a good approximation for the total gravitational matter (baryonic and dark matter). As will be discussed further in §1.2, the baryons in galaxies are not distributed isothermally. Thus, the dark matter halos themselves can not be isothermal either. Indeed, simulated dark matter halos generally have density profiles that are shallower than isothermal at small radii, and steeper at large radii.

Fitting functions used to describe simulated non-isothermal dark matter density profiles are generally two parameter models (normally a scale radius and mass enclosed within a scale radius), with a double power-law behaviour, in the sense that $\rho_d(r) \sim r^{-\gamma}$ for small radii and $\rho_d(r) \sim r^{-\beta}$ for large radii. In general, simulated halos are best fitted when $\gamma < 2$, and $\beta > 2$. In this context, there will be a single, well defined radius in a fitting function at which the logarithmic slope of the density is $d\ln\rho/d\ln r \equiv -2$.

This radius is denoted here as r_{-2}. Non-isothermal halos described by functions of this nature also lead to circular speed curves, $V_c(r)$, that are peaked (at a radius $r_{\rm pk} \neq r_{-2}$). Asymptotically, $V_c^2 \rightarrow r^{2-\gamma}$ at small radii, and $V_c^2 \rightarrow r^{2-\beta}$ at large radii. Given the limits of $\gamma < 2$ and $\beta > 2$, this naturally leads to a function with a maximum.

Figure 1.3 shows the density (top panel), mass (middle panel) and circular speed (bottom panel) profiles for a variety of functions used to fit simulated cold dark matter halos. These are all normalised to values at the scale radius, r_{-2}, with $\rho_{-2} \equiv \rho_d(r_{-2})$, $M_{-2} \equiv M_d(r_{-2})$ and $V_{-2} \equiv V_{\rm c,d}(r_{-2})$. For comparison, the SIS profiles are also included, shown by the dotted black line in each panel.

The solid red line in each of the panels corresponds to a model developed by Hernquist (1990) for describing the light distributions in early-type galaxies. Dubinski & Carlberg (1991) used this profile as a fit to their simulated dark matter halos. The density of the Hernquist (1990) profile is given by

$$\rho_d(r) = \frac{M_{\rm tot}}{2\pi r_0^3} \left(\frac{r}{r_0}\right)^{-1} \left(1 + \frac{r}{r_0}\right)^{-3}, \tag{1.9}$$

where $M_{\rm tot}$ is the total mass, r_0 is a scale radius and $r_{-2} = r_0/2$. The mass profile, given by

$$M_d(r) \equiv \int_0^{r/r_0} 4\pi u^2 \rho_d(u) du = M_{\rm tot} \left(\frac{r/r_0}{1 + r/r_0}\right)^2, \tag{1.10}$$

leads to a circular speed profile that, unlike the SIS, varies with radius;

$$V_{\rm c,d}^2(r) \equiv \frac{GM_d(r)}{r} = \frac{GM_{\rm tot}}{r_0} \frac{r/r_0}{(1 + r/r_0)^2}. \tag{1.11}$$

This clearly leads to a peaked circular-speed curve, at a radius $r_{\rm pk}/r_0 = 1$. Equation (1.11) is shown by the solid red line in the bottom panel of Figure 1.3.

Navarro, Frenk & White (1996) performed high resolution simulations to investigate dark matter halo formation for a range of halo masses. They identified halos as collapsed spheres, with the radius of each sphere encompassing an overdensity of $\Delta = 200$. They found that the density profiles were well fitted down to $0.01 r_{200}$ by the same model, for halo masses $10^{11} M_\odot \lesssim M_{200} \lesssim 10^{15} M_\odot$. The dark matter profile of Navarro, Frenk & White (1996, 1997, NFW), shown by the solid black line in Figure

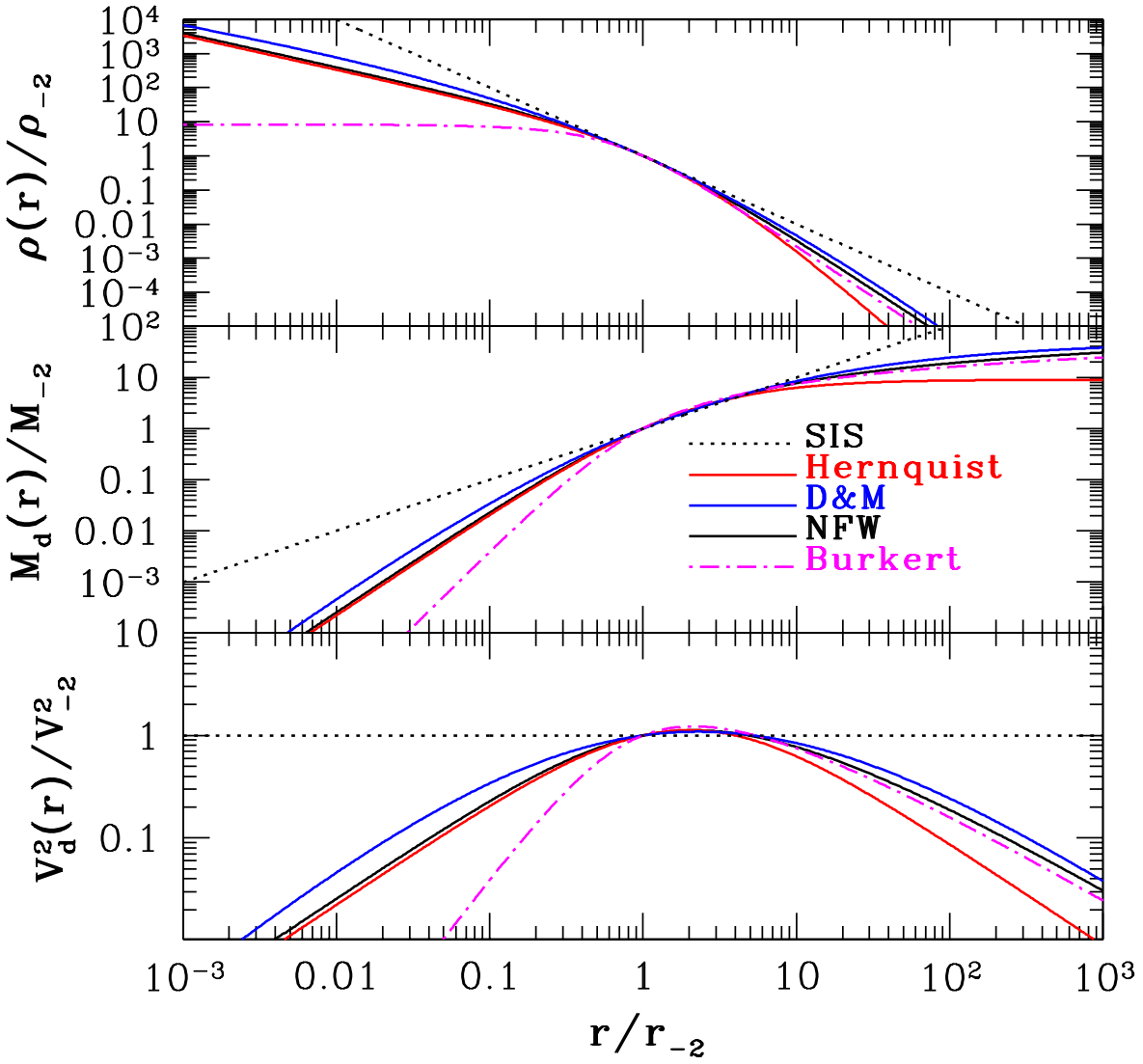

Figure 1.3: Density, $\rho_d(r)$ [top panel], mass, $M_d(r)$ [middle panel], and circular speed, $V_{\rm c,d}(r)$ [bottom panel] profiles for SIS (dotted black line), Hernquist (solid red line), Dehnen & McLaughlin (solid blue line), NFW (solid black line), and Burkert (dot-dash magenta line) models for dark matter halos. The x axis is normalised to the scale radius, r_{-2} [the radius at which the logarithmic slope of the density profile is $d\ln\rho/d\ln r = -2$], and the profiles are normalised to their values at this scale radius.

1.3, is given by

$$\rho_d(r) = 4\rho_0 \left(\frac{r}{r_0}\right)^{-1} \left(1 + \frac{r}{r_0}\right)^{-2}, \tag{1.12}$$

where r_0 is a scale radius, $\rho_0 \equiv \rho(r_0)$ and $r_{-2} = r_0$. This profile has the same slope as a Hernquist (1990) profile at small radii, but is shallower at large radii, as shown in the top panel of Figure 1.3. The NFW profile is as good a fit to simulated halos from Dubinski & Carlberg (1991) as the Hernquist (1990) profile.

The mass distribution for an NFW profile is given by

$$M_d(r) = 16\pi\rho_0 r_0^3 \left[\ln\left(1 + \frac{r}{r_0}\right) - \frac{r/r_0}{1 + r/r_0}\right], \tag{1.13}$$

leading to the circular speed profile

$$V_{\rm c,d}^2(r) = \frac{16\pi\rho_0 r_0^2}{r/r_0} \left[\ln\left(1 + \frac{r}{r_0}\right) - \frac{r/r_0}{1 + r/r_0}\right]. \tag{1.14}$$

At large radii, the mass profile for an NFW halo increases logarithmically to infinity. The circular speed once again has a singular peak, at $r_{\rm pk}/r_0 \simeq 2.16258$, shown in the bottom panel of Figure 1.3 (solid black line).

Dehnen & McLaughlin (2005) developed a family of halo models, motivated by the fact that $\rho_d(r)/\sigma_r^3(r)$ is a power-law in radius for simulated dark matter halos

$$\frac{\rho_d(r)}{\sigma_r^3(r)} \propto r^{-\alpha}, \tag{1.15}$$

over the full numerically resolved range. Taylor & Navarro (2001) were the first to notice this, finding $\alpha = 1.875$. Other studies have confirmed that $\rho_d(r)/\sigma_r^3(r)$ is a power-law in radius, with an exponent $\alpha \simeq 1.9 \pm 0.05$ (Diemand, Moore & Stadel 2004; Rasia, Tormen & Moscardini 2004; Ascasibar et al. 2004).

Combining the constraint on $\rho_d(r)/\sigma_r^3(r)$ with the anisotropic Jeans equation [cf. §1.3.2; equation (1.49)], the general density profile is given by

$$\rho_d(r) = \frac{(40/9) - 2\beta_0}{8\pi} \frac{M_{\rm tot}}{r_0^3} \left(\frac{r}{r_0}\right)^{-(7+10\beta_0)/9} \left[1 + \left(\frac{r}{r_0}\right)^{2(2-\beta_0)/9}\right]^{-3(2+\beta_0)}, \tag{1.16}$$

where β_0 is the central velocity anisotropy. For $\beta_0 = 0$ (velocity isotropy at $r = 0$), the density profile becomes

$$\rho_d(r) = \frac{5}{9\pi}\frac{M_{\rm tot}}{r_0^3}\left(\frac{r}{r_0}\right)^{-7/9}\left[1+\left(\frac{r}{r_0}\right)^{4/9}\right]^{-6}, \tag{1.17}$$

such that $r_{-2} = (11/13)^{9/4} r_0 \simeq 0.68669 r_0$. Integrating this leads to the mass distribution

$$M_d(r) = M_{\rm tot}\left[\frac{(r/r_0)^{4/9}}{1+(r/r_0)^{4/9}}\right]^5, \tag{1.18}$$

and the circular speed profile

$$V_{\rm c,d}^2(r) = GM_{\rm tot}r_0\,\frac{(r/r_0)^{11/9}}{\left[1+(r/r_0)^{4/9}\right]^5}. \tag{1.19}$$

This peaks at $r_{\rm pk}/r_0 = (11/9)^{9/4} \simeq 1.57068$.

The Dehnen & McLaughlin (2005) profiles are represented by the solid blue lines in Figure 1.3. At small radii, $\rho_d(r) \propto r^{-7/9}$, shallower than both the Hernquist (1990) and NFW profiles, and at large radii, $\rho_d(r) \propto r^{-31/9}$, intermediate between the other two. However, the (4/9)ths power of radius leads to a more gradual roll-over around the scale radius, hence the Dehnen & McLaughlin (2005) halo sits above the other two in the top panel of Figure 1.3. This is also seen in the circular-speed curve (bottom panel), where the smoother roll-over leads to a broader peak for the Dehnen & McLaughlin (2005) circular speed.

The three halos described above are all quite similar. They all have cuspy centres, so the dark matter density rises without limit to the centre, and have large radii density slopes, $d\ln\rho_d/d\ln r = 3$–4. The central cusps are consistent with simulated halos, but these have limitations. Even the highest resolution simulations can only resolve halo structure to approximately 0.1% of the virial radius. It is therefore possible that halo densities become even shallower at unresolved radii.

The Einasto (1965) density profile, first advocated in the context of dark matter density distributions by Graham et al. (2006), is

$$\rho(r) = \rho_{-2}\ \exp\left\{-\frac{2}{\alpha}\left[\left(\frac{r}{r_{-2}}\right)^{\alpha}-1\right]\right\}, \tag{1.20}$$

where r_{-2} is a scale radius, and $\rho_{-2} \equiv \rho(r_{-2})$. The third parameter, α (the Einasto shape parameter), depends weakly on total halo mass (Dutton & Macció 2014). For halo masses in the range $\sim 10^{10}$–$10^{15} M_{\odot}$, the shape parameter has values $\alpha \sim 0.15$–0.25. Due to this extra free parameter, the mass profile involves an incomplete gamma function, dependent on r/r_{-2} and α [see Retana-Montenegro et al. (2012) for more details]. The Einasto density profile tends to a constant value as $r \longrightarrow 0$, a result that is allowed by the resolution of the cosmological simulations. In the context of fitting dark matter halo distributions, the Einasto profile performs no better than the Dehnen & McLaughlin profile, when β_0 (the central velocity anisotropy) is used as a third parameter (Dehnen & McLaughlin 2005; Graham et al. 2006).

Burkert (1995) investigated the mass and circular-speed profiles in four dwarf galaxies. He found that the observed mass profiles are well fitted over the whole observed radius range by the phenomenological density distribution:

$$\rho_d(r) = \rho_0 \left[1 + \frac{r}{r_0}\right]^{-1} \left[1 + \frac{r^2}{r_0^2}\right]^{-1}, \tag{1.21}$$

where r_0 is a scale radius, $\rho_0 \equiv \rho_d(r_0)$ and $r_{-2} \simeq 1.52138 r_0$. Therefore, the mass profile is

$$M_d(r) = 2\pi\rho_0 r_0^3 \left[\ln(1 + r/r_0) + \frac{1}{2}\ln(1 + r^2/r_0^2) - \tan^{-1}(r/r_0)\right], \tag{1.22}$$

and the circular speed is

$$V_{\rm c,d}^2(r) = \frac{2\pi G\rho_0 r_0^2}{r/r_0} \left[\ln(1 + r/r_0) + \frac{1}{2}\ln(1 + r^2/r_0^2) - \tan^{-1}(r/r_0)\right]. \tag{1.23}$$

The Burkert (1995) halo, shown by the dot-dash magenta line in Figure 1.3, has a central density core (for large radii, $\rho_d(r) \propto r^{-3}$, the same as the NFW halo). Burkert & Silk (1997) propose that the halos of dwarf galaxies could well be cored. Modelling a dwarf galaxy with luminous and non-luminous baryonic matter, along with an extended dark matter halo, they suggest that the halo could undergo adiabatic contraction within a "core" radius, r_c, if the non-luminous baryonic component has comparable mass inside r_c. More recently, Pontzen & Governato (2012) suggest that initially steep density cusps in low-mass systems could be flattened to shallower profiles via galactic

winds from stellar feedback. As with the cuspy halos, the circular speed curve is again peaked, at $r_{\rm pk}/r_0 \simeq 3.24713$ [see Figure 1.3, bottom panel].

From the four halos introduced, Hernquist, NFW and Burkert profiles are all two parameter models, defined by a scale radius, and a mass within the scale radius.

1.1.5 Halo concentrations

The dark matter halo concentration is generally defined as the ratio of some over density radius (e.g. $r_{\rm vir}$ or r_{200}) to some scale radius (e.g. r_s or r_{-2}). It therefore connects the environment of a dark matter halo (i.e., $\rho_{\rm vir}$, $r_{\rm vir}$) to the internal structure. In the context of the work presented here, it provides a way to calculate the scale radius, r_{-2}, if the virial radius is known. N-body simulations of CDM structure formation consistently show that the concentration depends on halo mass, with more massive halos having lower concentrations on average (Navarro, Frenk & White 1996; Navarro, Frenk & White 1997; Bullock et al. 2001; Eke, Navarro & Steinmetz 2001; Macció, Dutton & van denBosch 2008; Dutton & Macció 2014). This mass dependence is typically found to be weak; most results are consistent with $c_{\rm vir} \equiv r_{\rm vir}/r_{\rm s} \propto M_{\rm d,vir}^{-0.1}$, with significant intrinsic scatter around this average trend. The redshift evolution has also been investigated by several authors (Bullock et al. 2001; Zhao et al. 2003b; Prada et al. 2012; Dutton & Macció 2014), with general agreement that at higher redshift, the mass dependence of $c_{\rm vir}$ becomes even weaker. Most of these simulations are only reliable for $z \lesssim 4$–5 and it is unclear how the concentration depends on $M_{\rm vir}$ for redshifts greater than this.

One way to calculate the concentration is by fitting a model (e.g. NFW) to the spherically averaged density profile of a halo. As discussed in the previous Section, the model dark matter halos are specified by two parameters: r_s and the mass within this radius, $M_d(r_s)$. Both of these are linked to the total halo mass, defined to be the virial mass [or $M_d(r_{200})$]. Given this, the ratio $c_{\rm vir} \equiv r_{\rm vir}/r_s$ (or $c_{200} = r_{200}/r_s$) is then calculated. However, the fitting process can be difficult, leading to underestimates of the halo concentration (Prada et al. 2012). This will occur if the fitting starts too

close to the centre, where the resolution is insufficient. The central density will be underestimated, leading to concentration values that are too low.

An alternative method considers the ratio of the peak of the circular-speed curve, $V_{\rm d,pk} \equiv V_{\rm d}(r_{\rm pk})$, to the virial circular-speed, $V_{\rm d,vir}$ or $V_{\rm d,200}$. Considering the circular-speed profiles in the bottom panel of Figure 1.3, where the radii are normalised to r_{-2}, this ratio can be written as

$$\left[\frac{V_{\rm d,pk}}{V_{\rm d,vir}}\right]^2 = \left[\frac{M_d(r_{\rm pk}/r_{-2})}{M_d(r_{\rm vir}/r_{-2})}\right] \frac{r_{\rm vir}/r_{-2}}{r_{\rm pk}/r_{-2}}. \tag{1.24}$$

The value of $r_{\rm pk}/r_{-2}$ is known for any specified dark matter halo (cf. §2.1.5). If the ratio $V_{\rm d,pk}/V_{\rm d,vir}$ is known, then the ratio $r_{\rm vir}/r_{-2}$ can be found numerically.

Dutton & Macció (2014) also consider the halo dependence of their derived concentrations. They compare NFW halo models to Einasto (1965) profiles, calculating r_{200}/r_{-2} for both. They find that concentration values do depend systematically on the choice of halo model, but only at the $\sim 10\%$ level at $z = 0$. In the context of the work presented here, the concentration dependence on both redshift and halo mass needs to be considered. This needs to be accounted for when connecting the dark matter halo properties in protogalaxies at $z > 0$ to the SMBHs at the same redshifts and to the observed $z = 0$ properties of galaxies.

1.1.6 Halo progenitors

If an SMBH at the centre of a protogalaxy ended its main quasar phase of growth by accretion at a redshift $z > 0$, with a mass determined by some global property of the dark matter halo at that time, then it is necessary to consider halos at higher redshifts. This makes it possible to relate any property at that earlier redshift to the property in the galaxy at $z = 0$ (which is what the observed BH–bulge relations will reflect).

The formation history of any given dark matter halo is characterised by its merger tree, describing how the progenitors merge and accrete over cosmic time. Merger trees can be constructed in one of two ways; from N-body simulations or from repeated realisations based on the extended Press-Schechter formalism (Press & Schechter 1974;

Bond et al. 1991; Bower 1991; Lacey & Cole 1993). As discussed in §1.1.2, the Press-Schechter formalism allows the dark matter halo mass distribution to be estimated. An extension of this allows for calculations of other properties of dark matter halo populations, including progenitor mass distribution, merger rates and clustering properties. The analytical nature of the Press-Schechter formalism leads to a better understanding of how properties of halo population relate to the cosmological framework. However, it is a non-rigorous method, hence why repeated realisations are required and why it is often used along side N-body simulations.

Tracing a merger tree back in time, each halo splits into progenitor halos, which themselves break up into progenitors and so on. There are different ways to define the "main" progenitor of a given halo. Some studies define it as the most *massive* progenitor (at a particular redshift) of the descendant halo (van den Bosch 2002; McBride, Fakhouri & Ma 2009; Fakhouri, Ma & Boylan-Kolchin 2010; Behroozi & Silk 2015; van den Bosch et al. 2014a), whereas others define it as the progenitor that contributes the most mass to the descendant halo (Wechsler et al. 2002; Zhao et al. 2003b; Zhao et al. 2003a; Zhao et al. 2009; Giocoli, Tormen & Sheth 2012). In the analytical EPS formalism, these definitions are assumed to be identical, but in numerical simulations this is not always true. To illustrate this, van den Bosch et al. (2014) give an example scenario. Consider two progenitors of a descendant halo with mass M: progenitor A with mass $M_A = 0.53M$ and progenitor B with mass $M_B = 0.51M$. Suppose B contributes all of its mass to the descendant, whereas A only contributes $0.49M$ (with the remaining $0.04M$ outside the boundary of the descendant halo). In such a situation, A is the most massive progenitor, whereas B is the most contributing progenitor of the descendant halo. With respect to using the most massive progenitor, the most contributing progenitor under-predicts halo masses for $z \gtrsim 1.5$, with differences of $\Delta \log\langle M(z)/M_0\rangle \simeq 0.1$–$0.2$ (Zhao et al. 2009; Giocoli, Tormen & Sheth 2012; van den Bosch et al. 2014a). The main branch of the merger tree is identified as the one containing the main progenitors. This main branch is referred to as the Mass Accretion History (MAH) of a dark matter halo and is used to define halo formation times.

There have been numerous studies of the MAHs of dark matter halos, revealing

several trends. One of these is that MAHs generally consist of two distinct phases: an initial rapid growth phase, followed by a later phase of slower growth (Zhao et al. 2003b; Zhao et al. 2003a; Tasitsiomi et al. 2004; Li et al. 2007). The early, rapid growth is characterised by major mergers, whereas the halo growth in the slower phase is primarily due to minor mergers. Studies also consistently find that more massive halos assemble their mass at later times, as a result of hierarchical structure formation in CDM cosmology (van den Bosch 2002; Maulbetsch et al. 2007; Zhao et al. 2009; Fakhouri, Ma & Boylan-Kolchin 2010; Giocoli, Tormen & Sheth 2012; van den Bosch et al. 2014a).

van den Bosch et al. (2014a) compare results from N-body simulations and EPS merger trees and find the two to be consistent. This is demonstrated in Figure 1.4, taken from the van den Bosch et al. paper. They have extracted halo assembly redshifts, z_f, defined as the redshift at which the most massive progenitor of a halo (with mass M_0 at $z = 0$) has a mass fM_0. The Figure shows results for $f = 0.5$ and $f = 0.04$ as indicated, with the red circles representing the median results obtained for the merger trees and the solid blue line show the results from the N-body simulations. For $z = 0$ halo masses $10^{15}M_\odot \gtrsim M_0/h^{-1} \gtrsim 10^{11}M_\odot$, van den Bosch et al. (2014a) find $z_{0.5} \sim 0.5$–1.5 and $z_{0.04} \sim 2$–5. They also compare their results to the prediction of Giocoli, Tormen & Sheth (2012), shown by the dashed green line. Different definitions of the main progenitor halo are used, with van den Bosch et al. using the most massive, and Giocoli et al. using the most contributing. The two agree very well for the $f = 0.5$ case, but the Giocoli et al. result somewhat under-predicts the $f = 0.04$ result from van den Bosch et al. The fact that z_f is a decreasing function of halo mass at $z = 0$ reflects the bottom-up nature of structure formation in ΛCDM cosmology — the largest structures form most recently.

In the context of SMBH feedback, it is the depth of the potential well, measured by the maximum circular-speed of the dark matter halo, $V_{\rm d,pk}$, that determines the critical SMBH mass that is required for quasar-mode blow-out. It is therefore the redshift evolution of $V_{\rm d,pk}$ that needs to be considered here.

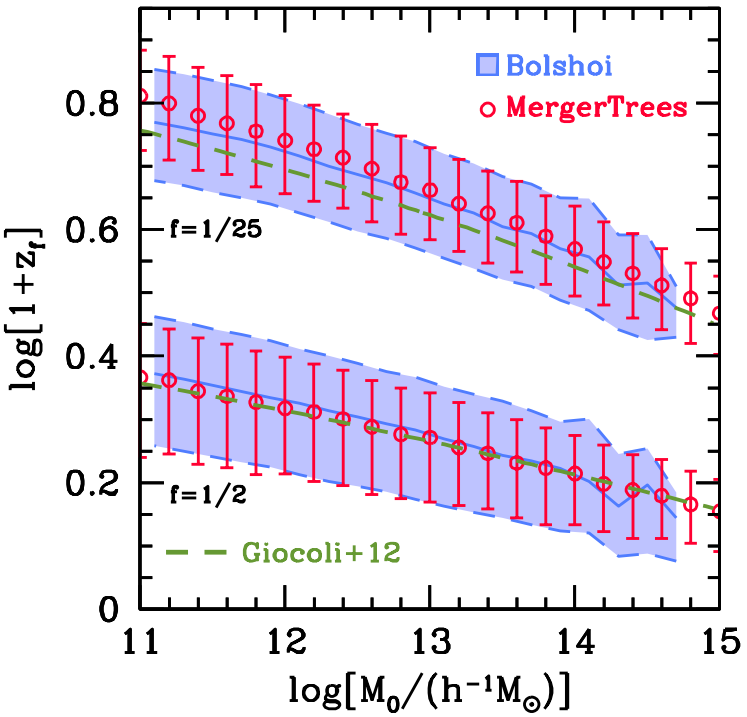

Figure 1.4: Figure taken from van den Bosch et al. (2014), showing halo formation redshifts, z_f, as a function of halo mass, M_0, for $f = 0.04$ and $f = 0.5$ as indicated in the Figure. The solid blue line indicates the median value from the simulations used by the authors, with the shaded blue region indicating the 68 percent confidence intervals. The red open circles are the median formation redshifts obtained for the EPS merger trees, the error bars reflecting the 68% range. The green dashed lines are the model predictions of Giocoli et al. (2012). This Figure demonstrates the good agreement between the merger tree and simulation results from van den Bosch et al.

1.2 Baryons in galaxies

Although the dark matter halos dominate the gravity of extra-galactic systems, it is baryonic matter in galaxies that is directly observed. In particular, the observed SMBH correlations in $z = 0$ quiescent galaxies involve stars, rather than the dark matter. In this context, the details of the stellar distribution, the amount of stars and interdependences between stellar properties all need to be considered. Ultimately, the stellar properties of $z = 0$ early-type galaxies need to be connected to properties of the dark matter halos at $z = 0$ and higher redshifts, to allow a critical SMBH mass prediction to be compared to the observed SMBH correlations at $z = 0$.

1.2.1 Stellar distributions

The distribution of light in early-type galaxies has been studied in great detail over the years. de Vaucouleurs (1948) proposed the classic $R^{1/4}$ law to fit the surface brightness profiles for three giant ellipticals:

$$I(R/R_e) = I_e \exp\left\{-7.669\left[(R/R_e)^{1/4} - 1\right]\right\}. \tag{1.25}$$

Here, R_e is the effective radius, the projected radius from within which half of the light of the system is emitted and I_e is the surface brightness at R_e. Kormendy (2012) suggested that this law provided the best fit for surface brightness profiles in all early-type galaxies. However, as more data became available, it was eventually realised that the $R^{1/4}$ law was only applicable for an intermediate range of surface brightness (Schombert 1986; Graham et al. 1996; Graham & Colless 1997).

A more flexible model is the Sérsic (1968) profile:

$$I(R/R_e) = I_e \exp\left\{-b_n\left[(R/R_e)^{1/n} - 1\right]\right\}. \tag{1.26}$$

n is the Sérsic index and the constant b_n is chosen to satisfy the definition of the effective radius:

$$\int_0^{R_e} 2\pi R I(R) dR = \frac{1}{2}\int_0^{\infty} 2\pi R I(R) dR. \tag{1.27}$$

Generally, this must be determined numerically, but is approximated with error less than $\simeq 10^{-6}$ by

$$b(n) = 2n - \frac{1}{3} + \frac{4}{405n} + \frac{46}{25515n^2}, \tag{1.28}$$

over the range $1 \leq n \leq 10$ (Ciotti & Bertin 1999).

Figure 1.5 shows surface brightness profiles for different values of the Sérsic index [$n = 1, 3, 4, 5$ and 7 respectively, with line colours indicated in the Figure], as a function of projected radius, R, normalised to R_e. For $n = 1$, equation (1.26) reduces to the exponential profile, used to describe the surface brightness distribution of dwarf galaxies. The $n = 4$ case is the classic de Vaucouleurs law. Makino, Akiyama & Sugimoto (1990) found that, for the range of radii usually investigated in observations — approximately $0.1 \leq R/R_e \leq 100$ (Ciotti 1991) — it is difficult to distinguish between de Vaucouleurs law and equation (1.26) for $3 \leq n \leq 7$.

Introducing n as a free parameter to move from the $R^{1/4}$ law to a generalised de Vaucouleurs law [equation (1.26)], had the unsurprising consequence of improved fits for surface brightness profiles. Caon, Capaccioli & D'Onofrio (1993) were the first to investigate correlations between the Sérsic n and global photometric parameters, namely the effective radius and total luminosity. Such correlations have implications for the connections between other stellar properties in early-type galaxies, discussed further in §1.2.3.

1.2.2 Stellar-to-dark matter mass ratios

The "global" baryon-to-dark matter mass ratio in a galaxy is often defined at the virial (or some nearby overdensity) radius. One might naively assume that this would be at or close to the cosmic average baryon fraction, $f_b \equiv \Omega_{\rm b,0}/\Omega_{\rm m,0}$ ($\simeq 0.15$ for Planck 2013 cosmology). However, there is a well-documented "missing baryons" problem (McGaugh et al. 2010), the global mass ratios only reach cosmic values on cluster size scales. The mass ratio then decreases systematically with decreasing halo mass (McGaugh et al. 2010; Zhang et al. 2011; Gonzalez et al. 2013).

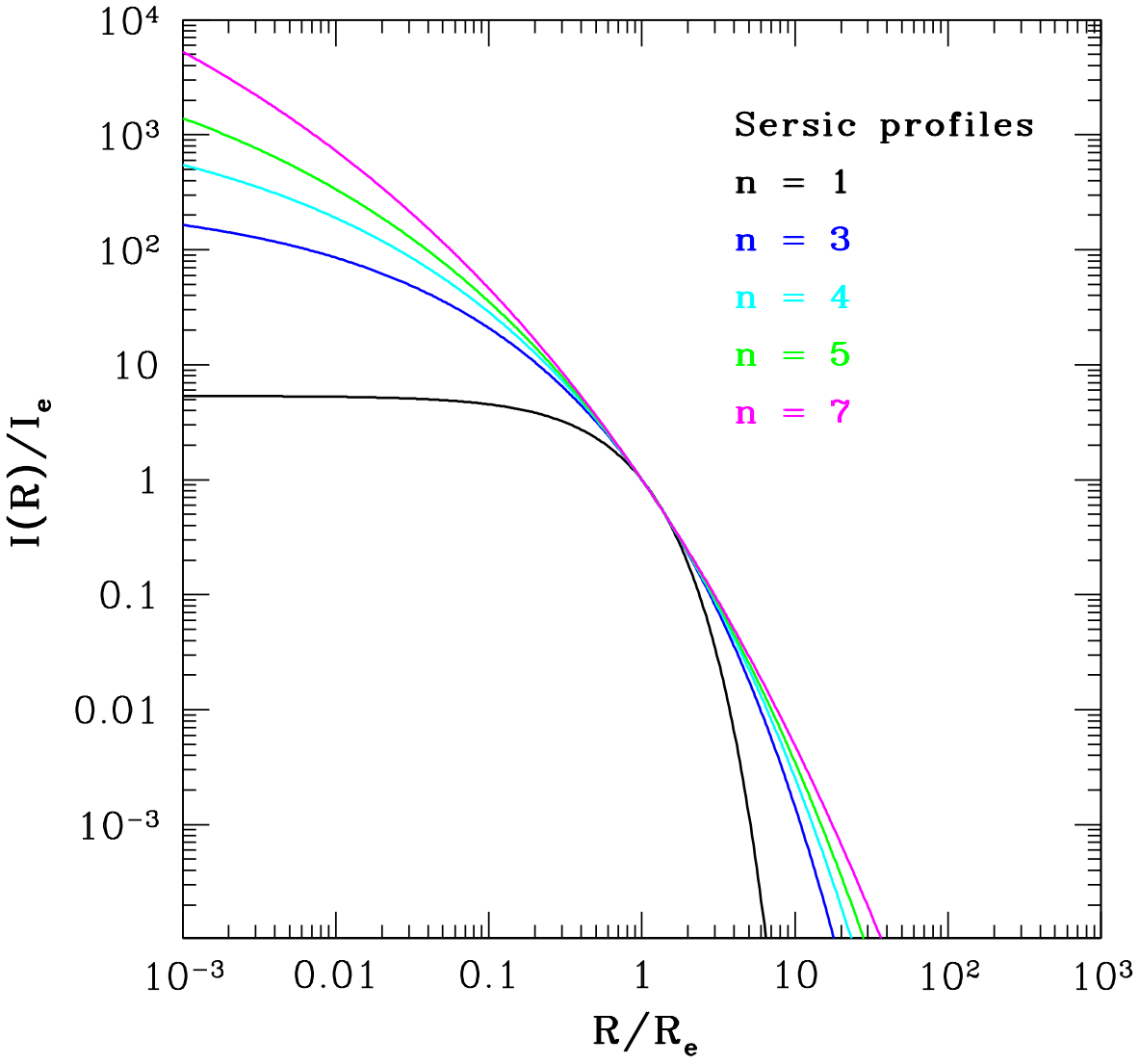

Figure 1.5: Surface brightness, described by Sérsic (1968) profiles [equation (1.26)], as a function of projected radius, R. $I(R)$ is normalised to the value at the effective radius, $I_e \equiv I(R_e)$. Four different values for the Sérsic index are shown; $n = 1$ (black line), $n = 3$ (dark blue line), $n = 4$ (light blue line), $n = 5$ (green line) and $n = 7$ (magenta line).

There have been several studies that attempt to quantify the missing baryons, in particular regarding the global ratio of stellar-to-dark matter mass in galaxies, discussed earlier in the context of galaxy formation efficiencies. Behroozi et al. (2013) compare several derivations of this function at $z \approx 0$ (Figure 1.2). The overall shape now has a well understood physical explanation, and was discussed in the context of feedback. For the smallest halos, supernova feedback and stellar winds are able to push gas out of the potential well of the galaxy (Dekel & Silk 1986), preventing further star formation, thus leading to low values of $M_*(r_{\rm vir})/M_d(r_{\rm vir})$. For larger halos, feedback from AGN leads to inefficient star formation. The feedback becomes more effective at preventing stars forming for higher mass halos, hence the stellar mass ratio decreases (Sijacki et al. 2015).

There are several different methods applied in the literature to derive the stellar-to-dark matter mass ratio as a function of halo mass. Some of these attempt to directly measure the halo mass through weak lensing (Hudson et al. 1998; Guzik 2002; Sheldon et al. 2004; Madelbaum et al. 2006; Hudson et al. 2015) or using satellite galaxies and/or stellar velocities as tracers of the halo potential well (Ashman, Salucci & Persic 1993; Zaritsky & White 1994; Prada et al. 2003; van den Bosch et al. 2004; Conroy et al. 2007). Identifying clusters through optical or X-ray selected cluster catalogs and directly measuring the galaxy content is another technique often used (Lin & Mohr 2004; Yang et al. 2007; Hansen et al. 2009). However, this technique is limited as it can clearly only be applied for cluster-size systems (halo masses of $\sim 10^{13}$–$10^{15} M_\odot$).

Several studies have made use of the Abundance Matching technique (AM; Guo et al. 2009; Moster et al. 2010; Behroozi, Conroy & Wechsler 2010; Moster et al. 2013; Behroozi, Conroy & Wechsler 2013). This involves assigning one central galaxy to each virialised halo in ΛCDM simulations of structure formation. The stellar mass is then determined by the virial mass of each parent halo, according to a prescription that is ultimately required to give agreement between the simulations and the observed galaxy luminosity function (or stellar mass function) at $z = 0$. Moster et al. (2010) give a useful parametrisation of the results they obtained via this method. They fit

their results with a double power-law function of the form,

$$\frac{M_*(r_{\rm vir})}{M_{\rm d}(r_{\rm vir})} = 2\left(\frac{M_*}{M_d}\right)_0 \left\{ \left[\frac{M_{\rm d}(r_{\rm vir})}{M_1}\right]^{-\gamma} + \left[\frac{M_{\rm d}(r_{\rm vir})}{M_1}\right]^{\beta} \right\}^{-1}. \tag{1.29}$$

In this equation, $(M_*/M_d)_0$ is a normalisation, M_1 is a characteristic mass scale and γ and β are the slope of the stellar mass ratio for small and large halos respectively.

The redshift evolution of the stellar-to-dark matter mass ratio has been considered in cosmological simulations for $0 \lesssim z \lesssim 4$ (Behroozi et al. 2010, 2013; Moster et al. 2010, 2013) and observations for $0 \lesssim z \lesssim 1$ (Hudson et al. 2015; Coupon et al. 2015). Moster et al. (2013) use the AM technique applied at multiple epochs to derive their results. They allow the four free parameters in equation (1.29) [$(M_*/M_d)_0$, M_1, β and γ] to evolve, assuming a linear dependence on the expansion parameter, $a = (1+z)^{-1}$. For each free parameter, Moster, Naab & White (2013) give an equation for the redshift dependence of the form

$$Y(z) = Y_0 + Y_1 \frac{z}{1+z}. \tag{1.30}$$

In this equation, $Y = (M_*/M_d)_0$, M_1, β or γ and a subscript of 0 gives the value for $z = 0$. The eight parameters are then constrained by fitting the model to a set of Stellar Mass Functions at different redshifts. Moster et al. (2013) find that as z gets larger, the maximum value of $f_{*,\rm vir}$ decreases and the corresponding halo mass increases. This evolution slows down towards the higher redshifts they consider ($z \sim 4$), due to the $(1+z)^{-1}$ dependence.

The most recent weak lensing studies (Hudson et al. 2015; Coupon et al. 2015) yield halo mass measurements over a range of stellar masses ($\sim 5 \times 10^8$–$2 \times 10^{11} M_\odot$) and redshifts ($0.2 < z < 0.8$). At redshifts $z \sim 0.5$, Hudson et al. (2015) report a maximum in the stellar-to-dark matter mass ratio of ~ 0.04, at $M_{\rm d,vir} \simeq 2 \times 10^{12} M_\odot$. They also find that $M_*(r_{\rm vir})/M_d(r_{\rm vir})$ evolves with redshift, in such a way that the maximum value and corresponding halo mass both increase as z gets larger. This is consistent with the findings of Behroozi, Wechsler & Conroy (2013), who find the same qualitative result for redshifts $0 \lesssim z \lesssim 1$.

For redshifts > 1, Behroozi, Wechsler & Conroy (2013) find that the maximum

value of the mass ratio begins to decrease for increasing z. For $1 \lesssim z \lesssim 3$, the corresponding halo mass continues to increase, but then decreases for larger redshift. However, Behroozi, Wechsler & Conroy (2013) urge caution in over-interpretation of their results for $z > 4$, due to concerns about the reliability of the galaxy luminosity functions at these redshifts.

1.2.3 Scaling relations of stellar properties

There are many connections and interdependences between the stellar properties of early-type galaxies. Before obtaining average trends between stellar and dark matter properties, these interdependencies need to be considered. The stellar properties that are connected include the total luminosity, L, the velocity dispersion, σ, effective radius, R_e, stellar mass, M_*, mass-to-light ratios, M/L, mean surface brightness inside R_e, $\langle I_e \rangle \equiv L_{\rm tot}/2\pi R_e^2$, and Sérsic index, n. It is essential to understand how the stellar properties are related before connecting them to dark matter halo properties.

A key step in this field was the discovery by Faber & Jackson (1976) of a relation between luminosity and velocity dispersion — $L \propto \sigma^\alpha$ with $\alpha \simeq 4$ — the so called Faber-Jackson relation. This is now expressed in various forms (e.g. with M_* instead of L, through a mass-to-light ratio) and is analogous to the Tully-Fisher relation for spirals (Tully & Fisher 1977). The Tully-Fisher relation connects the luminosity to the width of the HI 21-cm emission line, which is broadened due to different Doppler shifts at the opposite ends of the galaxy, caused by a rotating disk. The width of the 21-cm emission line is approximately twice the maximum of the rotation curve, $V_{\rm max}$. This is related to the luminosity through $L \propto V_{\rm max}^a$, with $a \simeq 2.5$–4.

Pre-dating the Faber-Jackson relation, Gudehus (1973) noted that larger galaxies have fainter effective surface brightnesses (i.e. R_e is inversely proportional to $\langle I_e \rangle$). Many years later, Djorgovski & Davis (1987) reported $R_e \propto \langle I_e \rangle^{-0.83 \pm 0.08}$. At the same time, Djorgovski & Davis (1987) and, in an independent study Dressler et al. (1987), realised that these relations are projections of what is now called the Fundamental

Plane (FP) of ellipticals, relating R_e, $\langle I_e \rangle$ and σ. Given that

$$L = 2\pi \langle I_e \rangle R_e^2, \tag{1.31}$$

the FP can equivalently be expressed as a relation between L, σ and $\langle I_e \rangle$ or between R_e, L and σ. By combining the stellar properties in such a way (i.e. through bivariate correlations), it is possible to significantly reduce the scatter, due to interdependencies between some of the properties. For example, the scatter around R_e and σ (for a given L or M_*) is anti-correlated. Therefore, certain combinations of σ and R_e plotted against luminosity (or stellar mass), have much smaller intrinsic scatter around them.

For early-type galaxies with $\sigma > 130\,\mathrm{km\,s^{-1}}$, Djorgovski & Davis (1987) found a tight correlation between the effective radius and a combination of the velocity dispersion and the mean effective surface brightness:

$$\log[R_e] = (1.39 \pm 0.14)\log[\sigma] - (0.90 \pm 0.1)\log[\langle I_e \rangle] + \text{const.} \tag{1.32}$$

They found the scatter around the FP to be characterised by the measurement errors, implying very small *intrinsic* scatter. Dressler et al. (1987) obtained a very similar result as this, for both elliptical and S0 galaxies. Both of these authors also suggested that the FP may be curved at the lower-mass end, and hence not linear.

For early-type galaxies at $z = 0$ with $\sigma > 130\,\mathrm{km\,s^{-1}}$, the ATLAS^{3D} survey (Cappellari et al. 2011; Cappellari et al. 2013b; Cappellari et al. 2013a) found

$$\log[R_e] = (1.37 \pm 0.09)\log[\sigma] - (0.86 \pm 0.03)\log[\langle I_e \rangle] + (0.13 \pm 0.01), \tag{1.33}$$

consistent with Djorgovski & Davis (1987). However, for their entire sample of 258 elliptical galaxies, Cappellari et al. (2013a) find

$$\log[R_e] = (1.06 \pm 0.04)\log[\sigma] - (0.77 \pm 0.02)\log[\langle I_e \rangle] + (0.19 \pm 0.01), \tag{1.34}$$

significantly different from the Djorgovski & Davis (1987), Dressler et al. (1987) and other results in the literature (Bernardi et al. 2003). The difference between equation (1.33) and (1.34) illustrates the importance of sample selection and that the parameters of the FP depend on the region of surface included (i.e., there is curvature in the FP).

To interpret the empirical FP relation, the observables above (i.e. $R_e, \langle I_e \rangle, \sigma$) need to be related to physical quantities. Djorgovski, de Carvalho & Han (1988) outlined the following argument, based on the virial theorem. For a bound, virialised system, $-E_P = 2E_K$, where E_P and E_K are the global potential and kinetic energy respectively. Defining a mean radius, $\langle R \rangle$, and a mean square velocity, $\langle V^2 \rangle$, that enter the expressions for the two energies, then

$$\frac{GM}{\langle R \rangle} = \langle V^2 \rangle. \tag{1.35}$$

The observables are then related to the physical quantities through simple proportionalities; $R_e = k_R < R >, \sigma^2 = k_V \langle V^2 \rangle$ and $L = 2\pi \langle I_e \rangle R_e^2$. The parameters k_R and k_V represent the density and kinematical structure of a given galaxy. Combining these with equation (1.35) and re-arranging for R_e yields a theoretical expression for the FP:

$$R_e = k_S \left(\frac{M}{L} \right)^{-1} \sigma^2 \langle I_e \rangle^{-1}, \tag{1.36}$$

where $k_S = (2\pi G k_R k_V)^{-1}$ combines the structural parameters. The observed FP [equation (1.33)] can also be expressed in this form;

$$R_e \simeq 1.55 \ \sigma^{1.37} \langle I_e \rangle^{-0.86}. \tag{1.37}$$

By comparing equations (1.36) and (1.37), it follows that $k_S (M/L)^{-1}$ cannot be constant if the virial theorem argument is to reproduce the observed tilt of the FP. Either the structure or the mass-to-light ratio (or both) must vary in a systematic way. There are many studies in the literature that investigate this (Bender, Burstein & Faber 1992; Bender, Burstein & Faber 1993; Guzman, Lucey & Bower 1993; Bender, Saglia & Gerhard 1994; Graham et al. 1996; Graham & Colless 1997; Trujillo, Burkert & Bell 2004; Cappellari et al. 2006; Chen et al. 2010; Cappellari et al. 2011; Cappellari et al. 2013b; Cappellari et al. 2013a).

One extreme is to assume that elliptical galaxies all have the same density distributions, meaning they are homologous. If ellipticals are homologous, then k_S is constant and the tilt of the FP is entirely due to systematic variations in the mass-to-light

ratios. Under this assumption, where the virial theorem gives $M \propto \sigma^2 R_e$, mass-to-light ratios (inferred from how the observed FP deviates from $L \propto \sigma^2 R_e$) have consistently been found to vary with luminosity (or stellar mass); a power-law of $(M/L) \propto L^{0.1-0.4}$ [$(M/L) \propto M^{0.1-0.3}$] is commonly reported (Dressler et al. 1987; Recillas-Cruz et al. 1990; Djorgovski & Santiago 1993; Magorrian et al. 1998; Cappellari et al. 2013b). More recently, Cappellari et al. (2013b) derived a relation between M/L and velocity dispersion, finding $M/L \propto \sigma^{0.72}$.

Another extreme is to assume a constant mass-to-light ratio for all ellipticals, with the entire tilt due to non-homology. The structural homology has been investigated by fitting the light profiles of ellipticals with Sérsic profiles, allowing for variable n. It has been shown that the Sérsic n does indeed depend on various observed properties of the galaxy including L (or M_*) and R_e, with more massive galaxies implying larger n (Graham et al. 1996; Graham & Colless 1997; Trujillo, Burkert & Bell 2004; Chen et al. 2010). This is shown in Figure 1.6, taken from the Graham & Colless (1997) paper, with total stellar mass plotted as a function of Sérsic index, n.

1.2.4 Population synthesis models

There are many correlations between stellar properties and the total stellar mass, $M_{*,\mathrm{tot}}$, as well as the M_{BH}–$M_{*,\mathrm{tot}}$ relation. However, $M_{*,\mathrm{tot}}$ cannot be measured directly. One possible way of calculating $M_{*,\mathrm{tot}}$ is to combine an integrated luminosity with a stellar mass-to-light ratio, M_*/L. These can be obtained from stellar population synthesis models, used to interpret the integrated light that is observed from galaxies. Population synthesis models are vast, and have many applications. The focus here is the mass-to-light ratios, in-particular for the normal, quiescent galaxies at $z = 0$ that are used to define the SMBH–bulge property correlations. Early-type galaxies at $z = 0$ with stellar masses in the range $10^{10} M_\odot \lesssim M_{*,\mathrm{tot}} \lesssim 10^{12} M_\odot$, typically have mean stellar ages of a few (7–11) Gyr, and metallicities $-1.7 \lesssim [Z/H] \lesssim 0.3$. This metallicity range corresponds to colours $0.5 \lesssim (g-r) \lesssim 1$. The mean stellar age corresponds to the time in Gyrs since the galaxy formed. For Planck (2014) cosmology, an age range of 7–11

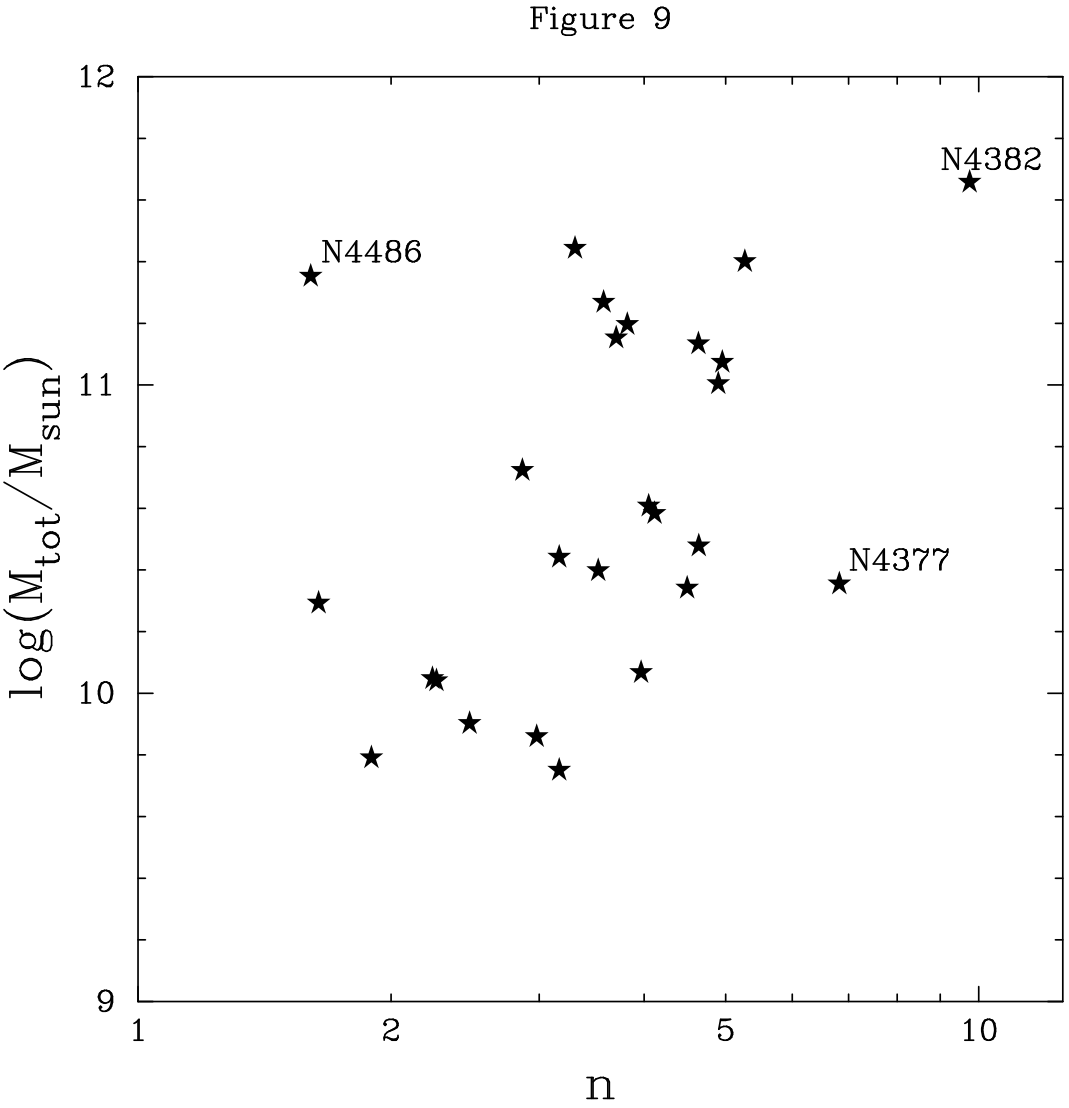

Figure 1.6: Taken from the Graham & Colless (1997) paper, with total stellar mass, $M_{\rm tot}$, as a function of Sérsic index, n. This appears to show a correlation between $M_{*,\rm tot}$ and n, although with a lot of scatter.

Gyr corresponds to redshifts $0.8 \lesssim z \lesssim 2.3$.

The integrated light includes information regarding mass-to-light ratios, line indices and colours. These quantities allow for some understanding regarding the mix of stars that give rise to the observed light. The most commonly used stellar population models are the single burst models, also referred to as Simple Stellar Populations (SSP; Maraston 1998, 2005; Bruzual & Charlot 2003). For these, all stars are assumed to form at the same time, with identical chemical composition and a chosen initial mass function (IMF). More advanced models take into account other physical factors such as ongoing star formation, and are called Composite Stellar Populations (CSP; Bruzual & Charlot 2003). However, these additional processes are not well understood in detail, so CSP models should be used with caution.

There are a few steps required to obtain the model predictions for either an SSP or CSP. Firstly, a set of theoretical stellar isochrones are needed, representing a population of stars of some age and metallicity, two of the input parameters. The isochrones include the physics of stellar evolution, including opacities and a recipe for dealing with convection. The next step requires transforming the theoretical properties of the isochrones (e.g. effective temperature, $T_{\rm eff}$, and luminosity, L) into observable quantities (e.g. colours, line indices and mass-to-light ratios).

Most population synthesis models give various outputs for mass-to-light ratios, with values for "alive" stars *only*, including remnants (white dwarves, neutron stars and stellar black holes) and/or including stellar ejecta. It is the normalisation of the mass-to-light ratios that changes depending on whether remnants and ejecta are included or not.

1.2.4.1 Initial Mass Functions (IMFs)

An initial mass function (IMF) is an empirical function that describes the distribution of the initial mass for a given population of stars. It is often given as a probability distribution function for the mass at which a star begins its evolution along the main sequence. Various forms exist in the literature and it is usually presented as $\phi(m)\,dm$

(or similar). By definition, $\phi(m)\,dm$ is the number of stars with masses in the range m to $m + dm$: $\phi(m) \equiv dN/dm$.

The IMF in our Galaxy was quantified by Salpeter (1955), who found

$$\phi(m) \propto \left(\frac{m}{M_\odot}\right)^{-2.35}. \tag{1.38}$$

However this is now known to largely over-estimate the number of stars with masses $< 1M_\odot$. More recent determinations suggest that the IMF deviates from a pure power law, becoming flatter at lower masses (Miller & Scalo 1979; Scalo 1986). IMFs in the form of broken power laws have been proposed by several authors (Scalo 1986; Kroupa 2001). Broadly speaking, these have the form

$$\phi(m) \propto \begin{cases} \left(\frac{m}{M_\odot}\right)^{-\alpha_1} & \text{for } \; m_1 \leq m < m_2 \\ \left(\frac{m}{M_\odot}\right)^{-\alpha_2} & \text{for } \; m_2 \leq m \leq m_3 \\ \left(\frac{m}{M_\odot}\right)^{-\alpha_3} & \text{for } \; m_3 < m. \end{cases} \tag{1.39}$$

For a Scalo (1986) IMF, the slopes are $\alpha_1 = 1.8, \alpha_2 = 3.25$ and $\alpha_3 = 2.45$, with $m_1 = 0.2M_\odot$, $m_2 = 1M_\odot$ and $m_3 = 10M_\odot$. This is shown by the dotted green line in Figure 1.7. The Kroupa (2001) IMF, shown by the broken red line in Figure 1.7, has slopes $\alpha_1 = 0.3, \alpha_2 = 1.3$ and $\alpha_3 = 2.3$, with $m_1 = 0.01M_\odot$, $m_2 = 0.08M_\odot$ and $m_3 = 0.5M_\odot$.

Finally, Chabrier (2003) gives a log-normal form of the IMF;

$$\phi(m) \propto \begin{cases} \frac{1}{m} \exp\left\{\frac{-[(\log m)^2 + 2.194 \log m]}{0.95}\right\}_{-2.3} & \text{for } \; m < 1M_\odot \\ \left(\frac{m}{M_\odot}\right)^{-2.3} & \text{for } \; m > 1M_\odot, \end{cases} \tag{1.40}$$

shown by the solid blue line in Figure 1.7. For $m \gtrsim 1M_\odot$, all of these IMFs roughly follow a power law, similar to the original Salpeter IMF. However, at smaller masses there are significant differences, with the most recent models predicting more realistic values for the number of lower mass stars.

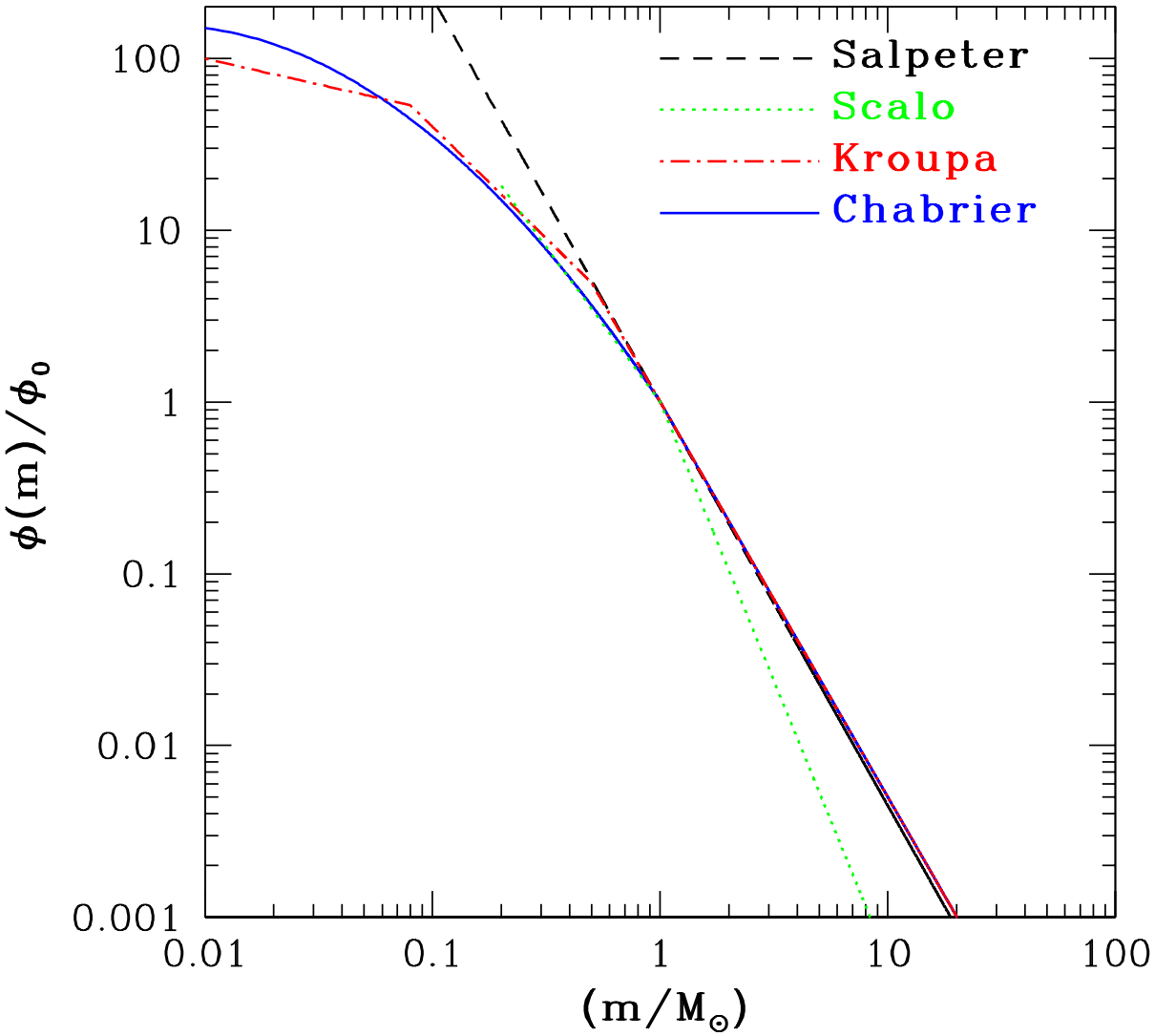

Figure 1.7: Initial Mass Function (IMF), $\phi(m)/\phi_0$, versus stellar mass, $m/M_\odot$ for four different models. For each, the IMF is normalised such that $\phi(m)/\phi_0 = 1$ at $m = 1M_\odot$. The dashed black line is the Salpeter (1955) IMF, the dotted green line the Scalo (1986) IMF, the broken red line is for the Kroupa (2001) IMF and the solid blue line represents the Chabrier (2003) IMF. The differences between these three IMFs are discussed in detail in the main text.

1.2.4.2 Mass-to-light ratios

Figure 1.8 shows mass-to-light ratios as a function metallicity, $[Z/H]$. The curves are all from the Maraston (1998) population synthesis models, with a mean stellar of 9 Gyr assumed. The different line colours are for the M/L values in different band-passes; the K-(red lines), V-(cyan lines) and B- (black lines) band. The dashed lines are for an assumed Salpeter IMF and the solid lines assume a Kroupa IMF. For a Salpeter IMF, the mass-to-light ratios are systematically higher, by a factor of $\sim$ 1.5- 2, depending on bandpass and metallicity. This is due to the over-prediction of the number of stars that the Salpeter IMF makes.

Figure 1.9 shows the stellar mass-to-light ratios as a function of age (in years) for six different band-passes. These are again from the Maraston (2005) population synthesis models, assuming a Kroupa (2001) IMF and a solar metallicity, $[Z/H] = 0$. From the shortest wavelength, the filters considered are the $B-$(black line), $g'-$(blue), $V-$(cyan), $r'-$(green), $z'-$(magenta) and $K-$(red) band. The Figure shows M/L values for ages between 1 Gyr and 20 Gyr. Over this range, the mass-to-light ratios for the shortest wavelengths change quite dramatically, from $M/L \sim 1$ to $M/L \sim 5.5$–6.5. For the longer wavelengths, most notably in the $K-$band, the M/L values vary much less.

Figure 1.10 demonstrates two things: how the mass-to-light ratios from population synthesis models vary as a function of colour (and hence metallicity) in the various band-passes, and how including stellar ejecta effects the normalisation. These are once again taken from Maraston's models, with the stellar age assumed to be 9 Gyr and for a Kroupa IMF. The left panel shows the total mass-to-light ratios (including remnants and ejecta) and the right panel shows the stellar mass-to-light ratios (including remnants but not ejecta). In both panels, the mass-to-light ratios are shown as a function of $(g - r)$ colour. M/L values corresponding to the shorter wavelengths (i.e. B-band, g-band and V-band) are more sensitive to changes in colour than the redder (longer) wavelengths. The K-band mass-to-light ratios are approximately constant over the $(g - r)$ colour range shown in the Figure. This is true more generally — the K-band

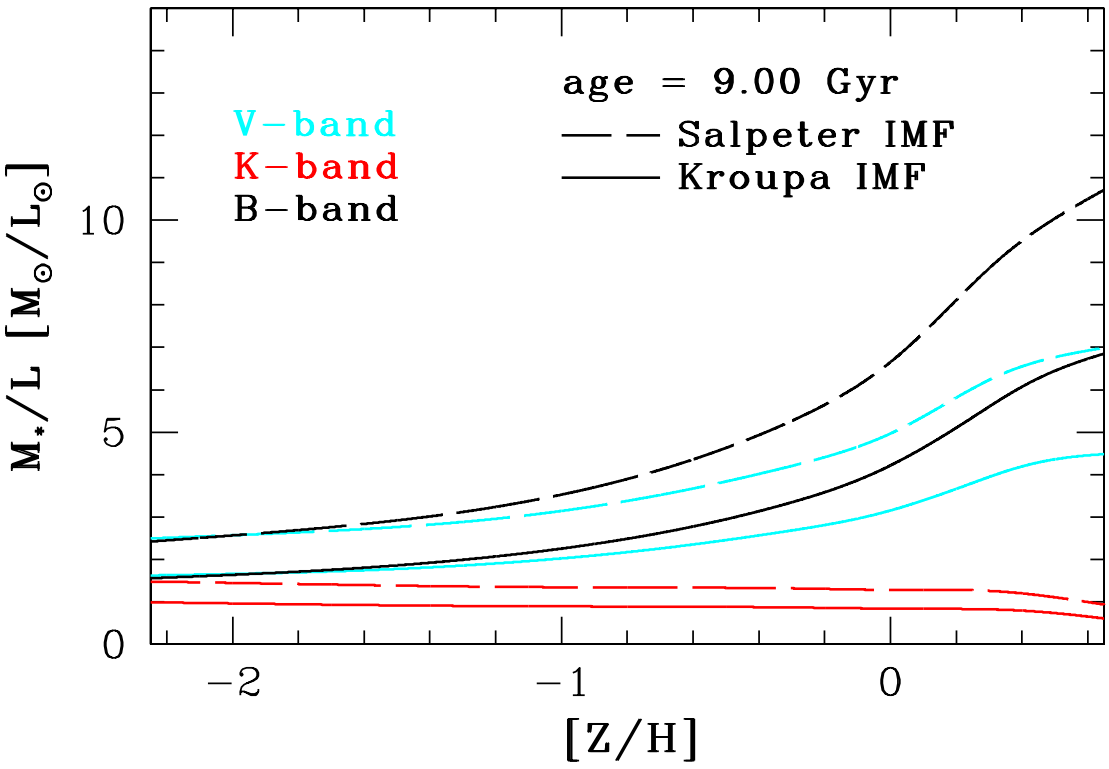

Figure 1.8: Stellar mass-to-light ratios, M_*/L, as a function of metallicity, $[Z/H]$, assuming a stellar age of 9 Gyr, from Maraston's population synthesis models (Maraston 1998, 2005). The broken lines are for an assumed Salpeter (1955) IMF and the solid lines assume a Kroupa (2001) IMF. The different line colours represent M/L values in the K-(red lines), V-(cyan lines) and B-(black lines) band-passes.

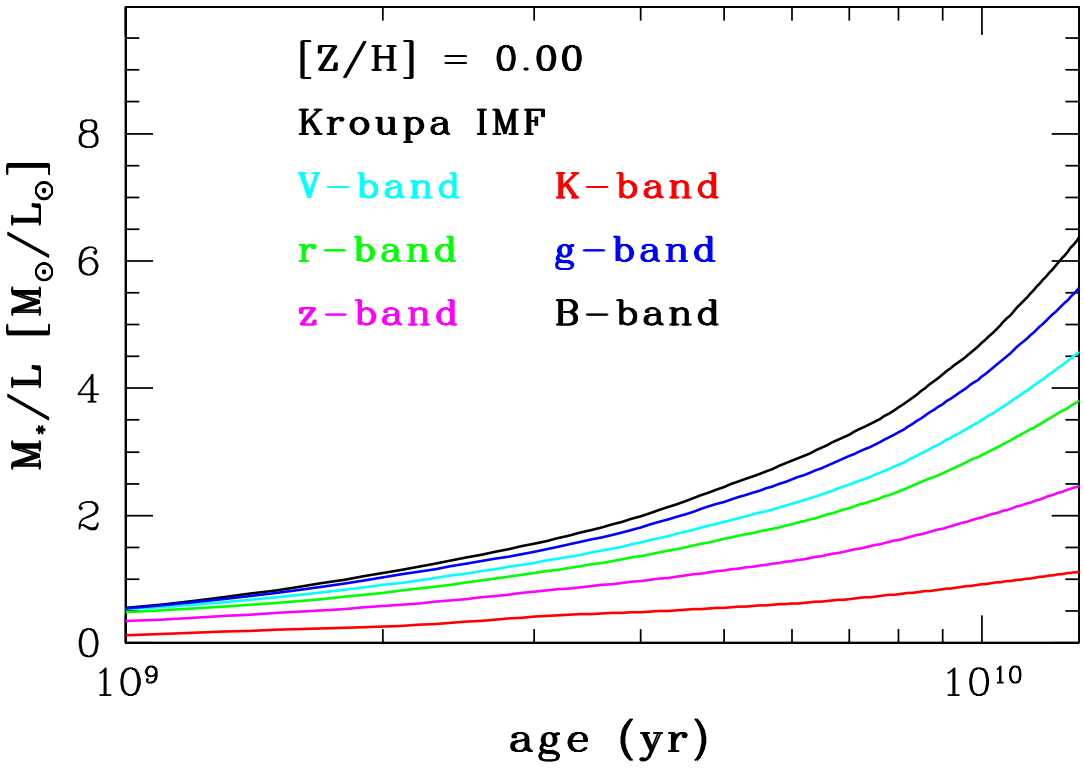

Figure 1.9: Stellar mass-to-light ratios, M_*/L, as a function of age (in years), assuming a Kroupa (2001) IMF and a solar metallicity, $[Z/H] = 0$, from Maraston's population synthesis models (Maraston 1998, 2005). The six curves correspond to M_*/L values in various bandpasses, with the different line colours indicated in the Figure.

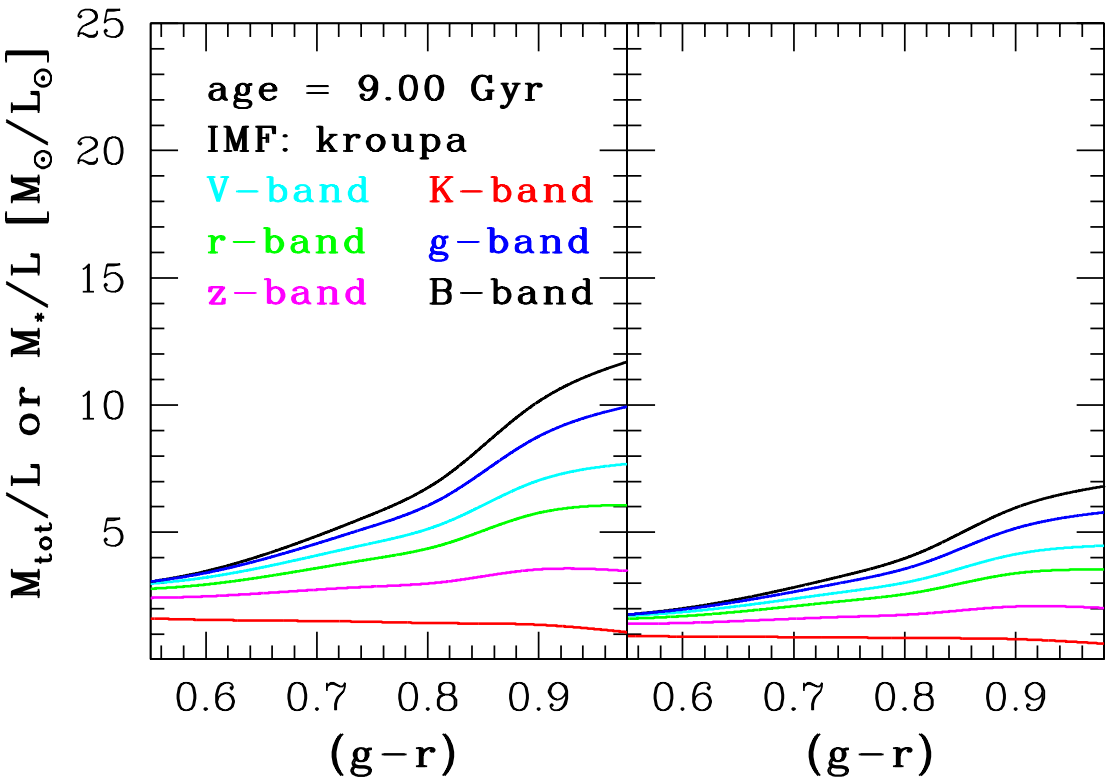

Figure 1.10: *Left panel:* Total(including remnants and stellar ejecta) mass-to-light ratios, $M_{\rm tot}/L$, as a function of $(g-r)$ colour, assuming a Kroupa (2001) IMF and a stellar age of 9 Gyr, from Maraston (2005). Line colours represent different band passes, as for the previous two Figures. *Right panel:* Same as above, but for stellar (remnants but no ejecta) mass-to-light ratios, M_*/L.

mass-to-light ratios do not show much variation as a function of colour/metallicity.

The difference between the two panels is the normalisation of the M/L values. Normalising masses to 1 solar mass ($M_{\odot}$), Maraston's population synthesis models yield a stellar mass (including remnants), $M_{*} \simeq 0.58$ for a Kroupa IMF and a stellar age of 9 Gyr. It is worth noting that this value varies by less than 1% for $-2.25 \leq [Z/H] \leq 0.67$ and by no more than $\sim 5\%$ for ages between 5 and 15 Gyr. Assuming that the remaining baryonic mass in these models is stellar ejecta, $M_{\rm ej}$, then $M_{\rm tot} \equiv M_{\rm ej} + M_{*} = 1$ (since the mass is normalised to $M_{\odot}$). To re-normalise the stellar mass-to-light ratios to include the stellar ejecta, M_{*}/L needs to be multiplied by $(M_{\rm ej} + M_{*})/M_{*} = 1M_{*} \simeq 1.72$. This also yields another useful number, the ratio of stellar ejecta mass to mass in stars, $F_{\rm ej} \equiv M_{\rm ej}/M_{*} \simeq 0.72$. In the context of the work presented here, stellar ejecta (particularly $F_{\rm ej}$) are important for calculations of stellar velocity dispersions.

1.2.4.3 Composite stellar populations

Star formation is not instantaneous in reality and potentially lasts for several Gyrs. It is therefore necessary to compare output quantities from SSPs and models with different star formation histories (e.g. Bruzual & Charlot 2003). In the context of this work, the important quantities to consider are the mass-to-light ratios and the amount of stellar ejecta. The *GALAXEV* library of stellar population synthesis models, computed from the isochrone synthesis code of Bruzual & Charlot (2003), allows for comparisons of both of these for different star formation histories. Mass-to-light ratios are calculated in various band passes, considering three scenarios for the star formation:

1. Single, instantaneous burst of star formation (SSP)
2. Star formation at a constant rate, up until some cut-off time, $t_{\rm cut}$
3. An exponentially declining star formation rate, with an e-folding time, τ and cut-off, $t_{\rm cut}$.

In order to make a comparison, a consistent definition of mean stellar age, T, is required. For the SSP case, this is straight forward — the time since the instantaneous

burst. For extended star formation, the mean stellar age is defined as

$$T(t) = t - \langle t_{\rm form} \rangle, \tag{1.41}$$

where

$$\langle t_{\rm form} \rangle = \frac{\int_0^t t' \psi(t') dt'}{\int_0^t \psi(t') dt'} \tag{1.42}$$

is a mean formation time. In equation (1.42), $\psi(t)$ is the star formation rate. For the SSP case, $\psi(t) = 0$, so $T = t$ since $t = 0$ is defined as the time of formation for single-burst synthesis models.

For a constant star formation rate, $\psi(t) = 1/t_{\rm cut}$ for $t \leq t_{\rm cut}$ and is equal to zero otherwise. From equations (1.41) and (1.42), this yields

$$T(t) = \begin{cases} t - \frac{1}{2}t & \text{if } \ t \leq t_{\rm cut} \\ t - \frac{1}{2}t_{\rm cut} & \text{if } \ t > t_{\rm cut}. \end{cases} \tag{1.43}$$

On the other hand, an exponentially declining star formation rate, with $\psi(t) = e^{-t/\tau}/\tau$ for $t \leq t_{\rm cut}$ (again zero otherwise), leads to

$$T(t) = \begin{cases} t - \dfrac{\tau[e^{t/\tau} - (1 + t/\tau)]}{e^{t/\tau} - 1} & \text{if } \ t \leq t_{\rm cut} \\ t - \dfrac{\tau[e^{t_{\rm cut}/\tau} - (1 + t_{\rm cut}/\tau)]}{e^{t_{\rm cut}/\tau} - 1} & \text{if } \ t > t_{\rm cut}. \end{cases} \tag{1.44}$$

The top two rows of Figure 1.11 show V-band (cyan lines) and K-band (red lines) mass-to-light ratios versus mean stellar age for a few values of $t_{\rm cut}$ and τ (see labels in Figure). A solar metallicity was assumed for these calculations. For the four panels in the top two rows, the dot-dash lines are for an SSP model, the solid lines are for a constant star formation rate and the dotted lines are for an exponentially declining star formation rate. The bottom row shows the ratio of (M/L) from the constant star formation model to (M/L) from the SSP model, for $t_{\rm cut} = 2$ Gyr (left) and $t_{\rm cut} = 4$ Gyr (right). For a mean stellar ages $\gtrsim 7$ Gyr, the M/L values are the same, to within $< 5\%$, for all three scenarios with star formation lasting up to 6 Gyr. Allowing for an extended star formation history therefore has little effect on the mass-to-light ratios required for calculating the total stellar masses of early-type galaxies at $z = 0$.

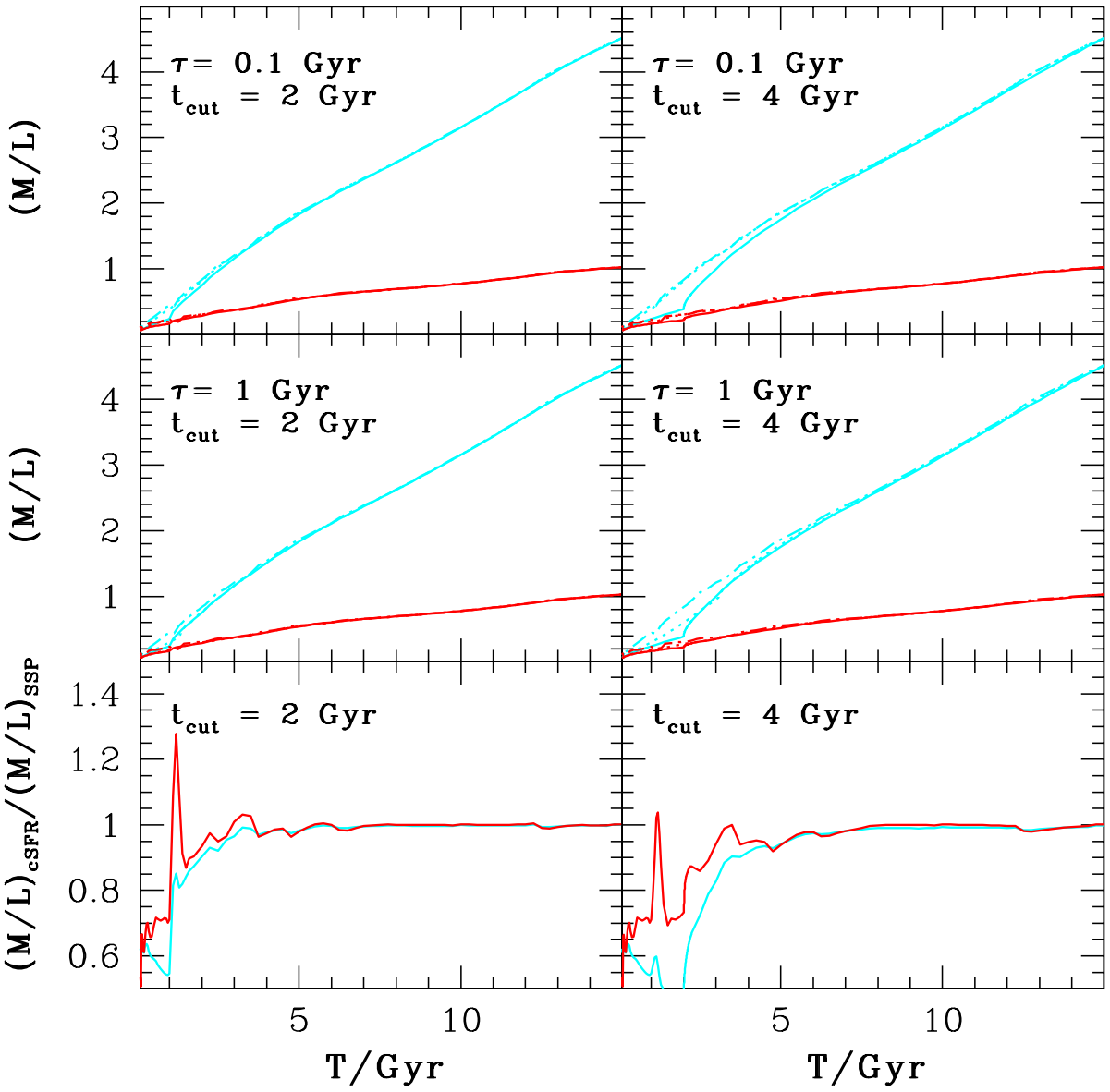

Figure 1.11: *Top two rows:* Mass-to-light ratios as a function of $T = t - \langle t_{\rm form} \rangle$ (defined in the text), for different values of two star formation rate parameters: cut-off time, $t_{\rm cut}$ and e-folding time, τ. In all four panels, the cyan lines are V-band and red lines are K-band mass-to-light ratios. The dot-dash lines are for stars formed from a single, instantaneous burst (SSP), the solid lines are for a constant star formation rate and the dotted lines are for an exponentially declining star formation rate. *Bottom row:* The ratio of M/L from the constant star formation model, to M/L from the SSP model, for $t_{\rm cut} = 2$ Gyr (left) and $t_{\rm cut} = 4$ Gyr. Line colours are the same as for the panels above.

As for the mass-to-light ratios, the effects of allowing for extended star formation on the value of $F_{\rm ej}$ are considered. The top two rows in Figure 1.12 shows $F_{\rm ej}$ as a function of the mean stellar age, T, as defined by equations (1.41) and (1.42). The three star formation histories (single burst, constant star formation rate, exponentially declining star formation rate) are compared, with a few different values for the cut-off time, $t_{\rm cut}$, and the e-folding time, τ (see labels in Figure 1.12). The bottom row shows the ratio $F_{\rm ej}$ calculated from a constant star formation model to $F_{\rm ej}$ from an SSP model. For mean stellar ages $\gtrsim 7$ Gyr, the value of $F_{\rm ej}$ is very robust to any changes in the star formation history, with a $< 2\%$ increase for extended star formation.

1.3 Supermassive Black Holes (SMBH)

Dark matter halos, and the baryonic matter within them, are the two main components of galaxies. The final piece of the puzzle to discuss is the Supermassive Black Holes (SMBHs) residing at the centre of galactic nuclei, and in particular their masses. As well as AGN and quasars, most early-type galaxies and bulges harbour a supermassive black hole (SMBH) in their centre, with masses $M_{\rm BH} = 10^6$–$10^{10} M_\odot$. The Milky Way, a typical large spiral galaxy, hosts a SMBH with $M_{\rm BH} \simeq (4.41 \pm 0.43) \times 10^6 M_\odot$ (Ghez et al. 2008; Meyer et al. 2012). The Andromeda galaxy (also known as M31), one of the closest galaxies to the Milky Way, is also a spiral galaxy with $M_{\rm BH} \simeq (1.4^{+0.9}_{-0.3}) \times 10^8 M_\odot$ (Bender et al. 2005).

The *idea* of SMBHs originates from the study of quasars. The discovery of the first quasars (Schmidt 1963; Oke 1963; Oke & Schmidt 1963; Burbridge, Burbridge & Sandage 1963; Sandage 1963) was a significant step forward for extra-galactic astronomy. These extremely luminous, high redshift objects are easily detected due to being many times brighter than normal, quiescent galaxies. Observations of small but extremely bright objects with similar variability time scales (of approximately 1 day) hinted at the prospect of a similar mechanism producing the large luminosities. It was soon realised that this mechanism would be powered by some central engine, inside

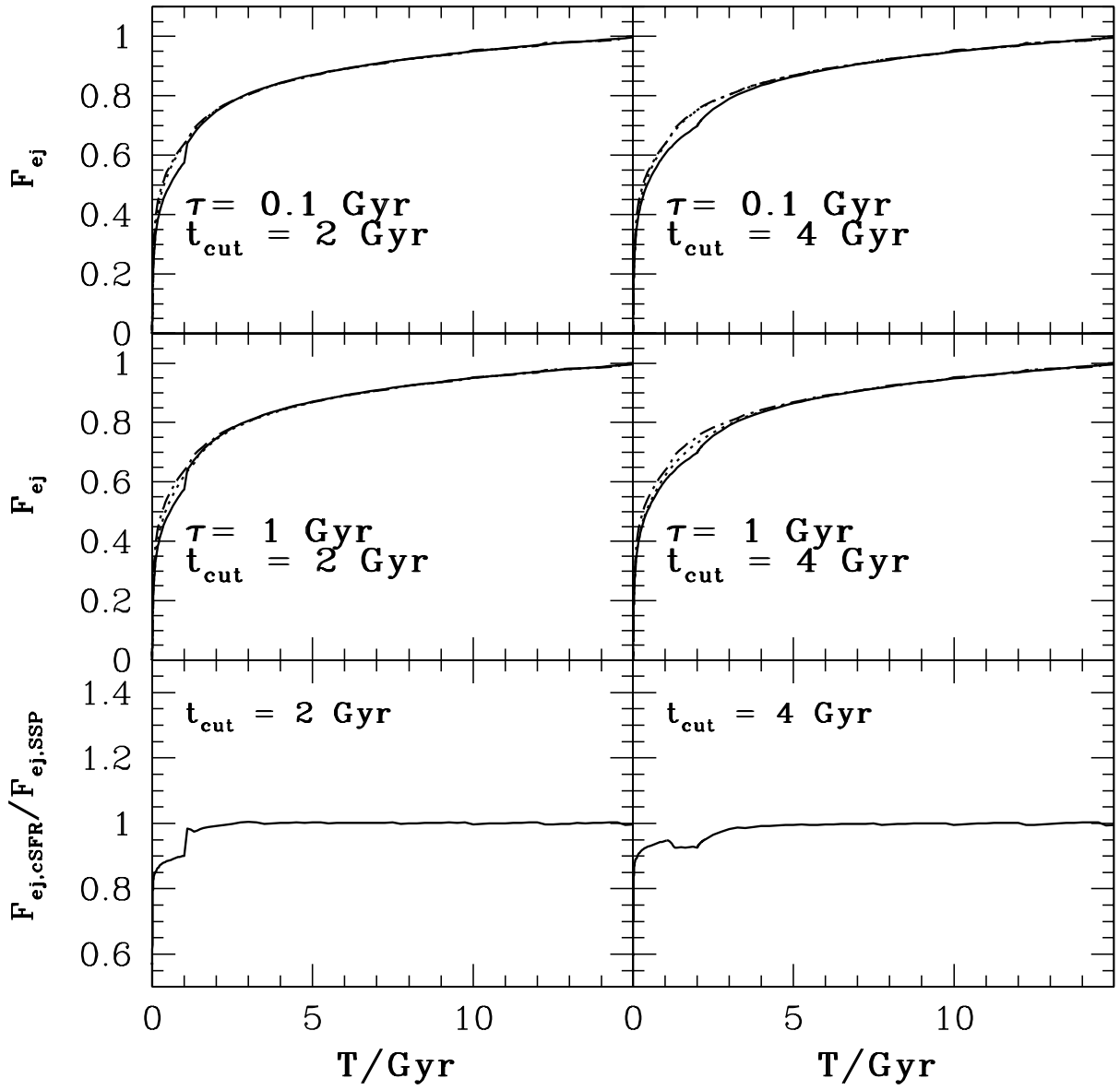

Figure 1.12: *Top two rows:* Stellar ejecta mass fraction, $F_{\rm ej} \equiv M_{\rm ej}/M_*$, versus mean stellar age for the three different star formation scenarios considered here. In all four panels, dot-dash lines are for SSP models, solid lines for a constant star formation rate and dotted lines an exponentially declining star formation rate. The values for the cut-off time, $t_{\rm cut}$, and e-folding time, τ, are shown in each individual panel. *Bottom row:* The ratio of $F_{\rm ej}$ calculated from the constant star formation model to $F_{\rm ej}$ from the SSP model, for $t_{\rm cut} = 2$ Gyr (left) and $t_{\rm cut} = 4$ Gyr (right).

Active Galactic Nuclei (AGN). The existence of SMBHs in AGN was first postulated by Salpeter (1964), with the hypothesis of an AGN powered by conversion of gravitational energy into radiation via matter accretion onto an SMBH quickly becoming the accepted theory (Lynden-Bell 1969; Lynden-Bell & Rees 1971). This only gained wider acceptance when Rees (1978) showed that there are multiple ways for an SMBH to form at the centre of a galactic nucleus, making it highly probable to happen.

1.3.1 SMBH formation

Rees (1978) postulated several methods for the initial formation of SMBHs, generally involving some seed black hole at redshifts $z > 0$ (Volonteri 2010). These then grow to the SMBH detected in galaxies at $z = 0$ via rapid accretion of gas. It is this rapid accretion that gives rise to quasar activity. However, the growth of the initial SMBHs remains a major challenge for theoretical models.

One scenario for the formation of the initial black hole seed is that they are remnants of the first generation of stars (Population III stars), formed out of zero metallicity gas. These first stars are expected to form in small ($\sim 10^6 M_\odot$) halos at high redshifts ($z \sim 20$–50). Simulations of the collapse of primordial molecular clouds suggest that many first generation stars have masses $> 100 M_\odot$ (Bromm, Coppi & Larson 1999; Bromm, Coppi & Larson 2002; Bromm & Loeb 2003; Yoshida et al. 2006). Such massive, low metallicity stars will directly form black holes, with masses approximately half the star's mass. However, there are problems with this formation scenario. If the remnant black hole is too light, it will not be dynamically stable (i.e., stationary) within the centre of the galaxy. Remnants with masses $> 150 M_\odot$, formed from stars with masses exceeding $250 M_\odot$, would be required to prevent the remnant from experiencing significant Brownian motion. It remains unclear if Population III stars would have been massive enough (Volonteri 2010).

Another theory is the heavy seed model. In this scenario, the initial black holes formed when massive gas clouds collapse to form supermassive stars with masses $M \sim 10^5$ (Volonteri 2010; Valiante et al. 2016). Such a star would only last a few million

years, before collapsing into a black hole. However, instead of a supernova explosion, the remaining matter puffs out, not dis-similar to a red giant. This leads to a seed black hole, with $M_{\rm BH} \sim 10^5 M_\odot$, that is able to grow to the masses that are measured today by rapidly accreting the surrounding matter.

1.3.2 Observational evidence

In order to dynamically detect an SMBH, the gravitational sphere of influence radius, $r_{\rm inf}$ needs to be resolved. Within this radius, the gravitational potential of an SMBH has a significant effect on the dynamics of stars (or gas) in the host galaxy. This radius is defined by

$$r_{\rm inf} \equiv \frac{GM_{\rm BH}}{\sigma^2} \simeq 10.8 \left(\frac{M_{\rm BH}}{10^8 M_\odot}\right) \left(\frac{\sigma}{200\,{\rm km\,s^{-1}}}\right)^{-2} {\rm pc}. \tag{1.45}$$

For the sphere of influence to be resolved, the angular size, $\theta_{\rm inf}$, needs to be greater than the resolution of a telescope. Denoting the distance to a galaxy as D, the angular size is

$$\theta_{\rm inf} \equiv \frac{r_{\rm inf}}{D} \simeq 0.2 \left(\frac{M_{\rm BH}}{10^8 M_\odot}\right) \left(\frac{\sigma}{200\,{\rm km\,s^{-1}}}\right)^{-2} \left(\frac{D}{10\,{\rm Mpc}}\right)^{-1} {\rm arcsec}. \tag{1.46}$$

For nearby galaxies at distances of $D = 1$–20Mpc, and for $r_{\rm inf} \sim 10$ pc, equation (1.46) corresponds to angular sizes in the range $2 \gtrsim \theta_{\rm inf} \gtrsim 0.1$ arcsec. This is right at the limit of telescope angular resolutions — a characteristic resolution limit for space-based observations (e.g. the *Hubble space telescope*) is $\theta = 0.1$.

1.3.2.1 Proper stellar motions

By far the most secure SMBH detection is the one at the centre of the Milky Way. Due to the close proximity of the Galactic centre, with $D \simeq 8.28 \pm 0.33$ kpc (Genzel, Eisenhauer & Gillessen 2010), the motion of individual stars can be followed through their orbits. One of the shortest orbital periods observed so far is approximately 15.8 years. More than one complete orbit of this star has already been observed, yielding

$M_{\rm BH} \simeq (4.30 \pm 0.36) \times 10^6 M_\odot$ (Genzel et al. 2010). Dozens of other stars in close orbit around the centre are being tracked, each of which will eventually provide an independent measure of $M_{\rm BH}$.

If the orbit of a star is observed to be closed (within errors), then essentially all of the attracting mass is located inside its pericentre radius. For the star mentioned above with more than one observed complete orbit, the pericentre radius is $\simeq 0.00059$ pc $\simeq 122$ AU (Kormendy & Ho 2013). This is the "effective" spatial resolution of the SMBH mass measurement in the Milky Way. The pericentre velocity of this star is $\gtrsim 6000\,{\rm km\,s^{-1}} \simeq 0.02c$ (Kormendy & Ho 2013). These observations set the standard for how close to the SMBH observations can get that provide estimates for $M_{\rm BH}$.

These results establish the existence and mass of the central dark object beyond any reasonable doubt. They also eliminate astrophysical plausible alternatives to an SMBH, including brown dwarfs, stellar remnants and even fermion balls (Ghez et al. 2005). The conclusion is that SMBHs are being detected, at the very least at the centre of the Milky Way.

1.3.2.2 Stellar dynamics

For normal, quiescent galaxies, SMBH detections are secure if the mass of the SMBH, $M_{\rm BH}$, can be estimated. The sphere of influence needs to be resolved in order to obtain an accurate estimate for $M_{\rm BH}$. If $r_{\rm inf}$ is resolved, then stellar and ionised gas dynamics can be used to estimate BH mass (Ferrarese & Ford 2005; Merritt 2013). Such estimates are based on velocities affected by the gravitational forces from mass within the galaxy nucleus (stars, gas), as well as the SMBH.

The following is a summary of the detailed discussion from Binney & Tremaine (2008) on distribution functions and the collisionless Boltzmann equation. To very good approximation, galaxies can be treated as collisionless stellar systems — each star moves through the combined gravitational potential, $\Phi(\mathbf{x}, \mathbf{t})$, of the other stars. The system can therefore be described analytically by a distribution function, $f(\mathbf{x}, \mathbf{v}, t)$, defined as the number of stars occupying a given six-dimensional phase-space volume,

$d^3\mathbf{x}d^3\mathbf{v}$. The distribution function has to obey a continuity equation, i.e. the rate of change of the number of stars in a given phase-space volume is equal to the amount of inflow minus the amount of outflow:

$$\frac{\partial f}{\partial t} + \mathbf{v}.\nabla f - \nabla\Phi(\mathbf{x},t).\frac{\partial f}{\partial \mathbf{v}} = 0. \tag{1.47}$$

This is known as the Collisionless Boltzmann Equation (CBE), with the potential Φ connected to the total mass density, ρ, by the Poisson equation:

$$\nabla^2\Phi(\mathbf{x},t) = 4\pi G\rho(\mathbf{x},t). \tag{1.48}$$

Generally speaking, the mass density and the six components of velocity and velocity dispersion are required. However, observational data only contain information on the surface brightness profile and the line of sight velocity and velocity dispersion only. Assuming the system is in a steady-state (time independent) and spherical symmetry, the first velocity moment of the CBE yields

$$\frac{1}{\rho(r)}\frac{d[\rho(r)\sigma_r^2(r)]}{dr} + 2\beta(r)\frac{\sigma_r^2(r)}{r} = -\frac{d\Phi(r)}{dr}. \tag{1.49}$$

This is the spherical, anisotropic Jeans equation, where $\sigma_r^2(r)$ is the radial velocity dispersion and $\beta(r)$ quantifies the degree of radial anisotropy. This is defined as:

$$\beta(r) = 1 - \frac{\sigma_\theta^2(r)}{\sigma_r^2(r)}, \tag{1.50}$$

where $\sigma_\theta^2(r)$ is the tangential velocity dispersion. If $\sigma_r^2 = \sigma_\theta^2$ so that $\beta(r) = 0$, the system is isotropic. For an isotropic stellar system, the Jeans equation is the same as the hydrostatic equilibrium equation for collisional fluids, with $\rho\sigma^2$ analogous to the pressure.

An application of the spherical Jeans equation is for estimating SMBH masses. For spherical distributions, $d\Phi/dr = GM(r)/r^2$, where $M(r)$ is the total (stars, dark matter and SMBH) mass inside radius r. Given this, equation (1.49) can be written as

$$M(r) = \frac{r\,\sigma_r^2(r)}{G}\left[-\frac{d\ln\rho(r)}{d\ln r} - \frac{d\ln\sigma_r^2(r)}{d\ln r} - 2\beta(r)\right]. \tag{1.51}$$

The first evidence for an SMBH in a quiescent galaxy was provided by Sargent et al. (1978) and Young et al. (1978), for the elliptical galaxy, M87, based on equation (1.51). They assumed isotropy, $\beta(r) = 0$, and did not include dark matter in their modelling. They analysed both the velocity dispersion and mass density (obtained from a luminosity density and an assumed mass-to-light ratio varying with r) as functions of radius. Sargent et al. found that the nucleus of M87 contains a compact mass of $M \sim 5 \times 10^9 M_\odot$, within $r < 100$pc.

Although it is reasonable to assume spherical symmetry (at least in the case of M87), there is no guarantee that $\beta = 0$ is accurate. Both Binney & Mamon (1982) and Richstone & Tremaine (1985) re-analysed the Sargent et al. (1978) data, with the assumption of isotropy relaxed. For M87, the mass-to-light ratio was constrained to be constant across the entire galaxy. With β allowed to be a free function of radius, a wide variety of mass profiles are consistent with the given dispersion and surface brightness profiles. For example, a model with $M/L_V \simeq 7.6$ and a highly anisotropic velocity dispersion for the inner 300 pc (Binney & Mamon 1982), fits the data equally as well as the Sargent et al. (1978) model. However, this anisotropic model (and other anisotropic models) has not been tested for dynamical stability (Ferrarese & Ford 2005). The problems encountered for M87 illustrates just how difficult modelling stellar kinematical data can be in general.

Given the observables, it is a non-trivial task to root out these difficulties. The degeneracy between a radially varying M/L and β, referred to as the "mass-anisotropy degeneracy", can be partly broken by analysing the line of sight velocity distribution (LOSVD). The LOSVD gives the fraction, $F(v_{\rm LOS})dv_{\rm LOS}$, of stars with line of sight velocities between $v_{\rm LOS}$ and $v_{\rm LOS} + dv_{\rm LOS}$. The second moment of the LOSVD, which is reflected in the shape of the absorption line profiles, depends on the level of anisotropy of the system (Gerhard 1993). For example, a radially anisotropic system ($\beta > 0$) corresponds to an LOSVD that is "cuspy" (lies above the isotropic case), and a tangentially anisotropic system ($\beta < 0$) has a "flat-topped" LOSVD (lies below the isotropic case). The presence of an SMBH stretches the wings of the LOSVD, due to stars orbiting in a Keplerian potential with high velocities (van der Marel 1994; Ferrarese & Ford 2005).

Accounting for anisotropy makes estimating SMBH masses based on stellar kinematics much more complex. The distribution function for a spherical, isotropic system requires only one integral of motion, the total energy of the system. This makes it possible to have a one-to-one correspondence between $\rho(r)$ and f, and hence the velocity dispersion can be determined once the distribution function is known. However, if the velocity dispersion is anisotropic, the distribution function depends on at least two integrals of motion. In the simplest case, the second is taken to be the square of the angular momentum, L^2.

Two-integral models require relating the second order velocity moments to the potential and density of the stellar system, and are handled by the Jeans equation in the following way. First, the observed surface brightness profile is de-projected and translated to a mass density by assuming a (generally spatially constant) M/L value and a central point mass (i.e., $M_{\rm BH}$). From this the gravitational potential can be calculated, and then the Jeans equation can be solved for the mean square velocities. These are projected onto the plane of the sky to obtain the line of sight velocity and velocity dispersion, then compared to the observed velocities. This process is repeated until the values of M/L and $M_{\rm BH}$ which produce the best fit to the data are found.

Unfortunately, 2 integrals of motion are not sufficient in most cases. However, Schwarzschild (1979) devised a method to construct model galaxies without any explicit knowledge of the integrals of motion. This requires defining the gravitational potential as the sum of the central point mass and the stellar density. "All possible orbits" in this mass distribution are then calculated as functions of energy and angular momentum, and integrated over many periods to give time-averaged densities, velocities and velocity dispersions (Kormendy & Ho 2013). The optimal combination of these orbital distributions is calculated to give the best fits to the light and velocity dispersion profiles. This method is widely applied in BH detection codes, i.e., the Nuker code (Gebhardt et al. 2000; Gebhardt et al. 2003). The Schwarzschild method still has drawbacks. For example, the inclination angle, i, is always assumed a priori. If i is not assumed, then there is an extra degree of freedom that cannot be constrained by observables. Despite the complexity of allowing for anisotropic velocity dispersions,

$M_{\rm BH}$ estimates through stellar kinematics are in reasonable agreement with estimates made from different methods.

1.3.2.3 Gas dynamics

As well as a stellar dynamical detection, M87 is also the closest galaxy for which $M_{\rm BH}$ has been estimated through gas dynamics (Macchetto et al. 1997). This analysis is based on the rotation of the ionised gas disk near the centre of M87, with Macchetto et al. (1997) finding $M_{\rm BH} \simeq (3.2 \pm 0.9) \times 10^9 M_\odot$. Ferrarese & Ford (2005) summarise the steps involved in estimating SMBH masses through gas dynamical data. In general, this involves calculating the contribution to the circular velocity at a given radius, from the stars and gas disk, by determining the mass of each component within that radius. An additional contribution from a central point mass, $M_{\rm BH}$, also needs to be considered, and this is left as a free parameter in the models.

The circular velocity is then projected along the line of sight, which requires an inclination angle of the disk, normally assumed a priori. The model is then compared to the observations, and the free parameters are tweaked until the best fit to the data is obtained. When possible, the free parameters are left as: $M_{\rm BH}$; the disk inclination; the mass-to-light ratio for the stars; the systematic velocity of the disk and the projected position of the centre of the slit relative to the kinematical centre of the disk.

Estimates of $M_{\rm BH}$ based on gas motions are generally easier than stellar-dynamically estimates for a number of reasons. Firstly, the enclosed mass can be obtained directly from the circular velocity of the gas

$$v_c^2(r) = \frac{G[M_*(r) + M_{\rm BH}]}{r}. \tag{1.52}$$

For stars, the velocities measured near the SMBH are "contaminated" by stars that orbit to much greater distances. Finally, the motion of the gas is characterised by one velocity at every radius. Hence, there is no anisotropy, as is potentially the case for stars.

1.3.2.4 Reverberation mapping

A useful method for SMBH detection in AGN is reverberation mapping (Blandford & McKee 1982; Netzer & Peterson 1997). Spectra of AGN exhibit broad emission lines at certain wavelengths, usually optical and ultraviolet. The widths of these emission lines are assumed to reflect Doppler broadening, with inferred velocity widths $500\,\mathrm{km\,s^{-1}} \lesssim \Delta V \lesssim 10^4\,\mathrm{km\,s^{-1}}$ (ΔV is the full width half maximum of the velocity broadening function). The emission line fluxes vary strongly with changes in the continuum (the light from the accretion disk near the SMBH), implying that they are due to ionising photons from the central source.

The response of the emission lines is also found to be delayed with respect to changes in the continuum, so associating these delays with light travel time, the size of the broad line emission region, R_{BLR}, can be estimated (found to be $R_{\mathrm{BLR}} \sim 0.01$–$0.1$ pc). Since the emission line gas is located well inside the SMBH sphere of influence, this leads directly to an estimate for the SMBH mass:

$$M_{\mathrm{BH}} = \frac{f\,R_{\mathrm{BLR}}\,(\Delta V)^2}{G}, \tag{1.53}$$

where f is a constant of order unity. The actual value for f depends on unknowns such as the geometry of the broad emission region and the radial emissivity of the gas. In spite of these unknowns, reverberation mapping mass estimates hold an important advantage over stellar dynamical detections. The ΔV term in equation (1.53) is due almost entirely due to the gravitational force of the SMBH, so the sphere of influence does not need to be resolved.

1.3.3 Correlations between SMBHs and galaxy properties

Observations of quiescent $z = 0$ galaxies show that the masses of the SMBH correlate with global properties of the host galaxy. These properties include bulge luminosity, L_{bulge} (Magorrian et al. 1998; Marconi & Hunt 2003; Gültekin et al. 2009; McConnell & Ma 2013; Kormendy & Ho 2013), bulge mass, M_{bulge} (Magorrian et al. 1998; Häring &

Rix 2004; McConnell & Ma 2013; Kormendy & Ho 2013), and stellar aperture velocity dispersion, $\sigma_{\rm ap}$ (Ferrarese & Merritt 2000; Gebhardt et al. 2000; Ferrarese & Ford 2005; Gültekin et al. 2009; McConnell & Ma 2013; Kormendy & Ho 2013), measured inside specific fractions of the stellar effective radius, R_e. The definition of $M_{\rm bulge}$ varies between authors (e.g. stellar or dynamical mass), as does the fraction of R_e chosen to measure the aperture velocity dispersion.

The black hole–galaxy correlations are often fitted by power-laws of the form

$$\log\left(\frac{M_{\rm BH}}{M_\odot}\right) = \alpha + \beta\log(X), \tag{1.54}$$

where X is the galaxy property in question. This is done as a first-order characterisation, allowing investigation of the intrinsic scatter: indeed it is the relatively low scatter around such fits that make these scaling relations interesting. However, there is generally no physical reason given for these relations to be power laws.

Figures 1.13–1.15 illustrate these correlations, using the data set compiled by Kormendy & Ho (2013), along with their best fitting power-laws. For $z = 0$ galaxies, Kormendy & Ho (2013) have collected together reliable black hole mass estimates for 35 elliptical and 41 bulges (at the centre of disk galaxies), along with absolute K-band magnitudes and aperture stellar velocity dispersions, $\sigma_{\rm ap}$. They also calculate bulge masses for each galaxy (cf. §1.3.3.2). Kormendy & Ho (2013) split their bulge sample into classical bulges and pseudo-bulges.

Kormendy & Ho (2013) claim that properties of classical bulges and ellipticals indeed correlate closely with $M_{\rm BH}$, but pseudo-bulges do not. For their best fitting power laws, they include only the classical bulges (red points in Figures 1.13 – 1.15) and ellipticals (black points), excluding pseudo-bulges (cyan points) and any mergers in process (green points). They also exclude three outlying systems one elliptical and two classical bulges, shown by black and red open squares respectively. The main reason for leaving out pseudo-bulges and the outliers was to reduce the amount of intrinsic scatter around a line of best fit. It is not clear whether they should be omitted when considering an actual physical model.

1.3.3.1 The $M_{\rm BH}$–$L_{\rm bulge}$ relation

Figure 1.13 shows the $M_{\rm BH}$–$L_{\rm K,bulge}$ data from Kormendy & Ho (2013). The dashed line shows their best fitting power-law, given by

$$\log\left(\frac{M_{\rm BH}}{M_\odot}\right) = (8.734 \pm 0.069) + (1.21 \pm 0.09)\log\left(\frac{L_{\rm K,bulge}}{10^{11}L_\odot}\right). \tag{1.55}$$

This fit is to the ellipticals (black points) and classical bulges (red points), excluding pseudo-bulges (cyan points), mergers in process (green points) and the three outliers (open squares). They find intrinsic scatter of ~ 0.31 dex, assuming typical errors in the absolute K-band magnitude of $\pm$0.2mag.

Other authors have considered the $M_{\rm BH}$–$L_{\rm bulge}$ relation in various band passes (Marconi & Hunt 2003; Gültekin et al. 2009; Sani et al. 2011; McConnell & Ma 2013), with similar best fitting power-laws ($\alpha \sim 8.2$–9.4 and $\beta \sim 0.9$–1.2). However, the intrinsic scatter found by Kormendy & Ho (2013) is lower than these previous studies (typically 0.35–0.5 dex depending on band pass). The reason for this decrease in scatter is partly because using K-band magnitudes minimizes the effects of internal absorption and young stars.

1.3.3.2 The $M_{\rm BH}$–$M_{\rm bulge}$ relation

Different methods for estimating $M_{\rm bulge}$ exist in the literature. Many authors use luminosities in a given band pass and multiply by a dynamical (dark matter included) or stellar mass-to-light ratio (Magorrian et al. 1998; Häring & Rix 2004; McConnell & Ma 2013). It is usually assumed that mass follows light (spatially constant M/L) when this method is applied, and/or that any contribution from dark matter is small in the central regions (i.e. inside the bulge). Other authors have also considered virial bulge mass estimates, calculated using

$$M_{\rm bulge} = k\frac{\sigma^2 R_e}{G}, \tag{1.56}$$

where k is related to the Fundamental Plane of ellipticals discussed in §1.2.3, with $k = (M/L)^2(k_R k_V)^{-1}$ in equation (1.56). When calculating virial bulge masses, it is

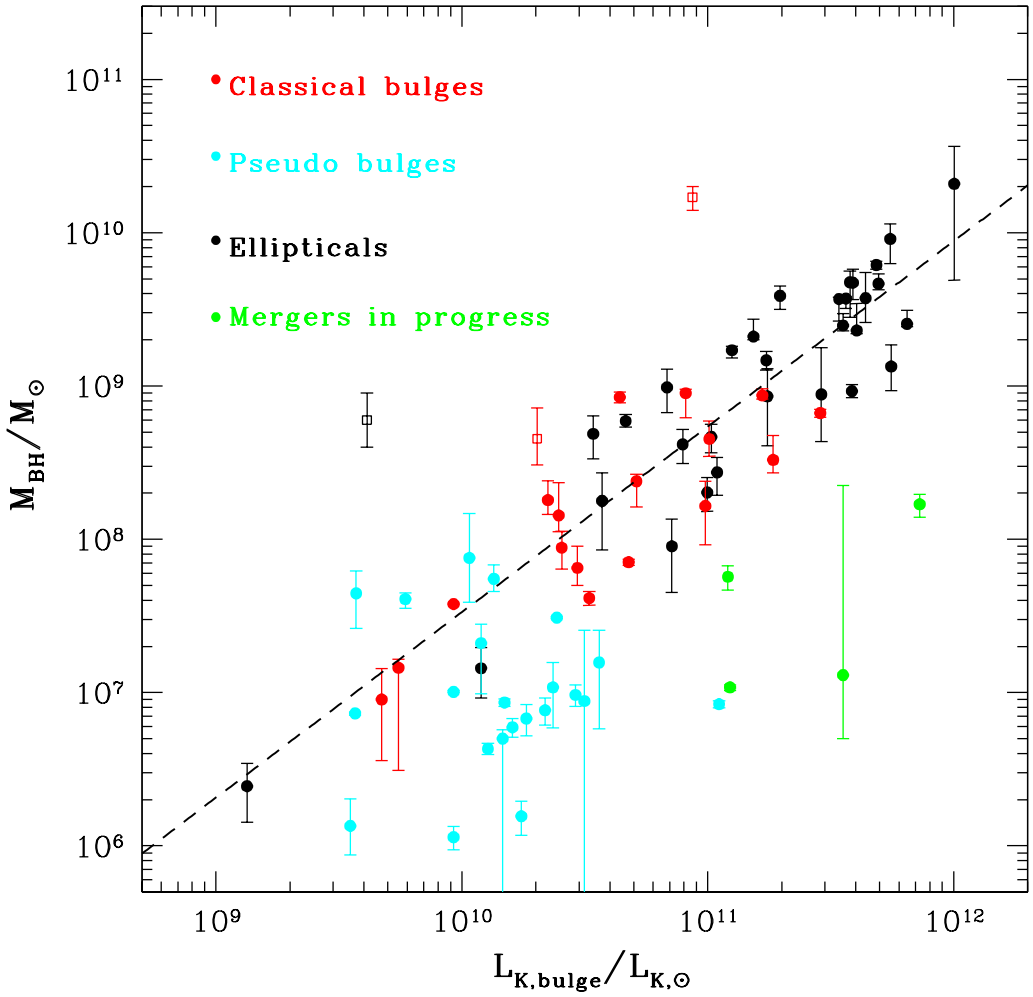

Figure 1.13: The $M_{\rm BH}$–$L_{\rm K,bulge}$ relation for early-type galaxies and bulges from the Kormendy & Ho (2013) sample. The different samples from their data are ellipticals (black points), classical bulges (red points) and pseudo-bulges (cyan points). They also identify mergers in process (green points) and BH monsters (squares). The black dashed line is a power-law fit to the ellipticals and classical bulges only: $\log(M_{\rm BH}/M_{\odot}) = 8.734 + 1.21\log(L_{\rm K,bulge}/10^{11}L_{\rm K,\odot})$.

often assumed that k is constant, with $k \sim 3$–8 (Marconi & Hunt 2003; Häring & Rix 2004; Cappellari et al. 2006; Wolf et al. 2010). However, the non-homology seen in galaxies (i.e. the density and/or kinematical structure are not constant with galaxy mass/luminosity) suggests that k in equation (1.56) is not constant. It will also depend on which velocity dispersion is used (i.e., inside R_e or the central value).

Figure 1.14 shows $M_{\rm BH}$–$M_{\rm bulge}$ data from Kormendy & Ho (2013), with the same point colours as Figure 1.13. The bulge masses have been calculated by Kormendy & Ho (2013) using the K-band luminosities combined with the mean of two, independent estimates of the mass-to-light ratio, $M/L_{\rm K}$. The first of these uses a dynamically measured correlation between $M/L_{\rm K}$ and the aperture velocity dispersion, measured inside R_e (Cappellari et al. 2006; Williams, Bureau & Cappellari 2009):

$$\log\left(\frac{M}{L_K}\right) = 0.2871 \log \sigma_{\rm ap}(R_e) - 0.6375. \tag{1.57}$$

The other K-band mass-to-light ratio comes from the galaxy's $(B-V)_0$ colour, through stellar population models (Into & Portinari 2013):

$$\log\left(\frac{M}{L_K}\right) = 1.055(B-V) - 0.9402. \tag{1.58}$$

The dashed black line is the best fit from Kormendy & Ho (2013) to the elliptical and classical bulge data:

$$\log\left(\frac{M_{\rm BH}}{M_\odot}\right) = (8.69 \pm 0.06) + (1.16 \pm 0.08) \log\left(\frac{M_{\rm bulge}}{10^{11} M_\odot}\right). \tag{1.59}$$

The similarity between this and the $M_{\rm BH}$–$L_{\rm K,bulge}$ relation in Figure 1.13 is unsurprising. Both the K-band mass-to-light ratios used by Kormendy & Ho (2013) depend weakly on velocity dispersion and colour respectively. This is consistent with the K-band mass-to-light ratios discussed earlier in the context of population synthesis models. Given the Faber-Jackson relation, $L \propto \sigma^4$, $M/L_{\rm K}$ is therefore approximately constant as a function of $L_{\rm K,bulge}$, with a "typical" value of $M/L_{\rm K} \sim 1$ for the luminosity range $10^9 L_\odot \lesssim L_{\rm K} \lesssim 10^{12} L_\odot$.

Despite the different methods for calculating $M_{\rm bulge}$, best fitting power-laws from previous work are broadly consistent with Kormendy & Ho (2013), with $\alpha \sim 8$–9

and $\beta \sim 0.96$–1.16. It is worth noting that a (weakly varying) ratio $M_{\rm BH}/M_{\rm bulge} \simeq (1.4-6)\times10^{-3}$ follows from this (Magorrian et al. 1998; H$\acute{}$aring & Rix 2004; McConnell & Ma 2013).

1.3.3.3 The $M_{\rm BH}$–$\sigma_{\rm ap}$ relation

The stellar velocity dispersion used to define the $M_{\rm BH}$–σ relation is the aperture dispersion, $\sigma_{\rm ap}$. This is a line of sight velocity dispersion, averaged over an aperture with a radius that is some fraction of the stellar effective radius, R_e. This fraction varies from group to group; many authors choose to work with $\sigma_{\rm ap}(R_e)$ (Gebhardt et al. 2000; Gültekin et al. 2009; McConnell & Ma 2013), whereas Ferrarese & Merritt (2000) measure inside $R_e/8$. Ferrarese & Merritt choose this fraction as it is a closer representation of the central velocity dispersion, used in the earliest studies of the fundamental plane of ellipticals (cf. §1.2.3).

Figure 1.15 shows $M_{\rm BH}$–σ data from Kormendy & Ho (2013), with the same point colours as the previous two Figures. The dashed line corresponds to the best fit from Kormendy & Ho (2013):

$$\log\left(\frac{M_{\rm BH}}{M_\odot}\right) = (8.49 \pm 0.049) + (4.38 \pm 0.29)\log\left(\frac{\sigma}{200\,{\rm km\,s^{-1}}}\right). \tag{1.60}$$

This best-fitting power law is consistent with previous studies, with other authors generally finding a slope of $\beta \simeq 4$–5, and an intercept $\alpha \simeq 8$–9 (Ferrarese & Merritt 2000; Gebhardt et al. 2000; Ferrarese & Ford 2005; Gültekin et al. 2009).

More recently than these, McConnell & Ma (2013) found an $M_{\rm BH}$–σ relation with a slope of $\beta \simeq 5.57$, significantly steeper than previous results. This is mainly due to the inclusion of new $M_{\rm BH}$ measurements in NGC 3842 and NGC 4889, two of the largest black hole masses that have been measured to date (McConnell et al. 2011; McConnell et al. 2012). Furthermore, McConnell & Ma (2013) do not distinguish between classical and pseudo bulges. Kormendy & Ho (2013) exclude pseudo bulges and the two largest black hole masses (NGC 3842 and NGC 4889) from their best fits, and hint that this is the reason for their shallower slope compared to McConnell & Ma (2013). This is

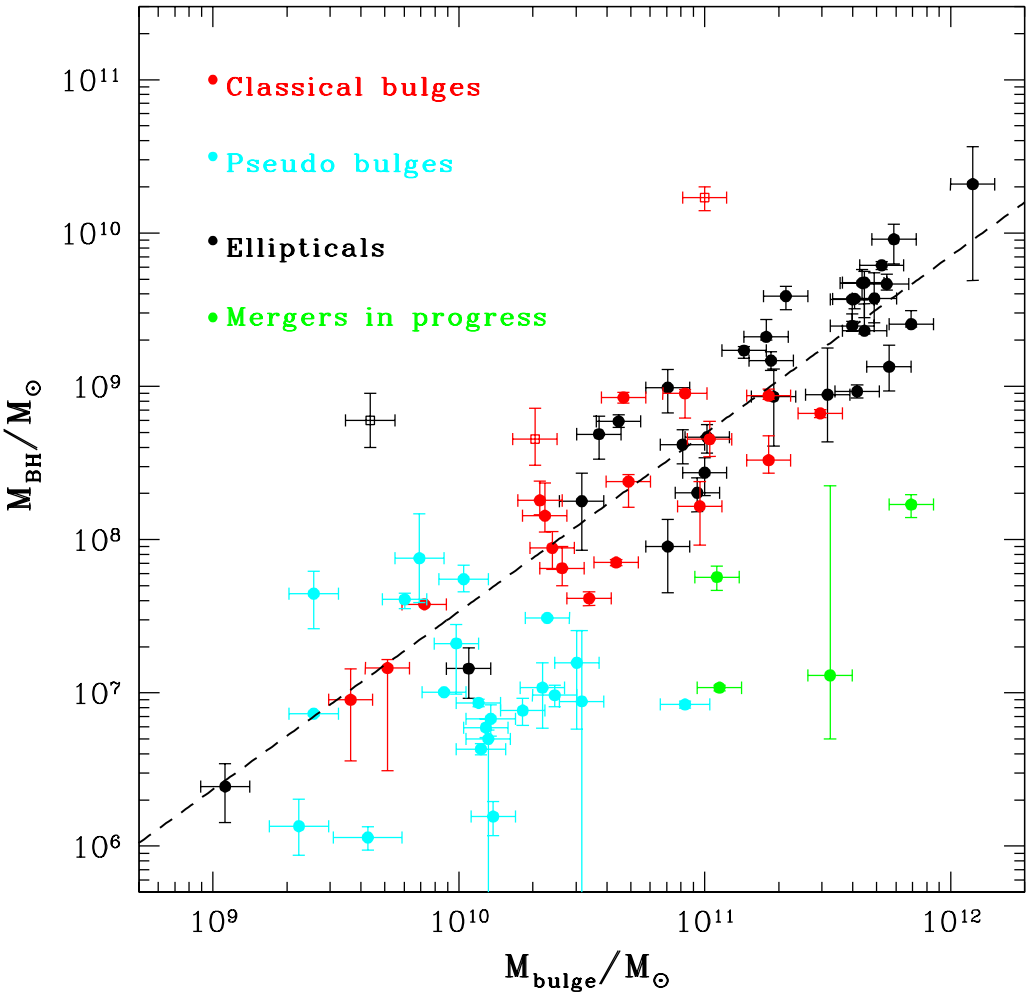

Figure 1.14: The $M_{\rm BH}$–$M_{\rm bulge}$ relation for galaxies from the Kormendy & Ho (2013) sample. The different point colours are indicated in the Figure, and are the same as for Figure 1.13. The black dashed line is their best fitting power-law (for ellipticals and classical bulges), given by $\log(M_{\rm BH}/M_{\odot}) = 8.69 + 1.16\log(M_{\rm bulge}/10^{11}M_{\odot})$. The bulge masses were calculated using the K-band absolute magnitudes, combined with an average of two K-band mass to light ratios (see text).

problematic and suggests that a single power law isn't appropriate if the slope depends so heavily on the inclusion (or not) of one or two points.

Log-quadratic fits to the $M_{\rm BH}$–σ relation have also been attempted (Wyithe 2006a; Wyithe 2006b; McConnell & Ma 2013) of the form

$$\log\left(\frac{M_{\rm BH}}{M_\odot}\right) = \alpha + \beta\log(\sigma/200{\rm km\,s^{-1}}) + \gamma\big[\log(\sigma/200{\rm km\,s^{-1}})\big]^2. \tag{1.61}$$

McConnell & Ma (2013) claim that such a fit does not decrease the intrinsic scatter, but they do find $\gamma > 0$ with 82% confidence, consistent with the results of Wyithe (2006a,b). The dot-dash line in Figure 1.15 shows the log-quadratic fit obtained by McConnell & Ma, with $\alpha = 8.28 \pm 0.07, \beta = 5.76 \pm 0.34$ and $\gamma = 1.68 \pm 1.82$ in equation (1.61). It is important to once again stress that there is no physical motivation for fitting a single power law, or indeed a log-quadratic fit, to any of the BH – galaxy correlations. These best fits take no account of any of the physics involved in establishing the observed correlations (cf. §1.4). It is more interesting to compare an actual physical model to the observed SMBH correlations, rather than fitting arbitrary curves chosen for simplicity. The work presented in Chapters 2 and 3 is the first attempt at doing this in a fully self-consistent way.

One reason for fitting power laws is to investigate how tight the relations are. If the scatter is small enough, then the correlation can be used to estimate (without direct measurement) SMBH masses. All of $L_{\rm bulge}$, $\sigma_{\rm ap}$ and $M_{\rm bulge}$ are easier to measure than $M_{\rm BH}$. Although it has previously been argued that the $M_{\rm BH}$–σ relation exhibits less scatter (consistent with zero; Ferrarese & Ford 2005), Kormendy & Ho (2013) suggest that all three correlations have very similar *intrinsic* scatter, approximately 0.3 dex. Either way, correlations between SMBH masses, significant on scales of $r_{\rm inf}$ (less than a few tens of parsecs), and global properties of the galaxy, usually measured on scales of R_e (few kiloparsecs), are strong evidence of a connection between their formation and evolution.

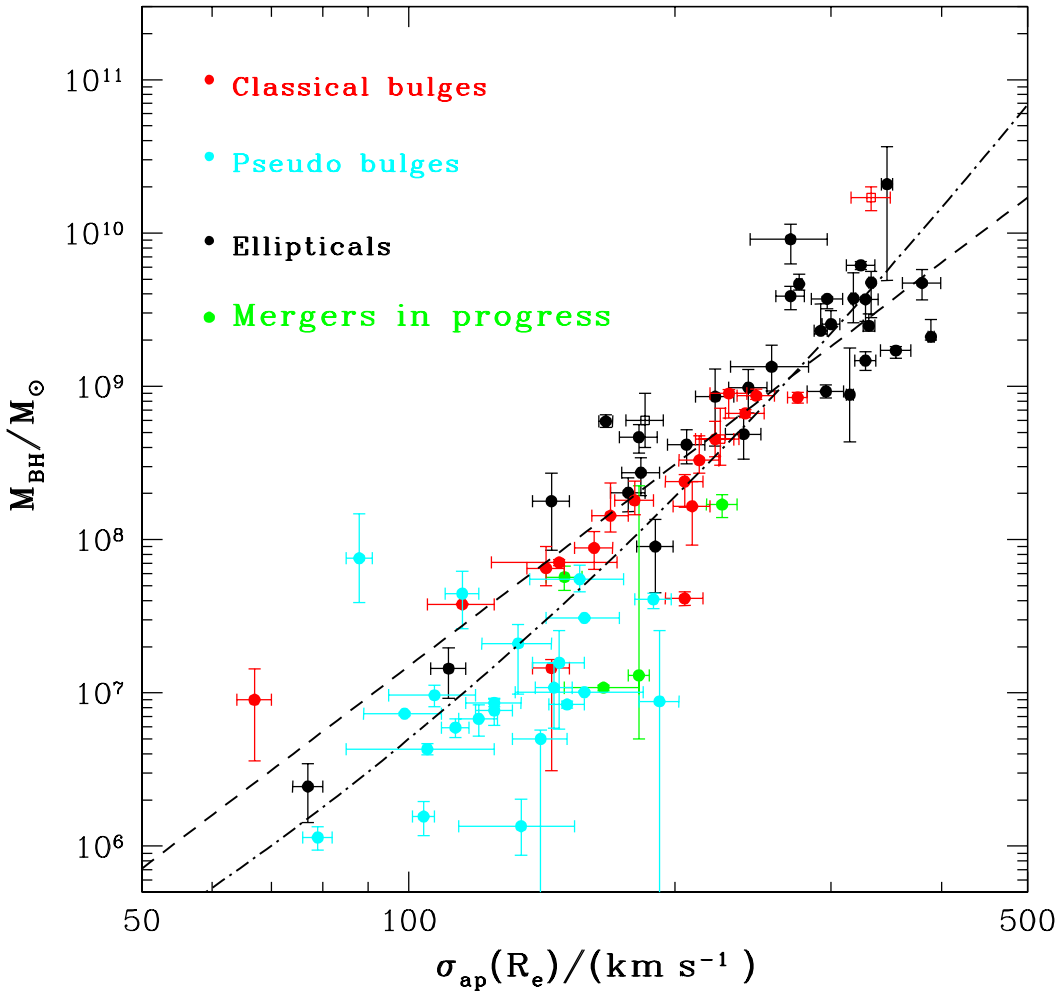

Figure 1.15: The $M_{\rm BH}$–$\sigma_{\rm ap}$ relation for $z = 0$ galaxies and galaxy bulges, with data from Kormendy & Ho (2013). Point colours are the same as previous Figures. The dashed line is again the best-fitting power law (ellipticals and classical bulges), given by $\log(M_{\rm BH}/M_{\odot}) = 8.49 + 4.38\log(\sigma/200\ {\rm kms}^{-1})$. The dash-dot line corresponds to the log-quadratic fit obtained by McConnell & Ma (2013): $\log(M_{\rm BH}/M_{\odot}) = 8.28 + 5.76\log(\sigma/200\ {\rm kms}^{-1}) + 1.68[\log(\sigma/200\ {\rm kms}^{-1})]^2$.

1.3.3.4 Other bulge property correlations

There are several other correlations between $M_{\rm BH}$ and other galaxy properties that have been proposed. Sani et al. (2011) explored a relation between black hole mass and stellar effective radius, R_e. They found that such a relation exhibits much more scatter than the three relations discussed above. Graham & Driver (2007) found a tight correlation between $M_{\rm BH}$ and the bulge Sérsic index, n, with similar scatter to the other correlations (Savorgnan et al. 2013; Savorgnan 2016). However, several authors have suggested that such a correlation is not as tight (Beifiori et al. 2012; Vika et al. 2012; Kormendy & Ho 2013). It is unclear whether a correlation between black hole mass and n is simply a result of a more fundamental $M_{\rm BH}$–bulge property relation, or if $M_{\rm BH}$–n is itself *the* main correlation (Graham & Driver 2007).

Beyond this, it has been suggested that correlations between $M_{\rm BH}$ and two of R_e, σ and $M_{\rm bulge}$ (or $L_{\rm bulge}$) are slightly tighter (~ 0.2 dex intrinsic scatter) than any single parameter correlation (Hopkins et al. 2007a,b). Such correlations are referred to (by Hopkins et al.) as the Black Hole Fundamental Plane (BHFP), and are analogous to the fundamental plane of ellipticals. The combination of velocity dispersion and effective radius proposed by Hopkins et al (2007a) is $M_{\rm BH} \propto \sigma_{\rm ap}^{3\pm0.30} R_e^{0.43\pm0.19}$. This is not dissimilar to the $M_{\rm BH}$–$M_{\rm dyn}$ relationship considered by Marconi & Hunt (2003), who considered a $M_{\rm BH}$–$M_{\rm dyn}$ correlation, with $M_{\rm dyn} \propto \sigma^2 R_e$ (Häring & Rix 2004; McConnell & Ma 2013). Marconi & Hunt also found that this relation is slightly tighter (~ 0.25 dex intrinsic scatter) than either $M_{\rm BH}$–$\sigma_{\rm ap}$ or $M_{\rm BH}$–L. It remains an open question whether any one correlation, or the BHFP, is more significant than the others, but as said above, collectively they are interpreted as evidence for co-evolution between SMBHs and host galaxies.

1.3.3.5 Correlations with the dark matter halo

The possibility of a correlation between $M_{\rm BH}$ and the virial mass of the dark matter halo, $M_{\rm DM}$, at $z = 0$, has been proposed by several authors (Ferrarese 2002; Baes et al.

2003; Croton 2009; Bandara, Crampton & Simard 2009; Dutton et al. 2010; Bogdán & Goulding 2015). For a sample of 20 elliptical galaxies (Kronawitter et al. 2000) and 16 spiral galaxies (Gebhardt et al. 2001), Ferrarese (2002) investigated an $M_{\rm BH}$–$M_{\rm DM}$ correlation. First of all, Ferrarese finds a tight correlation between $\sigma_{\rm ap}(R_e/8)$, and the galaxy's large scale circular velocity, V_c (Kronawitter et al. 2000 measure V_c at "the radius of the last kinematic data point." This is $\sim R_e$ for most of their galaxies). For both samples combined (ellipticals and spirals), Ferrarese concludes that

$$\log V_c = (0.84 \pm 0.09) \log \sigma_{\rm ap} + (0.55 \pm 0.19). \tag{1.62}$$

She then combines this V_c–$\sigma_{\rm ap}$ relation with the $M_{\rm BH}$–$\sigma_{\rm ap}$ relation from Ferrarese & Merritt (2000), given by

$$\log\left(\frac{M_{\rm BH}}{M_\odot}\right) = (8.15 \pm 1.3) + (4.80 \pm 0.54) \log\left(\frac{\sigma_{\rm ap}}{200\,{\rm km\,s^{-1}}}\right), \tag{1.63}$$

to give an $M_{\rm BH}$–V_c relation.

Ferrarese (2002) then estimates a relation between the masses of the SMBH and the dark matter halo, by combining this with the CDM simulations of Bullock et al. (2001) to connect V_c to $M_{\rm d,200}$ (dark matter mass inside the r_{200} radius). This radius defines a sphere within which the density is $\Delta = 200$ times the critical density of the Universe. Given this, and by virtue of the virial theorem, $M_{\rm d,200} \propto V_{200}^3$. Assuming an NFW model for the dark matter halo, and that V_c is flat out to the scale radius, r_s [so $V_c = V_c(r_s)$], Ferrarese then calculates the ratio $V_c(r_s)/V_{200}$, making use of the relation between halo concentration and halo mass from Bullock et al. (2001). Given all this, the $M_{\rm BH}$–$M_{\rm d,200}$ relation obtained by Ferrarese (2002) is

$$\frac{M_{\rm BH}}{10^8 M_\odot} \simeq 0.10 \left(\frac{M_{\rm d,200}}{10^{12} M_\odot}\right)^{1.65}. \tag{1.64}$$

Baes et al. (2003) performed an identical analysis (with the same assumptions and method) for 12 additional spiral galaxies, and found results consistent with Ferrarese (2002). Both authors point out that the uncertainties in the conversion from V_c–$\sigma_{\rm ap}$ to $M_{\rm BH}$–$M_{\rm d,200}$ (or indeed $M_{\rm d,vir}$) can be quite large. The assumption that the circular-speed curves are flat out to such large radii is incorrect in detail. The "true" difference

between the measured V_c and V_{200} will therefore be even greater. There is also model dependence to be aware of when calculating V_c/V_{200} to relate V_c to $M_{\rm d,200}$. For these reasons, equation (1.64) should be considered as a rough guideline only. The work in Chapters 2 and 3 allow for a more detailed analysis of how to relate total circular speeds, halo masses and SMBH masses.

For a sample of 792 galaxies, spanning a range of Hubble types, Ho (2007) found the V_c–$\sigma_{\rm ap}$ relation to exhibit much more scatter than previously shown. Ho also suggests that the zero point depends on galaxy morphology, bulge-to-disk ratio and light concentration. Part of the problem here is that for late-type galaxies with little or no bulge, Ho (2007) used the velocity dispersion of the central star cluster. This is a self-gravitating system and distinct from galaxy bulges. The larger scatter found by Ho (2007) was mainly due to these late-type galaxies.

More recently, there have been arguments both for (Volonteri, Natarajan & Gültekin 2011) and against (Kormendy & Bender 2011; Kormendy & Ho 2013) correlations between SMBHs and dark matter halos. Kormendy & Bender (2011) suggest that correlations between $M_{\rm BH}$ and $M_{\rm d,vir}$ (or indeed any other property of the dark matter halo) implies that it is the dark matter that supplies the material for growing the black hole, through exotic physics. They propose that there is no relation between V_c and σ, although the outliers in their relation are the late-types that use the velocity dispersion of the central star cluster.

Volonteri et al. (2011) found that $M_{\rm BH}$ is connected to V_c measured at large radii, suggesting $M_{\rm BH} \propto V_{\rm c}^{\rm p}$, with $p \approx 4$. At such large radii, the dark matter dominates the mass of the system. Volonteri et al. (2011) suggest that the $M_{\rm BH}$–V_c and $M_{\rm BH}$–$\sigma_{\rm ap}$ relations have similar slope and scatter.

It is important to note that a fundamental correlation between SMBH and dark matter halo properties does not in any way imply that dark matter is feeding the growth of the black hole, as suggested by Kormendy & Bender (2011). The stellar velocity dispersion is of course connected to the dark matter halo which dominates the potential of the galaxy. How the stellar properties and dark matter halo properties are connected is considered in detail in Chapter 2.

When considering a physical model (rather than assuming a best fit), there is no reason to expect any of the $M_{\rm BH}$–galaxy property relations to be linear in log–log space. The majority of what has been discussed regarding these correlations is about best-fitting power-laws, generally with no physical motivation. Therefore, assuming the actual relation to be linear, based on such a fit, does not necessarily make it more fundamental than any other relation. This was suggested by Kormendy & Ho (2013), who argued that the correlations between SMBHs and baryonic components ($M_{\rm bulge}$ and $\sigma_{\rm ap}$) are more fundamental than any correlation between SMBH and the dark matter halo.

Kormendy & Ho (2013) assume that correlations between $M_{\rm BH}$ and either bulge properties or dark matter halo properties, should be linear. They suggested that combining a $M_{\rm BH}$–$M_{\rm bulge}$ relation, assumed to be linear, with the non-linear M_*–$M_{\rm d,vir}$ relation (see §1.2.2) yields a correlation between $M_{\rm BH}$ and $M_{\rm d,vir}$ that cannot be linear. However, the $M_{\rm BH}$–$M_{\rm bulge}$ relation is *not* linear when considering a physical model (rather than assuming a best fit). This is discussed further in §3.3.3.

1.4 Physics of the $M_{\rm BH}$–bulge relations

The existence of correlations between the SMBH imply co-evolution between the black hole and galaxy. Galaxy formation models therefore need to reproduce the observed correlations. There have been several attempts at a theoretical explanation of how these correlations were established, with varying degrees of success.

The co-evolution most likely involved some form of self-regulated feedback. Most of the SMBH mass in large galaxies is grown in a quasar phase of Eddington (cf. §1.4.1) rate accretion (Yu & Tremaine 2002), at some high redshift. Such accretion deposits significant amounts of momentum and energy back into the gas supply, leading to possible blow out, halting further accretion onto the SMBH. In terms of the BH — bulge correlations, the stellar velocity dispersion holds particular significance, as it should reflect the depth of the potential well that the SMBH feedback had to overcome

to expel the gas from the protogalaxy. Galaxy formation simulations now routinely include prescriptions for halting SMBH growth via "quasar-mode" feedback (Springel, Di Matteo & Hernquist 2005; Di Matteo, Springel & Hernquist 2005; Sijacki et al. 2007; Di Matteo et al. 2008; DeGraf et al. 2012; Sijacki et al. 2015; DeGraf et al. 2015).

Two early works considering the quenching of SMBH accretion via feedback are Silk & Rees (1998) and Fabian (1999). These authors assumed an initial seed black hole at the centre of an isothermal protogalaxy, containing both dark matter and hot gas. Accretion of gas onto the black hole converts gravitational energy into radiation. Given that the total energy, $E_T \equiv E_K + E_P = E_P/2$, then half of the change in gravitational potential energy is radiated away. If this radiation is able to couple to the surrounding matter, this produces an outflow, sweeping the gas into a shell and driving it outwards. Silk & Rees argued that this leads to $M_{\rm BH} \propto \sigma^5$, whereas Fabian found that $M_{\rm BH} \propto \sigma^4$. Both of these are compatible with observations; the differences in the two results are due to different assumptions about the thermal physics driving the shell.

King & Pounds (2003) provide a simplified description for SMBH feedback, based on a Compton-thick wind resulting from accretion at or above the Eddington rate. Their analysis shows that the momentum flux is simply $dp_{\rm wind}/dt = L_{\rm Edd}/c$, implying high wind speeds of up to $\sim 0.1c$. The SMBH wind provides an outward force, sweeping up the ambient gas into a thin, radiative shell. If the outward thrust exceeds the gravitational force, then the gas shell is able to escape the potential well of the galaxy. This simple idea shows why a correlation is actually expected. When the forces are equal, there is a driving force proportional to $M_{\rm BH}$, equal to a gravitational force which is a function of σ.

Observations of local Active Galactic Nuclei (AGN) lend support to the idea that $dp_{\rm wind}/dt = L_{\rm Edd}/c$, with the detection of ultra-fast outflows. Pounds et al. (2003) was the first of these, observing a high velocity outflow ($v_w \sim 0.08c$) in the $z \simeq 0$ active galaxy, PG1211+143. Subsequent work has shown similarly high velocity outflows ($v_w \sim 0.03c$–$0.3c$) in other galaxies containing AGN (Reeves, O'Brien & Ward 2003; Chartas, Brandt & Gallagher 2003; O'Brien et al. 2005; Krongold et al. 2007;

Tombesi et al. 2011; Gofford et al. 2013). Observations of galaxy scale outflows also support this AGN feedback scenario (Tremonti, Moustakas & Diamond-Stanic 2007; Holt, Tadhunter & Morganti 2008; Bautista et al. 2010; Sturm et al. 2011; Rupke & Veilleux 2011; Veilleux et al. 2013; Perna et al. 2015) – these large scale outflows cannot be explained by stellar feedback alone, since the velocities are too high.

Normal, quiescent galaxies have evolved through cosmic time, and are likely to have experienced a quasar phase powered by SMBH accretion, at some time in the past. Given that quasars are analogous to local AGN, it is promising that the observations outlined above are compatible with the King & Pounds (2003) feedback scenario. Presumably then, it is this kind of self-regulated feedback that defines the quasar-phase, and ultimately leads to blow-out of the gas, leaving behind a dormant SMBH and a quiescent galaxy. The King & Pounds (2003) model, although a very simplified description, utilises some key physical concepts, including the Eddington luminosity, shock conditions and cooling time scales.

1.4.1 The Eddington luminosity

The Eddington luminosity is the maximum luminosity an object can sustain if radiative forces (on free electrons) are balanced by gravitational forces. For a fully ionised gas, the interaction between radiation and the gas is due to photons scattering off free electrons, known as Thomson scattering. The flux per unit area at a radius r from a source with luminosity L is given by $L/(4\pi r^2)$. The momentum of a photon is given by $p = E/c$, so the radiation force is $F_{\rm rad} \equiv \dot{p} = L/c$. Therefore, the force per unit area (i.e. the radiation pressure) is $L/(4\pi r^2 c)$. The effective cross-sectional area of an electron is given by the Thomson cross-section, $\sigma_T = \kappa m_{\rm p}$, where κ is the scattering opacity. The radiation force acting on an electron is therefore

$$F_{\rm rad} = \sigma_T \frac{L}{4\pi r^2 c}. \tag{1.65}$$

The gravitational force acting on a proton-electron pair by the source of the

luminosity, with a mass, M, is given by

$$F_{\rm grav} = \frac{GM(m_p + m_e)}{r^2} \simeq \frac{GMm_p}{r^2}, \tag{1.66}$$

because $m_p \gg m_e$ for the last equality. The Eddington luminosity is found by equating the radiation force and the gravitational force, giving

$$L_{\rm Edd} = \frac{4\pi G m_p c}{\sigma_T} M. \tag{1.67}$$

As can be seen, $L_{\rm Edd}$ is proportional to the mass of the object providing the luminosity. If an object exceeds its Eddington luminosity, it is unable to hold on to the material in the outer layers, resulting in a radiation-driven outflow.

In accretion-powered objects, such as AGN, the luminosity is produced by the conversion of rest mass, m, into energy, at some efficiency, η: $E = \eta mc^2$. The value of η can be approximated by considering a particle in an accretion disk, moving towards the innermost circular orbit. For a non-rotating black hole, the radius of this orbit is $R_{\rm ISCO} = 3R_{\rm Sch} = 6GM_{\rm BH}/c^2$, where $R_{\rm Sch}$ is the Schwarzschild radius, the radius inside of which photons cannot escape a black hole. If the particle is initially at infinity and reaches $R = R_{\rm ISCO}$, then the change in gravitational potential energy, E_P is $GM_{\rm BH}m/R_{\rm ISCO} = mc^2/6$. Given that half the change in E_P is radiated away, this leads to $E = mc^2/12$, and hence $\eta \sim 0.1$.

For an object accreting mass at a rate $\dot{M}$, the luminosity is given by $L = \eta \dot{M} c^2$ (found by differentiating the energy equation). For accretion to occur, $L \leq L_{\rm Edd}$ is required, suggesting an upper-limit on the rate of accretion:

$$\dot{M}_{\rm Edd} = \frac{L_{\rm Edd}}{\eta c^2} = \frac{4\pi GM}{\eta \kappa c}, \tag{1.68}$$

where $\kappa = \sigma_T / m_p$.

1.4.2 Eddington winds

The observed high velocity outflows mentioned above are a generic property of accretion events occurring at close to the Eddington limit, according to King & Pounds (2003).

Assuming a radial outflow occupying solid angle $4\pi b$, with a constant speed v_w, the mass conservation equation tells us

$$\dot{M} = 4\pi b v_w r^2 \rho(r), \tag{1.69}$$

where $\rho(r)$ is the mass density. Early observational work (Pounds et al. 2003; Reeves, O'Brien & Ward 2003) *assumed* quasi-spherical winds and a value of $b \sim 1$. More recently, the work of Nardini et al. (2015) managed to constrain the value of the solid angle for the galaxy PDS456, by considering the amount of absorbed ionizing radiation that is re-emitted across the spectrum. Nardini et al. (2015) found results consistent with $0.5 < b \lesssim 1$.

Following King & Pounds (2003), in the single-scattering limit, the electron scattering optical depth through the outflow, observed from infinity down to radius R is

$$\tau = \int_R^\infty \kappa \, \rho \, dr = \frac{\kappa \dot{M}}{4\pi b v_w R}. \tag{1.70}$$

Combining this with the Eddington accretion rate [equation (1.68)] and the Schwarzschild radius, $R_{\rm Sch} = 2GM_{\rm BH}/c^2$.

$$\tau = \frac{1}{2b\eta} \frac{R_{\rm Sch}}{R} \frac{c}{v_w} \frac{\dot{M}}{\dot{M}_{\rm Edd}}. \tag{1.71}$$

Defining the photo-spheric radius, $R_{\rm ph}$ as the radius at which $\tau = 1$, it follows from equation (1.71) that

$$\frac{R_{\rm ph}}{R_{\rm Sch}} = \frac{1}{2b\eta} \frac{c}{v_w} \frac{\dot{M}}{\dot{M}_{\rm Edd}}. \tag{1.72}$$

Given that $(2b\eta) < 1$ and $v_w/c < 1$, then $R_{\rm ph} > R_{\rm Sch}$ for any outflow rate $\dot{M}$ of the order $\dot{M}_{\rm Edd}$. Such outflows are therefore Compton-thick, and most of the photons will have scattered. These photons will transfer their momentum, leading to a non-radiative outflow.

To ensure matter reaches the escape speed, King & Pounds (2003) assume that $R_{\rm ph}$ is close to the escape radius, $R_{\rm esc}$:

$$R_{\rm ph} \sim R_{\rm esc} \equiv \frac{c^2}{v_w^2} R_{\rm Sch}. \tag{1.73}$$

Combining this with equation (1.71), the wind velocity is approximately

$$\frac{v_w}{c} \sim 2b\eta \frac{\dot{M}_{\rm Edd}}{\dot{M}}. \tag{1.74}$$

Furthermore, combining equation (1.74) with the definition for the Eddington accretion rate [equation (1.68)] and assuming v is constant, yields the momentum flux:

$$\dot{M} v_w \sim 2b \frac{L_{\rm Edd}}{c}. \tag{1.75}$$

1.4.3 The two-shock wind model

For accretion at rates comparable to the Eddington limit, assuming $\eta \sim 0.1$ and $b \lesssim 1$ leads to winds launched with initial velocities, $v_w \sim 0.1c$, from the SMBH. This wind will then interact with the interstellar medium (ISM) via two shocks, similar to the stellar wind problem (Lamers & Cassinelli 1999; Dopita & Sutherland 2003). Assuming a smooth and initially static ISM, an inner reverse shock, at a radius $R_{\rm SW}$, slows the central wind, as the outflow collides with the ambient ISM. An outer forward shock, at a radius R_S (the radius of the shell), drives into the ISM, sweeping it outwards ahead of the shocked wind. There is a contact discontinuity at radius R_c between the two shocks. Figure 1.16 shows a schematic diagram of the wind shock model outlined above (Faucher-Giguére & Quataert 2012).

The ambient gas is then swept up into a shell. The dynamics of the swept-up shell are determined by the behaviour of the shocked wind region. If the shocked wind is able to cool efficiently, it will condense and will be geometrically thin. The shell is then driven outwards by a direct transfer of momentum from the wind impacting on its inner side and is referred to as momentum-driven. If the wind cannot cool efficiently, the shocked wind region will remain hot and expand. The shell is then driven by the thermal pressure and is referred to as energy-driven.

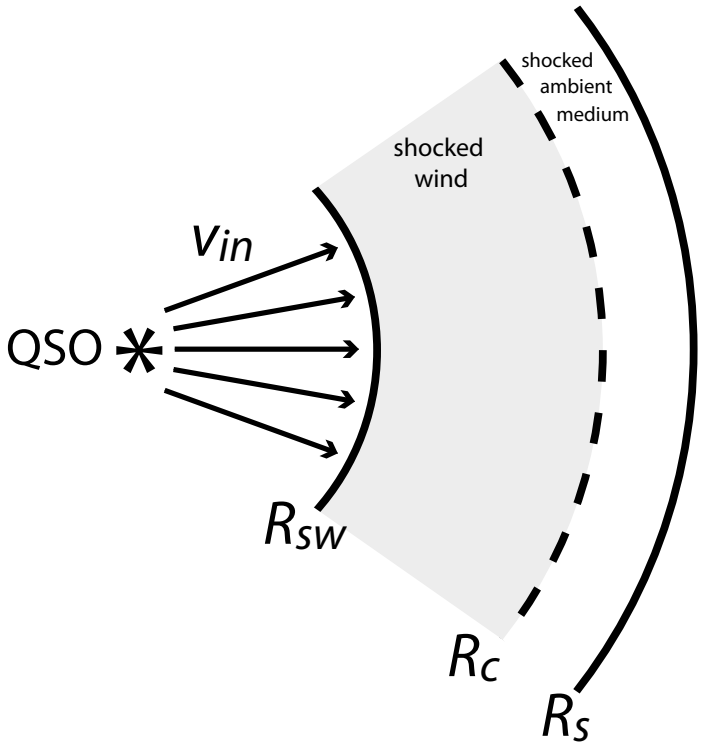

Figure 1.16: A schematic diagram of the wind shock from a central SMBH, from Faucher-Giguére & Quataert (2012). The AGN wind is launched from the nucleus with velocity, $v_{\rm in} \equiv v_w$. The wind is shocked at $R_{\rm SW}$, and the ISM is shocked at R_S (radius of the shell). The two shocks are separated by the contact discontinuity, R_c. It is the cooling of the shocked wind that determines the mechanism driving the outflow.

1.4.4 Cooling time-scales

The shocked wind region will be extremely hot and energetic. Faucher-Giguére & Quataert (2012) related the pre- and post-shock variables (pressure, density and velocity), combined with the equation of state, $P = \rho kT/(\mu m_p)$, to calculate the post-shock gas temperature. In the limit that the shock is strong ($v_w \gg c_s$ where c_s is the sound speed) and for a monatomic gas, the post-shock temperature is

$$T = \frac{3}{16}\frac{\mu m_p}{k} v_w^2 \sim 10^{10} \left(\frac{v_w}{0.1c}\right)^2 \text{K}. \tag{1.76}$$

The gas is therefore fully ionised, and the only cooling mechanisms are inverse Compton cooling and free-free emission. Inverse Compton cooling is when low-energy photons are scattered by relativistic electrons — the photons gain energy at the expense of the kinetic energy of the electrons, thus cooling the gas. Free-free emission is electromagnetic radiation generated when a charged particle decelerates in a plasma, when deflected by another charged particle. The moving particle loses kinetic energy, which is then converted into a photon.

For inverse Compton cooling in general, the energy loss rate of a relativistic electron is (Longair 2011)

$$\frac{dE}{dt} = \frac{4}{3}\kappa m_p c\, U_{\text{rad}} \left(\frac{v_e}{c}\right)^2 \left(\frac{E}{m_e c^2}\right)^2, \tag{1.77}$$

where v_e is the velocity of the electron, U_{rad} is the density of the radiation field and E is the energy of the electron, in the post-shock wind. The Compton cooling time of an electron of energy E is then

$$t_{\text{Comp}} = \frac{E}{dE/dt} = \left[\frac{4}{3}\kappa m_p c\, U_{\text{rad}} \left(\frac{v_e}{c}\right)^2 \frac{E}{(m_e\, c^2)^2}\right]^{-1}. \tag{1.78}$$

In the case of an SMBH wind, the density of the radiation field is given by $U_{\text{rad}} = L_{\text{Edd}}/4\pi r^2\, c$. The electron energy in the post-shock wind gas is $E = 3kT \simeq (9/16) m_p v_w^2$, where v_w is the wind velocity. The velocity of the electrons, v_e, can be determined using the electron energy:

$$E_{\text{e,kin}} = (\gamma - 1) m_e c^2 \simeq \frac{9}{16} m_p v_w^2, \tag{1.79}$$

where $\gamma = (1 - v_e^2/c^2)^{-1/2}$. For wind velocities $v_w/c \simeq 0.03$–0.1, the electrons are very relativistic, with $v_e \simeq 0.85$–$0.99c$. Combining the density radiation field, $U_{\rm rad}$, with the Eddington luminosity definition [equation (1.67)], along with the electron energy and velocities, the Compton cooling time for a black hole with mass $M_{\rm BH}$ is then

$$t_{\rm Comp} \simeq 2.7 \times 10^7 \left(\frac{r}{\rm kpc}\right)^2 \left(\frac{v_w}{0.1c}\right)^{-2} \left(\frac{v_e}{c}\right)^{-1} \left(\frac{M_{\rm BH}}{10^8 M_\odot}\right)^{-1} \text{yr}. \tag{1.80}$$

On the other hand, the free-free cooling time is approximately given by (Longair 2011)

$$t_{\rm ff} \simeq 2 \times 10^{11} \left(\frac{r}{\rm kpc}\right)^2 \left(\frac{M_{\rm BH}}{10^8 M_\odot}\right)^{-1} \text{yr}. \tag{1.81}$$

Clearly, inverse Compton cooling is the dominant cooling mechanism of the two when the electrons are relativistic. To determine how efficiently the shocked wind cools, it is necessary to compare the cooling time, $t_{\rm cool} \equiv t_{\rm Comp}$, with the dynamical time of the wind, $t_{\rm dyn} \equiv R_{\rm SW}/v_w$, and the flow time of the shell, $t_{\rm flow} \equiv R_S/v_{\rm sh}$. In these definitions, $R_{\rm SW}$ and R_S are defined in Figure 1.16. v_w and $v_{\rm sh}$ are the velocities of the wind and of the gas shell respectively.

1.4.5 Momentum-driven shell

If $t_{\rm cool} < t_{\rm dyn} \equiv R_{\rm SW}/v_{\rm w}$, then the shocked wind region has enough time to cool before more energy is injected. The shell will therefore be geometrically thin, and will be pushed outwards by the ram pressure of the wind, $\rho_w v_w^2$ (Koo & McKee 1990; Koo & McKee 1992). This is the momentum-driven regime, and is expected to always be the initial case for an SMBH wind, since the shock can cool efficiently via inverse Compton scattering.

For an initially static ambient medium that is both spherical and smooth, the shell's equation of motion is determined by the outward thrust ($F_{\rm rad} \equiv L_{\rm Edd}/c$), minus the gravitational effects from the BH and the mass inside the shell. Assuming that there are no stars, the only form of matter within the shell's radius will be dark matter, since the gas originally there has been swept up into the shell itself. The equation of

motion for a momentum-driven shell is therefore

$$\frac{d}{dt}[M_g(r)v] = \frac{L_{\rm Edd}}{c} - \frac{GM_g(r)}{r^2}[M_{\rm BH} + M_d(r)], \tag{1.82}$$

where $M_g(r)$ is the initial gas mass within radius r and $M_d(r)$ is the dark matter mass within radius r.

McQuillin & McLaughlin (2012) use equation (1.82) as their starting point for deriving a critical SMBH mass, $M_{\rm crit}$, required for a purely momentum-driven gas shell to escape a galaxy. They assume that there are no stars in the protogalaxy, and that the gas initially traces the dark matter. In detail, McQuillin & McLaughlin (2012) solve the equation of motion for the velocity fields, $v^2(r)$, of momentum-conserving shells driven from galaxy centres. To do this, they made use of the fact that

$$\frac{d[M_g(r)v(r)]}{dt} = \frac{1}{2M_g(r)}\frac{d[M_g^2(r)v^2(r)]}{dr}. \tag{1.83}$$

Combining this with $L_{\rm edd}/c = 4\pi GM_{\rm BH}/\kappa$, the equation of motion for a momentum-driven shell is

$$\frac{d[M_g^2(r)v^2(r)]}{dr} = \frac{8\pi G}{\kappa}M_{\rm BH}M_g(r) \; - \; \frac{GM_g^2(r)}{r^2}\left[M_d(r) + M_{\rm BH}\right]. \tag{1.84}$$

As mentioned, McQuillin & McLaughlin (2012) assumed that the gas initially traced the dark matter, so $M_g(r) = f_0 M_d(r)$, where f_0 is the gas-to-dark matter mass fraction. They then specify mass and radius units

$$M_\sigma = \frac{f_0\kappa\sigma_0^4}{\pi G^2} \quad \text{and} \quad r_\sigma = \frac{GM_\sigma}{\sigma_0^2}, \tag{1.85}$$

where κ is the Thomson-scattering opacity and σ_0 is a characteristic velocity dispersion, defined in terms of the peak of the dark matter circular-speed curve, $V_{\rm d,pk}$:

$$\sigma_0 = V_{\rm d,pk}/\sqrt{2}. \tag{1.86}$$

In order to solve for the velocity fields, McQuillin & McLaughlin (2012) define dimensionless radii and mass profiles in terms of the location of the peak, $r_{\rm pk}$:

$$x = \frac{r}{r_{\rm pk}}\,, \qquad m_d(x) = \frac{M_d(x)}{M_{\rm d,pk}} \qquad \text{and} \qquad m_g(x) = \frac{M_g(x)}{M_{\rm d,pk}}. \tag{1.87}$$

Defining $h(x) = m_d(x)/f_0 m_g(x)$ as a function describing how the gas traces the dark matter [McQuillin & McLaughlin ultimately set $h(x) = 1$ everywhere], and noting that $\widetilde{M} = M/M_\sigma$, the dimensionless equation of motion is

$$\frac{d}{dx}[h^2 m_d^2 \widetilde{v}^2(x)] \;=\; 4\,\widetilde{M}_{\rm BH} h(x) m_d(x) \;-\; 4\,\frac{\widetilde{M}_{\rm BH}}{\widetilde{M}_{\rm d,pk}}\frac{h^2(x)m_d^2(x)}{x^2} \;-\; 4\,\frac{h^2(x)m_d^3(x)}{x^2}. \quad (1.88)$$

Equation (1.88) can be solved once $\widetilde{M}_{\rm BH} \equiv M_{\rm BH}/M_\sigma$ and $\widetilde{M}_{\rm d,pk} \equiv M_d(r_{\rm pk})/M_\sigma$ have been specified, along with initial conditions — namely a value for the square of the momentum at $r = 0$, $C = [M_g(0)v(0)]^2$. There are also two free parameters that need to be specified. McQuillin & McLaughlin (2012) chose these to be $\widetilde{M}_{\rm BH} \equiv M_{\rm BH}/M_\sigma$ and $\widetilde{M}_{\rm d,pk} \equiv M_d(r_{\rm pk})/M_\sigma$. Figure 1.17 shows examples of the velocity fields for momentum-conserving shells. In all three panels, a Dehnen & McLaughlin dark matter halo is assumed, with $\widetilde{M}_{\rm d,pk} = 4000$. This corresponds to a Milky-Way sized halo, with $r_{\rm pk} \simeq 50\,{\rm kpc}$, $M_d(r_{\rm pk}) \simeq 4.7 \times 10^{11} M_\odot$ and $V_{\rm d,pk} \simeq 200\,{\rm km\,s^{-1}}$. From left to right, the panels correspond to $\widetilde{M}_{\rm BH} = 0.3, 1$ and 3. In each individual panel, the magenta line is the solution to equation (1.88) with $C = 0$. curves lying above this have $C > 0$, whereas curves below have $C < 0$. Unphysical parts of solutions are shown by dotted black lines.

Solutions to equation (1.88) for $v^2(r)$ with $C \geq 0$ decelerate with increasing r at small radii. If at any point $v^2 < 0$ for these solutions, then the corresponding shell has stalled and will not escape. Solutions with $C < 0$ will be unphysical, at least to begin with. However as the Figure shows, it is possible for such solutions that $v^2(r) \geq 0$ for some non-zero radius. For these, $v^2(r) = 0$ corresponds to a gas shell being launched from some $r > 0$, and will initially accelerate. At small launch radii, these shells will eventually decelerate with increasing r.

On the other hand, *any* solution to equation (1.88) will accelerate at large radii, if the shell is able to get there in the first place. There is therefore a large class of solutions with local minima in $v^2(r)$ at intermediate radii. This fact is the basis used by McQuillin & McLaughlin (2012) in obtaining a critical SMBH mass required for a gas shell to escape. Following McQuillin & McLaughlin (2012), if a local minimum

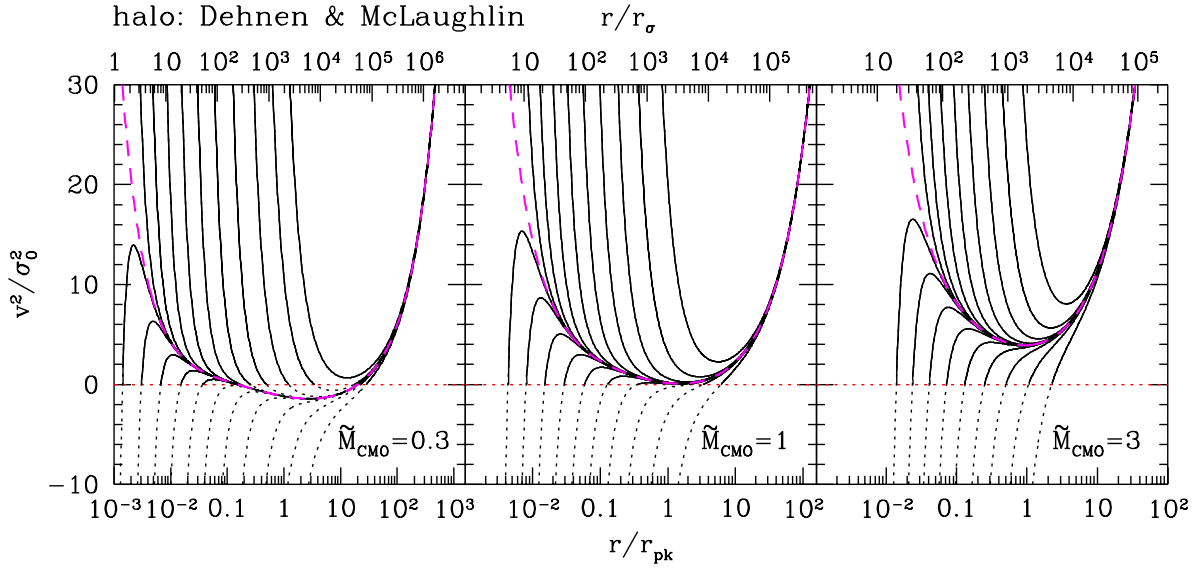

Figure 1.17: Taken from McQuillin & McLaughlin (2012). Velocity fields, $v^2(r)$ for $\widetilde{M}_{\rm BH} = 0.3, 1$ and 3 in a Dehnen & McLaughlin dark matter halo with a spatially constant gas fraction and $\widetilde{M}_{\rm d,pk} = 4000$. The top axis gives the radius in units of $r_\sigma = GM_\sigma/\sigma_0^2$ and the bottom axis in units of $r_{\rm pk}$. The magenta curve in each panel represents the solution with $C = 0$. The physical parts of each solution for $C \neq 0$ are shown by the solid lines.

exists then $dv/dr = 0$ at a radius $r_{\rm min}$, corresponding to $v^2_{\rm min}$. For the shell to escape, $v^2_{\rm min} > 0$ (i.e. it cannot stall), with $v^2_{\rm min} = 0$ corresponding to the critical case. This corresponds to an SMBH mass of $M_{\rm crit}$ and a radius $r_{\rm crit}$. Substituting these conditions into equation (1.88), the left-hand side becomes zero. Following the definitions from McQuillin & McLaughlin (2012) that $x_{\rm crit} = r_{\rm crit}/r_{\rm pk}$ and $m_{\rm d}(x) = M_{\rm d}(x)/M_{\rm d,pk}$, along with those introduced above, this leads to

$$\widetilde{M}_{\rm crit} = \frac{m^2(x_{\rm crit})}{x^2_{\rm crit}} \left[1 - \frac{1}{\widetilde{M}_{\rm d,pk}} \frac{m(x_{\rm crit})}{x^2_{\rm crit}} \right]^{-1} . \tag{1.89}$$

The value of $x_{\rm crit}$ depends on C and the dark matter halo parameters. The necessary condition for the escape of a purely momentum-driven shell with a particular value of C is then $\widetilde{M}_{\rm BH} \geq \widetilde{M}_{\rm crit}$.

Shells with different C values also have different values of $x_{\rm crit}$ and $\widetilde{M}_{\rm crit}$. To compare these, McQuillin & McLaughlin (2012) differentiate equation (1.89) with respect to $x_{\rm crit}$ for a fixed dark matter mass $\widetilde{M}_{\rm d,pk}$:

$$\frac{d\widetilde{M}_{\rm crit}}{dx_{\rm crit}} = \frac{2m^2(x_{\rm crit})x_{\rm crit}}{\left[x^2_{\rm crit} - m(x_{\rm crit})/\widetilde{M}_{\rm d,pk}\right]^2} \left\{ \left[\frac{d\ln m(x_{\rm crit})}{d\ln x_{\rm crit}} - 1 \right] - \frac{1}{2\widetilde{M}_{\rm d,pk}} \frac{1}{x_{\rm crit}} \frac{dm(x_{\rm crit})}{dx_{\rm crit}} \right\} \tag{1.90}$$

By definition, $d\ln m_d/d\ln x - 1 = d\ln V_d^2/d\ln x$ is positive for $x < 1$ and negative for $x > 1$. Hence, for sufficiently small $x_{\rm crit}$, $d\widetilde{M}_{\rm crit}/dx_{\rm crit} < 0$ and for sufficiently large $x_{\rm crit}$, $d\widetilde{M}_{\rm crit}/dx_{\rm crit} > 0$. For a given dark matter $m_d(x)$ and $\widetilde{M}_{\rm d,pk}$, setting $d\widetilde{M}_{\rm crit}/dx_{\rm crit} = 0$ therefore gives the momentum-driven shell with the largest SMBH mass required for escape.

This leads to the sufficient condition for the escape of any momentum-conserving shell: $\widetilde{M}_{\rm crit} \geq 1$. Combining this with the definition of M_σ leads to

$$M_{\rm crit} = \frac{f_0\kappa}{\pi G^2} \frac{V^4_{\rm d,pk}}{4} \simeq 1.14 \times 10^8 \ f_{0.2} \ \left(\frac{V_{\rm d,pk}}{200{\rm kms}^{-1}} \right)^4 \ M_\odot. \tag{1.91}$$

This equation holds for any halo with an associated circular-speed curve that has a single, global maximum. This is the case for all realistic descriptions of the halos formed in cosmological N-body simulations. Defining a characteristic velocity dispersion for

the dark matter halo as $\sigma_0 = V_{\rm d,pk}/\sqrt{2}$, equation (1.91) reduces to a result originally obtained by King (2003, 2005) for an SIS. Again, all of the results in this subsection are based on the assumption that the outflow is always momentum-driven.

1.4.6 Energy-driven shell

If $t_{\rm cool} > t_{\rm flow} \equiv R_S/v_{\rm sh}$, the shocked wind region can expand significantly before it cools. The shocked wind remains hot, and occupies the majority of the volume between $R_{\rm SW}$ and $R_{\rm S}$ (see Figure 1.16). This is expected to be the eventual outcome for high velocity winds from AGN (Faucher-Giguére & Quataert 2012; Zubovas & King 2012; McQuillin & McLaughlin 2013; Zubovas & Nayakshin 2014). This is the energy-driven regime, when the shell is pushed outwards by the thermal pressure from the hot, expanding wind. By equating the Compton cooling time to the flow time, McQuillin & McLaughlin (2013) show that Compton cooling is inefficient beyond $r \sim 11$pc. This implies that observed large scale outflows (Tremonti, Moustakas & Diamond-Stanic 2007; Holt, Tadhunter & Morganti 2008; Bautista et al. 2010; Sturm et al. 2011; Rupke & Veilleux 2011) must be energy-driven.

The equation of motion for an energy-driven shell is similar to the momentum-driven shell case [equation (1.82)]. The difference is the outward thrust term, so $L_{\rm Edd}/c$ is replaced by $4\pi r^2 P$, where P is the thermal pressure in the shocked region. Explicitly, the equation of motion is now given by

$$\frac{d}{dt}[M_g(r)v] = 4\pi r^2 P - \frac{GM_g(r)}{r^2}[M_{\rm BH} + M_{\rm d}(r)]. \tag{1.92}$$

For an energy-driven shell, the pressure also has to satisfy the energy equation,

$$\frac{d}{dt}\left[\frac{4}{3}\pi r^3 \frac{P}{\gamma - 1}\right] = \dot{E} - P\frac{d}{dt}\left[\frac{4}{3}\pi r^3\right] - \frac{GM_g(r)v(r)}{r^2}[M_{\rm BH} + M_{\rm d}(r)], \tag{1.93}$$

where γ is the ratio of specific heats. The last three terms on the right-hand side give the rates of work done on the expanding shell (both PdV work and the work *against* the gravity of the SMBH and the dark matter behind the shell).

The first term on the right-hand side of equation (1.93) is the rate of energy input, which is given by the kinetic energy flux of the wind:

$$\dot{E} = \dot{M}\frac{v_w^2}{2} = 2b\frac{v_w}{c}\frac{L_{\rm Edd}}{2}. \tag{1.94}$$

As pointed out by McQuillin & McLaughlin (2013), this differs slightly from previous works (e.g. King 2005, 2010), where it is stated that $\dot{E} = \eta L_{\rm Edd}/2$. However, this is based on the additional assumptions that $\dot{M} = \dot{M}_{\rm Edd}$ and $2b \simeq 1$, so that $v_w/c = \eta$. McQuillin & McLaughlin (2013) do not assume either in their analysis, and hence v_w/c remains as an explicit parameter.

Combining equations (1.92) and (1.93), an equation of motion can be derived with P eliminated. McQuillin & McLaughlin (2013) solve this for an SIS distribution of matter [i.e., $M_d(r) = 2\sigma_0^2 r/G$ and $M_g(r) = f_0 M_d(r)$]. With the criterion that the feedback escapes if the coasting speed of the shell at large radius exceeds the escape velocity of the SIS [$v_\infty \geq v_{\rm esc} = 2\sigma_0$], they find a critical value for the product of SMBH mass and wind speed, v_w:

$$\left[M_{\rm BH}\, v_w\right]_{\rm crit} = \frac{1}{2b}\frac{4(4\gamma-3)}{(\gamma-1)}\frac{\kappa f_0}{\pi G^2}\sigma_0^5. \tag{1.95}$$

Setting $\gamma \simeq 5/3$, this critical condition for the escape of any energy-driven shell is

$$\left(\frac{M_{\rm BH}}{10^8\, M_\odot}\right)\left(\frac{v_w}{c}\right) \simeq 6.68\times10^{-2}\frac{1}{2b}\left(\frac{f_0}{0.2}\right)\left(\frac{\sigma_0}{200\,{\rm km\,s^{-1}}}\right)^5. \tag{1.96}$$

Therefore, the relation $M_{\rm BH}v_w \propto \sigma_0^5$ is locked in for a purely energy-driven shell in an SIS halo. This is consistent with previous theoretical work (Silk & Rees 1998; King 2005), assuming v_w is uncorrelated to SMBH mass or halo velocity dispersion. If, say, $v_w \propto M_{\rm BH}^y$, then $M_{\rm BH} \propto \sigma_0^{5/(1+y)}$, a measurable difference from a power of 5, even for relatively small y.

1.4.7 Establishing the $M_{\rm BH}$–bulge relations

In §1.4.5 and §1.4.6, the critical SMBH mass condition for purely momentum-driven [equation (1.91)] and purely energy-driven [equation (1.96)] outflows, derived by McQuillin & McLaughlin (2012) and McQuillin & McLaughlin (2013) respectively, were

discussed. There are several caveats surrounding both predictions, based on necessary assumptions made in order to obtain the results. Some of these assumptions, such as spherical symmetry and a smooth ambient medium, are not fatal flaws (Zubovas & Nayakshin 2014). However, there are many that could affect the functional dependence of $M_{\rm BH}$ on a characteristic halo velocity scale (e.g., $V_{\rm d,pk}$ or $\sigma_0 = V_{\rm d,pk}/\sqrt{2}$).

In reality, the outflows will not be purely momentum- or energy-driven throughout the entire process. Both regimes are likely to manifest at some stage. As discussed, Compton cooling is initially efficient, so the outflow will be momentum-conserving (King 2003). However, after this initial radiative stage, the outflow is expected to become energy-driven (Zubovas & King 2012; McQuillin & McLaughlin 2013), as cooling becomes inefficient (when the outflow reaches $r \sim 11\,{\rm pc}$ according to McQuillin & McLaughlin 2013). It is unclear how this switch changes the critical SMBH mass required to clear the gas out of a galaxy. McQuillin & McLaughlin (2013) find that for an energy-driven outflow in an SIS, the velocity scale enters the SMBH prediction as σ^5 (rather than σ^4 for the momentum-driven outflow). However, their energy-driven result also depends on the wind velocity, v_w, which could alter this dependence if v_w is correlated to $M_{\rm BH}$ somehow.

On the other hand, Zubovas & Nayakshin (2014) consider an initially elliptical distribution of isothermal gas, directly tracing the dark matter. They show that the initial non-radiative (momentum-driven) outflow opens up a wide "escape route", allowing *most* of the outflow energy to escape. At the same time, in directions where an "escape route" hasn't been opened up, the ambient gas is affected mainly by momentum transferred from the outflow. To prevent the SMBH from growing, the momentum needs to be sufficient to stop the remaining ambient gas from falling inwards, towards the black hole. It is therefore the momentum of the outflow that limits SMBH growth. Zubovas & Nayakshin (2014) find that the SMBH mass required to drive out the ambient gas is $M_{\rm BH} \gtrsim \lambda^{-1} M_\sigma$, where $\lambda = 1/3b$ and M_σ is given by equation (1.85), independent of whether the outflow is momentum- or energy-driven. Given that $b \lesssim 1$ (§1.4.2), the Zubovas & Nayakshin (2014) result is similar to the momentum-conserving prediction from McQuillin & McLaughlin (2012).

Beyond the effects of distinguishing between momentum- and energy-conserving outflows, both predictions assume a wind moving into an initially static ambient medium, ignoring the ram pressure (Faucher-Gigúere & Quataert 2012). Related to this, cosmological infall of gas is also neglected. More recently, the simulations of Costa et al. (2014) have confirmed that for an isolated halo (with no infalling gas), momentum-driven outflows (with an input rate of $\sim L_{\rm Edd}/c$) can establish an $M_{\rm BH}$–σ relation similar to observations. However, these simulations also show that in full cosmological simulations, a larger momentum input rate is required to drive efficient outflows, due to infalling gas. Costa et al. show that the observed large scale outflows, driven by AGN, are likely to be energy-driven, and that such outflows can reach momentum fluxes of up to $10L_{\rm Edd}/c$.

Both predictions also neglect the presence of stars in the protogalaxy, which could contribute both to the feedback driving gaseous outflows (Murray, Quataert & Thomson 2005; Power et al. 2011) *and* to the gravity containing them. It is also assumed that the gas is virialised (traces the dark matter) in both cases, and that $M_{\rm BH}$ remains constant, corresponding to a steady wind. In reality, the SMBH will increase in mass during an accretion event. In addition, the energy-driven prediction is for an SIS distribution only (the momentum-driven prediction is for non-isothermal halos). In Chapter 3, where such predictions are compared to the observed SMBH – bulge correlations at $z = 0$, the momentum-conserving prediction is used since it is a more general result. In Chapter 4, the assumptions of having a virialised gas and no stars are relaxed, with a momentum-driven outflow into a static ambient medium still assumed. This allows non-isothermal halos to still be considered, and allows a direct comparison between equation (1.91) and the new prediction, in order to see the effects of relaxing the assumptions mentioned.

1.4.8 Matching predictions to data

Predictions like equations (1.91) and (1.96) connect the black hole mass to the potential wells of the protogalaxy, when blow-out occurred and accretion-driven SMBH growth

was halted. The observed correlations are in $z = 0$ galaxies, for early-types and bulges of late-type, and involve stars (not the dark matter or gas directly) in most cases. In order to compare the predictions to the data, it is necessary to connect the stellar properties at $z = 0$ to the global property of the protogalaxy that best measures the depth of the potential well, at some $z > 0$.

As a point of reference, Figure 1.18 shows the $M_{\rm BH}$–$\sigma_{\rm ap}$ relation for ellipticals (black points) and classical bulges (red points) at $z = 0$, with data from Kormendy & Ho (2013). The dashed line corresponds to the momentum-driven critical SMBH mass, with a gas to dark matter mass ratio $f_0 = 0.18$ (the cosmic average; Planck Collaboration 2014), and the naive substitution $V_{\rm d,pk} = \sqrt{2}\sigma_{\rm ap}$, applicable if the stars and dark matter are both distributed as isothermal spheres. The dotted line is for the energy-driven critical SMBH mass with $f_0 = 0.18$, a typical SMBH wind speed of $v_{\rm w} = 0.035$ (McQuillin & McLaughlin 2013) and the substitution $\sigma_0 = \sigma_{\rm ap}$. It is promising how close both predictions lie to the data, and certainly encourages taking seriously some of the simple physical ideas behind them, if not all the details.

Nevertheless, setting $V_{\rm d,pk} = \sqrt{2}\sigma_{\rm ap}$ (and $\sigma_0 = \sigma_{\rm ap}$) is problematic. It is only appropriate if all galaxies are modelled as isothermal spheres (The $\sqrt{2}$ proportionality), and if stars always trace the dark matter – neither of these are true in reality. This substitution also assumes that the $V_{\rm d,pk}$ in equation (1.91), referring to the protogalactic halo at some $z > 0$, is equal to $V_{\rm d,pk}$ at $z = 0$ — in reality, this is again not true.

More sophisticated modelling is required to relate the dark matter circular speed peak, $V_{\rm d,pk}$, to the stellar velocity dispersion, $\sigma_{\rm ap}(R_e)$. More generally, to compare a theoretical prediction established at $z > 0$ (between BH and dark matter) to an observed relation at $z = 0$ (between BH and stars), a proper translation between the dark matter halo property and stellar property in question is required. This Chapter has given an overview of some of the key physical concepts involved in galaxy formation, along with the necessary tools to translate between dark matter halo and stellar properties in a self-consistent manner.

Chapter 2 focusses on establishing average trends between stellar and dark matter properties at $z = 0$. This involves bringing together results from cosmological

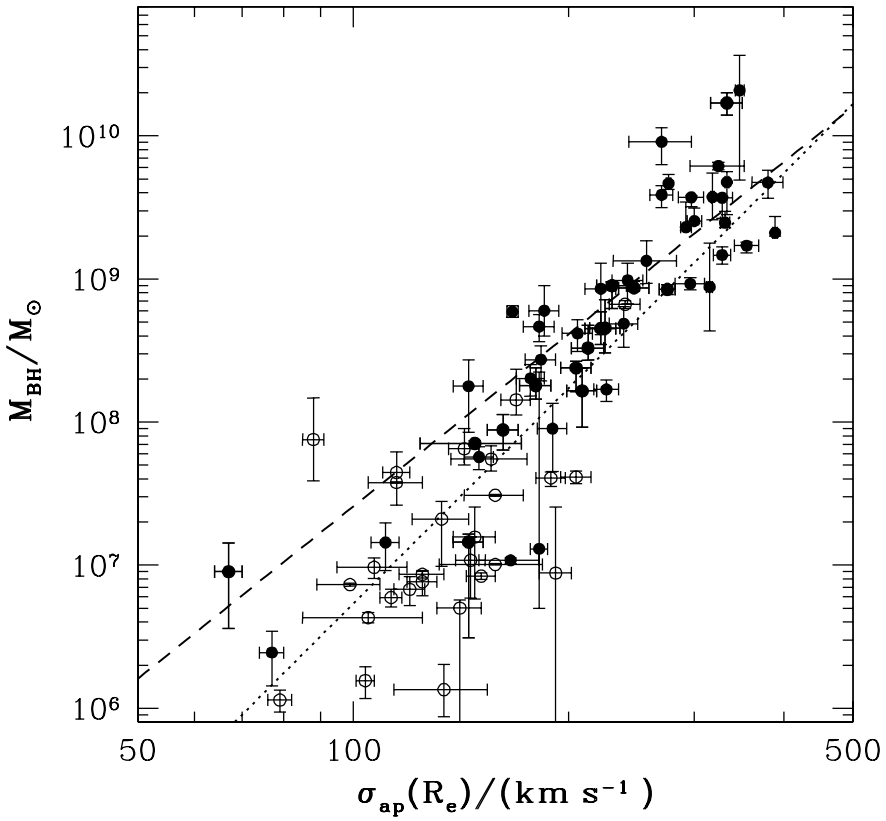

Figure 1.18: The $M_{\rm BH}$–σ relation for ellipticals (filled circles) and classical bulges (open circles) at $z = 0$, with data from Kormendy & Ho (2013). The dashed line corresponds to equation (1.91), assuming $V_{\rm d,pk} = \sqrt{2}\sigma_{\rm ap}(R_e)$ and a spatial constant gas-to-dark matter mass ratio, $f_0 \simeq 0.18$. This is only appropriate if all galaxies are isothermal spheres, stars always trace the dark matter and that $V_{\rm d,pk}$ in the prediction (established at some $z > 0$) is equal to $V_{\rm d,pk}$ in the halo at $z = 0$. The dotted line is for equation (1.96), with $f_0 - 0.18$, $v_{\rm w} = 0.035$ and assumes $\sigma_0 = \sigma_{\rm ap}(R_e)$.

simulations for virial properties, dark matter halo concentrations and for stellar-to-dark matter mass ratios. These then need to be combined with data samples from the literature for early-type galaxies at $z = 0$, covering stellar mass ranges that encompass the $M_{\rm BH}$–bulge property correlations ($10^{10} M_{\odot} \lesssim M_{*,\rm tot} \lesssim 10^{12} M_{\odot}$). This allows for trend lines relating any two of $M_{*,\rm tot}$, R_e, $M_{\rm d,vir}$, $r_{\rm vir}$, $f_{*,\rm vir}$, $r_{\rm pk}$, $V_{\rm d,pk}$ and $\sigma_{\rm ap}(R_e)$ at $z = 0$ to be obtained.

Chapter 3 combines the scalings from Chapter 2 with halo progenitor evolution, thus relating the dark matter properties [$M_{\rm d,vir}(z)$ and $V_{\rm d,pk}(z)$]at $z > 0$ to the dark matter and stellar properties at $z = 0$. Ultimately, this is combined with the momentum-driven SMBH critical mass prediction ($M_{\rm BH} \propto V_{\rm d,pk}^4$), leading to model predictions for the $M_{\rm BH}$–galaxy property relations ($\sigma_{\rm ap}(R_e)$, $M_{*,\rm tot}$, $M_{\rm d,vir}$ and combinations of $\sigma_{\rm ap}(R_e)$ and R_e) at $z = 0$. These model predictions are all highly non-linear in log–log space, due to taking into consideration the non-monotonic relation between $f_{*,\rm vir}$ and halo mass, and accounting for the way dark matter halo masses grow through hierarchical merging in a ΛCDM cosmology, after $M_{\rm BH}$ is set by feedback and the halo properties at $z > 0$. Nevertheless, the model predictions all describe the data reasonably well for redshifts $z \sim 2$–4.

The SMBH prediction used in Chapter 3 has several caveats and simplifying assumptions surrounding it. Chapter 4 focusses on relaxing two of these assumptions: (1) allowing for the presence of stars in the protogalaxy that can contribute to the gravity containing the outflow; (2) allowing for a non-virialised gas (so the gas doesn't have to trace the dark matter). The other assumptions are kept the same, so that the effects of changing these two can be investigated in detail. Given the constraints on $f_{*,\rm vir}$ as a function of both halo mass and redshift, the presence of stars has little impact on the critical SMBH mass. It is also found that the details of the gas distribution only changes the McQuillin & McLaughlin (2012) results by factors of 3–4, even in the most physically extreme cases. Chapter 5 summarises the work presented here, and discusses possible areas for future work based on these results.

2 Galaxy and dark matter halo scalings at $z = 0$

It is widely accepted that accretion-driven growth of supermassive black holes (SMBHs) is limited by quasar-mode feedback, and eventual gas blow-out in protogalaxies. The SMBH masses, $M_{\rm BH}$, are therefore connected to the depths of the dark matter potential wells at the point of blow-out, at redshifts $z > 0$. The observed $M_{\rm BH}$–bulge relations in $z = 0$ ellipticals and bulges are then presumably a reflection of this fundamental connection.

In order to relate a prediction relating $M_{\rm BH}$ to the depth of the protogalactic potential well at some redshift $z > 0$ to the observed correlations in $z = 0$ galaxies, it is first necessary to relate the stellar bulge properties to dark matter properties at $z = 0$. It is then possible to relate these to the dark matter properties in halo progenitors at $z > 0$, and hence to $M_{\rm BH}$. McQuillin & McLaughlin (2012) have derived a critical black hole mass required for blow-out, related to this global property of the dark matter halo, with $M_{\rm BH} \propto V_{\rm d,pk}^4$ [see equation (1.91)]. Despite several caveats, it contains enough relevant feedback physics to be interesting, and is a good test case for the general methods developed in Chapters 2 and 3.

The focus of the current Chapter is to establish scaling relations between galaxy properties at $z = 0$. §2.1 provides details of the distributions that are assumed for the stars and dark matter, along with pulling together results from cosmological simulations relating dark matter virial masses to virial radii and stellar masses. The data sets used for early-type galaxies at $z = 0$ are discussed at the beginning of §2.2. The rest of the Section provides details of how the average trends are obtained for stellar [$M_{*,\rm tot}$, R_e, $\sigma_{\rm ap}(R_e)$, $M_*(r)/M_{\rm d}(r)$] and dark matter halo [$M_{\rm d,vir}$, $r_{\rm vir}$, $r_{\rm d,pk}$, $V_{\rm d,pk}$] properties.

Some of the results from the literature represent average trends with significant scatter around them. The scaling relations obtained in §2.2 are also representative trend lines between various stellar and halo properties. Scatter around these trends is inevitable, and it can contain physical information. Although this is important,

the goal here is to simply establish the average trends. The tasks of explaining and characterising any of the scatter in detail, or predicting the net scatter around any scaling that come from combining others, are set aside. A discussion of the scatter is left for Chapter 5 when discussing future work.

2.1 Model setup

A simple, two-component model for early-type galaxies is assumed: spherical distributions of stars at the centres of spherical distributions of dark matter. These models are constrained by results from the literature regarding the global structure and baryon content of dark matter halos.

2.1.1 Stellar distribution

Giant elliptical galaxies with total stellar masses of approximately 10^{10}–$10^{12} M_{\odot}$, have brightness profiles that are well fitted by Sérsic (1968) profiles, with Sérsic index, $n \approx 3-7$ (Graham & Colless 1997). These masses correspond to the range spanned by the $z = 0$ galaxies that define empirical $M_{\rm BH}$–bulge correlations. A useful approximation to Sérsic profiles for this range of n is provided by the 3-D Hernquist (1990) profile, projected along the line of sight. The 3-D Hernquist density profile is expressed in terms of a total stellar mass, $M_{*,\rm tot}$, and a scale radius, a_*:

$$\rho_*(r) = \frac{M_{*,\rm tot}}{2\pi a_*^3} \left(\frac{r}{a_*}\right)^{-1} \left(1 + \frac{r}{a_*}\right)^{-3}. \tag{2.1}$$

To connect with data, it is more convenient to normalise to $M_{*,\rm tot}$ and the stellar effective radius, R_e:

$$\frac{\rho_*(r)}{M_{*,\rm tot}/R_e^3} = \left[\frac{(R_e/a_*)^2}{2\pi}\right] \left(\frac{r}{R_e}\right)^{-1} \left[1 + \frac{R_e}{a_*}\left(\frac{r}{R_e}\right)\right]^{-3}, \tag{2.2}$$

where $R_e/a_* \simeq 1.81527$ for a Hernquist (1990) profile. The mass profile is then

$$M_*(r/R_e) = \int_0^{r/R_e} 4\pi u^2 \rho_*(u) du = M_{*,\rm tot} \left[\frac{r/R_e}{r/R_e + a_*/R_e}\right]^2. \tag{2.3}$$

Equation (2.2) gives a 3-D density profile as a function of 3-D radius, r. This radius is related to the 2-D projected (onto the plane of the sky) radius, R, with $r = \sqrt{R^2 + z^2}$, where z is the line of sight of the observer. The mass density is then related to the surface density, $\Sigma(R)$, through the projection integral:

$$\Sigma(R) = 2 \int_0^\infty \rho(r) dz = 2 \int_R^\infty \rho(r) \frac{r dr}{\sqrt{r^2 - R^2}}. \tag{2.4}$$

The top panel of Figure 2.1 shows surface density profiles, $\Sigma(R)$, as a function of R. The solid red line shows the Hernquist surface density profile, obtained by projecting $\rho_*(r)$ along the line of sight. The other lines are for Sérsic (1968) profiles, which start from $\Sigma(R) \sim \exp[-(R/R_e)^{1/n}]$ rather than $\rho(r)$, for $n = 1$ (black line), $n = 3$ (blue), $n = 4$ (cyan), $n = 5$ (green) and $n = 7$ (magenta).

It is also possible to de-project a surface density profile, such as one of the Sérsic profiles, by using an Abel integral equation (Binney & Tremaine 2008):

$$\rho(r) = -\frac{1}{\pi} \int_r^\infty \frac{d\Sigma}{dR} \frac{dR}{\sqrt{R^2 - r^2}}. \tag{2.5}$$

The bottom panel of Figure 2.1 shows 3-D mass density profiles, $\rho(r)/[M_{*,\mathrm{tot}}/R_e^3]$ as a function of r/R_e. The solid red line is the Hernquist density profile, equation (2.2). The other lines are the de-projected Sérsic profiles for the same Sérsic indices as the top panel.

As the top panel of Figure 2.1 shows, projecting the Hernquist (1990) $\rho_*(r)$ along the line of sight gives a surface density profile that approximates a Sérsic profile with $n = 3, 4$ (the classic $R^{1/4}$ law) or 5 reasonably well. The same is true for the de-projections of these Sérsic profiles to $\rho(r)$, when compared to the Hernquist mass distribution [Figure 2.1, bottom panel]. The Hernquist profile therefore adequately represents the light distributions for the galaxies used to define the SMBH–bulge relations. The consequences of assuming a Hernquist (1990) stellar distribution, instead of the more general Sérsic (1968) profiles, are considered for all of the scaling relations likely to be affected. In general, it exposes the models to possible errors at the $\sim 10\%$ level or less.

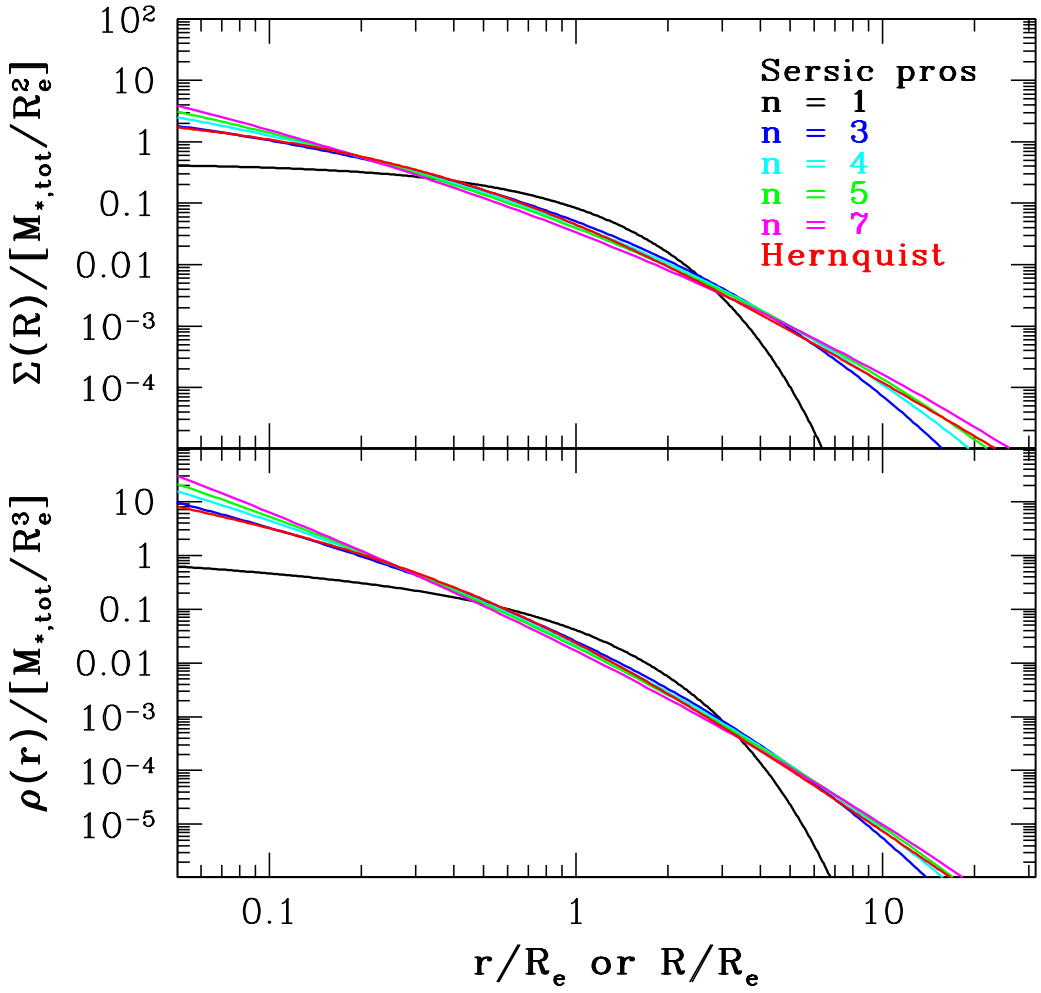

Figure 2.1: *Top panel:* Surface density profiles, $\Sigma(R)$ versus projected radius R/R_e. The solid red line represents the Hernquist (1990) density profile projected along the line of sight. The other lines are for the Sérsic profiles with Sérsic indices, $n = 1$ (black line), $n = 3$ (blue line), $n = 4$ (cyan line), $n = 5$ (green line) and $n = 7$ (magenta line). *Bottom panel:* Mass density profiles, $\rho(r)$, as a function of r/R_e. The red line corresponds to the Hernquist profile, given by equation (2.2). The other lines are the de-projected Sérsic profiles, with the same line colours as the top panel.

2.1.2 Dark matter distributions

The maximum of the dark matter circular speed, $V_{\rm d,pk}$, enters the critical SMBH mass prediction through a high power. It is therefore essential to consider the sensitivity of any scaling relations to details of the dark matter distribution. Four dark matter density profiles are considered (cf. §1.1.4): Three with central density cusps (Hernquist 1990; Navarro, Frenk & White 1996; Dehnen & McLaughlin 2005), as in N-body simulations of cluster-sized halos, and the other with a constant density core, perhaps more appropriate to dwarf-spheroidal sized systems (Burkert 1995).

To treat them uniformly, it is actually more convenient to normalise all radii to r_{-2}, where the logarithmic slope of the dark matter density profile is $d\ln\rho_d/d\ln r = -2$, and masses to $M_d(r_{-2})$. For the NFW density profile, these are the standard normalisations used in the original papers (i.e., $r_{-2} = r_0$):

$$\rho_d(r) \propto \left(\frac{r}{r_{-2}}\right)^{-1} \left(1+\frac{r}{r_{-2}}\right)^{-2}. \tag{2.6}$$

Given the definition

$$M_d(r) = \int_0^r 4\pi u^2 \rho_d(u) du, \tag{2.7}$$

the NFW mass profile is

$$\frac{M_d(r)}{M_d(r_{-2})} = \frac{\ln(1+r/r_{-2}) - (r/r_{-2})(1+r/r_{-2})^{-1}}{\ln(2) - 1/2}. \tag{2.8}$$

The circular speed of the dark matter halo, i.e., $V_d^2(r) = GM_d(r)/r$, is then given by

$$\frac{V_d^2(r)}{V_d^2(r_{-2})} = \frac{\ln(1+r/r_{-2}) - (r/r_{-2})(1+r/r_{-2})^{-1}}{(r/r_{-2})[\ln(2) - 1/2]}, \tag{2.9}$$

which peaks at

$$\frac{r_{\rm pk}}{r_{-2}} \simeq 2.16258. \tag{2.10}$$

The Hernquist (1990) profile, first fitted to simulated dark matter halos by Dubinski & Carlberg (1991), has the same central density cusp ($\rho_d \sim r^{-1}$) as an NFW halo, but a steeper large-radius slope ($\rho_d \sim r^{-4}$ instead of r^{-3}). The standard form of

the Hernquist density profile is given in equation (2.1). Given that $r_{-2}/a_* = 1/2$, the density and mass profiles in terms of r_{-2} and $M_d(r_{-2})$ are

$$\rho_d(r) \propto \left(\frac{r}{r_{-2}}\right)^{-1} \left(1 + \frac{1}{2}\frac{r}{r_{-2}}\right)^{-3} \tag{2.11}$$

and

$$\frac{M_d(r)}{M_d(r_{-2})} = 9\left(\frac{r/r_{-2}}{2 + r/r_{-2}}\right)^2. \tag{2.12}$$

This leads to a circular-speed curve,

$$\frac{V_d^2(r)}{V_d^2(r_{-2})} = \frac{9r/r_{-2}}{(2 + r/r_{-2})^2}, \tag{2.13}$$

peaking at

$$\frac{r_{\rm pk}}{r_{-2}} = 2. \tag{2.14}$$

The third halo with a central density cusp is from the family developed by Dehnen & McLaughlin (2005), based on $\rho_d(r)/\sigma_d^3(r)$ being a power-law function of r (see discussion in §1.1.4). Assuming velocity isotropy at $r = 0$, and using the fact that for this profile, $r_{-2}/r_0 = (11/13)^{9/4} \simeq 0.68669$, the density profile is

$$\rho_d(r) \propto \left(\frac{r}{r_{-2}}\right)^{-7/9} \left[1 + \frac{11}{13}\left(\frac{r}{r_{-2}}\right)^{4/9}\right]^{-6}. \tag{2.15}$$

This has a slightly shallower central cusp than the Hernquist or NFW models, and a large radius fall off, $\rho_d \sim r^{-31/9}$, that is between the two. The mass and circular-speed profiles are then

$$\frac{M_d(r)}{M_d(r_{-2})} = \left[\frac{24(r/r_{-2})^{4/9}}{13 + 11(r/r_{-2})^{4/9}}\right]^5 \tag{2.16}$$

and

$$\frac{V_d^2(r)}{V_d^2(r_{-2})} = \left[\frac{24(r/r_{-2})^{11/45}}{13 + 11(r/r_{-2})^{4/9}}\right]^5, \tag{2.17}$$

which peaks at

$$\frac{r_{\rm pk}}{r_{-2}} = \left(\frac{13}{9}\right)^{9/4} \simeq 2.28732. \tag{2.18}$$

The Burkert (1995) profile has a constant density core and therefore is significantly different from the other three halos in the central regions. Normalising to r_{-2}, with $\mathcal{R} = r_{-2}/r_0 \simeq 1.52138$, the Burkert density profile is

$$\rho_d(r) \propto \left(1 + \mathcal{R}\frac{r}{r_{-2}}\right)^{-1} \left(1 + \mathcal{R}^2\frac{r^2}{r_{-2}^2}\right)^{-1}. \tag{2.19}$$

The corresponding mass profile is

$$\frac{M_d(r)}{M_d(r_{-2})} = \frac{\ln\left[(1+\mathcal{R}r/r_{-2})\sqrt{1+\mathcal{R}^2(r/r_{-2})^2}\right] - \tan^{-1}(\mathcal{R}r/r_{-2})}{\ln[(1+\mathcal{R})\sqrt{1+\mathcal{R}^2}] - \tan^{-1}(\mathcal{R})}, \tag{2.20}$$

with a circular-speed,

$$\frac{V_d^2(r)}{V_d^2(r_{-2})} = \frac{\ln\left[(1+\mathcal{R}r/r_{-2})\sqrt{1+\mathcal{R}^2(r/r_{-2})^2}\right] - \tan^{-1}(\mathcal{R}r/r_{-2})}{(r/r_{-2})\ln[(1+\mathcal{R})\sqrt{1+\mathcal{R}^2}] - \tan^{-1}(\mathcal{R})}, \tag{2.21}$$

peaking at

$$\frac{r_{\rm pk}}{r_{-2}} \simeq 2.13433. \tag{2.22}$$

Figure 2.2 shows the circular-speed profiles for each halo, as given by equations (2.9), (2.13), (2.17) and (2.21). Relative to the NFW profile (black line), the Hernquist circular-speed (red line) has a narrower width due to a steeper decline beyond the peak. This is because of the steeper density profile, and hence convergent mass, as $r \to \infty$. The constant density core of the Burkert (1995) profile (broken magenta line) leads to a sharp increase in $V_d(r)$ from small r, and therefore a much narrower profile, relative to both Hernquist and NFW. The Dehnen & McLaughlin halo (blue line) has the broadest circular-speed curve considered here. This is largely due to how slowly the density profile, dependent on $r^{4/9}$ instead of r, rolls over from the central density cusp with $\rho_d(r) \propto r^{-7/9}$, to its large radius power-law behaviour, $\rho_d(r) \propto r^{-31/9}$. These features of the dark matter halos are important for the scaling relations involving the peak of the dark matter circular speed, $V_{\rm d,pk}$. Broken vertical lines show the concentrations $r_{\rm vir}/r_{-2}$ of halos with virial masses $M_{\rm d}(r_{\rm vir}) = 10^{15}M_\odot$ and $10^{11}M_\odot$ at $z = 0$.

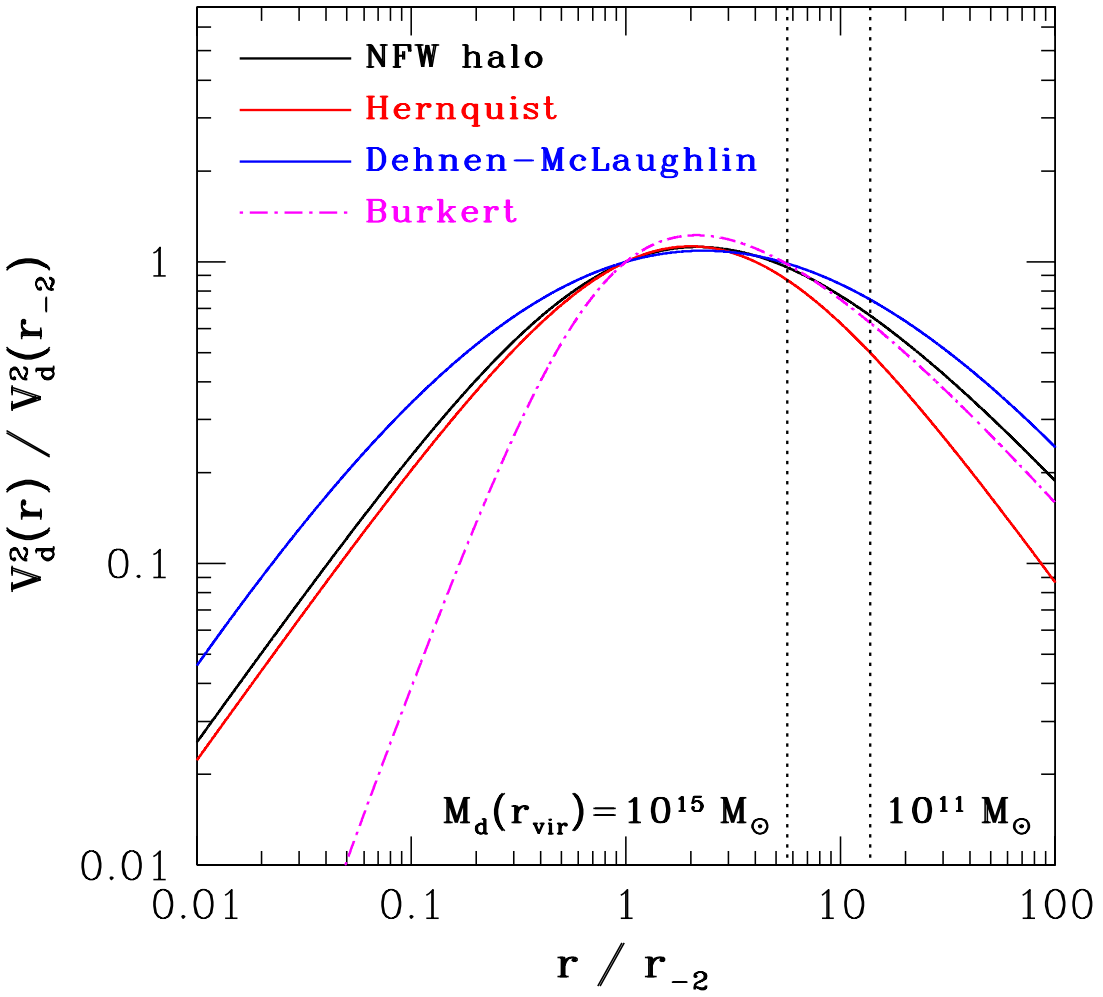

Figure 2.2: Circular-speed curves, $V_{\rm d}^2(r) = GM_{\rm d}(r)/r$ versus r, normalised to the radius r_{-2} where $d\ln\rho_{\rm d}/d\ln r = -2$, for the four dark-matter halo models considered here. These curves are also shown in the bottom panel of Figure 1.3. The peaks in $V_{\rm d}(r)$ occur at radii near $r_{\rm pk}/r_{-2} \approx 2$ in all cases (see text). Broken vertical lines show the concentrations $r_{\rm vir}/r_{-2}$ of halos with virial masses $M_{\rm d}(r_{\rm vir}) = 10^{15}\ M_\odot$ and $10^{11}\ M_\odot$ at $z = 0$ (see §2.1.5).

2.1.3 Virial radii and cosmological parameters

The virial theorem is applicable to a dark matter halo if, inside the virial radius $r_{\rm vir}$, the halo density is $\Delta_{\rm vir}$ times the critical density of the Universe: $\rho_d(r_{\rm vir}) = \Delta_{\rm vir}\,\rho_c$ (cf. §1.1.3). Bryan & Norman (1998) give a fitting formulae to calculate the overdensity, $\Delta_{\rm vir}$, relative to the critical density, at any redshift z. Assuming a flat Universe, with a cosmological constant ($\Omega_m + \Omega_\Lambda = 1$), this can be written as:

$$\begin{aligned}\Delta_{\rm vir}(z) \;&\equiv\; \frac{2\,GM(r_{\rm vir})}{H^2(z)\,r_{\rm vir}^3} \\ &\simeq\; 18\pi^2 \;-\; 82\,\frac{1-\Omega_{m,0}}{\left[H(z)/H_0\right]^2} \;-\; 39\,\frac{(1-\Omega_{m,0})^2}{\left[H(z)/H_0\right]^4}\;,\end{aligned} \tag{2.23}$$

with

$$\left[\frac{H(z)}{H_0}\right]^2 \;=\; 1 \;+\; \Omega_{m,0}\left[(1+z)^3 - 1\right]\;. \tag{2.24}$$

Rearranging the definition of $\Delta_{\rm vir}$ yields a convenient relationship between virial radius and virial mass at arbitrary redshift:

$$\left[\frac{M(r_{\rm vir})}{M_\odot}\right]\left[\frac{r_{\rm vir}}{\rm kpc}\right]^{-3} \;=\; 1166.1\,h_0^2\,\Delta_{\rm vir}(z)\,\left[\frac{H(z)}{H_0}\right]^2\;, \tag{2.25}$$

where $h_0 \equiv H_0/\left(100\ {\rm km\ s^{-1}\ Mpc^{-1}}\right)$ as usual. This form is also useful for calculating M/r^3 of spheres with other overdensities Δ besides the virial value (e.g., setting $\Delta(z) \equiv 200$ on the right-hand side gives another standard point of reference).

The value for $\Delta_{\rm vir}$ will depend on the chosen cosmology because of the $\Omega_{\rm m,0}$ term appearing in equations (2.23) and (2.24). For example, the cosmological parameters from the *Planck* 2013 results (Planck-Collaboration 2014) are $h_0 = 0.67$, with $\Omega_{m,0} = 0.32$ and $\Omega_{\Lambda,0} = 0.68$. The virial overdensity from equation (2.23) is then $\Delta_{\rm vir}(0) \simeq 104$ at $z = 0$. However, using the *WMAP5* (Spergel et al. 2003; Spergel et al. 2007) parameters ($h_0 = 0.72$,, $\Omega_{m,0} = 0.26$ and $\Omega_{\Lambda,0} = 0.74$) yields $\Delta_{\rm vir}(0) \simeq 96$. In both cases, the overdensity increases with redshift, with an upper limit of $\Delta_{\rm vir}(z) \leq 18\pi^2 \simeq 178$ (Bertschinger 1987).

Whenever applying equations (2.23) – (2.25), the Planck 2013 cosmological parameters are assumed. Some of the results from the literature are derived assuming the *WMAP5* cosmology (e.g. see §2.1.4). When this is the case the result from the literature is taken as it is given, with no attempt of any alterations to account for the small changes to the cosmology.

2.1.4 Stellar-to-dark matter mass ratios

Moster et al. (2010) give a useful parametrisation of the stellar-to-dark matter mass ratio. They assign one central galaxy to each virialised halo in ΛCDM simulations of structure formation, assuming *WMAP5* cosmology ($\Omega_{m,0} = 0.26$, $\Omega_{\Lambda,0} = 0.74$ and $H_0 = 72$ km s^{-1} Mpc^{-1}). Moster et al. use the abundance matching technique (cf. §1.2.2) to determine the stellar mass of any central galaxy from the virial mass of its parent halo according to a prescription that is required ultimately to give agreement between the simulations and the observed galaxy luminosity function. They fit their results for the central-galaxy mass fraction $M_*/M_{\rm d}$ within the virial radius $r_{\rm vir}$ at $z = 0$ with a double power-law function,

$$f_{*,\rm vir} \equiv \frac{M_*(r_{\rm vir})}{M_{\rm d}(r_{\rm vir})} = 0.0564 \left\{ \left[\frac{M_{\rm d}(r_{\rm vir})}{7.66 \times 10^{11}\ M_\odot} \right]^{-1.06} + \left[\frac{M_{\rm d}(r_{\rm vir})}{7.66 \times 10^{11}\ M_\odot} \right]^{+0.556} \right\}^{-1}. \tag{2.26}$$

Equation (2.26) again represents a mean trend, and scatter around it is to be expected as a result of differences in the global properties (concentration, spin, etc.) and the merger histories between any two dark-matter halos with the same mass at $z = 0$ (Moster et al. 2010; Behroozi, Wechsler & Conroy 2013).

The solid black line in Figure 2.3 shows the parametrisation given in equation (2.26). The broken blue line represents the cosmic average baryon fraction, $f_0 \equiv \Omega_{\rm b,0}/(\Omega_{\rm m,0} - \Omega_{\rm b,0}) \simeq 0.18$ (Planck-Collaboration 2014). The peak in $f_{*,\rm vir}$ at intermediate halo masses $M_{\rm d,vir} \sim 10^{12} M_\odot$ is worth noting. For the smallest halos ($M_{\rm d,vir} \leq 10^{11} M_\odot$), the stellar-to-dark matter mass ratio is low due to supernova feedback clearing out gas from the dwarf galaxies, preventing any further stars from being

formed (Dekel & Silk 1986). As the halo mass increases, the potential well depths of the halos become too large for supernova feedback to clear gas out of the galaxy, and hence $f_{*,\mathrm{vir}}$ increases. In the larger systems, it is AGN feedback that drives out gas from the central galaxies, and explains why $f_{*,\mathrm{vir}}$ decreases for larger halo mass (Sijacki et al. 2015).

Both Moster et al. (2010) and Behroozi, Wechsler & Conroy (2013) show that equation (2.26) is in good agreement with other theoretical work and/or with data, for halo virial masses $10^{11}\,M_\odot \leq M_\mathrm{d}(r_\mathrm{vir}) \leq 10^{15}\,M_\odot$ (see §1.2.2, Figure 1.2, taken from Behroozi et al. 2013). This corresponds to stellar masses $M_*(r_\mathrm{vir}) \sim 5 \times 10^8\ M_\odot$–$10^{12}\ M_\odot$ for the central galaxies. This range encompasses galaxies that are used to define the observed M–σ relation.

Equation (2.26) does not attempt to account for the total baryonic mass within the virial radius of any halo; it is only for stellar mass, and only that concentrated at the centre. There will be significantly more baryonic mass in large (cluster-sized) halos especially, in the form of intracluster light and X-ray gas, and in the stars of galaxies inside virialised, off-centre sub-halos. The implications of these additional baryons are discussed in §2.2.3 and §2.2.6.

2.1.5 Halo concentrations

N-body simulations of ΛCDM structure formation consistently show that c_vir (or indeed $c_{200} = r_{200}/r_{-2}$) correlates with halo mass ($M_\mathrm{d,vir}$ or $M_\mathrm{d,200}$), with larger halos having lower concentrations, at least at low redshifts (Navarro, Frenk & White 1996; Navarro, Frenk & White 1997; Bullock et al. 2001; Dutton & Macció 2014). This needs to be accounted for in the model galaxies in order to calculate the location and value of the dark matter circular-speed peak (or any other property of the dark matter halo that is not at r_vir), for any dark matter halo with a given virial mass and radius and an assumed density profile (with an associated r_pk/r_{-2}).

Dutton & Macció (2014) give a fitting formula for the concentrations r_vir/r_{-2} of simulated halos with masses $M_\mathrm{d,vir} \sim 10^{11}\,M_\odot$–$10^{15}\,M_\odot$, at redshifts $0 \leq z \lesssim 5$ in a

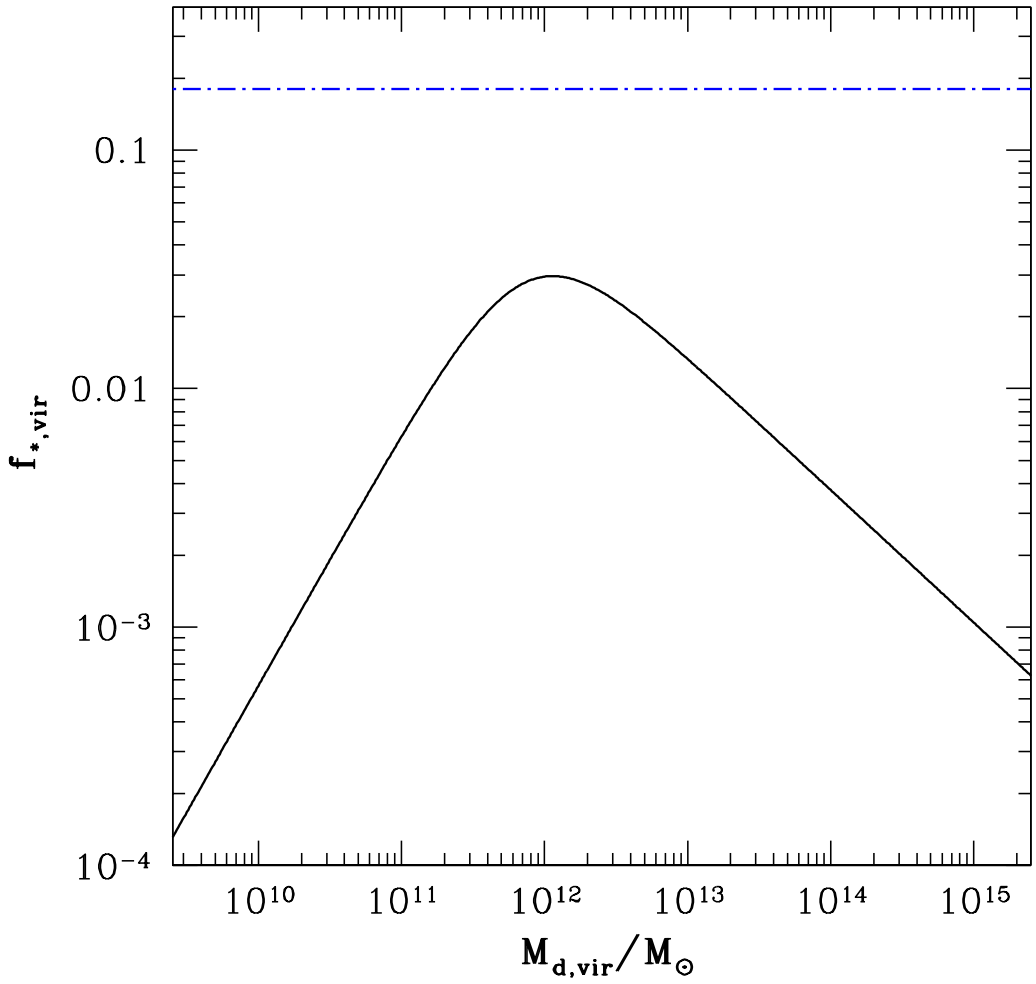

Figure 2.3: The global stellar-to-dark matter mass ratio, $f_{*,\mathrm{vir}}$, as a function of dark matter viral mass, $M_{\mathrm{d,vir}}$. The solid black line is the relation arrived at by Moster et al. (2010) in an abundance-matching analysis [equation (2.26)]. The broken blue line is the cosmic average baryon fraction according to *Planck* cosmology: $f_0 \simeq 0.18$.

Planck cosmology. Specifically,

$$\log\left[\frac{r_{\rm vir}}{r_{-2}}\right] \simeq a - b\log\left[\frac{M_{\rm d}(r_{\rm vir})}{10^{12}\,h_0^{-1}\,M_\odot}\right] \tag{2.27}$$

with

$$\begin{aligned} a &= 0.537 + 0.488\exp\left(-0.718\,z^{1.08}\right) \\ b &= 0.097 - 0.024\,z\ . \end{aligned} \tag{2.28}$$

This represents an average trend — there is intrinsic scatter around it, at the level of a few tens of percent in $r_{\rm vir}/r_{-2}$ for a fixed virial mass (Dutton & Maccio 2014; see also Bullock et al. 2001).

The top panel of Figure 2.4 shows the concentration, $c_{\rm vir}$, as a function of halo mass, $M_{\rm d,vir}$, as given by Dutton & Maccio (2014). The different curves correspond to redshifts $z = 0$ (black line), $z = 1$ (blue) $z = 2$ (cyan), $z = 3$ (green) and $z = 4$ (red). Clearly as the redshift increases, the correlation between $c_{\rm vir}$ and the halo mass becomes shallower, eventually flattening at around $z \sim 4$.

Dutton & Macció (2014) obtain equation (2.27) by fitting Navarro, Frenk & White (1997) density profiles to their simulated halos in order to measure the radius r_{-2}. They also investigate the use of Einasto (1965) profiles instead to fit for r_{-2} in estimating the alternative concentration, r_{200}/r_{-2}. In order to make a direct comparison, they calculate r_{200}/r_{-2} for the NFW halo as well.

The bottom panel of Figure 2.4 shows the ratio $(r_{200}/r_{-2})_{\rm Ein}/(r_{200}/r_{-2})_{\rm NFW}$ versus $M_{\rm d,200}$, for redshifts $z = 0$ (black line), $z = 2$ (cyan line) and $z = 4$ (red line). The concentration values depend systematically on the choice of model for the dark-matter density profile at the $\sim$ 10–15% level. For halos with $M_{\rm d,200} \simeq 10^{12} M_\odot$ (Corresponding to $M_{*,\rm tot} \sim 10^{10} M_\odot$) at $z = 0$, the difference in the Einasto and NFW concentrations is $\sim 20\%$. This decreases systematically as halo mass increases. The same trend is also evident for the higher redshifts. The differences between the c_{200} values for NFW and Einasto profiles are less than the typical scatter in the data around the mean trend [e.g. equation (2.27)], which is $\sim 30\%$ (Dutton & Maccio 2014).

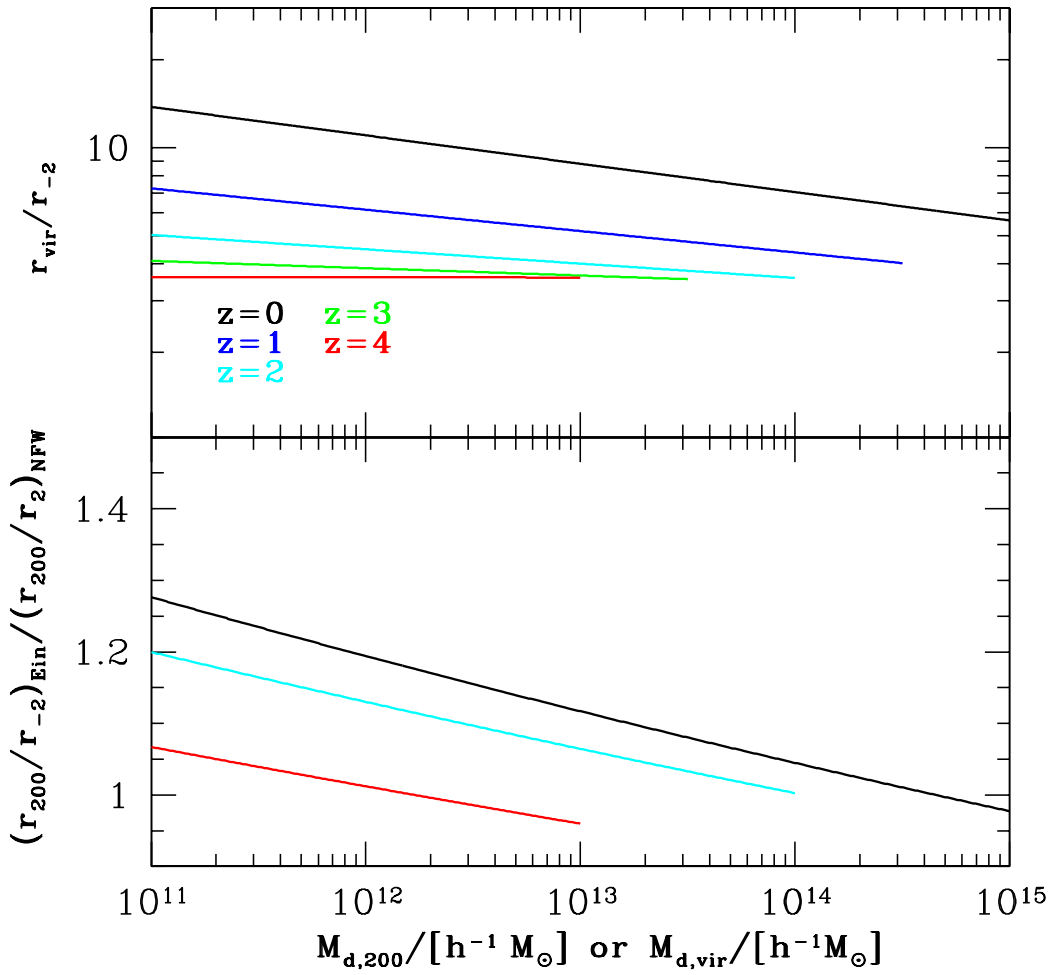

Figure 2.4: *Top panel:* Halo concentration, $r_{\rm vir}/r_{-2}$, as a function of dark matter virial mass, $M_{\rm d,vir}$. These curves are from the fitting function from Dutton & Macció (2014), given here in equation (2.27), assuming an NFW halo. The lines correspond to equation (2.27) evaluated at $z = 0$ (black line), $z = 1$ (blue line), $z = 2$ (cyan line), $z = 3$ (green line) and $z = 4$ (red line). *Bottom panel:* The ratio (Einasto-to-NFW) of the alternative concentration, c_{200}, as a function of dark matter mass $M_{\rm d,200}$, for redshifts $z = 0$ (black lines), $z = 2$ (cyan lines) and $z = 4$ (red lines).

It is also worth noting that Dutton & Macció (2014) derived equation (2.27) from simulations of halos consisting of dark matter *only*, completely free of baryons. Ideally, it would be useful to know how concentrations of simulated halos would depend on baryon fractions. However, global baryon fractions are generally small (see §1.2), with a maximum of the cosmic average (~ 0.18 for *Planck* cosmology) in cluster size halos. Therefore, any baryon-related differences in the halo structures would not affect the models significantly.

2.2 Scaling relations at $z = 0$

Two-component spherical galaxies are formally defined by four parameters: R_e and $M_{*,\rm tot}$ for the stars, and r_{-2} and $M_d(r_{-2})$ for the dark matter halo. However, there are constraints on the dark matter mass and radius scales from cosmological simulations (§2.1.3 – §2.1.4), and interdependencies between these parameters (e.g. between R_e and $M_{*,\rm tot}$; cf. §1.2.3). The models can therefore be fully defined by a single parameter, chosen here to be $M_{*,\rm tot}$.

Scaling relations between various stellar [R_e, $\sigma_{\rm ap}(R_e)$, $f_*(R_e) \equiv M_*(R_e)/M_d(R_e)$] and dark matter [$M_{\rm d,vir}$, $r_{\rm vir}$ $r_{\rm pk}$, $V_{\rm d,pk}$] properties in $z = 0$ galaxies are now investigated, in most cases as functions of $M_{*,\rm tot}$. Where possible, the average trends are shown against data from the literature, introduced in the next subsection. Again, there will be intrinsic scatter associated with these trend lines, due to the scatter in the halo concentrations and stellar-to-dark matter mass ratios introduced above, as well as the interdependency between R_e and $M_{*,\rm tot}$.

2.2.1 Data samples

Three data sets of early-type $z = 0$ galaxies are taken from the literature. The first of these is the ATLAS^{3D} survey (Cappellari et al. 2011; Cappellari et al. 2013b; Cappellari et al. 2013a), which considers various properties of 258 early-type galaxies (Elliptical E

and lenticular S0). This sample consists of nearby galaxies only (all within a distance $D < 42\,\mathrm{Mpc}$), with all of them brighter than $M_K < -21.5\,\mathrm{mag}$ (corresponding to stellar masses $M_{*,\mathrm{tot}} \gtrsim 9 \times 10^9$). Cappellari et al. also tabulate velocity dispersions within an effective radius for all 258 galaxies, with $50\,\mathrm{km\,s^{-1}} \leq \sigma_{\mathrm{ap}}(\mathrm{R_e}) \leq 300\,\mathrm{km\,s^{-1}}$, consistent with the range used to define the M–σ relation.

The second set of data are the 100 early-type galaxies (E and S0, as well as a few dwarf-ellipticals, dE) from the ACS Virgo Cluster Survey (Côté et al. 2004; Chen et al. 2010). As the survey name suggests, all of these galaxies are located in the Virgo Cluster, with luminosities spanning three orders of magnitude ($-22 \lesssim M_g \lesssim -12$), with stellar masses in the range $4 \times 10^8\,M_\odot \lesssim M_{*,\mathrm{tot}} \lesssim 5 \times 10^{11}\,M_\odot$. The Chen et al. (2010) paper also gives various integrated colours for individual galaxies, including $(g-r), (g-i)$ and $(g-z)$. Unpublished velocity dispersions for the ACSVCS galaxies (P. Côté, priv. comm.) are also used. These are measured inside $R_e/8$ and span a range $20\,\mathrm{km\,s^{-1}} \leq \sigma \leq 400\,\mathrm{km\,s^{-1}}$.

The final data set considered is the summary data for ∼16,000 (early-type) galaxies in the Sloan Digital Sky Survey [SDSS; Graves et al. 2009a, b]. The summary data are binned in slightly different ways in the two papers. In Graves, Faber & Schiavon (2009a), the galaxies are first sorted into six velocity dispersion bins (where σ is measured inside $R_e/8$), in the range $70\,\mathrm{km\,s^{-1}} \leq \sigma \leq 320\,\mathrm{km\,s^{-1}}$. The σ bins are then split into three r-band absolute magnitude bins, M_r, with a different range for each σ bin. The total range in absolute magnitude is approximately $-18.9 \geq M_r \geq -23$ ($7 \times 10^9\,M_\odot \lesssim M_{*,\mathrm{tot}} \lesssim 2 \times 10^{11}\,M_\odot$). Finally, the M_r bins are then split into three $(g-r)$ colour bins, with a total range $0.665 \leq (g-r) \leq 0.828$. In Graves, Faber & Schiavon (2009b), the galaxies are sorted by their fundamental plane properties. The data are initially sorted into the same six σ bins, each of which is then split into five bins of effective radius, R_e. The R_e bins are equally spaced logarithmically, over the range $-0.1 \leq \log R_e \leq 0.9$. Finally, each of these is divided into three surface brightness (measured inside R_e) residual bins, $\Delta \log I_e$, where I_e is computed in the V-band. The surface brightness bins are again evenly spaced logarithmically, for $-0.3 \leq \Delta \log I_e \leq 0.3$.

The ATLAS and ACSVCS data are initially used to calibrate an R_e–$M_{*,\rm tot}$ relation (cf. §2.2.2). Once an average trend is obtained for R_e as a function of stellar mass, further scaling relations are obtained by combining this with the results brought together in §2.1. The procedures leading to the scaling relations are detailed in the subsequent subsections. The ATLAS and ACSVCS data are also used in plots of $f_*(R_e) \equiv M_*(R_e)/M_d(R_e)$ (ATLAS only) and $\sigma_{\rm ap}(R_e)$ versus total stellar mass. This is to ensure that following the procedures taken, the average trends are in general agreement with the data. The SDSS data are included as an extra check for the R_e–$M_{*,\rm tot}$ and $\sigma_{\rm ap}(R_e)$–$M_{*,\rm tot}$ relations.

2.2.2 Stellar masses and effective radii

Figure 2.5 plots stellar effective radius, R_e, against $M_{*,\rm tot}$, with data from ATLAS (green squares), ACSVCS (magenta triangles) and SDSS (red circles). In all three data sets, effective radii are tabulated by the original authors, either in kpc or as angular sizes along with distances to the galaxies. Stellar masses have been calculated by combining the integrated luminosities provided by the authors with mass-to-light ratios from the single-burst population synthesis models (SSPs) of Maraston (1998, 2005), assuming a Kroupa (2001) IMF (§1.2.4.1), and stellar ages of 9 Gyr. The masses in these M/L ratios include luminous stars and dark remnants, but not the accumulated stellar ejecta (from stellar winds and supernovae over the lifetime of a galaxy). Allowing for extended star formation lasting up to 6 Gyrs gives the same M/L values, to within $\lesssim 5\%$, when the mean stellar age is 9 Gyr (cf. §1.2.4.3).

Cappellari et al. (2011) give K-band absolute magnitudes for the 258 ATLAS^{3D} galaxies. As discussed in §1.2, the population synthesis model mass-to-light ratios depend very weakly on colour (and hence metallicity) in this bandpass. Over the range $-1.7 \leq [Z/H] \leq 2.3$, interpolating the numbers tabulated by Maraston (2005) gives $0.93 \geq M_*/L_K \geq 0.82$ for a Kroupa (2001) IMF and stellar ages of 9 Gyr. Thus, for the ATLAS^{3D} galaxies, a representative $M_*/L_K = 0.88\, M_\odot/L_\odot$ is adopted. If the assumed mean age of the stars is changed by ± 2 Gyr, then the resulting mass-to-light ratios are

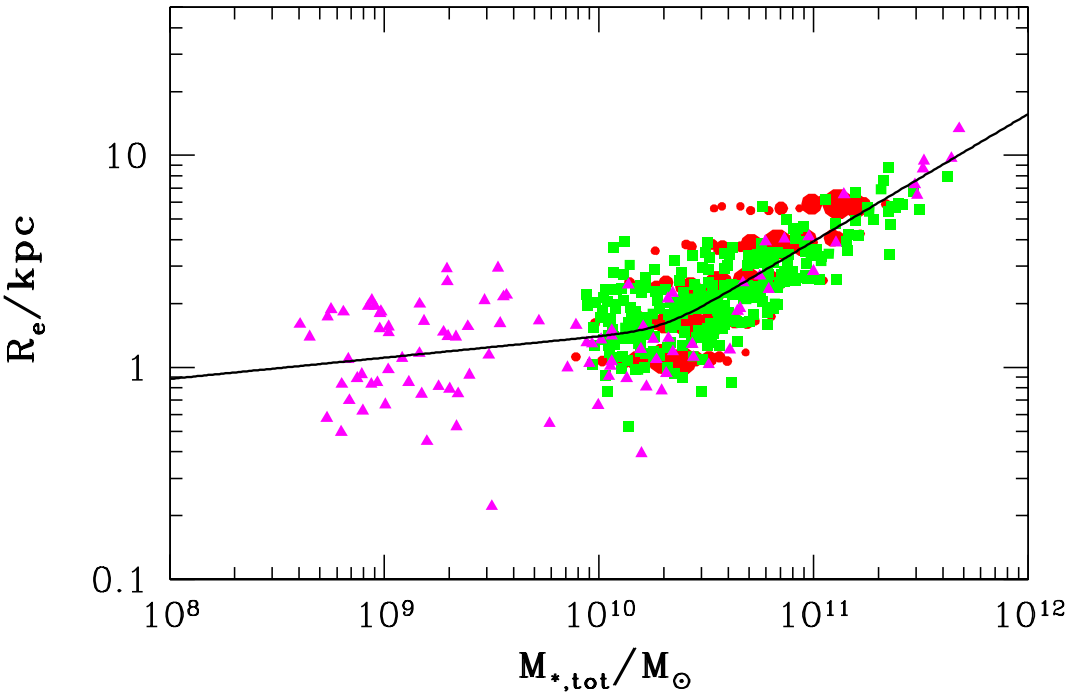

Figure 2.5: Stellar effective radius, R_e, against the total stellar mass, $M_{*,\mathrm{tot}}$. The filled squares (green) are the 258 early-type elliptical galaxies in the $ATLAS^{3D}$ data set, the filled triangles (magenta) are the 100 ACSVCS galaxies, and the filled circles (red) are the SDSS data. The SDSS data are placed into bins in Graves, Faber & Schiavon (2009b) [see text], and the circle size is proportional to the number of galaxies in each R_e bin. The solid line (black) is the parametrisation of R_e versus $M_{*,\mathrm{tot}}$, given in equation (2.29).

altered by approximately ±15%.

Chen et al. (2010) give g-band apparent magnitudes and $(g-z)$ colours for the ACSVCS galaxies. Combining these with the surface-brightness fluctuation distances from Blakeslee et al. (2009), the z-band absolute magnitudes are then calculated. For metallicities $-1.7 \leq [Z/H] \leq 2.3$, the Maraston models imply colours $0.87 \leq (g-z) \leq 1.56$, including all but a few of the ACSVCS data. The corresponding mass-to-light ratios fall in the range $1.40 \leq M_*/L_z \leq 2.00\, M_\odot/L_\odot$. The median colour in the ACSVCS sample is $(g-z) = 1.34$, for which $M_*/L_z \simeq 1.7\, M_\odot/L_\odot$. This is the value taken for all of the ACS galaxies to plot them in Figure 2.5. The mass-to-light ratios again change by approximately ±15% if the assumed age is changed by ±2 Gyr (i.e. approximate to the range of M/L anyway).

As mentioned, the summary data on $\sim 16,000$ galaxies from the SDSS sample have been placed into three-dimensional bins by Graves et al (2009a,b). From Graves et al. 2009a, each $(g-r)$ bin has a median $(g-r)$ colour assigned to it, along with the number of galaxies in the bin. These are used to calculate a weighted average $(g-r)$ for the six velocity dispersion bins. Interpolating with the Maraston (2005) models [assuming a Kroupa (2001) IMF and an age of 9 Gyr] gives a weighted average M_*/L_V value for each σ bin. In Graves et al. 2009b, each of the I_e bins has a median $\log R_e$ and $\log I_e$ value assigned to it. The latter of these can be used to calculate an average V-band luminosity, L_V, for each bin. This is then combined with the six mean $M_*/_V$ values for each σ bin to calculate a stellar mass. This gives average R_e and $M_{*,\rm tot}$ values, shown by the red circles in Figure 2.5, with the circle size proportional to the number of galaxies in a given effective radius bin.

The solid line going through the data in Figure 2.5 is a parametrisation of the R_e–$M_{*,\rm tot}$ correlation,

$$\frac{R_e}{\rm kpc} = 1.5 \left(\frac{M_{*,\rm tot}}{2\times10^{10}\, M_\odot}\right)^{0.1} \left[1 + \left(\frac{M_{*,\rm tot}}{2\times10^{10}\, M_\odot}\right)^{5}\right]^{0.1} . \qquad (2.29)$$

This was chosen to ensure that there are approximately equal numbers of ATLAS^{3D} & ACSVCS data points lying above and below the line. A change in the assumed stellar

age of ± 2 Gyr shifts the mass scale in equation (2.29) by approximately $\pm(0.3-0.4) \times 10^{10} M_{\odot}$, due to a change of $\sim 15\%$ in the mass-to-light ratios. Alternatively, if systems have different ages (for early-type galaxies, ages can generally range from 7–11 Gyr), the scatter will be increased along the $M_{*,\mathrm{tot}}$ axis.

It should be emphasised that equation (2.29) represents an average trend for the R_e–$M_{*,\mathrm{tot}}$ correlation. The scatter around the line, with a global standard deviation of ~ 0.13, is indicative of the fundamental plane for ellipticals, discussed in §1.2.3. For a fixed $M_{*,\mathrm{tot}}$, the data cover up to an order of magnitude in range over R_e. This scatter is due to a full description of an elliptical galaxy depending on a third parameter, i.e. stellar velocity dispersion.

The ATLAS^{3D} sample covers the range of stellar masses, $10^{10}\,M_{\odot} \leq M_{*,\mathrm{tot}} \leq 10^{12}\,M_{\odot}$, of the local galaxies used to define the $z = 0$ SMBH–bulge correlations. As discussed in §2.1.1, it is also over this mass range that a Hernquist (1990) profile adequately describes stellar distributions. The ACSVCS sample includes many galaxies with lower stellar masses, where surface brightness profiles are better fitted by low-index Sérsic (1968) profiles, tending towards exponentials (with $n = 1$). Such surface brightness profiles are not well approximated by a Hernquist (1990) profile. These lower mass systems are included in Figure 2.5 to ensure the change in slope in the R_e–$M_{*,\mathrm{tot}}$ data is incorporated correctly. The R_e–$M_{*,\mathrm{tot}}$ relation does *not* depend on the assumed stellar distribution, but other correlations investigated below do, building upon equation (2.29). In those cases, the implications of assuming a Hernquist stellar density distribution for all systems are considered.

2.2.3 Virial radii and halo virial masses

For any value of $M_{*,\mathrm{tot}}$, equation (2.29) gives a typical value for R_e. Assuming the stellar distribution is described by a Hernquist (1990) profile, the stellar-to-dark matter mass ratio within the virial radius of a galaxy can be written as [from the mass distribution

of Hernquist stars, given by equation (2.3)]

$$f_{*,\rm vir} \equiv \frac{M_*(r_{\rm vir})}{M_d(r_{\rm vir})} = \frac{M_{*,\rm tot}}{M_{\rm d,vir}} \left(\frac{r_{\rm vir}/R_e}{r_{\rm vir}/R_e \, + \, a_*/R_e} \right)^2 . \tag{2.30}$$

Associating $M_{\rm d,vir}$ with the dark matter mass of the main halo centred on the stars in the galaxy, $f_{*,\rm vir}$ is additionally constrained by cosmological simulations through the Moster et al. (2010) parametrisation (cf. §2.1.4):

$$f_{*,\rm vir} \;=\; 0.0564 \left\{ \left[\frac{M_{\rm d}(r_{\rm vir})}{7.66 \times 10^{11} \; M_\odot} \right]^{-1.06} \;+\; \left[\frac{M_{\rm d}(r_{\rm vir})}{7.66 \times 10^{11} \; M_\odot} \right]^{+0.556} \right\}^{-1} . \tag{2.31}$$

Finally, assuming the total mass within the virial radius is just the sum of the stellar and dark matter mass, i.e., $M(r_{\rm vir}) = M_{\rm d,vir}(1 + f_{*,\rm vir})$, then the connection between $M(r_{\rm vir})$ and $r_{\rm vir}$ [equation (2.25)], evaluated at $z = 0$ with the 2013 *Planck* cosmological parameters gives

$$f_{*,\rm vir} = 0.0544 \left[\frac{r_{\rm vir}}{100\,{\rm kpc}} \right]^3 \left[\frac{M_{\rm d,vir}}{10^{12} M_\odot} \right]^{-1} \; - \; 1. \tag{2.32}$$

Solving equations (2.30)–(2.32) for the three unknowns $f_{*,\rm vir}$, $r_{\rm vir}$ and $M_{\rm d,vir}$ as functions of $M_{*,\rm tot}$ gives the curves shown in Figure 2.6.

The peak in $f_{*,\rm vir}$ in the top panel, at a value of $\simeq 0.03$ at $M_{*,\rm tot} \simeq 3.4 \times 10^{10} M_\odot$ (or equivalently, $M_{\rm d,vir} \simeq 1.1 \times 10^{12} M_\odot$) comes directly from the form of equation (2.31), taken from Moster et al. (2010). The rapid decrease in $f_{*,\rm vir}$ towards higher masses corresponds to the rapid increase in $M_{\rm d,vir}$ with increasing $M_{*,\rm tot}$. Halos around central galaxies with $M_{*,\rm tot} \geq 10^{11} M_\odot$ have $M_{\rm d,vir} \geq 10^{13} M_\odot$ and $r_{\rm vir} \geq 500\,{\rm kpc}$, and so are encompassing entire groups and clusters.

The most massive systems are likely to contain baryons in the halo that are not directly associated with the stars in the central galaxy. These include intracluster light and gas, as well as off-centre satellite galaxies. Equation (2.26) does not take into account these extra baryons. To do so requires the additional constraint of the "global" baryon fraction, which is also a mass dependent quantity (Giodini et al. 2009; McGaugh et al. 2010; Zhang et al. 2011). At a radius of r_{500} (where the overdensity

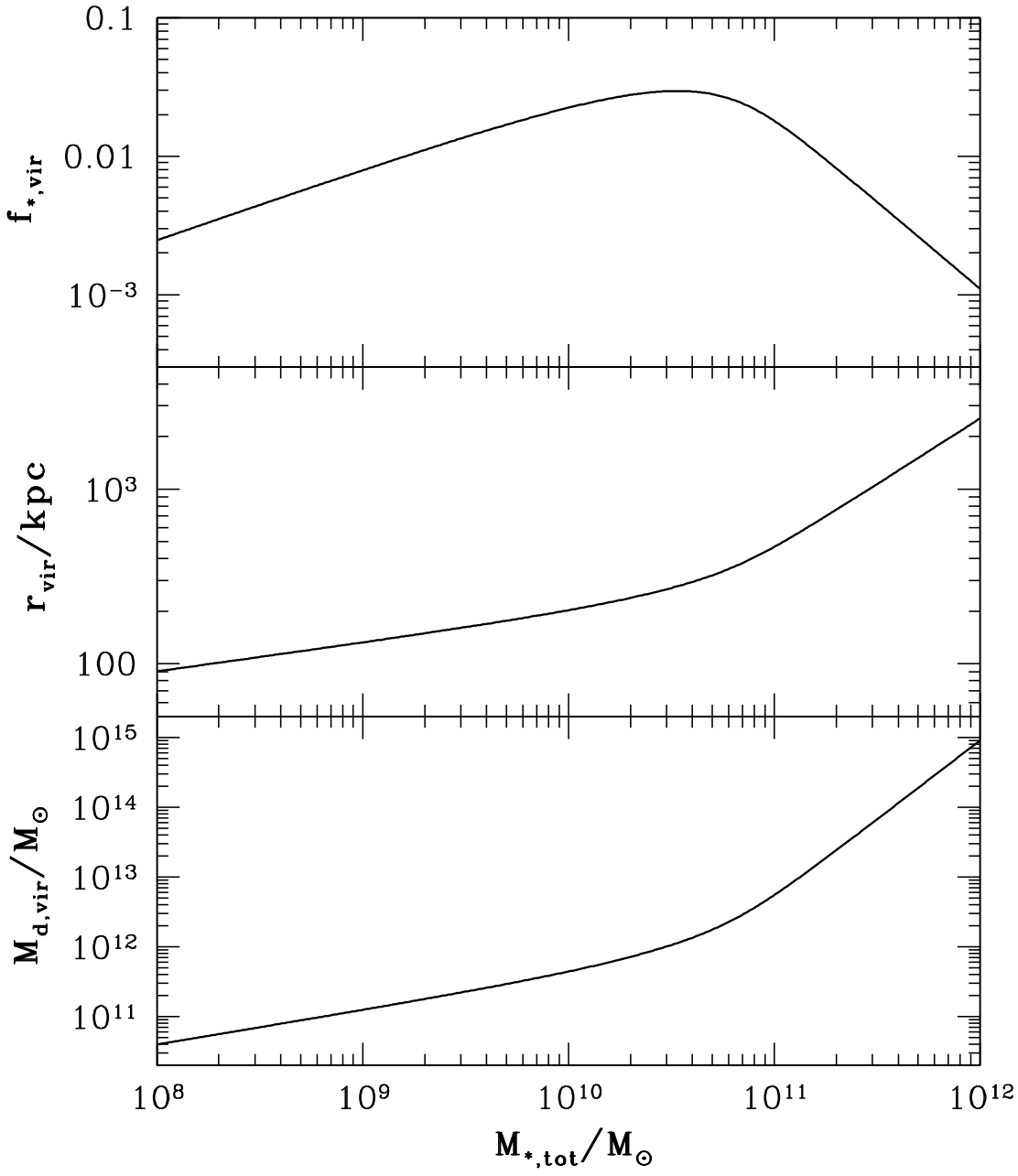

Figure 2.6: Average scaling relations for some virial properties of (early-type) galaxies as functions of total stellar mass. *Top panel*: The stellar-to-dark matter mass ratio within the virial radius, $f_{*,\mathrm{vir}}$, taken from Moster et al. (2010). *Middle panel*: Virial radius of the model galaxy, r_{vir}. *Bottom panel*: Dark matter mass inside the virial radius, $M_{\mathrm{d,vir}}$. These three quantities are calculated as functions of $M_{*,\mathrm{tot}}$ by solving equations (2.30)–(2.32).

$\Delta = 500$), Giodini et al. (2009) give the global baryon fraction as a function of total system mass within r_{500}:

$$f_{\mathrm{b},500} = (0.123 \pm 0.003) \times \left(\frac{M_{500}}{2 \times 10^{14} M_{\odot}} \right)^{0.09 \pm 0.03} . \tag{2.33}$$

They obtained this result by combining stellar mass fractions associated with individual galaxies at r_{500} with an estimate for the gas mass fraction, for 118 groups and clusters over a mass range of $10^{13} M_{\odot} \leq M_{500} \leq 10^{15} M_{\odot}$. Their estimate for the gas mass fraction comes from a mean trend established from an independent sample of well observed groups and clusters (Vikhlinin et al. 2006; Arnaud, Pointecouteau & Pratt 2007; Sun et al. 2009).

The relationship between M_{vir} and r_{vir} given by equation (2.25) provides a convenient way to calculate the masses, radii and mass fractions (stellar and baryon) at different overdensities. This is necessary to make a direct comparison between the Moster et al. (2010) relation for $f_{*,\mathrm{vir}}$ and the Giodini et al. (2009) relation for $f_{\mathrm{b},500}$. For overdensities Δ and Δ_{vir}, equation (2.25) evaluated at $z = 0$ implies

$$\frac{M_{\mathrm{vir}}}{M_{\Delta}} = \frac{\Delta_{\mathrm{vir}}}{\Delta} \left(\frac{r_{\mathrm{vir}}}{r_{\Delta}} \right)^3 . \tag{2.34}$$

Assuming that $M_{\mathrm{vir}} = M_{\mathrm{d,vir}} + M_{*,\mathrm{vir}}$ and $M_{\Delta} = M_{\mathrm{d},\Delta} + M_{*,\Delta}$, this can be written as

$$\frac{M_{\mathrm{d,vir}} + M_{*,\mathrm{vir}}}{M_{\mathrm{d},\Delta} + M_{*,\Delta}} \equiv \frac{1 + f_{*,\mathrm{vir}}}{\left(\frac{M_{\mathrm{d},\Delta}}{M_{\mathrm{d,vir}}} \right) + \left(\frac{M_{*,\Delta}}{M_{*,\mathrm{vir}}} \right) f_{*,\mathrm{vir}}} = \frac{\Delta_{\mathrm{vir}}}{\Delta} \left(\frac{r_{\mathrm{vir}}}{r_{\Delta}} \right)^3 . \tag{2.35}$$

For a given dark matter halo model and stellar distribution profile, the ratios $M_{\mathrm{d},\Delta}/M_{\mathrm{d,vir}}$ and $M_{*,\Delta}/M_{*,\mathrm{vir}}$ can be expressed as functions of r_{Δ}/r_{-2} and r_{Δ}/R_e respectively. From the scaling relations for the virial properties, specifying $M_{*,\mathrm{tot}}$ fixes r_{vir}, $f_{*,\mathrm{vir}}$ and $M_{\mathrm{d,vir}}$. This in turn fixes the concentration, and hence the r_{-2} radius. The effective radius is also known once a total stellar mass has been chosen, through the R_e–$M_{*,\mathrm{tot}}$ relation. Therefore the radius r_{Δ} is fixed by specifying $M_{*,\mathrm{tot}}$, through equation (2.35). Values for $M_{\mathrm{d},\Delta}/M_{\mathrm{d,vir}}$ and $M_{*,\Delta}/M_{*,\mathrm{vir}}$ are then calculated, and the stellar mass fraction at any overdensity radius is then

$$f_{*,\Delta} = \left[\frac{M_{*,\Delta}/M_{*,\mathrm{vir}}}{M_{\mathrm{d},\Delta}/M_{\mathrm{d,vir}}} \right] f_{*,\mathrm{vir}} . \tag{2.36}$$

For the total baryon fraction, $f_{\rm b,\Delta}$, the extra baryons that are not associated directly with stars in the central galaxies need to be considered. Denoting the mass in these extra baryons as M_g, and assuming that they trace the dark matter, then the mass fraction is constant as a function of radius:

$$f_g \equiv \frac{M_g}{M_d} = f_{\rm b,\Delta} - f_{*,\Delta} = f_{\rm b,vir} - f_{*,\rm vir}. \tag{2.37}$$

The last equality in equation (2.37) can be rearranged to give $f_{\rm b,vir}$ in terms of $f_{\rm b,\Delta}$ and the stellar mass fraction at the virial and r_Δ radii:

$$f_{\rm b,vir} = (f_{\rm b,\Delta} - f_{*,\Delta}) + f_{*,\rm vir}. \tag{2.38}$$

The baryon fraction at a given overdensity radius can therefore be transformed to a baryon fraction at any other overdensity radius through equations (2.34) – (2.38).

The top panel of Figure 2.7 shows the baryon- (black curve) and stellar- (green curve) to-dark matter mass ratios at the r_{500} radius, as a function of total system mass within this radius, M_{500}. The $f_{\rm b,500}$–M_{500} relation is the result from Giodini et al. (2009), given by equation (2.33). The stellar-to-dark mass ratio at r_{500} is from equation (2.36), assuming a Dehnen & McLaughlin model for the dark matter halo and for a Hernquist stellar distribution. The broken blue line corresponds to the cosmic average baryon fraction, $f_0 \simeq 0.18$ (Planck Collaboration 2014).

The bottom panel shows the baryon- (black curves) and stellar- (green curves) to-dark matter mass ratios inside the virial radius, $r_{\rm vir}$, versus $M_{\rm vir}$. The green curve is from the $f_{*,\rm vir}$ parametrisation from Moster et al. (2010). The black curve, showing the $f_{\rm b,vir}$–$M_{\rm vir}$ relation, is obtained using equation (2.38), assuming a Hernquist stellar distribution and a Dehnen & McLaughlin model for the dark matter. The broken blue line again shows the cosmic average baryon fraction.

It is only in the most massive clusters (with $M_{\rm d,vir} \geq$ few $\times\, 10^{14}{\rm M}_\odot$) that $f_{\rm b,vir}$ gets close to the cosmic average. It is to be expected that in these largest systems, the global baryonic content should approach the cosmic average. In lower mass systems, more of the intra-cluster baryons will lie further away from the centre of the system, even outside of $r_{\rm vir}$, as it will be easier for various feedback processes (AGN, supernova,

stellar winds etc.) to clear gas out of such systems. In galaxy-sized halos ($M_{\rm d,vir} \lesssim 10^{12} M_\odot$), the baryon fraction is generally consistent with the mass of stars, remnants and stellar ejecta in the galaxy, which are already fully accounted for. The qualitative result of Giodini et al. (2009) — the decrease in $f_{\rm b,500}$ (and hence $f_{\rm b,vir}$) with decreasing mass – is consistent with other studies in the literature that consider global baryon fractions (McGaugh et al. 2010; Zhang et al. 2011; Gonzalez et al. 2013).

In terms of virial properties then, the *maximum* effect of accounting for the extra baryons would be a $\sim 15\%$ increase in the total virial mass (the cosmic average baryon fraction) and a $< 5\%$ increase in the virial radius. This complication has little effect, at least as far as $r_{\rm vir}$ is concerned. The implications of an increased $M_{\rm vir}$ when calculating the stellar velocity dispersions are also considered (cf. §2.2.6).

For stellar masses in the range $10^8 M_\odot \lesssim M_{*,\rm tot} \lesssim 10^{12} M_\odot$, the models give virial-to-effective radius ratios in the range $110 \lesssim r_{\rm vir}/R_e \lesssim 170$. As a result, the stellar mass inside the virial radius is $M_*(r_{\rm vir}) \geq 0.99 M_{*,\rm tot}$ over the associated mass range ($10^8\, M_\odot \lesssim M_{*,\rm tot} \lesssim 10^{12}\, M_\odot$). Additionally, equation (2.30) gives $f_{*,\rm vir} \simeq M_{*,\rm tot}/M_{\rm d,vir}$, with only a weak dependence on $r_{\rm vir}/R_e$, since $r_{\rm vir}/R_e \gg a_*/R_e$. The mass of dark matter *alone* within $r_{\rm vir}$ is therefore determined [through equations (2.30) and (2.31)] almost independently of $r_{\rm vir}$. Thus, the calculated values of $M_{\rm d,vir}$ are not changed much by including these additional baryons outside of the central galaxies.

These results for the virial properties of the model galaxies will still hold true for stellar distributions described by Sérsic models that depart significantly from Hernquist profiles in projection, providing $M_*(r)$ converges within $r \leq 100 R_e$. This is always the case for Sérsic profiles with $1 \lesssim n \lesssim 10$ (cf. Figure 2.10). With this proviso, the curves for $f_{*,\rm vir}$, $r_{\rm vir}$ and $M_{\rm d,vir}$ are insensitive to the choice of stellar density profile.

2.2.4 Peak halo circular speeds

With virial radii and dark matter masses known as functions of $M_{*,\rm tot}$, the scale radius r_{-2} follows directly from equation (2.27) for the halo concentration, $r_{\rm vir}/r_{-2}$. The location of the peak of the dark matter circular-speed curve then comes from the ratio

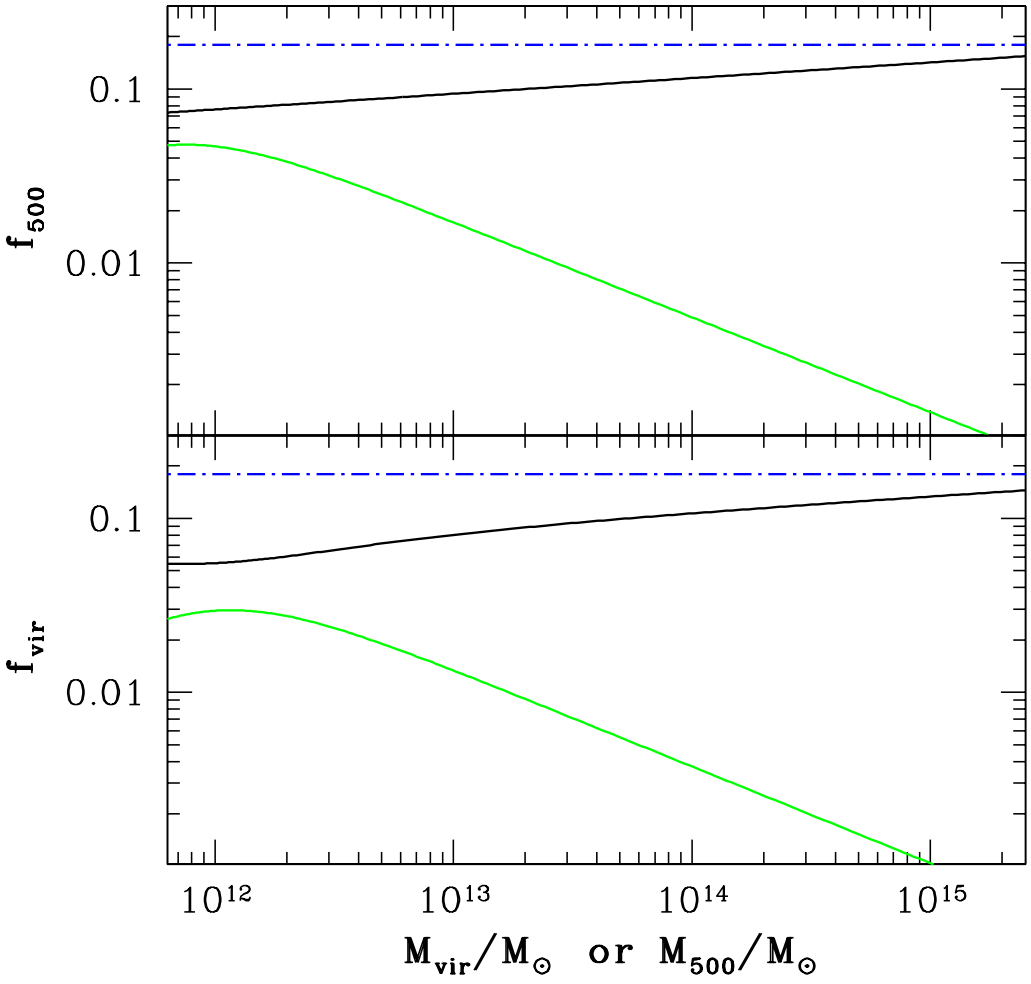

Figure 2.7: *Top panel:* The baryon-to-dark matter mass ratio at a radius of r_{500}, $f_{\rm b,500}$, as a function of total mass within r_{500}, M_{500}. The functional form of $f_{\rm b,500}$ is taken from Giodini et al. (2009), and is given in equation (2.33). The broken blue line shows the cosmic average baryon fraction according to the *Planck* cosmology, $f_0 \simeq 0.18$. The green curve shows the stellar-to-dark matter mass ratio at r_{500}, calculated as described in the text. *Bottom panel* the baryon (black curve) and stellar (green curve) mass fraction at the virial radius, $r_{\rm vir}$, as a function of the total virial mass, $M_{\rm vir}$. The broken blue line again corresponds to the cosmic average. $f_{*,\rm vir}$ is from the Moster et al. (2010) parametrisation. The calculation for obtaining $f_{\rm b,vir}$ from $f_{\rm b,500}$ is described in the text.

$r_{\rm pk}/r_{-2}$ specific to a choice of $\rho_d(r)$ for the dark matter. The top panel of Figure 2.8 shows the model curves of $r_{\rm pk}$ versus $M_{*,\rm tot}$ for all four dark matter halos. The curves are very similar because $r_{\rm pk}/r_{-2} \simeq 2$ to within 15% for all of these halos. They are also essentially independent of the choice of stellar distribution, due to the fact that $r_{\rm vir}$ and $M_{\rm d,vir}$ are as well. For stellar masses in the range $10^8 M_\odot \leq M_{*,\rm tot} \leq 10^{12} M_\odot$, the scaling relations imply $15 \leq r_{\rm pk}/R_e \leq 110$ and $0.14 \leq r_{\rm pk}/r_{\rm vir} \leq 0.40$, indicating that the peak is more representative of the dark matter halo on global scales.

The peak *value* of the dark matter circular-speed can be expressed as

$$V^2_{\rm d,pk} = \frac{V^2_{\rm d}(r_{\rm pk})}{V^2_{\rm d}(r_{-2})} \left[\frac{V^2_{\rm d}(r_{\rm vir})}{V^2_{\rm d}(r_{-2})}\right]^{-1} \frac{GM_{\rm d,vir}}{r_{\rm vir}}. \tag{2.39}$$

The normalised circular-speed profiles, $V^2_d(r)/V^2_d(r_{-2})$, are shown for each halo in Figure 2.2, and are given in equations (2.9), (2.13), (2.17) and (2.21). For a given dark matter density profile, evaluating the circular-speed profiles at $r = r_{\rm pk}$ (fixed by the density profile and independent of stellar distribution) and $r = r_{\rm vir}$ (dependent on $M_{*,\rm tot}$), and then folding in the dependences of $M_{\rm d,vir}$ and $r_{\rm vir}$ on $M_{*,\rm tot}$, yields $V_{\rm d,pk}$ as a function of total stellar mass. The bottom panel of Figure 2.8 shows this mean trend, again for all four dark matter halos.

The $V_{\rm d,pk}$ versus $M_{*,\rm tot}$ curves are once again insensitive to the choice of stellar distribution. The differences between the halos are mainly a result of the different widths of the circular-speed curves between $r_{\rm pk}$ and $r_{\rm vir}$. The differences are greater for smaller systems, as these have higher concentrations on average, leading to larger ratios $r_{\rm vir}/r_{\rm pk}$ and hence ratios $V_d(r_{\rm pk})/V_d(r_{\rm vir})$ that are more sensitive to the detailed shapes of the circular-speed curves.

The peak circular speeds in the largest systems, which represent the galaxies defining the upper end of the observed SMBH–bulge correlations, have very large values (above $1000\,{\rm km\,s^{-1}}$), far exceeding the stellar velocity dispersion measured within R_e in real galaxies. This is because dark matter halos centred on such massive galaxies correspond to entire clusters. At the same time, these larger halos will be the ones that grow the most at low redshifts, after the epoch of quasar activity that may have determined self-regulated black hole masses. Looking ahead to Chapter 3, a theoretical

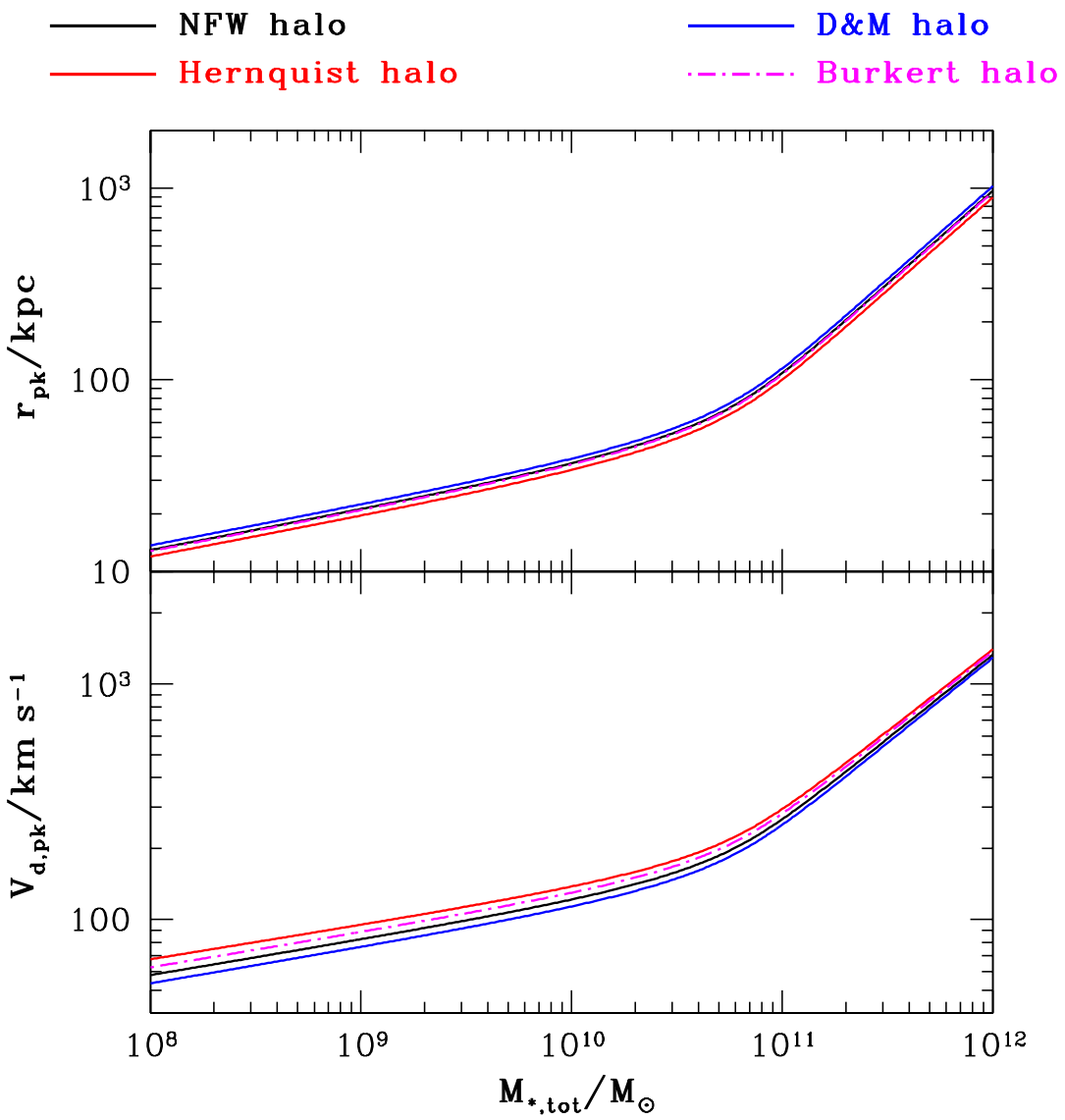

Figure 2.8: The location, $r_{\rm pk}$ (top panel), and value, $V_{\rm d,pk}$ (bottom panel), of the peak of the dark matter circular-speed curves at $z = 0$, as a function of total stellar mass, $M_{*,\rm tot}$. Both panels show the mean trends for the four dark matter halos I am considering; NFW (black line), Hernquist (red line), Dehnen & McLaughlin (blue line) and Burkert (broken magenta line).

prediction for a critical SMBH mass of the form $M_{\rm BH} \propto V_{\rm d,pk}^4$ (McQuillin & McLaughlin 2012) is considered. It is therefore essential that $V_{\rm d,pk}$ be calculated in the halo *progenitors* in order to compare such predictions to any observed $M_{\rm BH}$–bulge property correlation. Modelling galaxies in this way soon leads to the conclusion that the naive substitution, $V_{\rm d,pk} = \sqrt{2}\sigma_{\rm ap}(R_e)$ cannot suffice to make this comparison.

To summarise so far, scaling relations between total stellar mass, $M_{*,\rm tot}$, and various properties of early-type galaxies at $z = 0$ have been constructed. These are R_e, $f_{*,\rm vir}$, $M_{\rm d,vir}$, $r_{\rm vir}$, $V_{\rm d,pk}$ and $r_{\rm pk}$. The $V_{\rm d,pk}$–$M_{*,\rm tot}$ relation turns steeply upwards at approximately $4 \times 10^{11} M_\odot$, due to the non-monotonic behaviour of the stellar-to-dark matter mass ratio. This leads to $V_{\rm d,pk}$ values that far exceed $\sigma_{\rm ap}(R_e)$ in the most massive systems. However, in order to compare a prediction relating the black hole mass to a global property of the protogalactic dark matter halo to the $M_{\rm BH}$–$\sigma_{\rm ap}$ data (and other SMBH correlations), calculations of the dark matter properties at $z > 0$ are required. This is the focus of Chapter 3. In the meantime, $V_{\rm d,pk}$ at $z = 0$ needs to be connected to the aperture velocity dispersion, $\sigma_{\rm ap}(R_e)$, at $z = 0$. This ultimately requires solving the spherical Jeans equation (cf. §2.2.6.1), for which the stellar-to-dark matter mass ratio at more than one radius needs to be considered.

2.2.5 Stellar mass fractions at different radii

The stellar-to-dark matter mass ratio within radius r in a galaxy with a specified total stellar mass can be written as

$$f_*(r) \equiv \frac{M_*(r)}{M_d(r)} = f_{*,\rm vir}\,\frac{M_*(r)/M_{*,\rm vir}}{M_d(r)/M_{\rm d,vir}}. \tag{2.40}$$

Here, $f_{*,\rm vir}$ is known as a function of $M_{*,\rm tot}$ from §2.2.3. If the stars are described by a Hernquist profile, the normalised stellar mass profile comes from equation (2.3) and can be evaluated at any r (for a given $M_{*,\rm tot}$ and hence $M_{\rm d,vir}$), since R_e and $r_{\rm vir}$ are known once the total stellar mass has been specified. Once a dark matter halo has been chosen, its mass profile follows and can also be evaluated at any r since the concentration (and hence r_{-2} along with $r_{\rm vir}$) is also fixed by $M_{*,\rm tot}$.

Cappellari et al. (2013a,b) used dynamical Jeans modelling (cf. §1.3.2.2) to estimate the ratio of dark-to-total mass within $r = R_e$ for each of the 258 ATLAS^{3D} galaxies. In the current notation, this is related to the stellar-to-dark matter mass ratio inside R_e:

$$f_*(R_e) \equiv \frac{M_*(R_e)}{M_d(R_e)} = \frac{1 - M_d(R_e)/M(R_e)}{M_d(R_e)/M(R_e)}. \tag{2.41}$$

Although the Cappellari et al. modelling assumes that the dark matter halos have NFW density profiles, their results are not very sensitive to this detail, since they find $M_d(R_e) < M_*(R_e)$ by factors of several for most of their galaxies. Therefore, at radii around R_e, the stars are the dominant component of the galaxy.

Figure 2.9 shows the $f_*(R_e)$ values for the 258 ATLAS^{3D} galaxies. The arrows at the top represent galaxies consistent with having no dark matter inside R_e in their analysis. The curves show the average dependence on $M_{*,\rm tot}$ for the four different dark matter halos (line colours are indicated at the top of the Figure), obtained by evaluating equation (2.40) at $r = R_e$. The model curves depend on the *stellar* distribution through the normalised mass profile, $M_*(r)/M_{*,\rm vir} \simeq M_*(r)/M_{*,\rm tot}$, evaluated at $r = R_e$. For a Hernquist density profile, $M_*(R_e)/M_{*,\rm tot} \simeq 0.41576$. The top panel of Figure 2.10 shows stellar mass profiles as a function of r/R_e, for different integer values of the Sérsic index, n. In the region $r < R_e$, the shallowest profile corresponds to $n = 10$, with n decreasing by one when moving to the next curve. The steepest $M_*(r)$ curve in this plot is for $n = 1$. The bottom panel shows $M_*(R_e)/M_{*,\rm tot}$ as a function of Sérsic index, n, with the broken red line corresponding to the value for a Hernquist profile.

In the mass range $M_{*,\rm tot} \geq 10^{10} M_\odot$, stellar distributions are more accurately described by Sérsic (1968) profiles with Sérsic indices $3 \leq n \leq 7$. Figure 2.10 shows that describing the stars in this way, instead of using a Hernquist profile, alters $M_*(R_e)/M_{*,\rm tot}$ [and hence $f_*(R_e)$] by less than 5%. For the lower-mass systems, where there are no $f_*(R_e)$ data, the stellar profiles are described by profiles with smaller values of n, closer to exponential. For these, $f_*(R_e)$ can be up to $\sim 20\%$ lower than the Hernquist model value. This variations in $M_*(R_e)/M_{*,\rm tot}$ with n are relatively small, especially given the amount of scatter in the data in the $f_*(R_e)$–$M_{*,\rm tot}$ plot.

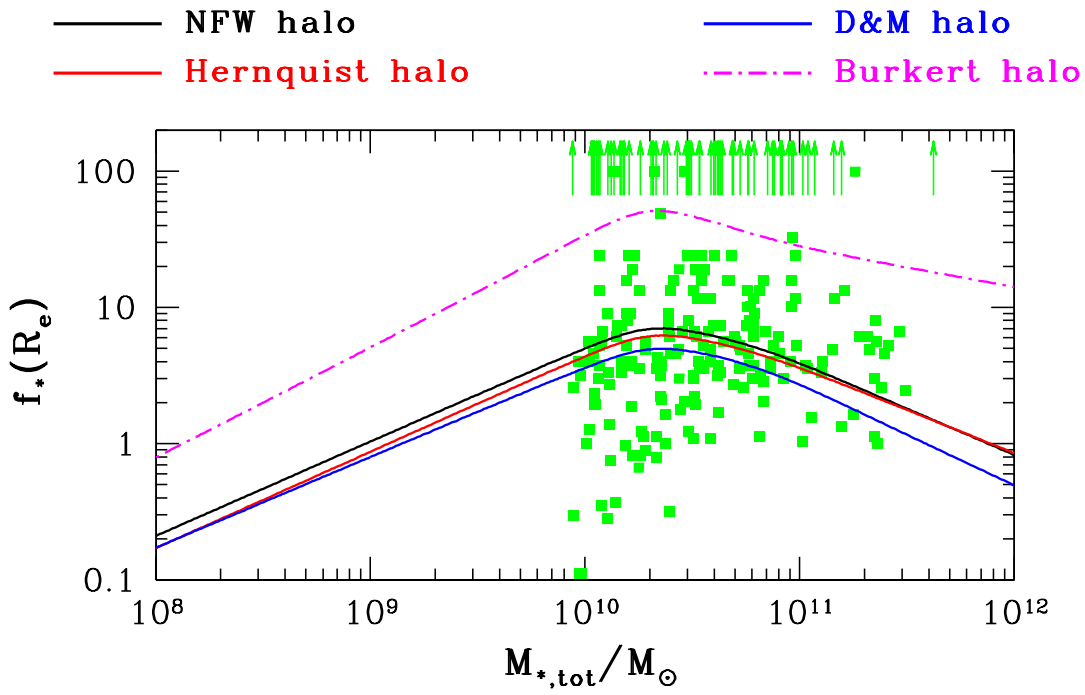

Figure 2.9: The stellar-to-dark matter mass ratio at the effective radius, $f_*(R_e)$, as a function of total stellar mass, $M_{*,\mathrm{tot}}$. The coloured lines show mean trends for the four dark matter halos I am considering; NFW (black line), Hernquist (red line), Dehnen & McLaughlin (blue line) and Burkert (broken magenta line). The data points are from dynamical modelling by the ATLAS survey, where the arrows represent galaxies consistent in their analysis with having no dark matter within R_e.

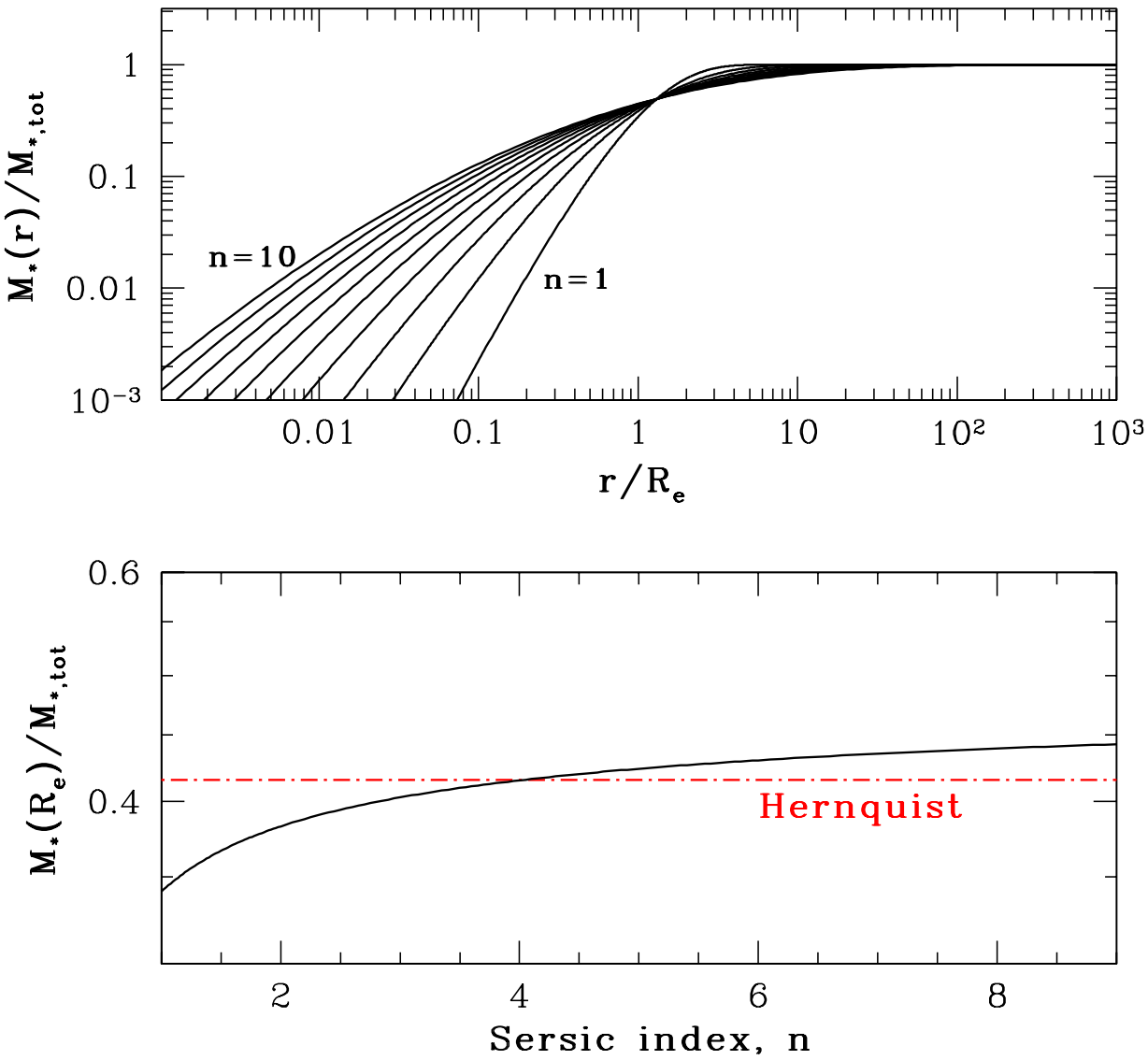

Figure 2.10: *Top panel:* Stellar mass profiles as a function of r/R_e, for various Sérsic profiles. These were calculated by de-projecting the surface density profile, and then integrating the resulting $\rho_*(r)$ profile. The different curves correspond to values of the Sérsic index, $n = 10, 9, 8, 7, 6, 5, 4, 3, 2, 1$ going from left to right at small r/R_e. *Bottom panel:* The stellar mass profile, $M_*(r)/M_{*,\rm tot}$, evaluated at $r = R_e$, as a function of Sérsic index, n. The broken red line corresponds to $M_*(R_e)/M_{*,\rm tot} \simeq 0.41576$, the value for a Hernquist stellar distribution.

It is clear from Figure 2.9 that the $f_*(R_e)$–$M_{*,\rm tot}$ relation is dependent on the choice of dark matter halo. The main source of the differences between the curves in Figure 2.9 is how steeply the enclosed dark matter mass, $M_d(r)$, decreases as $r \to 0$. Hernquist and NFW profiles have the same central density slope (i.e. $\rho_d(r) \propto r^{-1}$), and therefore have similar values for $M_d(R_e)/M_{\rm d,vir}$, and hence $f_*(R_e)$, for a fixed $M_{*,\rm tot}$. Dehnen & McLaughlin (2005) halos have significantly shallower mass profiles than NFW or Hernquist. These therefore have larger values of $M_d(R_e)/M_{\rm d,vir}$, and hence smaller $f_*(R_e)$. Conversely, the central density core of the Burkert (1995) halo leads to a mass profile that is much steeper than the three cuspy halos at small radii. This puts relatively more dark matter at larger radii in the Burkert halos, giving lower values of $M_d(R_e)/M_{\rm d,vir}$, and higher $f_*(R_e)$ for a fixed $M_{*,\rm tot}$.

The three halos with central density cusps all imply $f_*(R_e)$ values that are broadly consistent with the ATLAS^{3D} data, for total stellar masses $\geq 10^{10} M_\odot$. However, the Burkert halo models over-predict the data. This is not a surprising outcome, as the Burkert profile was originally proposed in connection with dwarf spheroidal galaxies, not regular ellipticals.

2.2.6 Stellar velocity dispersions

2.2.6.1 Jeans modelling

To calculate (model) stellar velocity dispersions, the isotropic Jeans equation (cf. §1.3.2) is solved. Including contributions to the gravitational potential from dark matter, stars and the accumulated ejecta from stellar winds and supernovae, the Jeans equation is

$$\frac{d[\rho_*(r)\sigma_*^2(r)]}{dr} = -\frac{G\rho_*(r)}{r^2}\Big[M_d(r) + M_*(r) + M_{\rm ej}(r)\Big]. \qquad (2.42)$$

Intracluster baryons (in the form of intracluster gas and light or satellite galaxies) are not included in this calculation. The consequences of this are discussed at the end of the Section.

For the stellar ejecta, there are two extreme possibilities to consider. Either

the ejecta could be confined to the central regions of the overall potential well or they could be expelled from the centre of the galaxy. If the ejecta are pushed well away from the centre, most likely in lower-mass galaxies, they can become part of the intracluster baryons, or can be driven out of the system entirely. However, if the ejecta are confined to the central regions, then they are likely to approximately follow the stellar distribution, so the mass profile is $M_{\rm ej}(r) \approx F_{\rm ej} M_*(r)$, with $F_{\rm ej}$ constant. The value of $F_{\rm ej}$ comes directly from the population synthesis models used to calculate mass-to-light ratios in §2.2.2. For a Kroupa (2001) IMF and stellar ages greater than several Gyr, Maraston (2005) gives the ratio of current-to-initial mass in stars and remnants as $\simeq 0.58$ for the single-burst models, implying $(1 + F_{\rm ej}) \simeq 1/0.58 \longrightarrow F_{\rm ej} \simeq 0.72$.

Defining the normalised quantities

$$\widetilde{r} = \frac{r}{R_e}\,; \qquad \widetilde{\rho}_* = \frac{\rho_*}{M_{*,\rm tot}/R_e^3}\,; \qquad \widetilde{\sigma}_*^2 = \frac{\sigma_*^2}{GM_{*,\rm tot}/R_e}, \tag{2.43}$$

where ρ_* and σ_* are the stellar density and one-dimensional velocity dispersion profiles, the dimensionless Jeans equation is

$$\frac{d}{d\widetilde{r}}\big[\widetilde{\rho}_*(\widetilde{r})\widetilde{\sigma}_*^2(\widetilde{r})\big] = -\,\frac{\widetilde{\rho}_*(\widetilde{r})}{\widetilde{r}^2}\,\frac{M_*(\widetilde{r})}{M_{*,\rm tot}}\left[(1+F_{\rm ej}) + \frac{1}{f_*(\widetilde{r})}\right]. \tag{2.44}$$

The dimensionless stellar density, $\rho_*(r)$, and mass, $M_*(r)/M_{*,\rm tot}$, profiles are known for a Hernquist distribution, and the function $f_*(r)$ is known in full for any specified $M_{*,\rm tot}$ and chosen dark matter halo, as discussed in §2.2.5. Using the boundary condition that $\widetilde{\rho}_*\widetilde{\sigma}_*^2 \to 0$ as $\widetilde{r} \to \infty$, equation (2.44) can therefore be solved for the dimensionless $\sigma_*^2/(GM_{*,\rm tot}/R_e)$ as a function of r/R_e in a galaxy with any given total stellar mass.

2.2.6.2 The aperture velocity dispersion

The velocity dispersion in data is the aperture velocity dispersion over a circular disc on the plane of the sky. This comes from projecting $\sigma_*^2(r)$ along the line of sight and then taking a luminosity-weighted average (Binney & Tremaine 2008). If r is the 3-D spatial radius, R is the 2-D projected radius on the plane of the sky and z is along the

line of sight of the observer, then $r = \sqrt{R^2 + z^2}$. Defining a dimensionless $\widetilde{R} = R/R_e$ and $\widetilde{z} = z/R_e$, the stellar surface-density profile is then

$$\widetilde{\Sigma}_*(\widetilde{R}) \equiv \frac{\Sigma_*(R)}{M_{*,\rm tot}/R_e^2} = 2\int_0^\infty \widetilde{\rho}_*(\widetilde{r})\,d\widetilde{z} = 2\int_{\widetilde{R}}^\infty \widetilde{\rho}_*(\widetilde{r})\,\frac{\widetilde{r}\;d\widetilde{r}}{(\widetilde{r}^2\;-\;\widetilde{R}^2)^{1/2}}, \tag{2.45}$$

and the projected stellar velocity dispersion is therefore given by

$$\widetilde{\sigma}_p^2(\widetilde{R}) = \frac{2}{\widetilde{\Sigma}_*(\widetilde{R})}\int_0^\infty \widetilde{\rho}_*(\widetilde{r})\widetilde{\sigma}_*^2(\widetilde{r})\,d\widetilde{z} = \frac{2}{\widetilde{\Sigma}_*(\widetilde{R})}\int_{\widetilde{R}}^\infty \widetilde{\rho}_*(\widetilde{r})\;\widetilde{\sigma}_*^2(\widetilde{r})\,\frac{\widetilde{r}\;d\widetilde{r}}{(\widetilde{r}^2\;-\;\widetilde{R}^2)^{1/2}}. \tag{2.46}$$

Taking the luminosity-weighted average of this, the aperture dispersion within a projected radius $R_{\rm ap}$ is

$$\widetilde{\sigma}_{\rm ap}^2(R_{\rm ap}) = \frac{\int_0^{R_{\rm ap}/R_e}\widetilde{\sigma}_p^2(\widetilde{R})\,\widetilde{\Sigma}_*(\widetilde{R})\,\widetilde{R}\,d\widetilde{R}}{\int_0^{R_{\rm ap}/R_e}\widetilde{\Sigma}_*(\widetilde{R})\,\widetilde{R}\,d\widetilde{R}}. \tag{2.47}$$

For a given aperture size, and with the stellar density profile the same in all galaxies, $\sigma_{\rm ap}$ is determined by the form of the dark matter density profile and the value of $M_{*,\rm tot}$ (which also determines the value of $M_{\rm d,vir}, r_{\rm vir}$ and $f_{*,\rm vir}$). These fix the dimensionless unprojected velocity dispersion and the value of R_e. Setting $R_{\rm ap} = R_e$ in the equation above yields the dispersion corresponding to the measured values in the ATLAS sample, and in many $M_{\rm BH}$–σ relations (Gültekin et al. 2009; McConnell & Ma 2013; Kormendy & Ho 2013).

2.2.6.3 Comparison with data

Figure 2.11 shows velocity dispersion data for the ATLAS^{3D} galaxies (green squares, Cappellari et al. 2011, 2013a,b) and the SDSS galaxies (red circles, Graves et al. 2007a,b). For the latter, the circle size is proportional to the number of galaxies in each σ bin in the Graves et al. summary data. Also included are unpublished velocity dispersions for the ACSVCS galaxies (magenta triangles; P. Côté, priv. comm.). The curves show the model aperture velocity dispersion, calculated for each of the four dark matter halos.

All of the cuspy halos yield curves that run through the middle of the $\sigma_{\rm ap}(R_e)$ data for galaxies with $M_{*,\rm tot} \geq 10^{10} M_\odot$, while the cored halo predicts dispersions higher

than the observed average for a given total stellar mass. This is because for a fixed $M_{*,\rm tot}$, and hence $M_{\rm d,vir}$, the Burkert halo has more of its mass at larger radii than the cuspy halos do. The unprojected $\sigma_*(r)$ is substantially higher for $r \geq R_e$ as a result, inflating the line-of-sight dispersion even inside R_e. For lower-mass systems, with $M_{*,\rm tot} < 10^{10} M_\odot$, the model stellar velocity dispersions calculated with the three cuspy halos lie above most of the data. It is in this stellar mass range that the robustness of the models is most uncertain.

As an extra comparison, Figure 2.12 shows the curve for a Dehnen & McLaughlin halo (solid blue line) compared to the fit using SDSS data from Gallazzi et al. (2006), given by (see Dutton et al. 2010);

$$\log\left[\frac{\sigma_{\rm ap}(R_e)}{\rm km\,s^{-1}}\right] = 2.054 + 0.286\,\left(\log\left[\frac{M_{*,\rm tot}}{10^{10}h^{-2}M_\odot}\right]\right). \tag{2.48}$$

This is valid for stellar masses $10^{10} M_\odot \lesssim M_{*,\rm tot} \lesssim 10^{12} M_\odot$. The calculations from the Jeans modelling outlined in §2.2.6.1 show excellent agreement with equation (2.48), especially for $M_{*,\rm tot} \gtrsim 10^{10} M_\odot$. For smaller galaxies, where equation (2.48) is an extrapolation, both are inconsistent with the ACSVCS data.

For a self-consistent Hernquist sphere containing stars only [$F_{\rm ej} = 0$ and $1/f_*(r) \equiv 0$], the dimensionless aperture velocity dispersion inside R_e is $\sigma^2_{\rm ap}(R_e)/(GM_{*,\rm tot}/Re) \simeq 0.151$. If the stellar ejecta and dark matter are included, the stellar velocity dispersions can be usefully approximated by

$$\frac{\sigma_{\rm ap}(R_e)}{\sqrt{GM_{*,\rm tot}/R_e}} \approx 0.389\sqrt{(1+F_{\rm ej}) + \frac{0.86}{f_*(R_e)}}\,, \tag{2.49}$$

where the term under the square-root represents the ratio of an "effective" total mass to the total *stellar* mass. This approximation reproduces the aperture dispersion values from the full Jeans-equation and projection calculations with relative error $< 2.5\%$ for Hernquist stars inside any of the three cuspy halos, as long as $f_*(R_e) > 0.1$.

The values of $\sigma^2_{\rm ap}(R)/(GM_{*,\rm tot}/R_e)$ have also been calculated for self-gravitating Sérsic (1968) $R^{1/n}$ spheres of stars, without any dark matter. This is done by de-projecting the surface brightness profiles to obtain $\rho_*(r)$ for each n. From this the mass

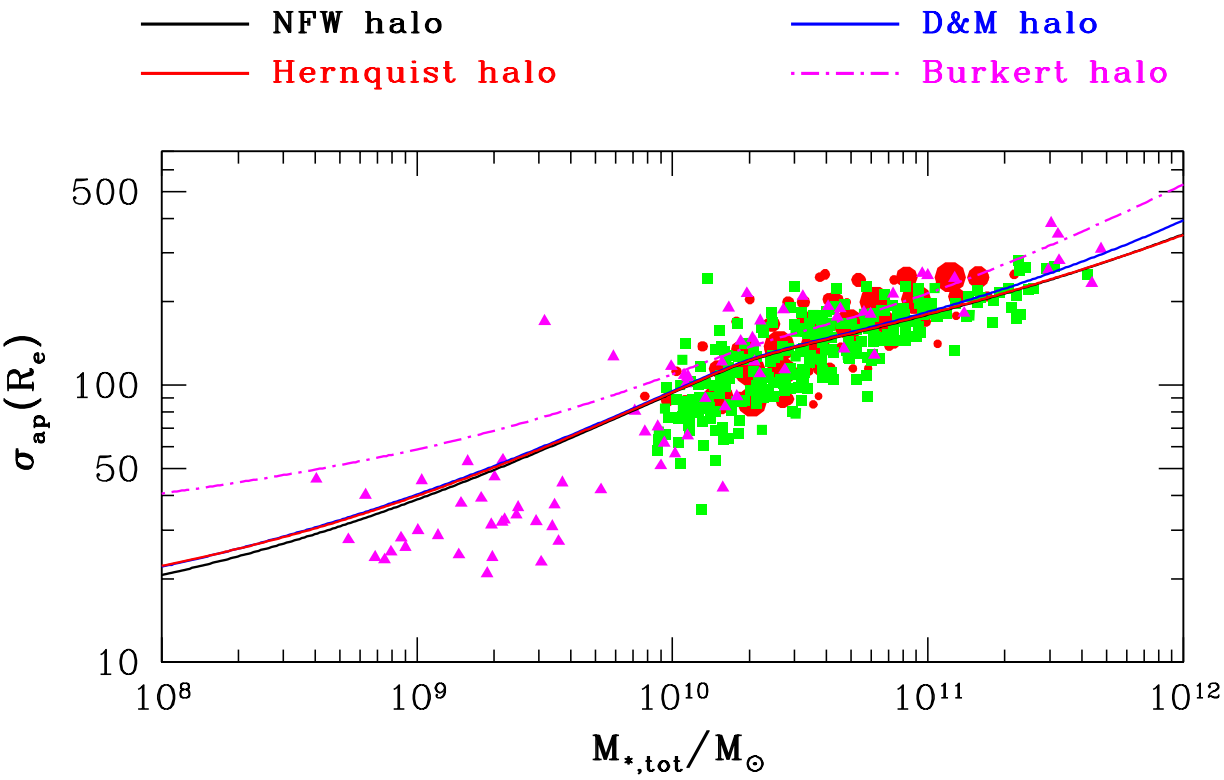

Figure 2.11: Stellar velocity dispersion, $\sigma_{\rm ap}(R_e)$, within an aperture of radius R_e as a function of $M_{*,\rm tot}$. Green squares are from the ATLAS survey, and red circles are from the summary data for $\sim 16,000$ galaxies in the SDSS sample (Graves et al. 2007a,b). The circle size is proportional to the number of galaxies in each σ bin from the Graves et al. papers. The magenta triangles are from the ACSVCS data set. The curves show the implied aperture dispersions for the four different halos, with line colours indicated at the top of the Figure.

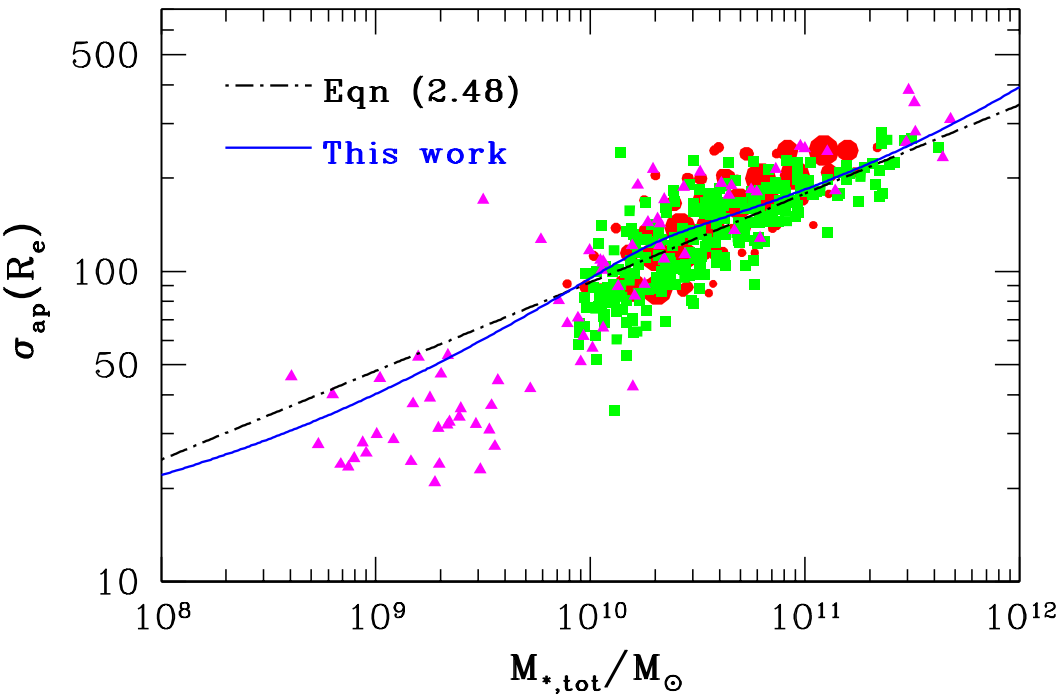

Figure 2.12: Stellar velocity dispersion, $\sigma_{\rm ap}(R_e)$, within an aperture of radius R_e as a function of $M_{*,\rm tot}$. Green squares are from the ATLAS survey, and red circles are from the summary data for $\sim 16,000$ galaxies in the SDSS sample (Graves et al. 2007a,b). The circle size is proportional to the number of galaxies in each σ bin from the Graves et al. papers. The magenta triangles are from the ACSVCS data set. The solid blue line is the $\sigma_{\rm ap}(R_e)$–$M_{*,\rm tot}$ relation from the Jeans modelling outlined in §2.2.6.1, assuming a Dehnen & McLaughlin density profile for the dark matter halo. The broken black line shows the fit to SDSS data (velocity dispersion versus stellar mass) from Gallazzi et al. (2006), [see equation (2.48)].

profile, $M_*(r)$, is obtained, and then the spherical Jeans equation is solved. This is to investigate the consequences on the aperture dispersion (at R_e) of assuming Hernquist stars for all galaxies. The Sérsic $\sigma_{\rm ap}(R)$ profiles are shown in the top panel of Figure 2.13, for Sérsic indices $n = 1$–10 in integer steps, as a function of R/R_e. The bottom panel shows $\sigma^2_{\rm ap}(R)/(GM_{*,\rm tot}/Re)$ evaluated at $R = R_e$ as a function of Sérsic index, n.

For indices $n \leq 5$, applicable for elliptical galaxies with stellar masses $M_{*,\rm tot} \sim 10^8 M_\odot$–$10^{11} M_\odot$, the dimensionless aperture dispersion is $0.36 \leq \widetilde{\sigma}_{\rm ap}(R_e) \leq 0.43$, compared to $\widetilde{\sigma}_{\rm ap}(R_e) \simeq 0.389$ for the Hernquist model. The model curves for $\sigma_{\rm ap}(R_e)$ in Figure 2.11 are therefore vulnerable at only the $< 10\%$ level to a bias resulting from the use of a Hernquist profile. This bias will be a slight tilt, due to the correlation between Sérsic index, n, and $M_{*,\rm tot}$ (cf. §1.2.3). The most massive ellipticals, with $M_{*,\rm tot} \geq 2 - 3 \times 10^{11} M_\odot$, are best described by higher $n \sim 5$–7, for which $\sigma_{\rm ap}(R_e)/(GM_{*,\rm tot}/R_e)^{1/2} \simeq 0.43$–$0.49$ rather than 0.389 (for Hernquist).

One potential reason for the disagreement between the model curves and data for $M_{*,\rm tot} < 10^{10} M_\odot$ that needs to be checked is the fact that the ACSVCS velocity dispersions are measured inside $R_e/8$, rather than R_e (P. côté, priv. comm.). Figure 2.14 shows the ratio $\sigma_{\rm ap}(R_e/8)/\sigma_{\rm ap}(R_e)$ as a function of Sérsic index, n. The solid red line corresponds to a self-consistent sphere of Hernquist stars only [$F_{\rm ej} = 0$ and $1/f_*(r) = 0$], with $\sigma_{\rm ap}(R_e/8)/\sigma_{\rm ap}(R_e) \simeq 1.07$. In terms of the curves then, calculating the velocity dispersion at $R_e/8$ instead of R_e would shift them upwards by $\sim 7\%$, even further away from the ACSVCS data for low-mass systems. For Sérsic models with $n \lesssim 4$, corresponding to $M_{*,\rm tot} \lesssim 10^{10}\, M_\odot$, the two aperture dispersions are the same to within $\sim 10\%$, a similar difference as for Hernquist. Therefore, accounting for the difference of within which radius $\sigma_{\rm ap}$ is measured does not explain the disagreement between the curves and data for $M_{*,\rm tot} < 10^{10}\, M_\odot$.

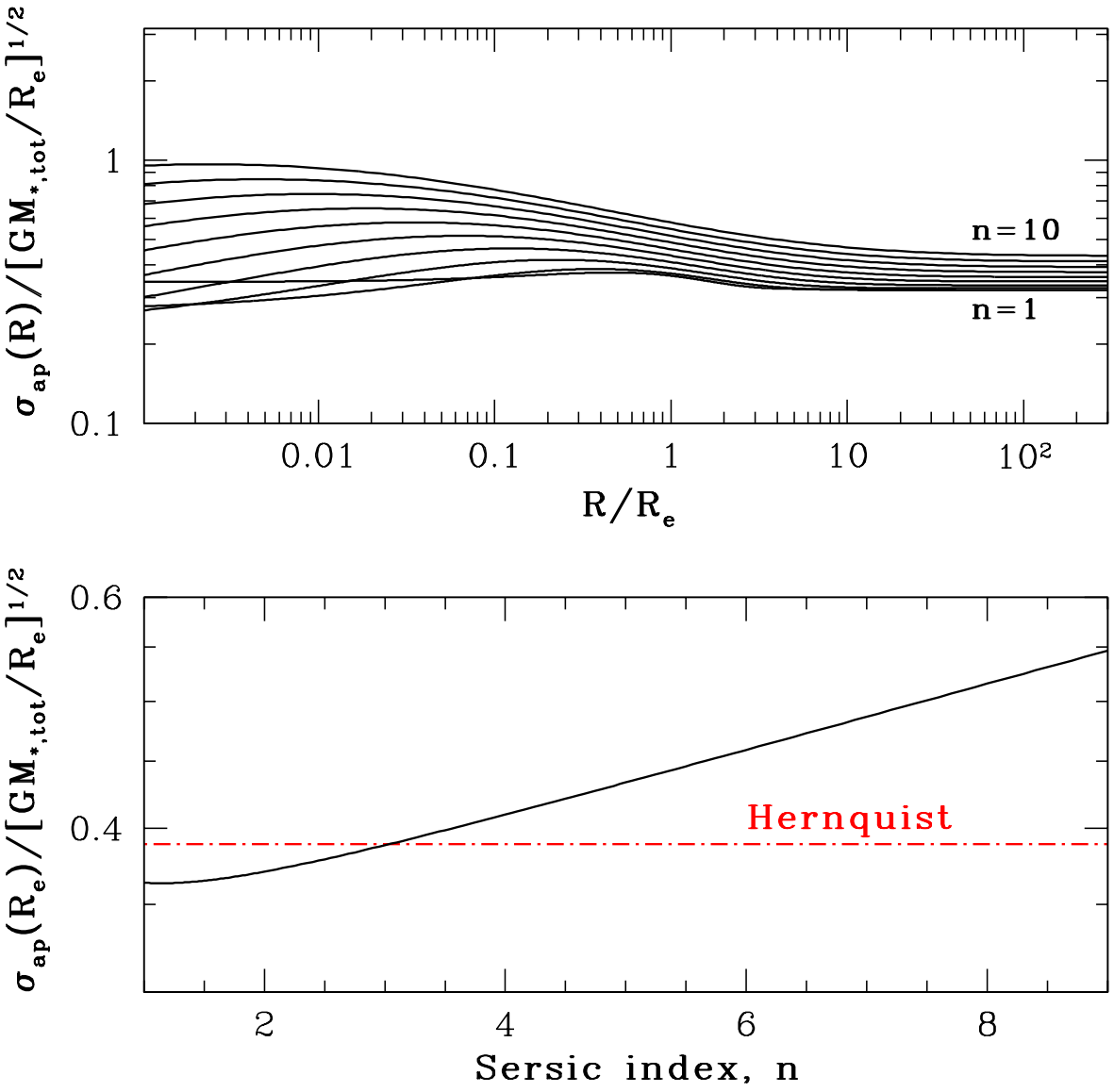

Figure 2.13: *Top panel:* Stellar aperture velocity dispersion profiles as a function of R/R_e, for various Sérsic profiles. The different curves correspond to integer values of the Sérsic index, $n = 1$–10. *Bottom panel:* The stellar aperture velocity dispersion, $\sigma_{\rm ap}(R)/\sqrt{GM_{*,\rm tot}/R_e}$, evaluated at $R = R_e$, as a function of Sérsic index, n. The broken red line shows the value for a self-consistent Hernquist sphere of stars — $\sigma_{\rm ap}(R_e)/\sqrt{GM_{*,\rm tot}/R_e} \simeq 0.389$.

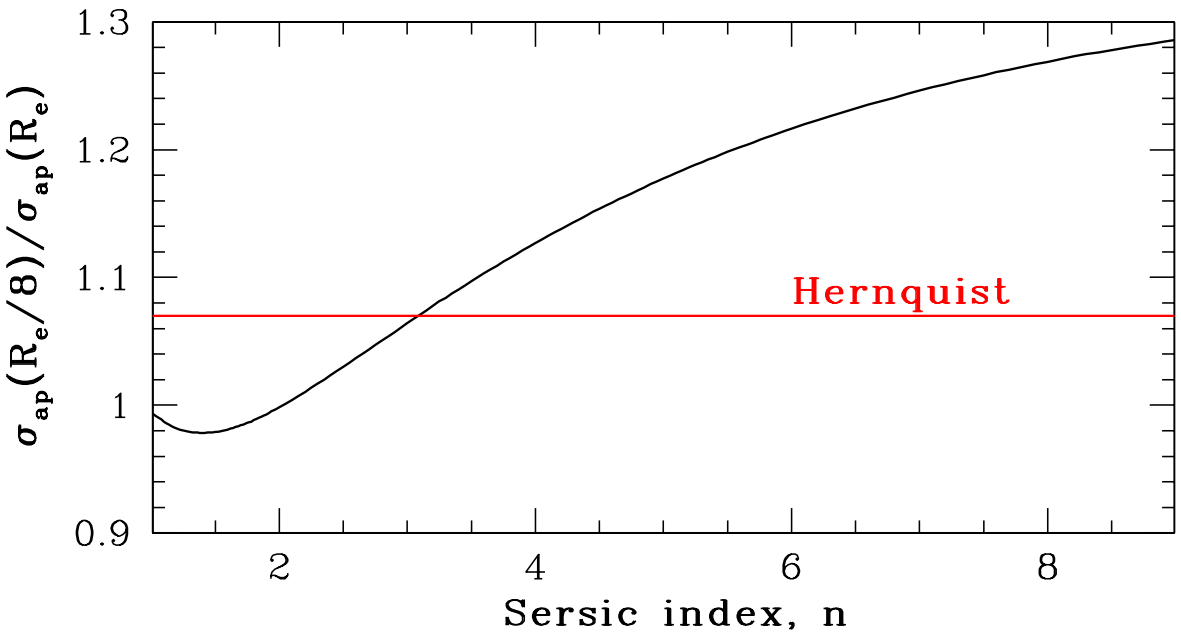

Figure 2.14: The ratio of the aperture stellar velocity dispersion measured inside $R_e/8$ to $\sigma_{\rm ap}(R_e)$, versus Sérsic index, n. The solid red line corresponds to $\sigma_{\rm ap}(R_e/8)/\sigma_{\rm ap}(R_e) \simeq 1.07$, the value for a Hernquist stellar distribution.

2.2.6.4 Stellar ejecta

The choice of a Hernquist profile to describe the stellar distribution in all galaxies is obviously not very accurate for low mass galaxies, whose surface brightness profiles are closer to exponential. However, as discussed above, accounting for this in the models would alter the stellar velocity dispersions by $< 10\%$. There are more important physical considerations that affect the accuracy with which the models can describe the lowest mass galaxies, with $M_{*,\rm tot}$ less than a few $\times 10^9 M_\odot$.

To calculate the stellar velocity dispersions, $\sigma_{\rm ap}(R_e)$, the stellar ejecta were assumed to be retained near the bottom of any galaxy's potential well. However, supernova-driven winds are likely to actually expel the ejecta from many dwarf ellipticals to far beyond the stellar distribution (Dekel & Silk 1986). In this case, it is more appropriate to have $F_{\rm ej} = 0$ in equations (2.44) and (2.49). Making this change lowers the model $\sigma_{\rm ap}(R_e)$ values by $\sim 30\%$ at a given $M_{*,\rm tot}$.

This expected limiting physical behaviour of the stellar ejecta suggests an ejecta-to-stellar mass fraction, $F_{\rm ej}$, that ought to depend on total stellar mass. Presumably, such a dependency should lead to $F_{\rm ej} \simeq 0.72$ for the largest galaxies, where supernova driven winds are unable to lift the ejecta from the bottom of the potential wells. $F_{\rm ej}$ would then decrease with $M_{*,\rm tot}$, tending to zero for the lowest mass systems. An ad-hoc $F_{\rm ej}$–$M_{*,\rm tot}$ relation given by

$$F_{\rm ej} = 0.72 \left(\frac{M_{*,\rm tot}/10^{10} M_\odot}{1 + M_{*,\rm tot}/10^{10} M_\odot} \right) \tag{2.50}$$

satisfies these high- and low-mass limits for the mass ejecta. As an ad-hoc relation, this only has any sort of physical justification in the limiting cases just outlined.

Figure 2.15 shows $\sigma_{\rm ap}(R_e)$ versus $M_{*,\rm tot}$. Data are from ATLAS (green squares), ACSVCS (magenta triangles) and SDSS (red circles). All three curves are obtained from the Jeans modelling (§2.2.6.1) for a Dehnen & McLaughlin halo. Both NFW and Hernquist are very similar. The solid blue line assumes a constant ejecta-to-stellar mass fraction of $F_{\rm ej} \simeq 0.72$, with the solid black line corresponding to $F_{\rm ej} = 0$. The dashed line assumes $F_{\rm ej}$ depends on $M_{*,\rm tot}$ as described by equation (2.50). The lower-

mass galaxy data (mainly from the ACSVCS sample) are clearly better described by the model with $F_{\rm ej} = 0$, as expected. Over the mass range shown, the data are well described by the curve that incorporates the ad-hoc $F_{\rm ej}$ dependence on total stellar mass. From this point onwards, the $\sigma_{\rm ap}(R_e)$–$M_{*,\rm tot}$ model curve at $z = 0$ assumes $F_{\rm ej}$ depends on $M_{*,\rm tot}$ as in equation (2.50).

On the other hand, these same galactic winds may cause changes in the central structures of the dark matter halos of dwarfs, from initially steep density cusps, to shallower profiles, perhaps closer to the Burkert (1995) model (Burkert & Silk 1997; Pontzen & Governato 2012). Subsequent tidal stripping could have led to further, larger-scale modifications of the halos in many cases. Substantial, systematic alterations to the dark matter density profiles could well impact the inferred values for $V_{\rm d,pk}$, $f_*(R_e)$ and $\sigma_{\rm ap}(R_e)$ from a given $M_{*,\rm tot}$. The relation between $M_{*,\rm tot}$ and $M_{\rm d,vir}$, ultimately given by equation (2.26), could also be in error when extrapolated to halo masses with $M_{\rm d,vir} \leq 10^{11} M_\odot$, the lower limit in the Moster et al. (2010) semi-analytical models (Behroozi, Wechsler & Conroy 2013). All in all, more comprehensive modelling is required to be confident in any details of the models for systems with stellar masses below $10^{10} M_\odot$.

2.2.6.5 Intracluster baryons

As discussed in §2.2.3, the scaling relations presented here do not take into account any baryonic mass in intracluster light, X-ray gas or in off-centre cluster galaxies. Any effects on the results will be most significant for the largest galaxies, associated with cluster-sized dark matter halos. These "extra" baryons are expected to be spatially distributed like the dark matter, rather than the stars in the central galaxy. As such, they can be included in the full Jeans-equation derivation of $\sigma_{\rm ap}(R_e)$ by simply increasing the dark matter mass $M_d(r)$ by a constant factor at all radii, or equivalently, decreasing $f_*(r)$ by the same factor. However, equation (2.49) [on p.123] provides a convenient way to estimate any possible affects on the model stellar velocity dispersions.

The correction factor will be largest if the global baryon fraction in a cluster is

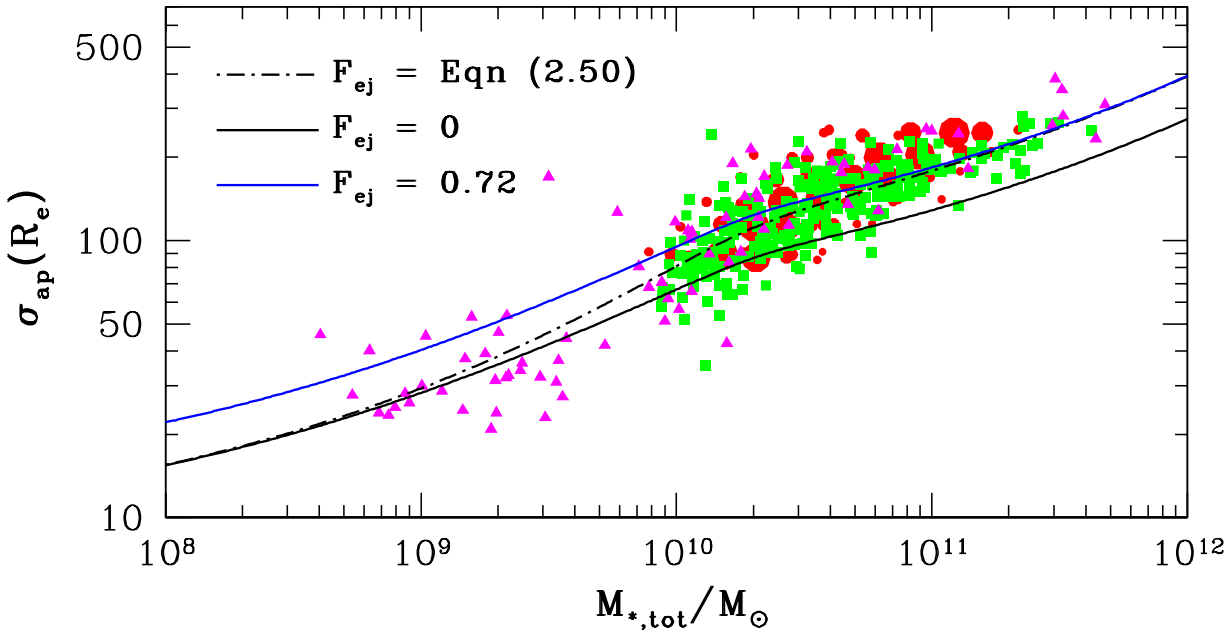

Figure 2.15: Stellar velocity dispersion, $\sigma_{\rm ap}(R_e)$, within an aperture of radius R_e as a function of $M_{*,\rm tot}$. Green squares are from the ATLAS survey, and red circles are from the summary data for $\sim 16,000$ galaxies in the SDSS sample (Graves et al. 2007a,b). The circle size is proportional to the number of galaxies in each σ bin from the Graves et al. papers. The magenta triangles are from the ACSVCS data set. The solid blue curve is for $F_{\rm ej} \simeq 0.72$ and assumes a Dehnen & McLaughlin halo — identical to Figure 2.11. The solid black line corresponds to $F_{\rm ej} = 0$, and again assumes a Dehnen & McLaughlin halo. The broken line corresponds to the ad-hoc relation between $F_{\rm ej}$ and $M_{*,\rm tot}$, introduced in equation (2.50).

equal to the cosmic average value and only a negligible, trace amount is bound up in the central galaxy itself. It will therefore be less than $(1 - \Omega_{\rm b,0}/\Omega_{\rm m,0})^{-1} \simeq 1.18$ (for *Planck* 2013 cosmology). This could plausibly be the case in the largest cluster halos, with $M_{\rm d,vir} \sim 10^{15} M_{\odot}$ (Gonzalez et al. 2013). However, as discussed in §2.2.3, the global baryon fraction is found to decrease systematically with decreasing halo mass (McGaugh et al. 2010; Zhang et al. 2011; Gonzalez et al. 2013). In fact, on the scales of individual galaxies, it should not be significantly larger than the mass fraction in stars and stellar ejecta (see Figure 2.7), already fully accounted for in the models.

The maximum effect on $\sigma_{\rm ap}(R_e)$ implied by equation (2.49) is obtained by comparing the value of the right-hand side with $(1 + F_{\rm ej}) = 1/0.58$ and $f_*(R_e) = 0.5$ (the lowest value in any of the model curves at $M_{\rm d,vir} \simeq 10^{15} M_{\odot}$), to the value using $f_*(R_e) = 0.5/1.18$ instead. The result is an increase of $< 5\%$ in the velocity dispersion, similar to the maximum effect on the values for the halo virial radii in §2.2.3.

2.2.6.6 Dark matter halo properties versus $\sigma_{\rm ap}(R_e)$ at $z = 0$

Now that average scalings relating galaxy and dark matter halo properties to the total stellar mass have been obtained, it is possible to consider any two properties plotted against one another. Looking forward to Chapter 3, it is useful here to consider the dark matter properties at $z = 0$ as functions of stellar velocity dispersion (as well as stellar mass). It is global properties of the dark matter at *higher* redshifts that are expected to be connected to the SMBH mass. For example, McQuillin & McLaughlin (2012) relates $M_{\rm BH}$ to $V_{\rm d,pk}(z)$. It should be emphasised that $V_{\rm d,pk}(z)$ refers to the dark matter circular-speed peak when blow-out occurred in the protogalaxy, generally at redshifts $z > 0$, and not the $V_{\rm d,pk}$ from §2.2.4, the $z = 0$ circular-speed peak.

Figure 2.16 shows the dark matter virial mass, $M_{\rm d,vir}$ (top panel), and the peak of dark matter circular speed curve, $V_{\rm d,pk}$ (bottom panel), as functions of $\sigma_{\rm ap}(R_e)$. In both panels, the different lines correspond to the four dark matter halos considered throughout the modelling, with the line colours indicated at the top of the Figure. The dashed black line in the bottom panel shows $V_{\rm d,pk} = \sqrt{2}\sigma_{\rm ap}(R_e)$. For $\sigma_{\rm ap}(R_e) < 200\,{\rm km\,s^{-1}}$,

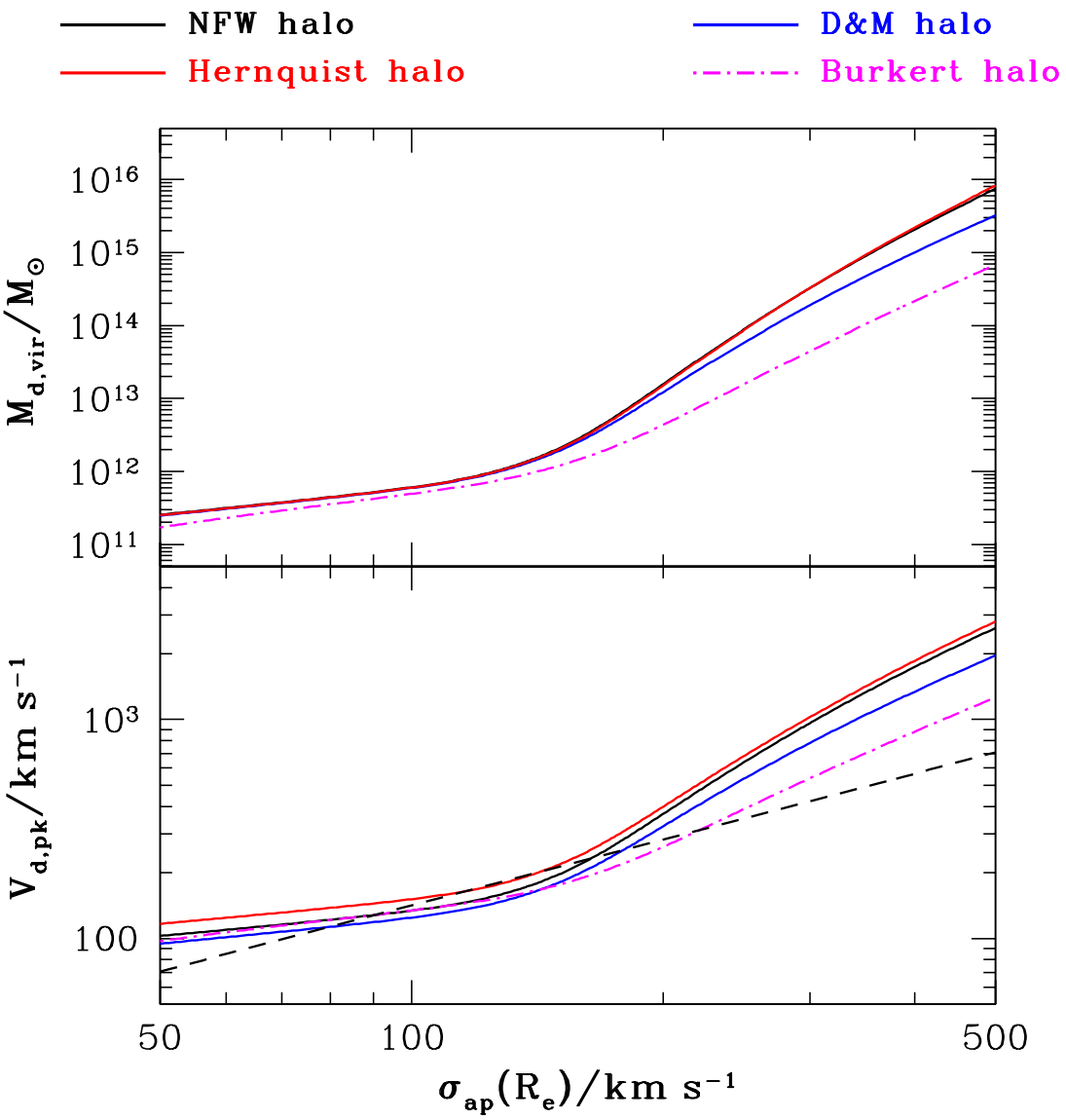

Figure 2.16: *Top panel*: Dark matter virial mass, $M_{\rm d,vir}$, at $z = 0$, as a function of aperture stellar velocity dispersion, $\sigma_{\rm ap}(R_e)$, also at $z = 0$. The different curves represent the four dark matter halos, with colours indicated at the top of the Figure. *Bottom panel*: Peak of the dark matter circular-speed, $V_{\rm d,pk}$, at $z = 0$, again as a function of $\sigma_{\rm ap}(R_e)$, for the four dark matter halos considered in these models. The dashed black line is for $V_{\rm d,pk} = \sqrt{2}\sigma_{\rm ap}(R_e)$, and is shown for reference only.

this simplistic substitution is actually not a bad representation of the scaling relations for all four halos.

For intermediate to low velocity dispersions ($70\,\mathrm{km\,s^{-1}} \lesssim \sigma_{\rm ap}(R_e) \lesssim 200\,\mathrm{km\,s^{-1}}$), the calculated values for $V_{\rm d,pk}$ are within $\sim 30\%$ (depending on dark matter halo) of the value implied by the simple substitution. However, $V_{\rm d,pk} = \sqrt{2}\sigma_{\rm ap}(R_e)$ is clearly a poor substitute for the implied relation between the two velocities at $z = 0$ for $\sigma_{\rm ap}(R_e) \geq 200\mathrm{km\,s^{-1}}$, corresponding to the velocity dispersion range of the majority of current SMBH data. At the largest $\sigma_{\rm ap}(R_e)$, this substitution under-estimates $V_{\rm d,pk}$ (relative to the scaling relations) by up to factors of $\sim$ 3–4. As with the plots versus $M_{*,\rm tot}$ earlier, the upward inflection in $M_{\rm d,vir}$ and $V_{\rm d,pk}$ is due to the rapid decrease in $f_{*,\rm vir}$ beyond $M_{*,\rm tot} \sim 10^{11} M_\odot$ [equivalently $\sigma_{\rm ap}(R_e) \sim 150\mathrm{km\,s^{-1}}$]. It is unsurprising that the $V_{\rm d,pk}$ values for the most massive galaxies far exceed the stellar velocity dispersions since these dark matter halos correspond to entire clusters.

2.2.7 Comparing to individual systems

Properties from the literature are collected for a few galaxies and halos spanning the range of mass and stellar velocity dispersion covered by local galaxy samples used to define empirical SMBH M–σ relations. Numerical values are then extracted from the $z = 0$ scalings obtained throughout the Chapter to compare with the measurements.

2.2.7.1 Stellar and halo properties from the literature

Table 2.1 lists observed stellar properties of the Milky Way, M87 (at the centre of Virgo subcluster A), M49 (at the centre of Virgo B) and NGC 4889 (in the Coma Cluster). Properties of the dark matter halos are also given, from dynamical modelling in the literature. The analysis is clearly not meant to describe disc galaxies, but the Milky Way is included as a useful check on the implications for $\sim L^\star$ galaxies in general.

The Milky Way In the first row of Table 2.1, the total stellar mass, the radius r_{200} of mean overdensity $\Delta \equiv 200$ and the dark-matter mass $M_{\rm d,200}$ inside this are all taken from McMillan (2011). Combining his best-fitting NFW concentration, $r_{200}/r_{-2} \simeq 9.55$, with his values of $M_{\rm d,200}$ and r_{200} plus $r_{\rm pk}/r_{-2} = 2.16258$ for an NFW halo, yields $r_{\rm pk} \simeq 52\,{\rm kpc}$ and $V_{\rm d,pk} \simeq 185\,{\rm km\,s^{-1}}$. These are consistent with separate modelling of the Milky Way by Dehnen, McLaughlin & Sachania (2006).

The second row of Table 2.1 contains the total stellar mass of the Milky Way bulge only, according to McMillan (2011). He does not record the effective radius of the bulge or the aperture dispersion inside it, so we take $R_e \simeq 2.7$ kpc from Freeman (1985) and $\sigma_{\rm ap}(R_e) \simeq 103$ km s^{-1} from McConnell & Ma (2013).

M87 and M49 For M87 and M49, Table 2.1 quotes total stellar masses based on three different sources: the ATLAS$^{\rm 3D}$ survey (Cappellari et al. 2011), the ACSVCS (Chen et al. 2010) and McConnell & Ma (2013). The original authors give total luminosities, to which the mass-to-light ratios from Maraston (2005) models have been applied, for a Kroupa (2001) IMF and a stellar age of 9 Gyr: $M_{*,\rm tot}/L_K \simeq 0.88\,M_\odot\,L_\odot^{-1}$ for the ATLAS$^{\rm 3D}$ luminosity, $M_{*,\rm tot}/L_z \simeq 1.7\,M_\odot\,L_\odot^{-1}$ for the ACSVCS value and $M_{*,\rm tot}/L_V \approx 3.15\,M_\odot\,L_\odot^{-1}$ for McConnell & Ma (2013). Both galaxies have R_e values in the ATLAS$^{\rm 3D}$ survey and the ACSVCS, and velocity dispersions in ATLAS and McConnell & Ma (2013).

McLaughlin (1999) and Côté et al. (2001) fitted the kinematics of stars and globular clusters in M87, plus the kinematics of Virgo-cluster galaxies and the total mass profile derived from intracluster X-ray gas, with a two-component mass model comprising the stars (plus remnants and stellar ejecta) in the body of M87 and an NFW dark-matter halo with $r_{200} \simeq 1.55$ Mpc and $M_{\rm d,200} \simeq 4.2 \times 10^{14}\,M_\odot$. This clearly identifies the dark matter in and around M87 with the halo of the entire Virgo A subcluster. McLaughlin (1999) and Côté et al. (2001) have an NFW concentration of $r_{200}/r_{-2} = 2.8 \pm 0.7$ for the M87/Virgo A halo, so (with $r_{\rm pk}/r_{-2} = 2.16258$ again) $r_{\rm pk} \sim 1.2$ Mpc and $V_{\rm d,pk} \simeq 1100$ km s^{-1}.

For M49/Virgo B, Côté et al. (2003) similarly use a two-component mass model consisting of the galaxy's stars plus a single NFW dark-matter halo, to fit the stellar and globular cluster kinematics on 50-kpc scales and the X-ray mass profile out to $\sim$ Mpc radii. The Côté et al. (2003) analysis implies $r_{200} \simeq 950$ kpc with $M_{\rm d,200} \simeq 9.4 \times 10^{13}\ M_\odot$, and $r_{200}/r_{-2} \simeq 4.8$. The dark-matter circular speed therefore peaks at $r_{\rm pk} \simeq 425$ kpc, where $V_{\rm d,pk} \simeq 710$ km s^{-1}.

NGC 4889 NGC 4889 is the brightest galaxy in Coma and not far from the nominal central galaxy, NGC 4874. According to McConnell & Ma (2013), NGC 4889 has $L_V \simeq 3.0 \times 10^{11} L_\odot$ and hence (for $M_*/L_V \approx 3.15\ M_\odot\, L_\odot^{-1}$ from the Maraston (2005) population-synthesis models) $M_{*,\rm tot} \approx 9.5 \times 10^{11}\ M_\odot$. It is at the uppermost end of the range of stellar masses plotted for the $\sigma_{\rm ap}(R_e)$–$M_{*,\rm tot}$ relation (but it does not appear on those plots since it is not in the ATLAS$^{\rm 3D}$ survey), and it hosts one of the largest supermassive black holes yet measured: $M_{\rm BH} = (2.1 \pm 1.6) \times 10^{10}\ M_\odot$ (McConnell et al. 2011; McConnell et al. 2012). The effective radius $R_e = 27$ kpc and velocity dispersion $\sigma_{\rm ap}(R_e) = 347$ km s^{-1} in Table 2.1 are from McConnell & Ma (2013) and McConnell et al. (2011, McConnell et al. (2012).

The global dark matter properties of the Coma Cluster are taken from dynamical modelling by Lokas & Mamon (2003). They give values for $r_{\rm vir}$ and $M_{\rm d,vir}$, rather than r_{200} and $M_{\rm d,200}$ like the other galaxies in Table 2.1, and a best-fitting NFW concentration of $r_{\rm vir}/r_{-2} = 9.4$. Together these imply $r_{\rm pk} \simeq 670$ kpc and $V_{\rm d,pk} \simeq 1585$ km s^{-1}.

2.2.7.2 Comparison to models

Taking the total stellar mass $M_{*,\rm tot}$ as a starting point for each of the systems in Table 2.1, the other stellar and halo properties are estimated from the scaling relations developed in this Chapter. Table 2.2 shows the results for R_e, $\sigma_{\rm ap}(R_e)$, $V_{\rm d,pk}$, $r_{\rm pk}$, $M_{\rm d,200}$ or (for NGC 4889/Coma) $M_{\rm d,vir}$, and r_{200} or (for NGC 4889/Coma) $r_{\rm vir}$.

Table 2.1: Values of stellar and dark matter halo properties at $z = 0$, taken from various sources in the literature. References: 1 – McMillan (2011), 2 – Freeman (1985), 3 – McConnell & Ma (2013), 4 – Cappellari et al. (2011), 5 – Cappellari et al. (2013a), 6 – Chen et al. (2010), 7 – McLaughlin (1999), 8 – Côté et al. (2003), 9 – Lokas & Mamon (2003).

Galaxy	$M_{*,\rm tot}$ ($M_\odot$)	R_e (kpc)	ref.	$\sigma_{\rm ap}(R_e)$ (km s^{-1})	ref.	$V_{\rm d,pk}$ (km s^{-1})	$r_{\rm pk}$ (kpc)	$M_{\rm d,200}$ or $M_{\rm d,vir}$ ($M_\odot$)	r_{200} or $r_{\rm vir}$ (kpc)	ref.
Milky Way	6.4×10^{10}	–	1	–	–	190	45	1.26×10^{12}	230	1
MW bulge	9.0×10^{10}	2.7 ± 0.3	1,2	103 ± 20	3	–	–	–	–	–
M87	2.9×10^{11}	6.8 ± 1.5	4	264 ± 13	5	1100	1200	4.2×10^{14}	1550	6
	3.2×10^{11}	8.7 ± 1.1	7	–	–	–	–	–	–	–
	3.7×10^{11}	–	3	324^{+28}_{-16}	3	–	–	–	–	–
M49	4.2×10^{11}	7.9 ± 1.7	4	250 ± 13	5	710	425	9.4×10^{13}	950	8
	4.7×10^{11}	13.4 ± 1.1	7	–	–	–	–	–	–	–
	3.7×10^{11}	–	3	300 ± 15	3	–	–	–	–	–
NGC4889	9.5×10^{11}	27 ± 2.0	3	347 ± 17	3	1585	670	1.2×10^{15}	2900	9

$L^\star$ galaxies: $\sigma_{\rm ap}(R_e) \sim$ 100–150 km s^{-1} For $M_{*,\rm tot} \simeq 6.4 \times 10^{10} M_\odot$ (the *total* Milky Way mass), the scalings give the stellar effective radius as $R_e \simeq 3$ kpc and the velocity dispersion as $\sigma_{\rm ap}(R_e) \simeq 160$ km s^{-1}. This dispersion is higher than the value typically used to put the Milky Way on the black hole M–σ relation: for example, McConnell & Ma (2013) take $\sigma_{\rm ap}(R_e) = 103$ km s^{-1} for the Galaxy. However, this value is meant to represent the bulge only. For the *bulge* mass of $M_{*,\rm tot} \simeq 9 \times 10^9\ M_\odot$, the relations give $R_e \simeq 1.4$ kpc and $\sigma_{\rm ap}(R_e) \simeq 90$ km s^{-1}.

For the total Galactic stellar mass of $6.4 \times 10^{10} M_\odot$ and assuming an NFW halo, the scalings lead to a peak circular speed of $V_{\rm d,pk} \simeq 200$ km s^{-1}, occurring at $r_{\rm pk} \simeq 75$ kpc. Using equations (2.8), (2.27) and (2.25) to go from the virial radius implied by $M_{*,\rm tot}$ to the radius of mean overdensity $\Delta = 200$ leads to $M_{\rm d,200} \simeq 2 \times 10^{12} M_\odot$ and $r_{200} \simeq 270$ kpc. For the mass of the bulge alone, $M_{*,\rm tot} \simeq 9 \times 10^9 M_\odot$, the average trends imply $V_{\rm d,pk} \sim 120$ km s^{-1}, $r_{\rm pk} \sim 35$ kpc, $M_{\rm d,200} \sim 3.6 \times 10^{11} M_\odot$ and $r_{200} \sim 150$ kpc.

M87 and M49: $\sigma_{\rm ap}(R_e) \sim$ 250 km s^{-1} For each of these galaxies, the mean of $M_{*,\rm tot}$ from the three different values in Table 2.1 is used. Thus, $M_{*,\rm tot} = 3.3 \times 10^{11}\ M_\odot$

Table 2.2: Stellar and dark matter halo properties at $z = 0$ according to the scaling relations. For each galaxy, the starting point is $M_{*,\rm tot}$, taken from the literature.

Galaxy	$M_{*,\rm tot}$ ($M_\odot$)	R_e (kpc)	$\sigma_{\rm ap}(R_e)$ (km s^{-1})	$V_{\rm d,pk}$ (km s^{-1})	$r_{\rm pk}$ (kpc)	$M_{\rm d,200}$ or $M_{\rm d,vir}$ ($M_\odot$)	r_{200} or $r_{\rm vir}$ (kpc)
Milky Way	6.4×10^{10}	3.0	160	200	75	2.0×10^{12}	270
MW bulge	9.0×10^{9}	1.4	90	120	35	3.6×10^{11}	150
M87	3.3×10^{11}	8.0	245	600	330	6.0×10^{13}	830
M49	4.2×10^{11}	9.3	265	720	420	1.0×10^{14}	1000
NGC 4889	9.5×10^{11}	15.2	345	1285	925	8.0×10^{14}	2450

for M87, and $M_{*,\rm tot} = 4.2 \times 10^{11}\ M_\odot$ for M49. The parametrisation of R_e versus $M_{*,\rm tot}$ in §2.2.2 then gives the values recorded in Table 2.2, which broadly agree with the measurements of R_e. The model values in Table 2.2 for $\sigma_{\rm ap}(R_e)$, $V_{\rm d,pk}$, $r_{\rm pk}$, $M_{\rm d,200}$ and r_{200} assume an NFW halo around each galaxy (as the analyses from the literature do). The predicted velocity dispersions compare well to the measurements for M87 and M49 in the ATLAS$^{\rm 3D}$ survey but not quite as well to the values recorded by McConnell & Ma (2013), which are 20% higher.

The value of r_{200} for M87/Virgo A in Table 2.1, from McLaughlin (1999), is $\simeq$80% bigger than the one in Table 2.2, implied by the scaling relations. McLaughlin's $M_{\rm d,200}$ is consequently larger by about a factor of $1.8^3 \simeq 6$. Similarly, the circular-speed curve of the halo in McLaughlin (1999) peaks at $r_{\rm pk} \sim 1.2$ Mpc (with a very large uncertainty) rather than $r_{\rm pk} \simeq 330$ kpc as expected here, and it has $V_{\rm d,pk} \simeq 1100$ km s^{-1} rather than $V_{\rm d,pk} \simeq 600$ km s^{-1}.

These discrepancies for M87/Virgo A may simply reflect the inevitable scatter in the properties of individual systems around the typical values given by the average trend lines. For M49/Virgo B, all of the halo properties in Table 2.2 obtained from the scalings are remarkably close to the values in Table 2.1 from Côté et al. (2003).

NGC 4889: $\boldsymbol{\sigma_{\rm ap}(R_e) \sim 350\,{\rm km\,s^{-1}}}$ For $M_{*,\rm tot} = 9.5 \times 10^{11}\ M_\odot$, the scalings give $R_e = 15.2$ kpc and (assuming an NFW halo) $\sigma_{\rm ap}(R_e) \simeq 345$ km s^{-1}. The velocity dispersion agrees with the value in McConnell et al. (2011, McConnell et al. (2012),

although the effective radius is smaller than their adopted 27 kpc. Further, the virial and halo mass are estimated to be $r_{\rm vir} \simeq 2.45$ Mpc and $M_{\rm d,vir} \simeq 8.0 \times 10^{14}\ M_{\odot}$, which compare well to the values in Table 2.1 determined by Lokas & Mamon (This is even though NGC 4889 is not precisely at the centre of the Coma Cluster).

Assuming an NFW halo density profile, the average trends imply $r_{\rm pk} \simeq 925$ km s^{-1} and $V_{\rm d,pk} \simeq 1285$ km s^{-1} for the peak of the dark-matter circular speed in NGC 4889/Coma—different by $\sim$30% from the Lokas & Mamon (2003) numbers. Comparing to the peak radii and speeds above for M87/Virgo A and M49/Virgo B emphasises the clear visual impression given by Figures 2.6 (bottom panel) and 2.8 (bottom panel): In large galaxies $V_{\rm d,pk}$, along with $M_{\rm d,vir}$, is a much more sensitive function of galaxy stellar mass than the stellar $\sigma_{\rm ap}(R_e)$ is. (This follows directly from the steep decline at high masses in the cosmological connection between $M_{*,\rm tot}$ and $M_{\rm d,vir}$ adopted from Moster et al. 2010.) It therefore seems natural to expect much more scatter and many more apparent "outliers" in $M_{\rm BH}$ among very massive galaxies, if SMBH masses are connected fundamentally to the global properties of dark-matter halos rather than to stellar velocity dispersions directly.

2.2.8 Total circular speeds

Many authors have attempted to connect the total (stars and dark matter) circular-speed, V_c (at various radii depending on the author), to the stellar aperture velocity dispersion, usually measured within R_e or $R_e/8$ (Gerhard et al. 2001; Ferrarese 2002; Padmanabhan et al. 2004; Pizzella et al. 2005; Couteau et al. 2007; Dutton et al. 2010; Volonteri, Natarajan & Gültekin 2011). This is often used as a "stepping stone" to deriving a connection between $M_{\rm BH}$ and the halo mass, normally defined to be $M_{\rm d,200}$ or $M_{\rm d,vir}$ (Ferrarese 2002; Shankar et al. 2006; Bandara, Crampton & Simard 2009; Dutton et al. 2010; Volonteri, Natarajan & Gültekin 2011; Bogdán & Goulding 2015). Broadly speaking, $M_{\rm BH}$ and halo mass are connected in the literature by combining an $M_{\rm BH}$–σ relation with σ–V_c and V_c–$M_{\rm DM}$ relations (cf. §1.3.3.5). It is usually assumed that the total circular-speed curves are flat out to the virial radius (or r_{200}) in order

to connect $M_{\rm BH}$ and halo mass. However, this is not necessarily the case given the dependence on $M_{*,\rm tot}$ of $f_{*,\rm vir}$, $M_{\rm d,vir}$ and $\sigma_{\rm ap}(R_e)$ in the average trends obtained in this Chapter.

Before looking at how V_c at various radii and $\sigma_{\rm ap}(R_e)$ are connected, the total circular-speed profiles, $V_c(r)$, need to be considered. This is to see if the assumption of a flat circular speed curve (out to $r_{\rm vir}$) is realistic. As will be discussed, these profiles are fully determined by choosing a dark matter halo model, a stellar distribution (taken here to be Hernquist) and specifying a total stellar mass, $M_{*,\rm tot}$. $V_c(r)$ can then be evaluated at any given radius, and connected to the stellar or dark matter halo properties at $z = 0$. Thus, average trends between V_c and any property are obtained, once again with inevitable scatter around them.

2.2.8.1 Circular-speed profiles

The total circular speed profile can be written in dimensionless form by normalising to $GM_{*,\rm tot}/R_e$:

$$\frac{V_c^2(r)}{[GM_{*,\rm tot}/R_e]} = \frac{1}{r/R_e}\left[\frac{M_*(r)}{M_{*,\rm tot}} + \frac{M_d(r)}{M_{*,\rm tot}}\right] = \frac{M_*(r)/M_{*,\rm tot}}{r/R_e}\left[1 + \frac{1}{f_*(r)}\right]. \qquad (2.51)$$

The dimensionless stellar mass profile, $M_*(r)/M_{*,\rm tot}$ is known for a Hernquist profile as a function of r/R_e. The function $f_*(r)$ is the stellar-to-dark matter mass ratio as a function of radius. Once a dark matter halo model and a stellar distribution have been chosen, $f_*(r)$ is fixed by $M_{*,\rm tot}$. Specifying $M_{*,\rm tot}$ gives a value for $f_{*,\rm vir}$. The stellar mass profile can be evaluated at any r, since both R_e and $r_{\rm vir}$ are also determined by $M_{*,\rm tot}$. The same is true for the dark matter mass profiles, as the halo concentration (and hence r_{-2}) are fixed once $M_{*,\rm tot}$ has been chosen.

Figure 2.17 shows the total circular-speed profiles, $V_c(r)$, as a function of r/R_e for a range of $M_{*,\rm tot}$ values. The different line colours correspond to $M_{*,\rm tot} = 10^9 M_\odot$ (black line), $10^{10} M_\odot$ (blue line), $10^{11} M_\odot$ (green line) and $10^{12} M_\odot$ (red line). This range of stellar mass covers the majority of the data used for the scaling relations in this Chapter, as well as encompassing the mass range used to define the $M_{\rm BH}$–bulge

property correlations. All of the curves shown in the Figure are for Hernquist stars and a Dehnen & McLaughlin dark matter halo. The NFW and Hernquist halos are qualitatively the same. The non-monotonic behaviour seen between different $M_{*,\mathrm{tot}}$ is a reflection of how the virial stellar-to-dark matter mass ratio varies with stellar mass (i.e. the top panel of Figure 2.6).

There has been some debate in the literature surrounding the shapes of the total circular-speed profiles for elliptical galaxies. It has been speculated that there is a "conspiracy" between luminous and dark matter to produce flat circular-speed curves over a large range in radius(Kronawitter et al. 2000; Gerhard et al. 2001; Koopmans et al. 2006; Gavazzi et al. 2007; Koopmans et al. 2009). For a sample of 21 ellipticals, Kronawitter et al. (2000) calculate the density and potential of the luminous matter from the surface brightness profile. They specify a *total* gravitational potential, consisting of an isothermal dark matter component and a luminous component. From this, they find total circular-speed curves that are consistent with being flat for $0.3R_e \lesssim R \lesssim 1$–$2.5R_e$, where R is a projected radius.

More recently, Dutton et al. (2010) considered the optical circular-speed, V_{opt}, defined to be the total circular speed inside an effective radius for early-types, $V_c(R_e)$, whereas for late-types they use 2.2 disc scale lengths as the defining radius, $V_{\mathrm{opt}} \equiv V_{2.2}$. Taking $M_{*,\mathrm{tot}}$ as a starting point, they obtain V_{opt} for the early-types by combining a fit to SDSS data from Gallazzi et al. (2007) for $\sigma_{\mathrm{ap}}(R_e)$–$M_{*,\mathrm{tot}}$ [equation (2.48)], with a result from Padmanabhan et al. (2004) that $v_c(R_e) = 1.5\sigma_{\mathrm{ap}}(R_e)$ [cf. §2.2.8.2]. For the late-types, Dutton et al. (2010) use a connection between $V_{2.2}$ and $M_{*,\mathrm{tot}}$ for SDSS data from Pizagno et al. 2007.

Dutton et al. (2010) connect V_{opt} to V_{200}, the total circular speed measured at $r = r_{200}$, for both late- and early-type galaxies. Again starting with the total stellar mass, they obtain V_{200} through a parametrisation of $M_{*,\mathrm{tot}}$–$M_{\mathrm{d},200}$ similar to the connection used here between $M_{*,\mathrm{tot}}$ and $M_{\mathrm{d,vir}}$ from Moster et al. (2010). For stellar masses $7\times10^9 M_\odot \lesssim M_{*,\mathrm{tot}} \lesssim 7\times10^{11} M_\odot$, Dutton et al. (2010) found that although the circular speed curves of late-type galaxies were consistent with being flat, the curves for early-types do not flatten off towards large radii [i.e., $V_c(R_e) \neq V_{200}$ in general].

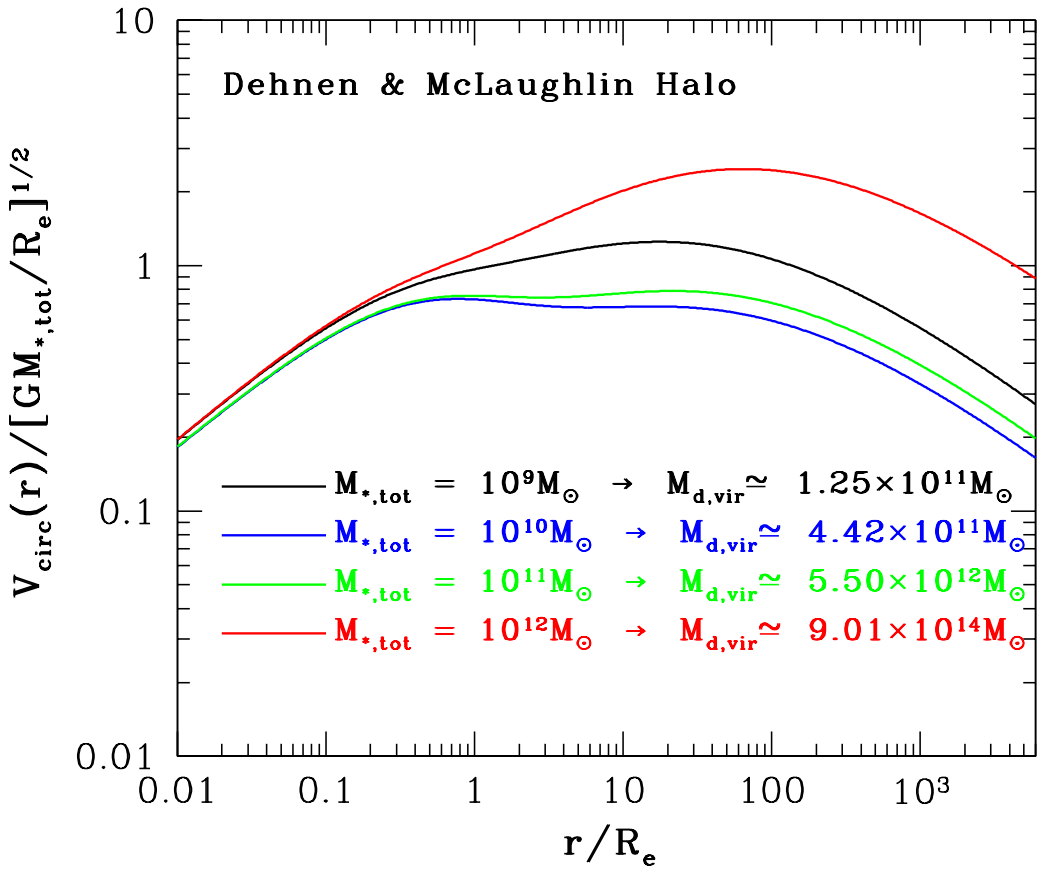

Figure 2.17: Total circular-speed profiles, $V_c(r)/[GM_{*,\rm tot}/R_e]^{1/2}$, as a function of r/R_e. All curves are for Hernquist stars and a Dehnen & McLaughlin dark matter halo. The different line colours represent different total stellar masses; $M_{*,\rm tot} = 10^9 M_\odot$ (black line), $10^{10} M_\odot$ (blue line), $10^{11} M_\odot$ (green line) and $10^{12} M_\odot$ (red line).

For stellar masses $10^{10} M_{\odot} \lesssim M_{*,\rm tot} \lesssim 10^{11} M_{\odot}$, the curves in Figure 2.17 are approximately flat for $r/R_e \sim 1$–50. However, for the largest galaxies, with $M_{*,\rm tot} \sim 10^{12} M_{\odot}$, the circular-speed profile is definitely not flat between these radii. The same is true for small systems, with $M_{*,\rm tot} \sim 10^{9} M_{\odot}$. This is because the smallest and largest systems contain significant amounts of dark matter, even at smaller radii, reflected in the $f_{*,\rm vir}$–$M_{*,\rm tot}$ and $f_*(R_e)$–$M_{*,\rm tot}$ relations. Therefore, the circular-speed profile of the *dark matter* will "kick in" at smaller radii and will have a larger peak value. This causes the *total* (stars and dark matter) circular speed to continue increasing out to larger radii for the higher mass systems. It is also worth noting that at radii beyond $\sim 50 R_e$, the circular-speed profiles begin to drop off. This is because the radius at which the dark matter circular-speed has a maximum, $r_{\rm pk}$, has been passed *and* the stellar circular speed, $V^2_{\rm c,*} \rightarrow r^{-1}$ as $r \rightarrow \infty$. Therefore, $V_c(r)$ is significantly different at the virial radius ($r_{\rm vir}$ or r_{200}), consistent with the results obtained by Dutton et al. (2010) for early-type galaxies.

2.2.8.2 Connecting $\sigma_{\rm ap}(R_e)$ and $V_c(R_e)$

The total circular speed can be evaluated at any radius r, and then related to any of the stellar or dark matter halo properties at $z = 0$. One such relation to look at is between the total circular speed inside an effective radius, $V_c(R_e)$, and the stellar velocity dispersion, also inside R_e. The connection between total circular speed and $\sigma_{\rm ap}(R_e)$ have been looked at before, but only as power-law fits to data (Gerhard et al. 2001; Ferrarese 2002; Seljak 2002; Padmanabhan et al. 2004; Wolf et al. 2010). These previous works do not account for the stellar mass dependence of $f_{*,\rm vir}$ or the halo mass dependence of $r_{\rm vir}/r_{-2}$. Both of these are likely to influence how $V_c(R_e)$ and $\sigma_{\rm ap}(R_e)$ are related.

Figure 2.18 shows the $V_c(R_e)$–$\sigma_{\rm ap}(R_e)$ relation (top) and the ratio $V_c(R_e)/\sigma_{\rm ap}(R_e)$ (bottom) as a function of $\sigma_{\rm ap}(R_e)$. The solid blue lines are the average trends obtained by combining the $\sigma_{\rm ap}(R_e)$–$M_{*,\rm tot}$ and $f_*(R_e)$–$M_{*,\rm tot}$ relations with equation (2.51) for the total circular speed, evaluated at R_e. These curves assume a Dehnen & McLaughlin

model for the dark matter halo and that the stellar ejecta mass fraction, $F_{\rm ej}$, depends on $M_{*,\rm tot}$ through the ad-hoc relation given by equation (2.50). The dashed black lines corresponds to $V_c(R_e) = \sqrt{2}\sigma_{\rm ap}(R_e)$, with the green lines for $V_c(R_e) = 1.65\,\sigma_{\rm ap}(R_e)$ [Padmanabhan et al. 2004; Dutton et al. 2010], the red lines for $V_c(R_e) = 1.5\,\sigma_{\rm ap}(R_e)$ [Seljak 2002] and the cyan lines the results from Ferrarese (2002), with a correction applied to the aperture velocity dispersion — $\sigma_{\rm ap}(R_e/8) \simeq 1.07\sigma_{\rm ap}(R_e)$ for a self-consistent sphere of Hernquist stars.

It has previously been assumed that $V_c(R_e) \propto \sigma_{\rm ap}(R_e)$, and a constant of proportionality then estimated by fitting to the observations (Seljak 2002; Padmanabhan et al. 2004; Wolf et al. 2010). Generally, this leads to the ratio $V_c(R_e)/\sigma_{\rm ap}(R_e) \simeq 1.5$–$1.7$. Ferrarese (2002) did not make this assumption, but her results are consistent with a linear proportionality. For 21 elliptical galaxies analysed by Kronawitter et al. (2000), Ferrarese (2002) related the aperture velocity dispersion measured within $R_e/8$ to the total circular speed. The total circular speed was taken to be within the kinematic radius, $r_{\rm kin}$, defined by Kronawitter et al. (2000) to be " the radius of the last kinematic data point", with typical values of $r_{\rm kin} \sim R_e$ [and hence $V_c(r_{\rm kin}) \sim V_c(R_e)$]. Ferrarese found a best fitting power-law given by (cf. §1.3.3.5)

$$\log[V_c(R_e)] = (0.94 \pm 0.11)\log[\sigma_{\rm ap}(R_e/8)] + (0.31 \pm 0.26), \tag{2.52}$$

consistent with $V_c(R_e) \propto \sigma_{\rm ap}(R_e/8)$ within the errors.

The average trend lines are broadly consistent with the results from the literature. In the bottom panel, the minimum of $V_c(R_e)/\sigma_{\rm ap}(R_e) \simeq 1.4$ at $\sigma_{\rm ap}(R_e) \sim 170\,{\rm km\,s^{-1}}$ can be traced back to the peak in $f_{*,\rm vir}$ at $M_{*,\rm tot} \sim 3$–$4 \times 10^{10} M_\odot$. This peak propagates through to the $f_*(R_e)$–$M_{*,\rm tot}$ relation, and appears as a minimum in the bottom panel of Figure 2.18 due to the $1/f_*(r)$ term in the total circular speed equation. With the additional constraints on $f_{*,\rm vir}$ and $r_{\rm vir}/r_{-2}$, a linear proportionality between $V_c(R_e)$ and $\sigma_{\rm ap}(R_e)$ is not expected. Instead, the ratio $V_c(R_e)/\sigma_{\rm ap}(R_e)$ is a non-monotonic function of aperture dispersion within R_e (and hence of $M_{*,\rm tot}$ as well), spanning the range of the results in the literature.

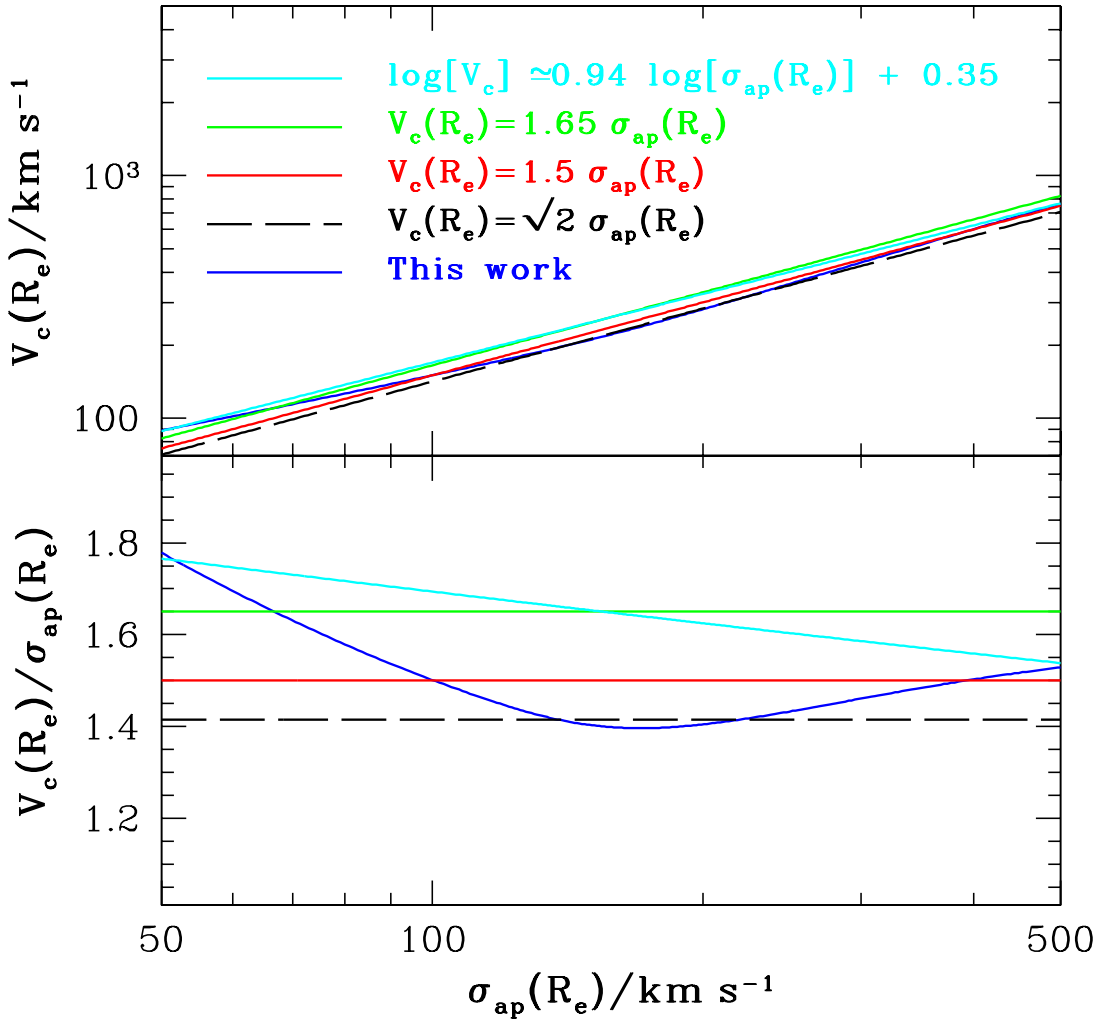

Figure 2.18: *Top panel:* Total circular-speed at the effective radius, $V_c(R_e)$, as a function of $\sigma_{\rm ap}(R_e)$. *Bottom panel:* The ratio $V_c(R_e)/\sigma_{\rm ap}(R_e)$, as a function of $\sigma_{\rm ap}(R_e)$. In both panels, the dashed black lines correspond to $V_c(R_e) = \sqrt{2}\sigma_{\rm ap}(R_e)$, the green lines $V_c(R_e) = 1.65\sigma_{\rm ap}(R_e)$ (Padmanabhan et al. 2004, Dutton et al. 2010), the red lines $V_c(R_e) = 1.5\sigma_{\rm ap}(R_e)$ (Seljack 2002) and the cyan lines are the relation from Ferrarese (2002), using $\sigma_{\rm ap}(R_e/8) \simeq 1.07\sigma_{\rm ap}(R_e)$. The blue curves are from the scaling relations, assuming Hernquist stars, a Dehnen & McLaughlin dark matter halo and an ad-hoc relation between the stellar ejecta mass fraction, $F_{\rm ej}$, and $M_{*,\rm tot}$.

2.2.8.3 Connecting $V_c(R_e)$ and $V_c(r_{200})$

As discussed, when connecting the circular speed at R_e to the total halo mass ($M_{\rm d,vir}$ or $M_{\rm d,200}$), it is common practice in the literature to set the observed circular velocity (in the optical part of a galaxy, $V_{\rm opt}$), to the circular velocity at the virial (or r_{200}) radius: $V_{\rm opt} = V_{200}$ or $V_{\rm opt} = V_{\rm vir}$ (Ferrarese 2002; Croton 2009; Bandara, Crampton & Simard 2009). However, as is pointed out by several authors, the circular speed, after first increasing, does decrease towards larger radii. The total circular speed is dominated by the dark matter out towards the virial radius, and any realistic shape of the dark matter density profile leads to a $V_c(r)$ profile that decreases towards $r_{\rm vir}$ or r_{200}. The circular-speed curves in Figure 2.17 are in agreement with this conclusion, with $V_c(r)$ beginning to decrease for $r/R_e \gtrsim 50$. For stellar masses in the range $10^8 M_\odot \lesssim M_{*,\rm tot} \lesssim 10^{12} M_\odot$, the constraints on R_e and $r_{\rm vir}$ lead to $110 \lesssim r_{\rm vir}/R_e \lesssim 170$ (and given that $r_{200}/r_{\rm vir} \simeq 0.8$, $85 \lesssim r_{200}/R_e \lesssim 140$).

The top panel of Figure 2.19 shows $V_c(r)$ evaluated at $r = R_e$ (dashed lines) and at $r = r_{200}$ (solid lines) as functions of $M_{*,\rm tot}$. The different line colours are for the three cuspy halo models used throughout; NFW (black), Dehnen & McLaughlin (blue) and Hernquist (red). According to these average trends, setting $V_c(R_e) = V_{200}$ is not a realistic assumption. V_{200} is clearly a non-linear function of total stellar mass, with $V_c(R_e) > V_{200}$ for $M_{*,\rm tot} \lesssim 10^{11} M_\odot$ and $V_c(R_e) < V_{200}$ for $M_{*,\rm tot} \gtrsim 10^{11} M_\odot$.

The bottom panel shows the ratio $V_c(R_e)/V_{200}$ for the three dark matter halos, again as a function of total stellar mass. This further demonstrates how $V_c(R_e) \neq V_{200}$ in general. This compares well to the work of Dutton et al. (2010), who also derived this result. They derive a mean relation between $V_{\rm opt}$ and V_{200}, for late- and early-type galaxies separately. As discussed, they begin by relating stellar mass to halo mass, $M_{\rm d,200}$, considering measurements from weak lensing, satellite kinematics and abundance matching (Moster et al. 2010, Behroozi et al. 2010) techniques (cf. §1.2.2). For the average trends calculated here, the global stellar-to-dark matter mass ratio, $f_{*,\rm vir}$, from Moster et al. (2010) is used. In their paper, this is presented as the mean of the log of stellar mass as a function of halo mass: $\langle \log(M_*) \rangle (M_{\rm d,vir})$.

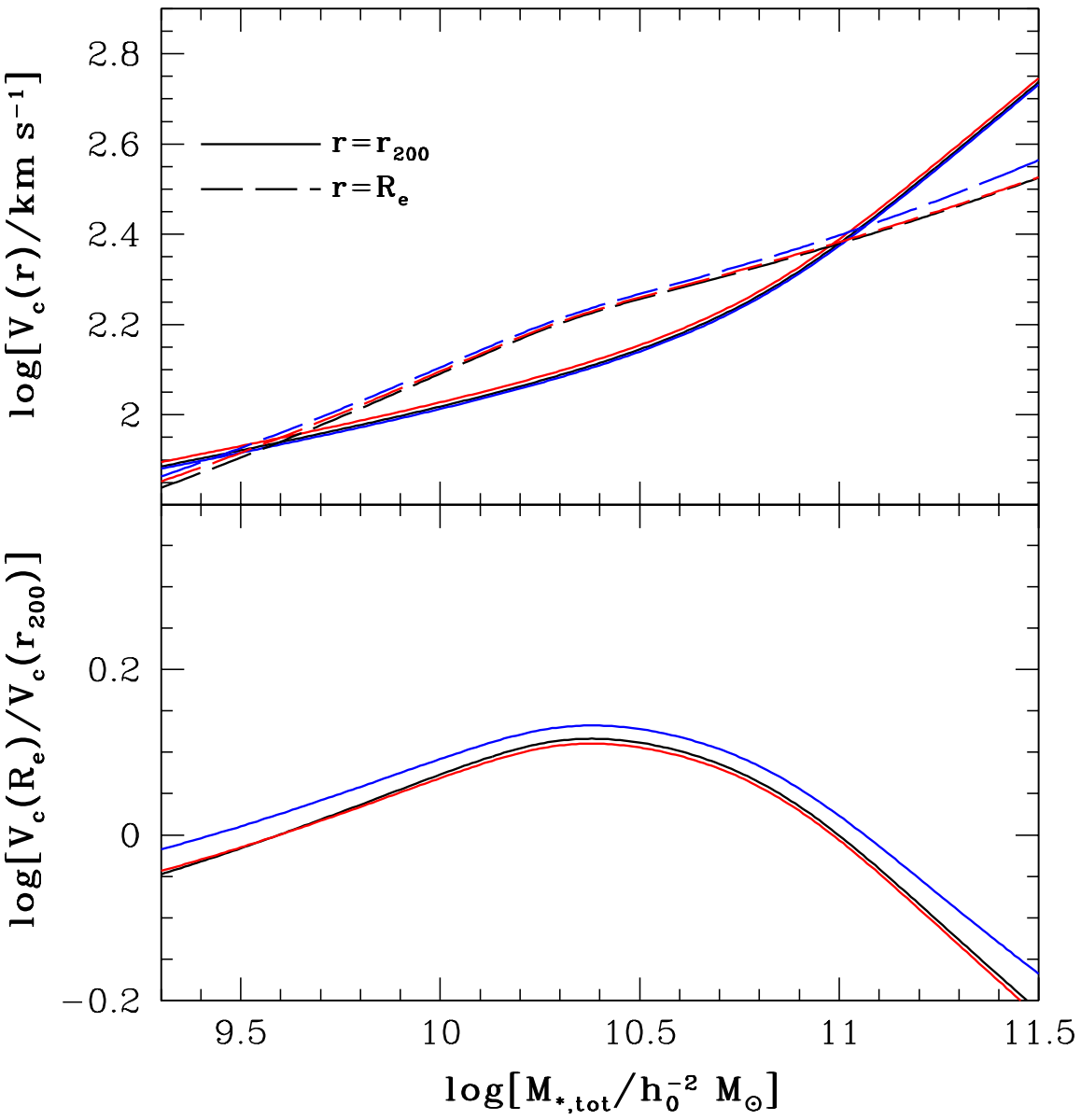

Figure 2.19: *Top panel:* Total circular-speed at the effective radius, $V_c(R_e)$ (dashed lines), and the $\Delta = 200$ overdensity radius, $V_c(r_{200})$ (solid lines) as a function of total stellar mass, $M_{*,\rm tot}$. The different line colours are for the three cuspy halos used throughout the calculations; NFW (black lines), Dehnen & McLaughlin (blue lines) and Hernquist (red lines). *Bottom panel:* The ratio $V_c(R_e)/V_c(r_{200})$ as a function of total stellar mass. The line colours are the same as for the top panel.

As discussed in §2.2.5, the stellar-to-dark matter mass ratio can be calculated at any other radius once a total stellar mass has been specified, giving $f_{*,200}$ [or equivalently $\langle \log(M_*) \rangle (M_{\rm d,200})$]. Since the weak lensing and satellite kinematics techniques give the log of the mean halo mass as a function of stellar mass: $\log\langle M_{\rm d,200} \rangle (M_*)$, Dutton et al. (2010) also choose to do this for the abundance matching masses. This leads to differences at the high mass end, with the method used by Dutton et al. yielding systematically lower halo masses (for a fixed stellar mass) than the results used here. However this subtlety, along with there distinction between late-and early-types, does not significantly affect the results for $V_{\rm opt}/V_{200}$.

The top two panels of Figure 2.20 shows the $V_c(r)$–$M_{*,\rm tot}$ relation from Dutton et al. (2010) for early-types (left panel) and late-types (right panel), for both $V_{\rm opt}$ and V_{200}. The curves in the bottom two panels show their $V_{\rm opt}/V_{200}$ ratios for early-types (left panel) and late-types (right panel). For both, the average trends obtained here (Figure 2.19) are at worst in error at a level of $\sim$ 15–20% compared to the Dutton et al. results and lie within their shaded regions, corresponding to the 2σ uncertainties. This level of discrepancy is expected for these sort of scaling relations, given the associated scatter around the mean trends used as a starting point. The consistency between curves in the bottom panel of Figure 2.19 and both the late- and early-type curves from Dutton et al. indicates that distinguishing between galaxy type is not significant to the overall mean trend.

Ultimately, a non-linear relation between $V_c(R_e)$ and V_{200} has implications for connecting $M_{\rm d,200}$ to $M_{\rm BH}$ in the next Chapter. Dutton et al. (2010) looked at this themselves and found, based on their results for an average $V_{\rm opt}$–V_{200} relation, that a $M_{\rm BH}$–$M_{\rm d,200}$ trend line is not linear. However, the Dutton et al. result is based on a linear $M_{\rm BH}$–$\sigma_{\rm ap}(R_e)$ relation from a best-fitting power law. Now that average trends have been obtained for various stellar and dark matter halo properties at $z = 0$, these can be combined with halo progenitor evolution, and thus model predictions for *all* of the SMBH correlations will be obtained. Assuming a power-law fit for $M_{\rm BH}$–$\sigma_{\rm ap}$ to connect $M_{\rm BH}$ and $M_{\rm d,200}$ will therefore not be necessary in the context of the work presented here.

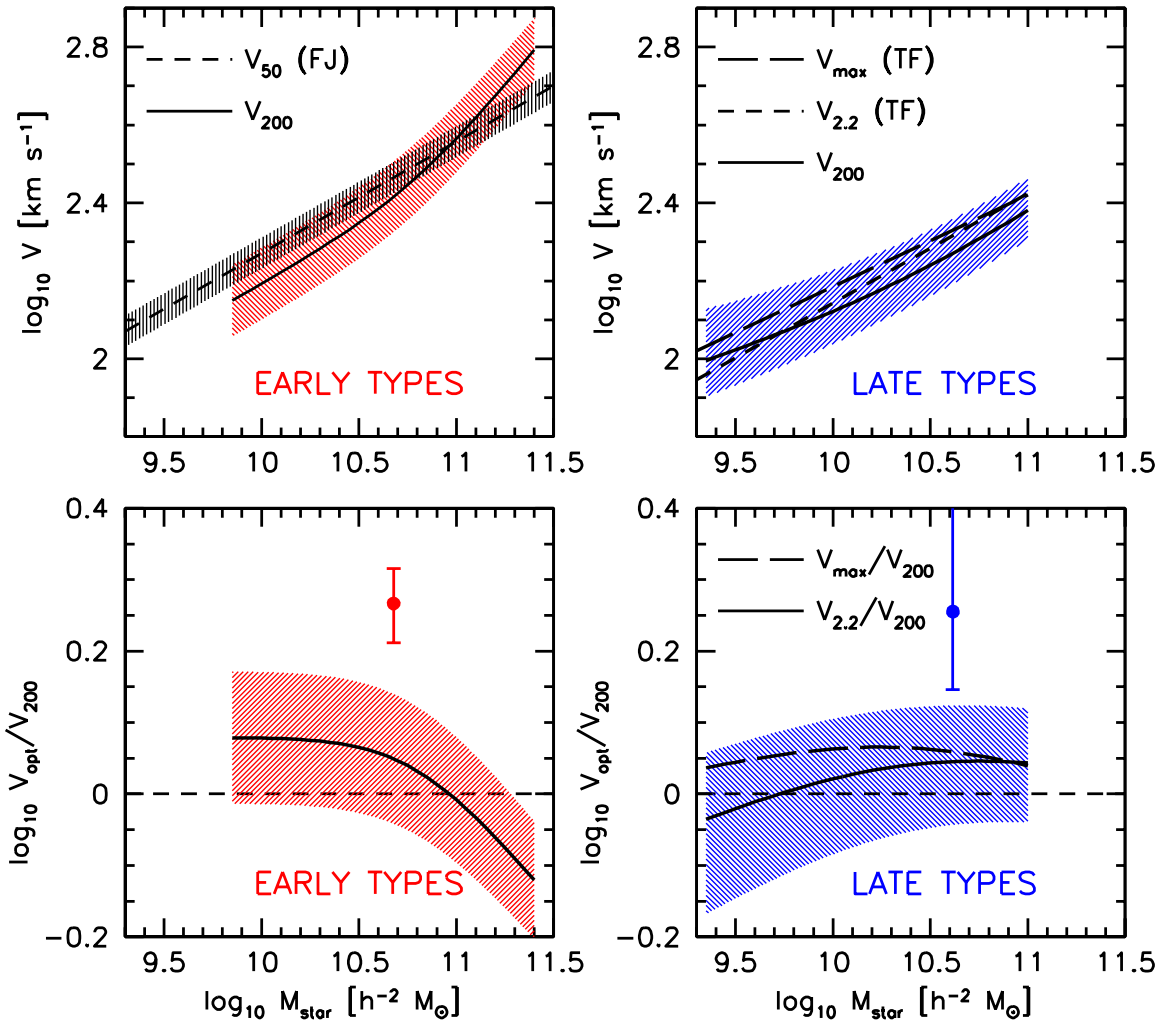

Figure 2.20: Figure from Dutton et al. (2010). *Top panel:* Circular velocity versus stellar mass relations for early- (left) and late-types (right). Shaded regions correspond to the 2σ uncertainties. The Tully-Fisher and Faber-Jackson relations are given by the dashed lines. For the Faber-Jackson relation, Dutton et al. converted velocity dispersions into circular-speeds assuming $V_c(R_e) = 1.65\,\sigma_{\rm ap}(R_e)$, with the uncertainty given by the black shaded region. The lower panels show the difference between the Tully-Fisher and Faber-Jackson relations and the halo virial velocity relations. The points with error bars (2σ) show the values of $V_{\rm opt}/V_{200}$ derived for $L_\star$ galaxies by Seljak (2002).

3 SMBH–bulge correlations at $z = 0$

In the previous Chapter, mean trend scalings between various stellar and dark matter halo properties at $z = 0$ were established. These relations give $M_{\rm d,vir}$ and $V_{\rm d,pk}$, and any other property of the dark matter halo, directly as a function of $M_{*,\rm tot}$. They were then re-cast to give $M_{\rm d,vir}(0)$ and $V_{\rm d,pk}(0)$ directly as functions of the observable $\sigma_{\rm ap}(R_e)$. McQuillin & McLaughlin (2012) derived a critical SMBH mass that suffices to expel a virialised ambient medium (gas tracing dark matter, with no stars) to beyond the virial radius of a non-isothermal dark matter halo (cf. §1.4.5). This critical SMBH mass is

$$M_{\rm BH} \simeq 1.14 \times 10^8 \, M_\odot \left(\frac{f_0}{0.2}\right) \left(\frac{V_{\rm d,pk}}{200 {\rm km \, s^{-1}}}\right)^4 , \tag{3.1}$$

where f_0 is the spatially constant gas-to-dark matter mass fraction in the protogalaxy. $V_{\rm d,pk}$ refers to the peak value of the circular speed, $V_d^2(r) = GM_d(r)/r$ in a dark matter halo. This prediction connects $M_{\rm BH}$ to $V_{\rm d,pk}$ at some time in the past, when quasar-mode blow-out occurred. Therefore, in order to predict the dependence of $M_{\rm BH}$ on $\sigma_{\rm ap}(R_e)$ (or any other galaxy properties) now, it is necessary first to connect the halo properties at $z > 0$ to those at $z = 0$.

As discussed, equation (3.1) is derived assuming that the shell is driven out by momentum-transfer from the wind only. However, the outflows are expected to become energy-driven (non-radiative) after an initial radiative phase (Zubovas & King 2012; McQuillin & McLaughlin 2013). This is just one of the possible caveats surrounding equation (3.1). It is unclear in detail how the inevitable switch to an energy-driven outflow may (Silk & Rees 1998; McQuillin & McLaughlin 2013) or may not (Zubovas & Nayakshin 2014) alter the functional dependence of a critical $M_{\rm BH}$ for blow-out on the dark matter $V_{\rm d,pk}$ or any other characteristic halo velocity scale. The equation also assumes the ambient medium is initially static, ignoring any cosmological infall of gas and an additional, confining ram pressure associated with hierarchical galaxy formation (Costa, Sijacki & Haehnelt 2014). It also neglects the presence of any stars in the protogalaxies, which could contribute both to the feedback driving gaseous outflows

(e.g. Murray et al. 2005; Power et al. 2011) *and* to the gravity containing them.

Despite these limitations, equation (3.1) provides a good example to help understand how expected relationships between SMBH masses and protogalactic dark matter halos are reflected in the observed SMBH–bulge relations. The equation is simple and transparent but still contains enough relevant feedback physics to be of interest, even with the caveats mentioned above. It is also the only such relation (connecting $M_{\rm BH}$ to a global property of the protogalactic dark matter halo), which does not assume that dark matter halos are isothermal spheres.

In equation (3.1), $V_{\rm d,pk}$ measures the potential well of a *protogalaxy* that just fails to contain the quasar-mode feedback of an SMBH with mass $M_{\rm BH}$. It therefore refers to the peak of the dark matter circular speed at some higher redshift, $z > 0$, marking the end of the period when the SMBH grew rapidly (and almost to completion), via sustained accretion at Eddington or super-critical rates. This redshift is denoted $z_{\rm qso}$, and it will be different for each galaxy. Generally, the range of $z_{\rm qso}$ should correspond to the epoch of peak quasar number density and SMBH accretion rate, i.e. $z \sim 2$–4 (Richards et al. 2006; Hopkins, Richards & Hernquist 2007; Delvecchio et al. 2014; Di Matteo et al. 2008; Sijacki et al. 2007; Sijacki et al. 2015).

The relevant halo properties are calculated at $z > 0$ in §3.1, by tracking the redshift evolution of halo virial mass and the maximum circular speed of the dark matter, through mass accretion histories of halo progenitors. §3.2 then details how $M_{\rm d,vir}(z)$ and $V_{\rm d,pk}(z)$ can be expressed as functions of $M_{*,\rm tot}$ and $\sigma_{\rm ap}(R_e)$ at $z = 0$. Once these are known, they can be combined with equation (3.1) to give model curves for $M_{\rm BH}(z)$ versus different galaxy properties at $z = 0$. After introducing the SMBH data in §3.3.1, these model curves are then compared to the observed SMBH correlations at $z = 0$, including those between $M_{\rm BH}$ and stellar velocity dispersion, total stellar mass, halo virial mass, and combinations of $\sigma_{\rm ap}(R_e)$ and R_e.

3.1 Dark matter properties at $z > 0$

Hierarchical growth of dark matter halos is usually tracked by merger-tree and/or N-body simulations of ΛCDM halos (cf. §1.1.6). For halos with virial masses at $z = 0$ in the range $10^{11}\,M_\odot \leq M_{\rm d,vir}(0) \leq 10^{15}\,M_\odot$, van den Bosch et al. (2014a) use both of these to extract for each halo the redshift $z_{1/2}$ at which its *most massive progenitor* had a virial mass $M_{\rm d,vir}(z_{1/2}) = 0.5\,M_{\rm d,vir}(0)$. Given the bottom-up nature of structure formation in CDM cosmologies, $z_{1/2}$ is a decreasing function of $M_{\rm d,vir}(0)$ in general and is approximated by (cf. §1.1.6)

$$z_{1/2} \;=\; 2.05\left[\frac{M_{\rm d,vir}(0)}{10^{12}\,h_0^{-1}\,M_\odot}\right]^{-0.055} \;-\; 1\;, \tag{3.2}$$

with $h_0 = 0.67$ according to Planck cosmology. Given $z_{1/2}$, the virial mass of the most massive progenitor of a halo at any other redshift can be approximated by an exponential function (e.g., Zhao et al. 2009),

$$\frac{M_{\rm d,vir}(z)}{M_{\rm d,vir}(0)} \;=\; \exp\left[-\,\frac{z\,\ln(2)}{z_{1/2}}\right]\,. \tag{3.3}$$

Figure 3.1 shows the results from the van den Bosch et al. (2014a) paper for both the simulations (top left panel) and merger trees (right panel), along with the curves from Equations (3.2) and (3.3) for different virial masses at $z = 0$ (bottom panel). The top two panels are taken directly from the van den Bosch et al. paper. For the simulation results, each line corresponds to the average obtained from all halos in a given mass bin. The solid lines show average mass accretion histories over the redshift range where the main progenitors of more than 90% of all host halos can be traced. Dotted lines are extensions obtained from taking an average over all host halos. The merger tree results are averages obtained using 2000 realisations. In the bottom panel, the different line colours correspond to different values for $M_{\rm d,vir}(0)$, as indicated in the Figure. Equations (3.2) and (3.3) give good approximations to the van den Bosch et al. (2014a) results for redshifts $z \lesssim 5$ [$\log(1+z) \lesssim 0.8$].

This approximation can then be used to obtain the evolution of any property of the dark matter halo that is related to its total mass. The peak of the dark matter

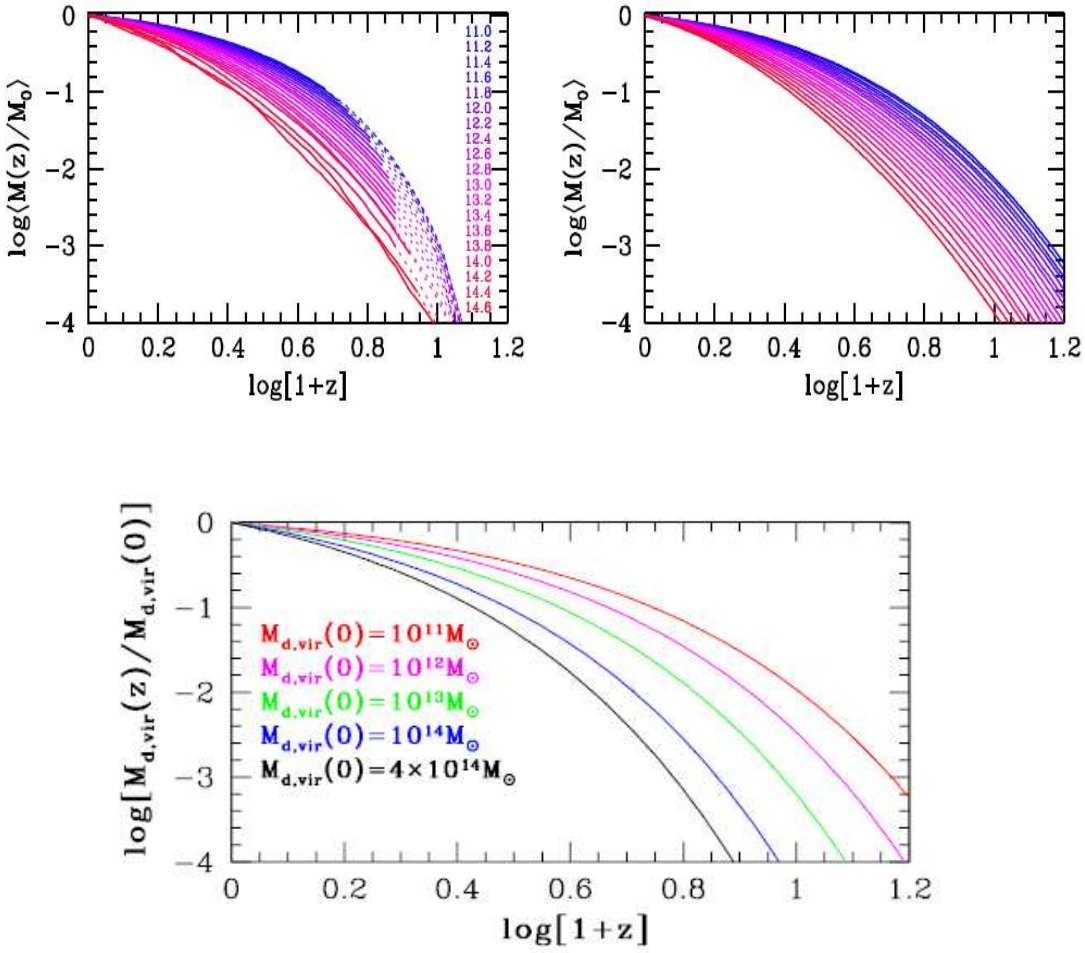

Figure 3.1: All panels show $\log[M_{\rm d,vir}(z)/M_{\rm d,vir}(0)]$ as a function of $\log[1+z]$. The top row is taken directly from Figure 2 of van den Bosch et al. (2014). *Top left panel*: Results from the simulations, where each line is the average obtained from all halos in a mass bin that is 0.2 dex wide. The mass range covered is $10^{11}M_\odot \leq M_{\rm d,vir}(z) \leq 10^{14.6}M_\odot$. The solid lines show average mass accretion histories over the range where the main progenitors of more than 90% of all host halos can be traced. Dotted lines are extensions obtained taking the average over all host halos. *Top right panel:* Results from merger trees, where each average is obtained using 2000 realisations. *Bottom panel:* $M_{\rm d,vir}(z)/M_{\rm d,vir}(0)$ calculated using equations (3.2) and (3.3), for different $M_{\rm d,vir}(0)$ values. These are represented by different line colours, as indicated in the Figure.

circular-speed curve in a halo at $z > 0$, connected to the black hole mass through equation (3.1), can be written (for any z) as

$$\frac{V^2_{\rm d,pk}}{V^2_{\rm d,vir}} \equiv \frac{V^2_{\rm d}(r_{\rm pk})}{V^2_{\rm d}(r_{\rm vir})} = \frac{g(r_{\rm pk}/r_{-2})}{g(r_{\rm vir}/r_{-2})} \tag{3.4}$$

where $g(r/r_{-2}) \equiv V^2_d(r)/V^2_d(r_{-2})$ is the normalised circular-speed curve of the dark matter.

Since the ratio $r_{\rm pk}/r_{-2}$ (and hence $g(r_{\rm pk}/r_{-2})$) is independent of redshift (it is fixed by assuming a basic form for the dark-matter density profile), equation (3.4) can be used to write

$$\begin{aligned}\frac{V^2_{\rm d,pk}(z)}{V^2_{\rm d,pk}(0)} &= \frac{g\left[(r_{\rm vir}/r_{-2})_{z=0}\right]}{g\left[(r_{\rm vir}/r_{-2})_z\right]} \times \frac{V^2_{\rm d,vir}(z)}{V^2_{\rm d,vir}(0)} \\ &= \frac{g\left[(r_{\rm vir}/r_{-2})_{z=0}\right]}{g\left[(r_{\rm vir}/r_{-2})_z\right]} \times \left[\frac{M_{\rm d,vir}(z)}{M_{\rm d,vir}(0)}\right]^{2/3} \left[\frac{\Delta_{\rm vir}(z)}{\Delta_{\rm vir}(0)}\right]^{1/3} \left[\frac{H(z)}{H_0}\right]^{2/3} ,\end{aligned} \tag{3.5}$$

where the last line uses the fact that $V^2_{\rm d}(r) \propto M_{\rm d}(r)/r$ and $M_{\rm d,vir} \propto r^3_{\rm vir}$, at a given z. For any choice of dark-matter halo model, and thus the function $g(r/r_{-2})$, the right-hand side of equation (3.5) is known in terms of z and $M_{\rm d,vir}(0)$. Choosing a redshift gives values for the overdensity, $\Delta_{\rm vir}(z)$, and the Hubble constant, $H(z)$. If the dark matter halo mass at $z = 0$ is also specified, then this fixes the halo mass at the chosen z through the approximations for $z_{1/2}$ and $M_{\rm d,vir}(z)$. Hence the concentration $r_{\rm vir}/r_{-2}$ at that redshift is also fixed.

The top panel of Figure 3.2 shows the virial masses of the most massive progenitors, relative to the $z = 0$ virial masses, as a function of $M_{\rm d,vir}(z = 0)$, at redshifts $z = 1, 3$ and 5. The middle panel then shows the masses of the largest progenitors at the same redshifts directly as a function of halo mass at $z = 0$. Finally, the bottom panel shows the ratio of progenitor-to-present $V_{\rm d,pk}$ at $z = 1, 3$ and 5 against $M_{\rm d,vir}(0)$. These curves depend on the choice of dark matter density profile, through equation (3.5), with Hernquist (red curves) and Dehnen & McLaughlin (blue curves) shown here. The curves for NFW and Burkert lie in between those shown.

The gradual flattening towards higher masses of the curves for $M_{\rm d,vir}(z)$ versus $M_{\rm d,vir}(0)$ in the middle panel, and how this sets in at more modest halo masses for

larger z, is significant. This is a generic feature of structure formation via hierarchical merging. Halos in any given mass range at $z = 0$ have progenitors drawn from increasingly narrow mass ranges, on average, at progressively higher redshifts. This high-mass flattening is more pronounced at higher z, as more of their growth has occurred more recently.

The $z = 5$ curve in the middle panel of Figure 3.2 appears to imply a maximum. However, this is specific to the relation between $z_{1/2}$ and $M_{\rm d,vir}(0)$ in equation (3.2). Along with equation (3.3), these are both *approximations* to the numerical results of van den Bosch et al. (2014a) for the median most massive progenitors of halos, with $10^{11} \leq M_{\rm d,vir}(0)/M_{\odot} \leq 10^{15}$. Any fine details following from them are therefore not definitive, especially at the high end of the $z = 0$ mass range, or beyond $z \sim 5$ [for larger redshifts, the approximation for $M_{\rm d,vir}(z)/M_{\rm d,vir}(0)$ given by equation (3.3) breaks down]. However, the flattening of $M_{\rm d,vir}(z)$ as a function of $M_{\rm d,vir}(0)$ is qualitatively robust. It ultimately has implications for the shape of the $M_{\rm BH}$–bulge relations at the high mass end and is discussed further in §3.3.

In the bottom panel of Figure 3.2, the difference in $V_{\rm d,pk}(z)/V_{\rm d,pk}(0)$ between the Dehnen & McLaughlin and Hernquist model halos increases towards lower virial masses, for a fixed redshift. This can be traced back to the dependence of halo concentration on $M_{\rm d,vir}(z)$ — lower mass halos generally have higher concentrations, $r_{\rm vir}/r_{-2}$, and therefore higher ratios of $r_{\rm vir}/r_{\rm pk}$. Thus, the ratio $V_{\rm d,pk}/V_{\rm d,vir}$ is more sensitive in lower mass halos to the model-dependent steepness of the circular-speed curve at radii $r > r_{\rm pk}$. $V^2_{\rm d,vir}(z) \propto M_{\rm d,vir}(z)/r_{\rm vir}(z)$ is independent of the halo density profile, so only $V_{\rm d,pk}$ is actually model-dependent. Since NFW and Burkert (1995) haloes have circular-speed curves that are intermediate in steepness to Dehnen & McLaughlin and Hernquist models beyond $r_{\rm pk}$, the curves for $V_{\rm d,pk}(z)/V_{\rm d,pk}(0)$ versus $M_{\rm d,vir}(0)$ in these other models lie between the two shown in Figure 3.2.

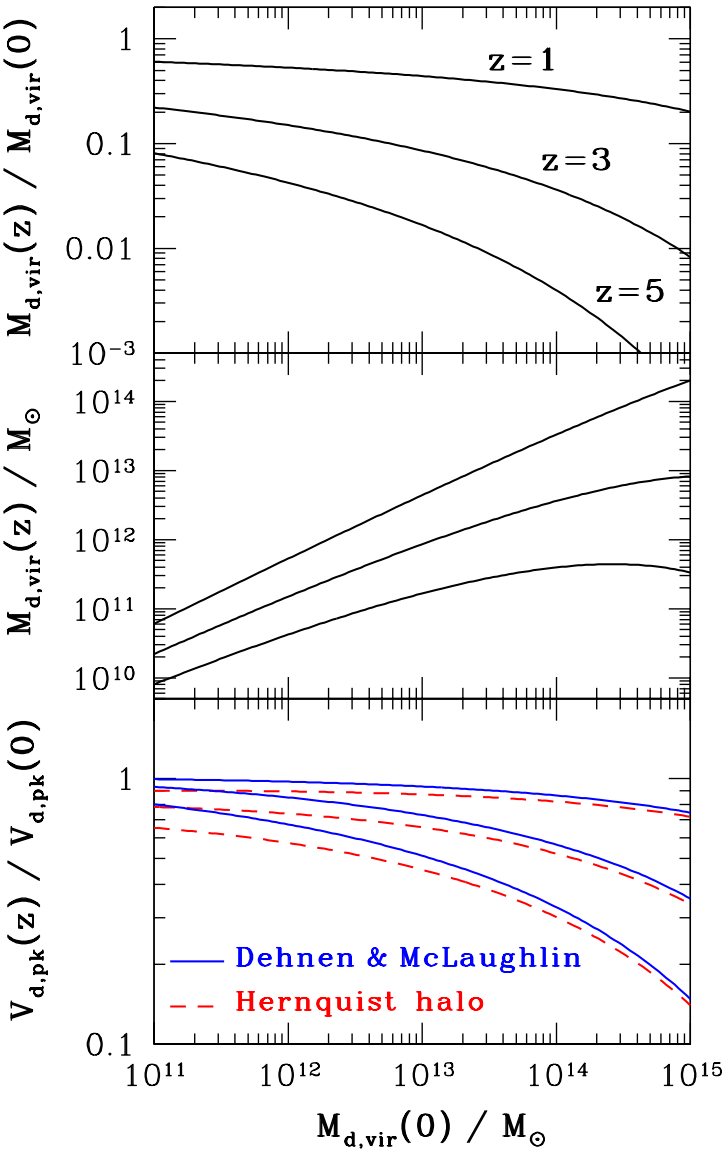

Figure 3.2: *Top panel*: Relative virial masses $M_{\rm d,vir}(z)/M_{\rm dvir}(0)$ for the most massive progenitors of halos with masses $M_{\rm d,vir}(0)$ at $z = 0$, as given by equations (3.2) and (3.3). From top to bottom, the curves are for the progenitors at fixed redshifts $z = 1, 3$ and 5. *Middle panel*: Virial masses of the most massive progenitor halos at $z = 1$, 3 and 5 (for the curves from top to bottom) plotted directly against the $z = 0$ halo mass. *Bottom panel*: Peak circular speeds $V_{\rm d,pk}(z)$ in the most massive progenitors at $z = 1$, 3 and 5, relative to the peak speeds $V_{\rm d,pk}(0)$ in the final halos at $z = 0$, from equation (3.5). The solid (blue) lines are for halos with a Dehnen & McLaughlin (2005) density profile and the dashed (red) lines are for halos with a Hernquist (1990) profile. These bracket the corresponding curves for NFW and Burkert (1995) halos at the same redshifts.

3.2 Dark matter halo properties at $z > 0$ versus stellar properties at $z = 0$

§3.1 details how properties of the dark matter halo at $z > 0$ compare to those at $z = 0$. Combining this with results from Chapter 2 relating $M_{\rm d,vir}$ and $V_{\rm d,pk}$ at $z = 0$ to $M_{*,\rm tot}$ and $\sigma_{\rm ap}(R_e)$ also at $z = 0$, the properties in the halo progenitors are connected to the stellar properties at $z = 0$. Folding in the $M_{\rm BH} \propto V_{\rm d,pk}^4$ prediction, model predictions connecting $M_{\rm BH}$ to $\sigma_{\rm ap}(R_e)$ and $M_{*,\rm tot}$ are obtained. This will ultimately allow for a comparison between the critical SMBH mass prediction in equation (3.1) and the SMBH–bulge correlations in §3.3.

The top row of Figure 3.3 shows halo progenitor masses (for the most massive progenitor), $M_{\rm d,vir}(z)$, as a function of total stellar mass (left panel) and stellar velocity dispersion (right panel) at $z = 0$, for various redshifts. The curves in the top left panel are obtained by combining the approximation for $M_{\rm d,vir}(z)/M_{\rm d,vir}(0)$ and $z_{1/2}$ with the average trend for$M_{\rm d,vir}$–$M_{*,\rm tot}$ at $z = 0$ from §2.2.3. The curves in the top right panel follow from this by folding in the $\sigma_{\rm ap}(R_e)$–$M_{*,\rm tot}$ trend lines from §2.2.6.

The curves for $M_{\rm d,vir}(z)$ versus $M_{*,\rm tot}$ do not depend on the choice of stellar density profile or dark matter halo model. The blue curves in Figure 3.3 correspond to Dehnen & McLaughlin (2005) models for the halo density profiles and the red curves to Hernquist (1990) profiles. These bracket the curves obtained using NFW halo profiles, while the cored halo profiles of Burkert (1995) are not considered for the SMBH correlations, due to yielding trend lines that were incompatible with the $\sigma_{\rm ap}(R_e)$–$M_{*,\rm tot}$ ATLAS data. The dashed lines show halo properties at $z = 0$, whereas the solid lines are for larger redshifts, with $z_{\rm qso} = 1, 3$ and 5.

For $\sigma_{\rm ap}(R_e) \leq 200\,{\rm km\,s^{-1}}$, the two halo models are indistinguishable in the top right panel, whereas for larger velocity dispersions, a Hernquist profile (red curve) implies a larger $M_{\rm d,vir}(0)$ than a Dehnen & McLaughlin profile (blue curve), for a fixed $\sigma_{\rm ap}(R_e)$. This behaviour is a reflection of the halo dependence seen in the $\sigma_{\rm ap}(R_e)$–$M_{*,\rm tot}$ relation at $z = 0$. Both the virial stellar-to-dark matter mass ratio and the value

of $M_{*,\rm vir}/M_{*,\rm tot}$ are independent of the choice of halo model. Therefore any differences in the $\sigma_{\rm ap}(R_e)$–$M_{*,\rm tot}$ relation due to the chosen dark matter density profile are reflected in the $M_{\rm d,vir}(z)$–$\sigma_{\rm ap}(R_e)$ relation.

The middle row of Figure 3.3 shows $V_{\rm d,pk}$ in the most massive progenitor at $z_{\rm qso} = 0$ (dashed lines) and $z_{\rm qso} = 1, 3$ and 5 (solid lines), as a function of $M_{*,\rm tot}$ (left panel)and $\sigma_{\rm ap}(R_e)$ (right panel) at $z = 0$. The dashed black line corresponds to $V_{\rm d,pk} = \sqrt{2}\sigma_{\rm ap}(R_e)$. This is clearly a poor substitute for the actual relationship between the two velocities at $z = 0$ in galaxies with $\sigma_{\rm ap}(R_e) \gtrsim 200\,{\rm km\,s^{-1}}$ (or $M_{*,\rm tot} \gtrsim 3 \times 10^{11} M_\odot$). It does come closer to correctly estimating the dependence of $V_{\rm d,pk}$ at $z_{\rm qso} = 3$ on $\sigma_{\rm ap}(R_e)$ at $z = 0$; but this appears to be entirely coincidental, and the situation is reversed for $\sigma_{\rm ap}(R_e) \lesssim 200\,{\rm km\,s^{-1}}$.

At a given value of $\sigma_{\rm ap}(R_e)$ or $M_{*,\rm tot}$, the downward "corrections" to $M_{\rm d,vir}$ and $V_{\rm d,pk}$ from their values at $z = 0$ to the progenitors at $z_{\rm qso} > 0$, are systematically larger for larger systems. This is a restatement of the flattening towards higher masses in the dependence of $M_{\rm d,vir}(z)$ on $M_{\rm d,vir}(0)$ in Figure 3.2. Again, it is fundamentally because in a (Λ)CDM cosmology, more massive halos were assembled and virialised more recently. The mass difference between any two halos at a fixed redshift is therefore greater, on average, than the mass difference between the typical largest progenitors of the halos at some higher redshift. This contrast is greater for higher mass halos, as these are the ones that have formed most recently.

Equations (3.2) – (3.5), which underpin the curves in Figure 3.3 are approximations to results from van den Bosch et al. (2014a) for the mass accretion histories of simulated halos. These simulations only extend up to $z = 0$ halo masses of $M_{\rm d,vir} = 10^{15} M_\odot$, corresponding to $\sigma_{\rm ap}(R_e) \simeq$ 350–400km s^{-1} (depending on choice of dark matter density profile). Beyond this, the equations are not only approximate, but also extrapolations, and should not be read too literally. For example, the peaks around $\sigma_{\rm ap}(R_e) \approx 400\,{\rm km\,s^{-1}}$ in the curves for $M_{\rm d,vir}$ and $V_{\rm d,pk}$ at $z_{\rm qso} = 3$ in the top two right panels of Figure 3.3, may not be accurate. However, the relative flatness in the curves at high velocity dispersions *is* a secure result. As the Figures show, curves for $M_{\rm d,vir}$ and $V_{\rm d,pk}$ at any $z_{\rm qso} > 0$ flatten at some high $\sigma_{\rm ap}(R_e)$ or $M_{*,\rm tot}$ at $z = 0$.

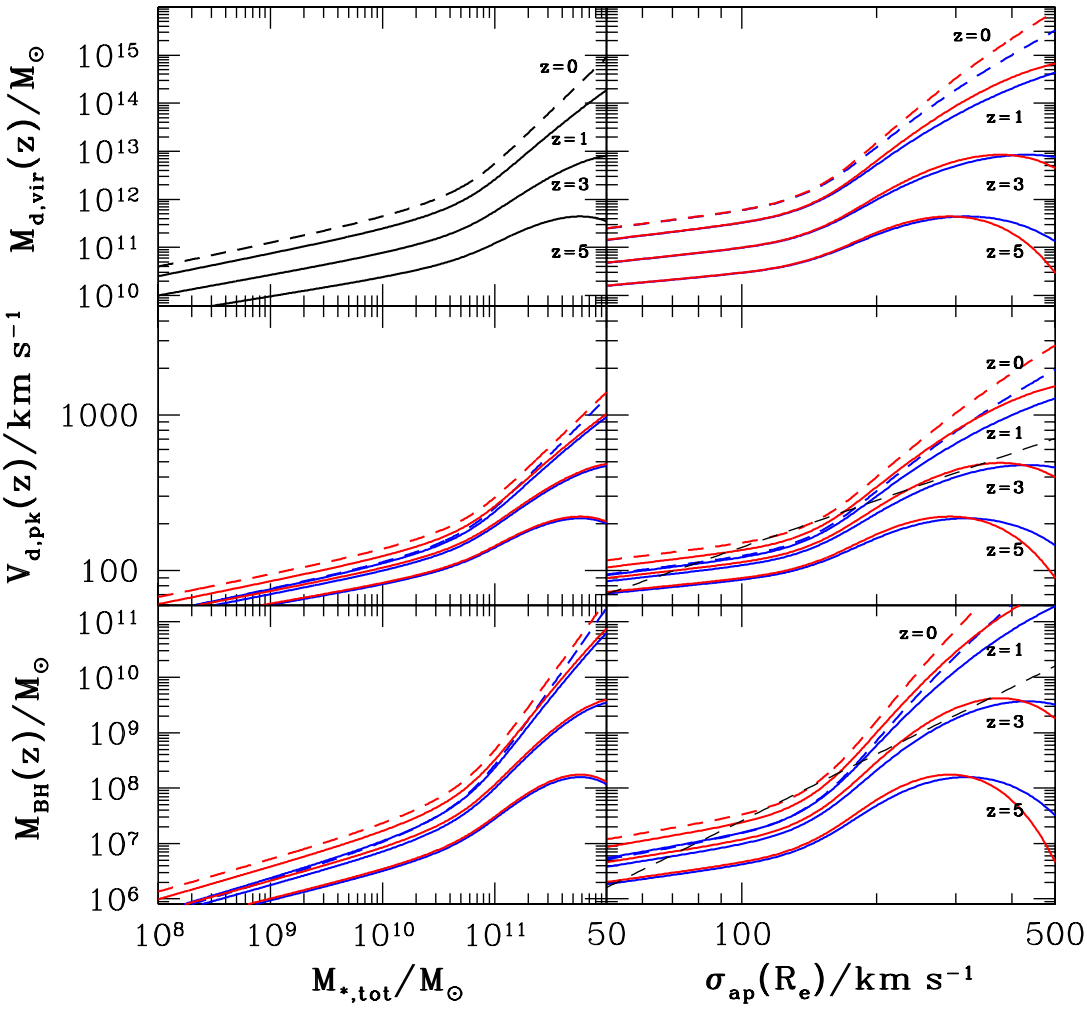

Figure 3.3: In all panels, red curves are for a Hernquist halo, and blue curves are for a Dehnen & McLaughlin halo. *Top row:* Halo progenitor masses, $M_{\rm d,vir}(z)$, at $z = 0$ (dashed lines) and $z_{\rm qso} = 1, 3$ and 5 (solid lines), as a function of total stellar mass (left panel) and stellar velocity dispersion (right panel) at $z = 0$. For $z_{\rm qso} > 0$, $M_{\rm d,vir}(z)$ corresponds to the mass of the *most massive progenitor* at that redshift. *Middle row:* Peak circular speeds $V_{\rm d,pk}(z)$ at $z = 0$ (dashed lines) and $z = 1$, 3 and 5 (solid lines), as a function of $M_{*,\rm tot}$ (left) and $\sigma_{\rm ap}(R_e)$ (right) at $z = 0$. The broken black line corresponds to $V_{\rm d,pk} = \sqrt{2}\sigma_{\rm ap}(R_e)$. *Bottom row:* $M_{\rm BH}(z)$ at $z = 0$ (dashed lines) and $z = 1$, 3 and 5 (solid lines), as a function of $M_{*,\rm tot}$ (left) and $\sigma_{\rm ap}(R_e)$ (right) at $z = 0$. Curves are obtained by applying the critical SMBH mass prediction [equation (3.1)] to $V_{\rm d,pk}(z)$.

This effect will propagate through to predicted SMBH – bulge relations that involve halo masses or circular speeds at $z_{\rm qso} > 0$.

The bottom row of Figure 3.3 shows SMBH mass versus $M_{*,\rm tot}$ (left panel) and $\sigma_{\rm ap}(R_e)$ (right panel) at $z = 0$. The curves (blue for Dehnen & McLaughlin and red for Hernquist) are obtained from the McQuillin & McLaughlin critical SMBH mass [equation (3.1)], with a protogalactic gas fraction of $f_0 = 0.18$ (for the 2013 Planck cosmology) and with $V_{\rm d,pk}$ depending on $\sigma_{\rm ap}(R_e)$ (or $M_{*,\rm tot}$) as shown in the middle row of Figure 3.3. Given that $M_{\rm BH} \propto V_{\rm d,pk}^4$ in equation (3.1), these curves are just scaled and shifted versions of the $V_{\rm d,pk}$ versus $\sigma_{\rm ap}(R_e)$ and $M_{*,\rm tot}$ curves in the middle panels. The dashed black line in the bottom right panel, shown for reference purposes only, is also for equation (3.1) evaluated with $f_0 = 0.18$, but with the simplistic substitution $V_{\rm d,pk} = \sqrt{2}\sigma_{\rm ap}(R_e)$.

The broken blue and red curves are for $V_{\rm d,pk}$ at $z_{\rm qso} = 0$ versus stellar mass and stellar velocity dispersion at $z = 0$. These are the predictions of equation (3.1) for the critical SMBH masses required to clear halos filled with virialised gas in an 18% mass ratio, via quasar-mode feedback *now*. The solid curves are for $V_{\rm d,pk}$ at $z_{\rm qso} = 1, 3$ and 5 versus $M_{*,\rm tot}$ and $\sigma_{\rm ap}(R_e)$ at $z = 0$. These are predictions for the SMBH correlations in quiescent galaxies at $z = 0$, if they come from an $M_{\rm BH} \propto V_{\rm d,pk}^4$ relationship established by quasar-mode feedback and blow-out from gaseous protogalaxies at $z_{\rm qso} > 0$ (with negligible subsequent SMBH growth via coalescence in mergers). These curves are discussed in more detail in §3.3.2, where they are compared to current SMBH data.

For the mass of the halo progenitor, the mass of the *most massive progenitor* is used, thus identifying this to be the halo progenitor that ultimately defines the centre of the larger potential well at $z = 0$. The distinction between the most massive progenitors and most contributing progenitors (discussed in §1.1.6) *could* have some implications for the final $M_{\rm BH}$–bulge property relations, possibly leading to a small amount of scatter relative to the final curves.

3.3 Model SMBH–bulge relations compared to data

In the last subsection, it was shown how connections between dark matter halo properties at $z > 0$ and stellar properties at $z = 0$ can be combined with a critical SMBH mass prediction to obtain model predictions for $M_{\rm BH}$ versus $\sigma_{\rm ap}(R_e)$ and $M_{*,\rm tot}$ at $z = 0$. Ideally, these predictions would be compared to the ATLAS^{3D} data (Cappellari et al. 2011; Cappellari et al. 2013b; Cappellari et al. 2013a), since this sample was used to construct the trend lines in Chapter 2. However, there are only 22 galaxies in ATLAS with confirmed $M_{\rm BH}$ values. It is therefore necessary to consider a larger sample for the SMBH data, provided by the compilation from Kormendy & Ho (2013). Before comparing the model predictions to the data then, these two samples need to be compared to one another, to look at selection effects and to make comparisons of the measured stellar properties between data sets for the same galaxies. It is well documented that galaxies with $M_{\rm BH}$ measurements tend to have higher than average velocity dispersions, for a given stellar mass (Bernardi et al. 2007; van den Bosch et al. 2014b). It has been suggested that this is a selection effect associated with the SMBH data (Shankar et al. 2016). It has also been noted that $\sigma_{\rm ap}(R_e)$ values cited in $M_{\rm BH}$–σ samples are systematically higher than values for the *same* galaxies in large data sets of early-type galaxies (Kormendy & Ho 2013).

3.3.1 Data

In the Kormendy & Ho (2013) sample, there are 60 galaxies flagged as early-types (ellipticals and lenticulars). There are also late-type galaxies, but these are excluded here, since the average trends constructed in Chapter 2 do not allow for the presence of discs. For each galaxy, Kormendy & Ho tabulate values and uncertainties for SMBH mass, K-band magnitudes and stellar velocity dispersions (measured within an effective radius, R_e). Total stellar masses are calculated here by combining K-band magnitudes with the mass-to-light ratios from Maraston's population synthesis models (assuming a Kroupa IMF and a stellar age of 9 Gyr).

The Kormendy & Ho (2013) compilation contains two compact ellipticals, M32 and NGC 4486B. Both of these are satellite galaxies, with M32 a companion of the Andromeda galaxy (M31), and NGC 4486B orbiting M87. Compact ellipticals are characterised by unusually high surface brightness for their given luminosity. Equivalently, they have a lower than average R_e compared to galaxies with similar luminosities (or stellar masses). It has been suggested that compact ellipticals occupy a similar parameter space to bulges of disk galaxies, so the two types could be related (e.g. Bender et al. 1992). The compact ellipticals in the Kormendy & Ho sample are flagged up as cyan points in plots including data for the rest of this Chapter.

In total, there are 22 galaxies (E and S0) that appear in both Kormendy & Ho and the ATLAS sample, with both tabulating $\sigma_{\rm ap}(R_e)$ and M_K values for each galaxy. Stellar masses are calculated by combining the absolute K-band magnitudes with $M_*/L_K = 0.88 M_\odot\, L_\odot^{-1}$, the value adopted for all of the ATLAS^{3D} galaxies in Chapter 2.

The top panel of Figure 3.4 shows total stellar mass versus stellar velocity dispersion, for various data sets. The magenta triangles are galaxies in the ACSVCS sample and the green squares are galaxies in the ATLAS sample. The black points are from the Kormendy & Ho (2013) data set, with red points representing ATLAS galaxies that also appear in Kormendy & Ho: these points are connected by red lines. The two cyan points correspond to the compact ellipticals M32 and NGC 4486B. The blue curve represents the average trend obtained in §2.2.6, assuming a Dehnen & McLaughlin (2005) dark matter halo and an ad-hoc relation between $F_{\rm ej}$ and $M_{*,\rm tot}$ (cf. §2.2.6.4).

This Figure shows two different issues with the SMBH data. Firstly, there appears to be a selection effect in the $M_{\rm BH}$–$\sigma_{\rm ap}(R_e)$ data. The black points generally lie to the right of the mean trend curves in the $M_{*,\rm tot}$–$\sigma_{\rm ap}(R_e)$ plane. Therefore, if a galaxy has a measured SMBH mass, then for a given $M_{*,\rm tot}$ (or equivalently, luminosity), the aperture velocity dispersion is likely to be larger than the average expected for galaxies of similar stellar mass. This bias has been discussed in the literature (Bernardi et al. 2007; van den Bosch et al. 2014b; Shankar et al. 2016), but it is an unsettled question as to why it exists.

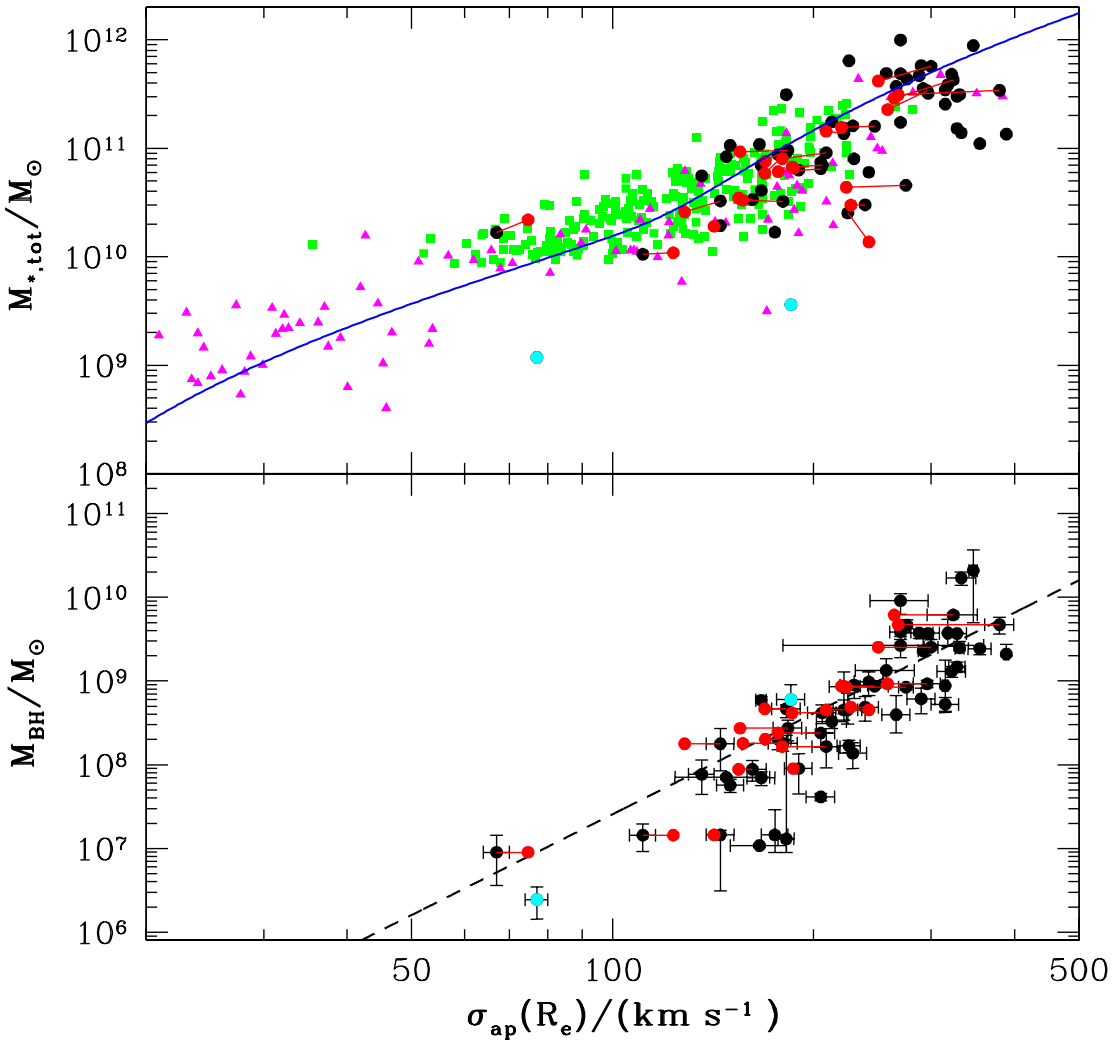

Figure 3.4: *Top panel:* Total stellar mass, $M_{*,\rm tot}$, at $z = 0$ versus stellar velocity dispersion at $z = 0$, $\sigma_{\rm ap}(R_e)$. The blue curve is for the average relation from the Jeans modelling calculation, discussed in §2.2.6, for a Dehnen & McLaughlin dark matter density profile and assuming the $F_{\rm ej}$–$M_{*,\rm tot}$ relation given by equation (2.50). The green squares represent galaxies in the ATLAS^{3D} survey, magenta triangles correspond to the ACSVCS data and black circles are early-type galaxies from the Kormendy & Ho (2013) compilation. Red circles represent galaxies in ATLAS that have a $M_{\rm BH}$ value in Kormendy & Ho. These are joined to the corresponding black points by red lines. *Bottom panel:* SMBH mass versus stellar velocity dispersion measured inside R_e at $z = 0$. The black points represent galaxies flagged as early types in Kormendy & Ho (2013) and the red points are galaxies in ATLAS with $M_{\rm BH}$ values. The cyan points are the two compact ellipticals, M32 and NGC 4886B.

Perhaps of more significance however is the disagreement between ATLAS and Kormendy & Ho on the value for $\sigma_{\rm ap}(R_e)$ in the same galaxies. The differences are shown by the red lines, connecting the location of a galaxy in the $\sigma_{\rm ap}(R_e)$–$M_{*,\rm tot}$ plane according to ATLAS (red points), to the location in this plane according to values cited by Kormendy & Ho (black points). In all but three of the galaxies in common, the measured velocity dispersion according to ATLAS is *lower* than the value in Kormendy & Ho (2013). In some cases, the difference between the two velocity dispersions is larger than 20%. Using the ATLAS velocity dispersions therefore moves the galaxies with measured $M_{\rm BH}$ to the left in the $M_{*,\rm tot}$–$\sigma_{\rm ap}(R_e)$ plane. This moves them back towards the average trend line and hence for the red points (galaxies with measured SMBH mass and velocity dispersions taken from ATLAS), there doesn't appear to be a selection bias.

The bottom panel of Figure 3.4 shows SMBH mass versus $\sigma_{\rm ap}(R_e)$. The black data points are for the E and S0 galaxies in the Kormendy & Ho (2013) compilation, except for the two compact ellipticals (M32 and NGC 4486B), shown by the cyan points. Red points are galaxies that are in both Kormendy & Ho and ATLAS, with velocity dispersions taken from ATLAS. Due to the Kormendy & Ho velocity dispersions generally being larger, using the ATLAS dispersions shifts the majority of the points in common to the left in the $M_{\rm BH}$–$\sigma_{\rm ap}(R_e)$ plane. Most of these have $\sigma_{\rm ap}(R_e) \lesssim 200\,{\rm km\,s^{-1}}$. However, the key point is that for $\sigma_{\rm ap}(R_e) > 200\,{\rm km\,s^{-1}}$, where the majority of the current M–σ data lies, there are very few galaxies with velocity dispersion measurements also in ATLAS. The ones that do are again shifted to the left.

Figure 3.5 shows stellar velocity dispersion at $z = 0$ (top panel) and SMBH mass (bottom panel) versus total stellar mass (at $z = 0$). The top panel is equivalent to the top panel of Figure 3.4. This once again illustrates the apparent selection bias associated with the $M_{\rm BH}$–σ sample; the black points generally lie above the mean trend, corresponding to larger $\sigma_{\rm ap}(R_e)$. However, for galaxies in common between ATLAS and Kormendy & Ho, using the ATLAS data for the $\sigma_{\rm ap}(R_e)$ and $M_{*,\rm tot}$ values (the red points), this selection bias disappears. The bottom panel supports the earlier claim that for the majority of the $M_{\rm BH}$–σ (and $M_{\rm BH}$–M_*) data, $\sigma_{\rm ap}(R_e) > 200\,{\rm km\,s^{-1}}$ and

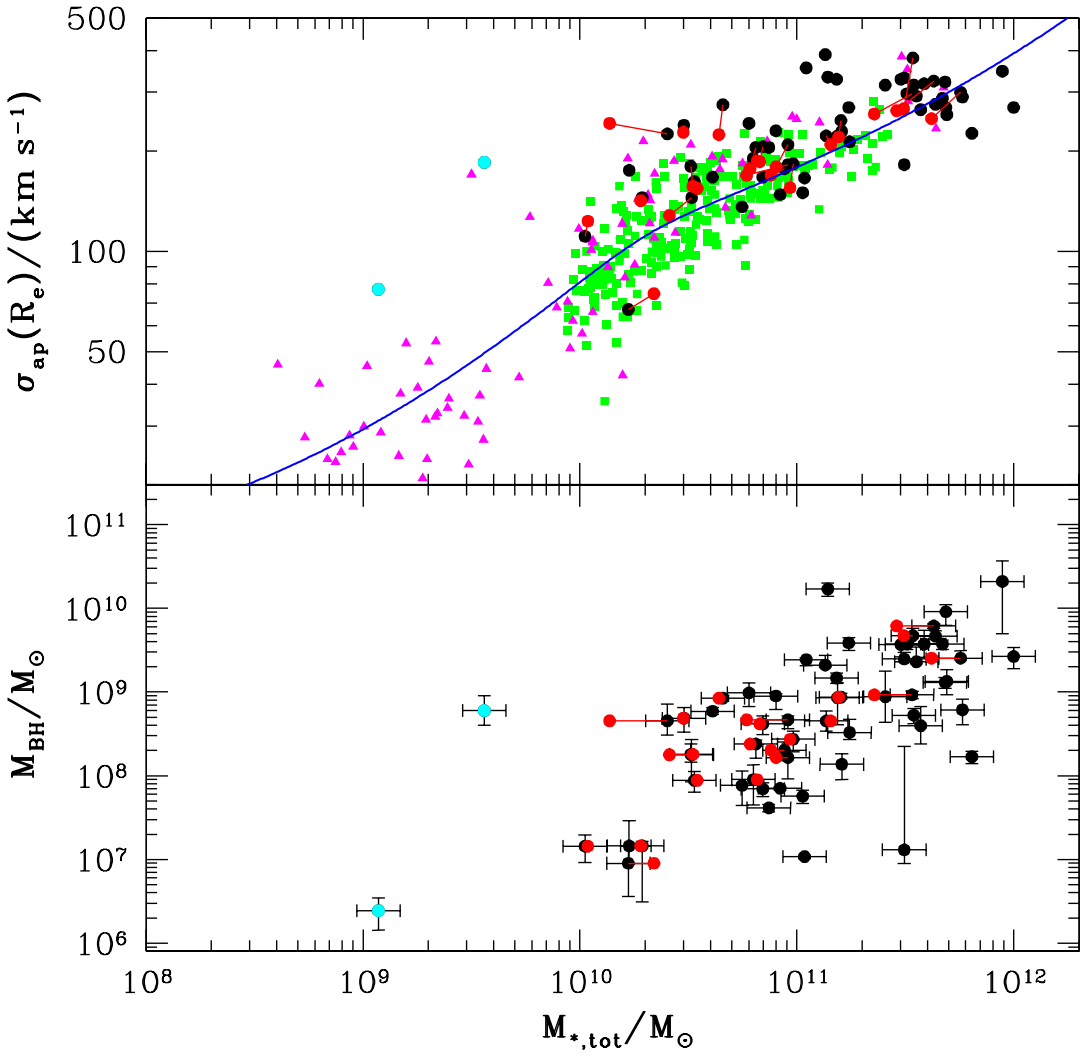

Figure 3.5: *Top panel:* Stellar velocity dispersion, $\sigma_{\rm ap}(R_e)$, at $z = 0$ versus total stellar mass, $M_{*,\rm tot}$, also at $z = 0$. As for the previous Figure, green points are ATLAS galaxies, magenta triangles are from ACSVCS and black points are from Kormendy & Ho (2013). Red points are also ATLAS galaxies, but have an $M_{\rm BH}$ value in Kormendy & Ho and are joined to the corresponding black points. The blue curves are the mean trend relations for a Dehnen & McLaughlin halo and the ad-hoc dependence of $F_{\rm ej}$ on total stellar mass. *Bottom panel:* $M_{\rm BH}$ versus total stellar mass at $z = 0$. Black points are from Kormendy & Ho, cyan points are the compact ellipticals (again from Kormendy & Ho) and red points are galaxies from ATLAS.

$M_{*,\mathrm{tot}} > 10^{11} M_{\odot}$. In this region, there are very few galaxies for which the Kormendy & Ho values can be "checked" against ATLAS. As for the velocity dispersions, stellar masses in ATLAS are generally smaller, so red points lie to the left of the corresponding black points.

Figure 3.6 shows the ratios (Kormendy & Ho to ATLAS) of stellar mass (top panels) and stellar velocity dispersion (bottom panels), as functions of the ATLAS σ_{ap} (left) and ATLAS $M_{*,\mathrm{tot}}$ (right), for each of the 22 galaxies in common. Typical error bars are shown in the top left corner of each panel. The horizontal error bars are calculated by taking the typical errors from ATLAS ($\sim 5\%$ for velocity dispersions and $\sim 1\%$ for K-band magnitudes, implying $\sim 20\%$ for $M_{*,\mathrm{tot}}$), and finding the rms average for the 22 galaxies in common — $\Delta\sigma_{\mathrm{ap}}(\mathrm{AT}) \equiv \langle[0.05\sigma_{\mathrm{ap}}(\mathrm{AT})]^2\rangle^{1/2}$ and $\Delta M_{*,\mathrm{tot}}(\mathrm{AT}) \equiv \langle[0.2M_{*,\mathrm{tot}}(\mathrm{AT})]^2\rangle^{1/2}$. Vertical error bars are calculated by a combining the ATLAS and Kormendy & Ho (2013) errors for each galaxy, giving an error bar for each ratio, and finding the rms average of these.

The Kormendy & Ho velocity dispersions and stellar masses are systematically higher than the ATLAS values, with $\langle\log[\sigma_{\mathrm{ap}}(KH)/\sigma_{\mathrm{ap}}(AT)]\rangle \simeq 0.040$ and $\langle\log[M_*(KH)/M_*(AT)]\rangle \simeq 0.05$. This implies that both stellar velocity dispersions and stellar masses are typically $\sim 10\%$ larger in Kormendy & Ho. For the stellar masses, this difference is less than the typical errors in the ratios, so isn't significant. However, there is a genuine disagreement for the measured velocity dispersions between ATLAS and M_{BH}–σ sample. The bottom right panel suggests that this discrepancy increases with stellar mass.

The issue with the velocity dispersions was also noted by Kormendy & Ho (2013). Kormendy & Ho propose that the difference in the $\sigma_{\mathrm{ap}}(R_e)$ values between themselves and ATLAS is due to how the aperture dispersion is defined. They suggest that ATLAS obtain σ_{ap} by averaging the projected dispersion, $\sigma_{\mathrm{p}}(R)$, weighted by luminosity:

$$\sigma_{\mathrm{ap}}(R_e) = \frac{\int_0^{R_e} I(R)\sigma_{\mathrm{p}}(R)RdR}{\int_0^{R_e} I(R)RdR}. \tag{3.6}$$

On the other hand, Kormendy & Ho work with the "Nuker" definition, which they

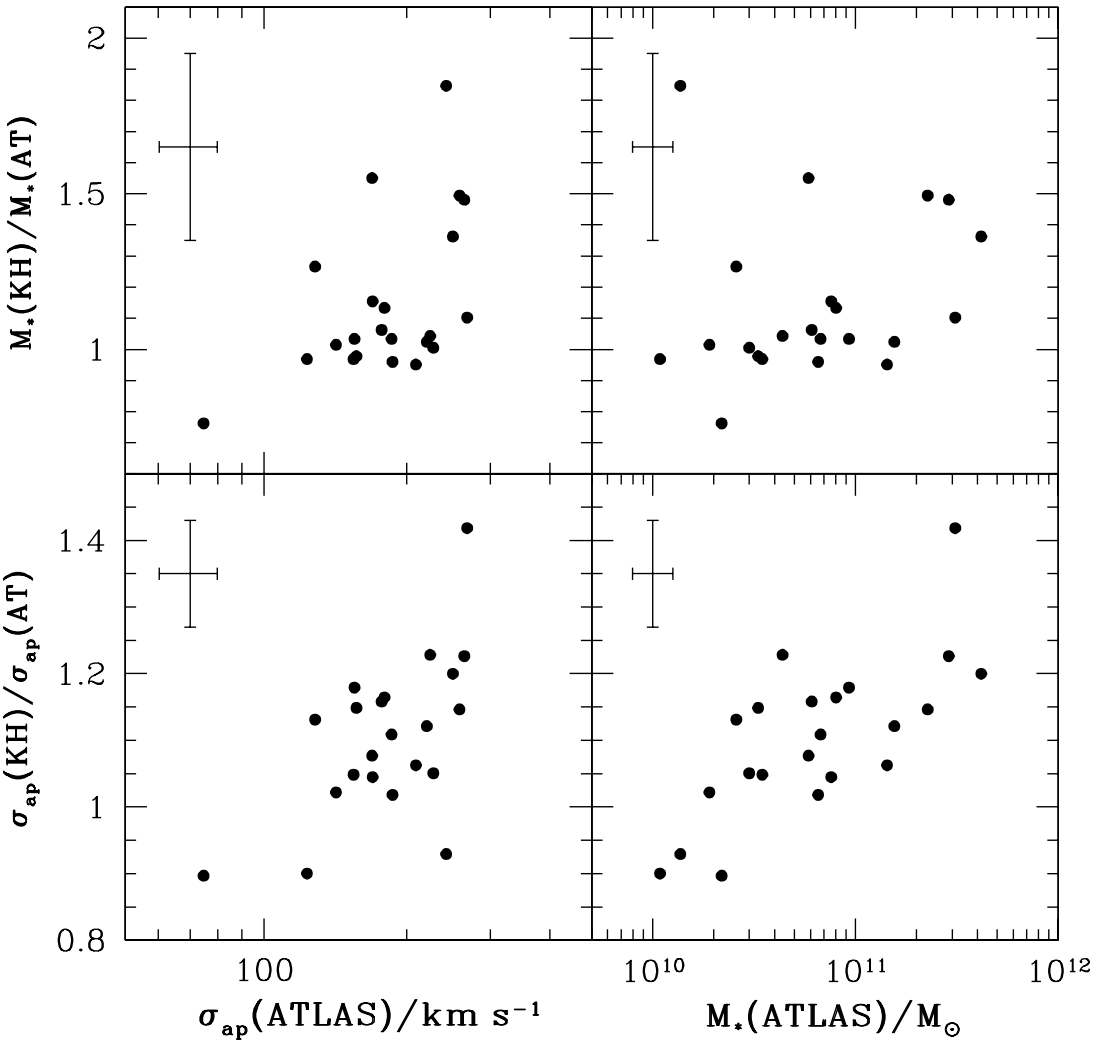

Figure 3.6: Data comparison for the 22 galaxies in common between Kormendy & Ho (2013) and ATLAS^{3D}. *Top panels:* Ratio of total stellar mass in Kormendy & Ho to stellar mass in ATLAS, as a function of ATLAS stellar velocity dispersion (left panel) and ATLAS $M_{*,\rm tot}$ (right panel). For both, the stellar mass was calculated using the K-band magnitudes in the two data sets, combined with the mass-to-light ratios used throughout. These are from the Maraston population synthesis models, for a Kroupa (2001) IMF and an assumed age of 9 Gyr, yielding $M/L_K \simeq 0.88$. *Bottom panels:* Ratio of stellar velocity dispersion (measured within R_e) in Kormendy & Ho to that in ATLAS, versus $\sigma_{\rm ap}$ (left) and $M_{*,\rm tot}$ (right; both from ATLAS). Typical error bars are shown in the top right corner of each panel. The calculation of these error bars is discussed in the text.

claim to be

$$\sigma^2_{\rm ap}(R_e) = \frac{\int_0^{R_e} I(R)\sigma^2_{\rm p}(R)dR}{\int_0^{R_e} I(R)dR}, \tag{3.7}$$

therefore averaging $\sigma^2_{\rm p}$, weighted by intensity.

The suggestions made by Kormendy & Ho appear to be inaccurate on two accounts. Firstly, it is clear from the ATLAS papers (Emsellem et al. 2007; Cappellari et al. 2011; Cappellari et al. 2013b; Cappellari et al. 2013a) that they do *not* define an aperture velocity dispersion as in equation (3.6). In fact, they define $\sigma_{\rm ap}(R_e)$ by averaging $\sigma^2_{\rm p}$ and weighting by luminosity. This is the same definition used to calculate $\sigma_{\rm ap}(R_e)$ here, i.e.,

$$\sigma^2_{\rm ap}(R_e) = \frac{\int_0^{R_e} I(R)\sigma^2_{\rm p}(R)RdR}{\int_0^{R_e} I(R)RdR}. \tag{3.8}$$

Secondly, it isn't clear that the "Nuker" definition is what Kormendy & Ho suggest [equation (3.7)]. One of the earlier Nuker papers (Gebhardt et al. 2000) clearly states that they define an aperture dispersion as "the luminosity-weighted line-of-sight dispersion inside a radius R_e." This is equivalent to the definition in equation (3.8).

To summarise then, there are significant issues with the data. Comparing the SMBH data to the larger sample of early-type galaxies from ATLAS appears, at first, to show a selection bias. For a given stellar mass, velocity dispersions in the SMBH data are higher than average. However, for galaxies in common between ATLAS and the Kormendy & Ho compilation, there is a disagreement for what the value of $\sigma_{\rm ap}(R_e)$ should be. If the ATLAS value for the velocity dispersion is used instead, then there is no selection bias for these galaxies. The discrepancy between the ATLAS velocity dispersions and the ones cited by Kormendy & Ho is presumably a measurement issue and is not understood, and as yet has not been well explained.

In terms of the work here, the Kormendy & Ho (2013) compilation is used to compare to the model predictions obtained from average trend lines. The average trends were calibrated against the ATLAS data, for which there are only 22 systems with measured SMBH masses. It is necessary to compare the predictions against the largest possible data set, provided by Kormendy & Ho (2013). Furthermore, the

majority of the $M_{\rm BH}$–σ data have $\sigma_{\rm ap}(R_e) \gtrsim 200\,{\rm km\,s^{-1}}$ (or $M_{*,\rm tot} \gtrsim 10^{11} M_\odot$). In this region, there are only 9 or so galaxies in ATLAS that also have $M_{\rm BH}$, an insufficient sample size for comparing against model curves.

3.3.2 $M_{\rm BH}$ versus $\sigma_{\rm ap}(R_e)$

The model predictions for the $M_{\rm BH}(z)$–bulge property relations are now compared directly against the SMBH data. As for the trend lines in Chapter 2, there is significant intrinsic scatter around the model predictions. This is inevitable and can contain physical information, but is not characterised or explained here, although it is quantified by considering the rms scatter and errors of the data. A discussion on the scatter is left for Chapter 5.

Figure 3.7 shows SMBH mass versus $\sigma_{\rm ap}(R_e)$ at $z = 0$. The data points are for the 60 E and S0 galaxies in the Kormendy & Ho (2013) compilation. The two cyan points are for the compact ellipticals, M32 and NGC 4486B. Both of these galaxies appear unremarkable in the $M_{\rm BH}$–$\sigma_{\rm ap}(R_e)$ plane. The blue curves in the top panel of Figure 3.7 come from equation (3.1), with $V_{\rm d,pk}$ at $z_{\rm qso} = 0, 1, 2, 3$ and 4 given as a function of $\sigma_{\rm ap}(R_e)$ at $z = 0$. These curves are also shown in the bottom right panel of Figure 3.3. They all assume a Dehnen & McLaughlin (2005) dark matter density profile; the results for an NFW halo and a Hernquist (1990) halo are shown in the middle panel (black curves) and bottom panel (red curves) respectively. The black dashed line in each of the panels, shown only for reference, corresponds to equation (3.1) evaluated with a protogalactic gas-to-dark matter mass ratio of $f_0 = 0.18$ [the value of $\Omega_{\rm b,0}/(\Omega_{\rm m,0} - \Omega_{\rm b,0})$ in the 2013 *Planck* cosmology], and the simplistic substitution $V_{\rm d,pk} = \sqrt{2}\sigma_{\rm ap}(R_e)$.

The curves that assume an $M_{\rm BH}$–$V_{\rm d,pk}$ relation from the clearing of protogalaxies by quasar-mode feedback at redshifts $2 \leq z_{\rm qso} \leq 4$ enclose almost all of the M–σ data at $z = 0$. The correspondence of this redshift range with the epoch of peak quasar activity and SMBH accretion rate in both observations (Richards et al. 2006; Hopkins, Richards & Hernquist 2007; Delvecchio et al. 2014) and cosmological simulations (Di Matteo et al. 2008; Sijacki et al. 2007; Sijacki et al. 2015) is particularly encouraging. Equation

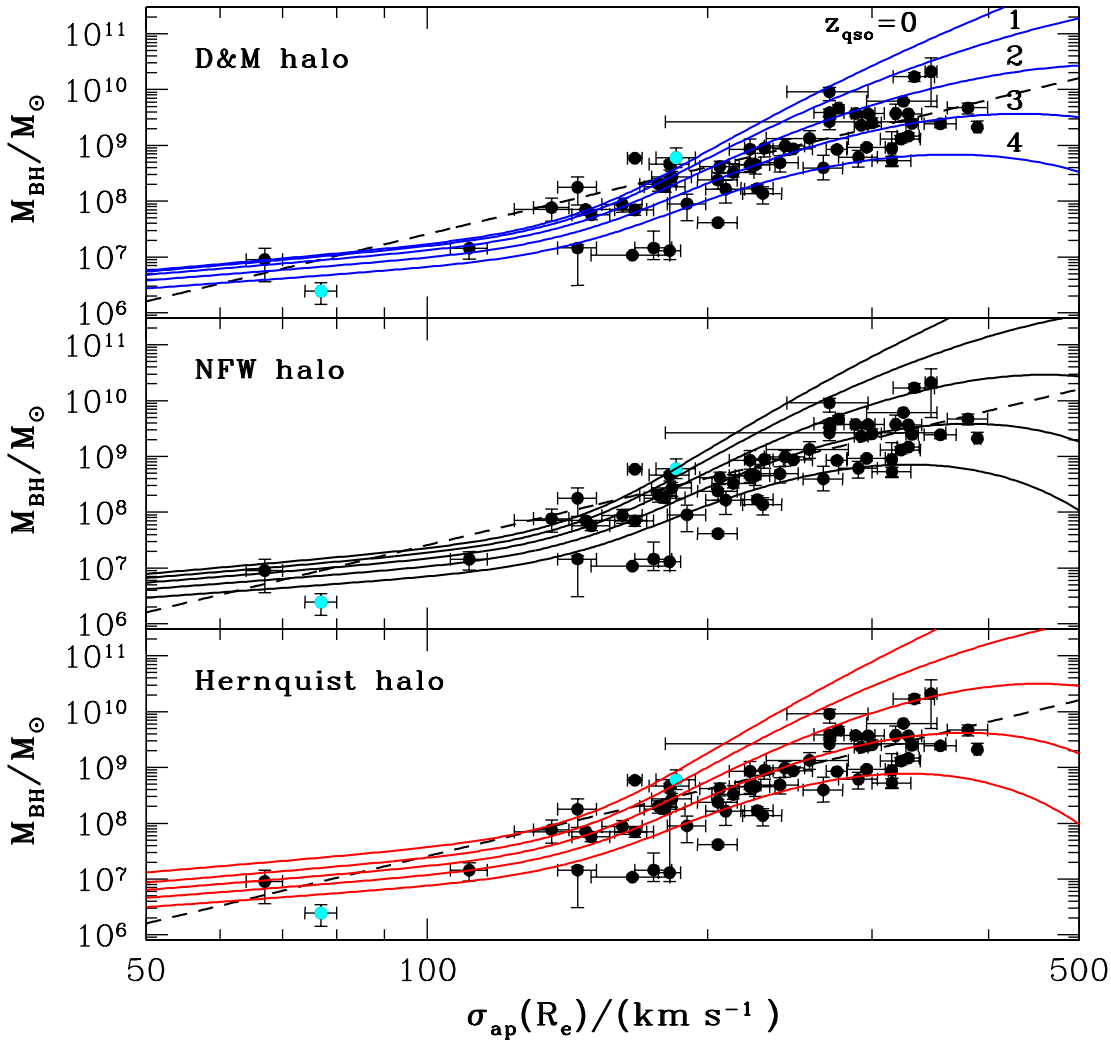

Figure 3.7: SMBH mass versus stellar velocity dispersion measured inside R_e at $z = 0$. The data points represent galaxies flagged as early types in Kormendy & Ho (2013). *Top panel:* The solid blue curves are the models for $M_{\rm BH}$ versus $\sigma_{\rm ap}(R_e)$ at $z = 0$, assuming a relation $M_{\rm BH} \propto V_{\rm d,pk}^4$ was established by accretion-driven feedback, according to equation (3.1), at redshift $z_{\rm qso} = 0, 1, 2, 3$ or 4. These curves all assume a Dehnen & McLaughlin halo for the dark matter density profile, and a spatially constant gas-to-dark matter mass ratio $f_0 = 0.18$ in the protogalaxies. They do not include any SMBH growth between $0 < z < z_{\rm qso}$; see text for discussion. *Middle panel:* Same as top panel, but for an NFW halo for the dark matter (black curves). *Bottom panel:* Same as top two panels, but for a Hernquist halo for the dark matter (red curves). In all three panels, the dashed black line shows equation (3.1) with $V_{\rm d,pk} = \sqrt{2}\sigma_{\rm ap}(R_e)$.

(3.1) represents a simplified picture of just a few processes at a critical stage of galaxy and SMBH formation, as well as assuming purely momentum-driven feedback, but the fundamental connection it makes between the protogalactic dark matter halos and SMBH masses appears to be along the right lines.

A simple $M_{\rm BH}$–$V_{\rm d,pk}$ prediction leads to model curves for $M_{\rm BH}$–$\sigma_{\rm ap}(R_e)$ that are distinctly non-linear. Contrary to the suggestion by Kormendy & Ho (2013), this curvature is easily accommodated by the data, and is reminiscent of the log-quadratic fitting by Wyithe (2006a,b). The upward bend seen in all the curves around $\sigma_{\rm ap}(R_e) \approx 140\,{\rm km\,s^{-1}}$ can be traced back to the peak at $M_{*,\rm tot} \simeq 3.4 \times 10^{10} M_\odot$ (at $z = 0$) in the global ratio of stellar-to-dark matter mass, $f_{*,\rm vir}$, for the central galaxies of halos (see the top panel of Figure 2.6). This leads to a highly non-linear relation between the dark matter $V_{\rm d,pk}$ at any redshift and $\sigma_{\rm ap}(R_e)$ at $z = 0$ (see middle right panel of Figure 3.3), ultimately leading to the distortion of the linear $M_{\rm BH}$–$V_{\rm d,pk}$ relation. Roughly speaking, the curves with $2 \leq z_{\rm qso} \leq 4$ in Figure 3.7 have average slopes $\Delta \log M_{\rm BH} / \Delta \log \sigma_{\rm ap}(R_e) \approx 1.5$–$2$ for velocity dispersions $50 \leq \sigma_{\rm ap}(R_e) \leq 100\,{\rm km\,s^{-1}}$, and much steeper $\Delta \log M_{\rm BH} / \Delta \log \sigma_{\rm ap}(R_e) \approx 5$–$6$ for $200 \leq \sigma_{\rm ap}(R_e) \leq 300\,{\rm km\,s^{-1}}$.

The intrinsic scatter around any one of the model curves can be calculated. First of all, the rms scatter, $\Delta^2_{\rm rms}$, around a curve in the vertical direction is calculated. This is quantified by squaring the difference between the measured $M_{\rm BH}$ and the expected $M_{\rm BH}$ (from the curve) for each galaxy, adding all these up and dividing by the total number of galaxies in the sample. The rms error, $\sigma^2_{\rm rms}$, is calculated by summing over the squares of the $M_{\rm BH}$ error bars for each galaxy. Finally, the intrinsic scatter is then $\sqrt{\Delta^2_{\rm rms} - \sigma^2_{\rm rms}}$.

For the model prediction with $z_{\rm qso} = 3$ in the $M_{\rm BH}$–$\sigma_{\rm ap}(R_e)$ plot, the intrinsic scatter around the curve is $\simeq 0.39$ dex. This is an encouraging result, given the curve is based on a physical model, and is not a best fit to the data. As discussed, Kormendy & Ho (2013) found for a linear best fit that the intrinsic scatter was ~ 0.3 dex (although this also included classical bulges that are not considered here). Some of the intrinsic scatter seen in the SMBH data around the model curve *could* be due to the value of $z_{\rm qso}$, but it is unclear how much given all the other sources of scatter (around the

average trends used to obtain the model predictions and due to gas-poor mergers at low redshifts; see below).

The flattening of the model $M_{\rm BH}$–$\sigma_{\rm ap}(R_e)$ relations at very high $\sigma_{\rm ap}(R_e) \geq 300$–$350\,{\rm km\,s^{-1}}$ is more pronounced for higher $z_{\rm qso}$. This reflects the behaviour of progenitor masses and circular-speed peaks at $z > 0$ as functions of $M_{\rm d,vir}(0)$ and $\sigma_{\rm ap}(R_e)$ at $z = 0$, discussed in §3.2. However, this feature is not expected to be seen in any M–σ data. It is most prominent in the galaxy mass range where gas-poor mergers at low redshifts should increase SMBH masses by the most from $M_{\rm BH}$ at $z = z_{\rm qso}$.

3.3.2.1 Gas-poor mergers at low redshift

Volonteri & Ciotti (2013) perform cosmological simulations of black hole growth in the central galaxies of halos with $10^{13} M_\odot \leq M_{\rm d,vir}(0) \leq 10^{15} M_\odot$ at $z = 0$. They track contributions from gas accretion and from SMBH coalescences in gas-poor merger separately. For six example halos with $M_{\rm d,vir}(0) = 10^{15} M_\odot$, their results show that SMBH growth via accretion is essentially finished by $z \approx 2$–3. This redshift is what I refer to as $z_{\rm qso}$. Coalescences in gas-poor mergers drive any growth for $z < z_{\rm qso}$, ultimately increasing the SMBH masses by a wide range of factors, $f_{\rm co} \equiv M_{\rm BH}(0)/M_{\rm BH}(z_{\rm qso}) \simeq 1$–$30$. For a larger sample of $10^{15} M_\odot$ mass halos, Volonteri & Ciotti (2013) report an average $\langle f_{\rm co} \rangle \approx 11 \pm 10$. The scaling relations presented in Chapter 2 give $M_{*,\rm tot} \simeq 10^{12} M_\odot$ and $\sigma_{\rm ap}(R_e) \approx 350$–$400\,{\rm km\,s^{-1}}$ (depending on dark matter density profile) for $M_{\rm d,vir}(0) = 10^{15} M_\odot$. The highest data point in Figure 3.7 lies close to this region: NGC4889 in the Coma Cluster, with $\sigma_{\rm ap}(R_e) = 347 \pm 17 {\rm km\,s^{-1}}$, according to McConnell et al. (2012).

For lower mass systems, there is typically much less SMBH growth via dry mergers at redshifts $z < z_{\rm qso}$. For the central galaxies of halos with $2 \times 10^{13} M_\odot \leq M_{\rm d,vir}(0) \leq 10^{14} M_\odot$ (implying $M_{*,\rm tot} \simeq 2$–$4 \times 10^{11} M_\odot$ and $\sigma_{\rm ap}(R_e) \simeq 220$–$275\,{\rm km\,s^{-1}}$), Volonteri & Ciotti (2013) give average $\langle f_{\rm co} \rangle \approx 2 \pm 1$. Further, for a set of $10^{13} M_\odot$ mass halos (corresponding to $M_{*,\rm tot} \simeq 1.4 \times 10^{11} M_\odot$ and $\sigma_{\rm ap}(R_e) \simeq 200\,{\rm km\,s^{-1}}$), they find $\langle f_{\rm co} \rangle \approx 1.8 \pm 1.8$ (suggestive of a small systematic effect, with a few strong outliers). It

should be noted that Volonteri & Ciotti (2013) do not show explicitly for any of their halos with $M_{\rm d,vir}(0) < 10^{15} M_{\odot}$ that accretion driven growth of the SMBH is negligible after $z_{\rm qso} \sim 2$–3. However, other simulations imply that this is generally the case (e.g. Sijacki et al. 2007; Di Matteo et al. 2008).

Overall then, at the top end of the M–σ relation, dry mergers are expected to scatter the data significantly upwards from the model curves in Figures 3.7, by up to an order of magnitude in some cases. This will erase the flattening of the curves in the range $\sigma_{\rm ap}(R_e) \approx 300$–$350\,{\rm km\,s^{-1}}$ and could ultimately appear as a much steeper mean relation there. At more modest $\sigma_{\rm ap}(R_e) \leq 300\,{\rm km\,s^{-1}}$, there will still be some upward scatter of the data from gas-poor merging, but less of it. The net shift in the mean-trend curves in Figure 3.7 could possibly amount to a factor of $\approx$ 2–3 in the main (possibly less for the lowest $\sigma_{\rm ap}(R_e) \leq 200\,{\rm km\,s^{-1}}$) and should largely preserve their overall shape.

3.3.2.2 Discussion

There are some obvious reasons why the curves in Figure 3.7 may represent upper limits to the self-limiting SMBH mass from accretion driven growth at $z \geq z_{\rm qso}$. First, if the baryon-to-dark matter mass ratio in a gaseous protogalaxy is anything less than the cosmic average during a quasar-mode accretion event, then equation 3.1 should be evaluated with $f_0 < 0.18$. At a fixed $z_{\rm qso}$ and $V_{\rm d,pk}$, this will decrease the critical $M_{\rm BH}$ for blow-out, since $M_{\rm BH} \propto f_0$. Second, equation (3.1) ignores any prior work done by a growing SMBH to push the protogalactic gas outwards before the final blow-out, and therefore over-estimates the required SMBH mass to clear a halo at $z_{\rm qso}$. Related to this, lower $M_{\rm BH}$ values than equation (3.1) may be sufficient to clear the gas to regions that are "far enough" away from a central SMBH to shut down growth via accretion, without expelling it past the virial radius.

Cosmological simulations are required to evaluate the balance between these effects pulling the model $M_{\rm BH}$–$\sigma_{\rm ap}(R_e)$ relations downwards and the competing effects of low-redshift mergers pushing them upwards. However at this level, the more funda-

mental simplifications behind the SMBH critical mass prediction need to be improved first. In Chapter 4, the effects of the protogalactic gas *not* being virialised (gas does not trace dark matter), and allowing for the presence of stars in the protogalaxies are investigated. The analytical scalings developed in Chapter 2, and the general procedure applied in this Chapter provide a way to assess the main implications of any changes, by checking them against the M–σ data, without resorting immediately to numerical simulations.

Before looking at this, there are correlations between SMBH mass and other galaxy properties ($M_{*,\mathrm{tot}}$ and $M_{\mathrm{d,vir}}$, as well as combinations of σ_{ap} and R_e) to be considered. The empirical M_{BH}–σ_{ap} correlation takes on particular importance in the context of self-regulated feedback models, as the velocity dispersion should reflect the depth of the potential well from which SMBH feedback had to expel the protogalactic gas. However, whether any one of the observed correlations is more fundamental than the others remains an open question (Kormendy & Ho 2013; Shankar et al. 2016).

3.3.3 M_{BH} versus M_*

Figure 3.8 show SMBH mass versus $M_{*,\mathrm{tot}}$ at $z = 0$. The data points are again for the E and S0 galaxies in the Kormendy & Ho (2013) data set. The cyan points are again the two compact ellipticals, M32 and NGC 4886B. For early-type galaxies, $M_{*,\mathrm{tot}}$ is equivalent to stellar bulge mass, M_{bulge}. The blue curves in the top panel of Figure 3.8 represent equation (3.1) evaluated with $f_0 = 0.18$ and $V_{\mathrm{d,pk}}(z_{\mathrm{qso}})$ at $z_{\mathrm{qso}} = 0, 1, 2, 3$ and 4. These curves are also shown in the bottom left panel of Figure 3.3 and are for a Dehnen & McLaughlin (2005) dark matter density profile: the NFW (middle panel) and Hernquist (bottom panel) profiles are also shown.

Before discussing the M_{BH}–$M_{*,\mathrm{tot}}$ relation in detail, it is first worth noting the cyan point lying furthest above the curves (with $M_{*,\mathrm{tot}} \simeq 4 \times 10^9 M_\odot$ and $M_{\mathrm{BH}} \simeq 6 \times 10^8 M_\odot$), representing the compact elliptical NGC 4486B. This small early-type is a satellite galaxy of M87, the giant elliptical at the centre of the Virgo A cluster. NGC 4486B clearly has an SMBH that is far too big for its given stellar mass. One

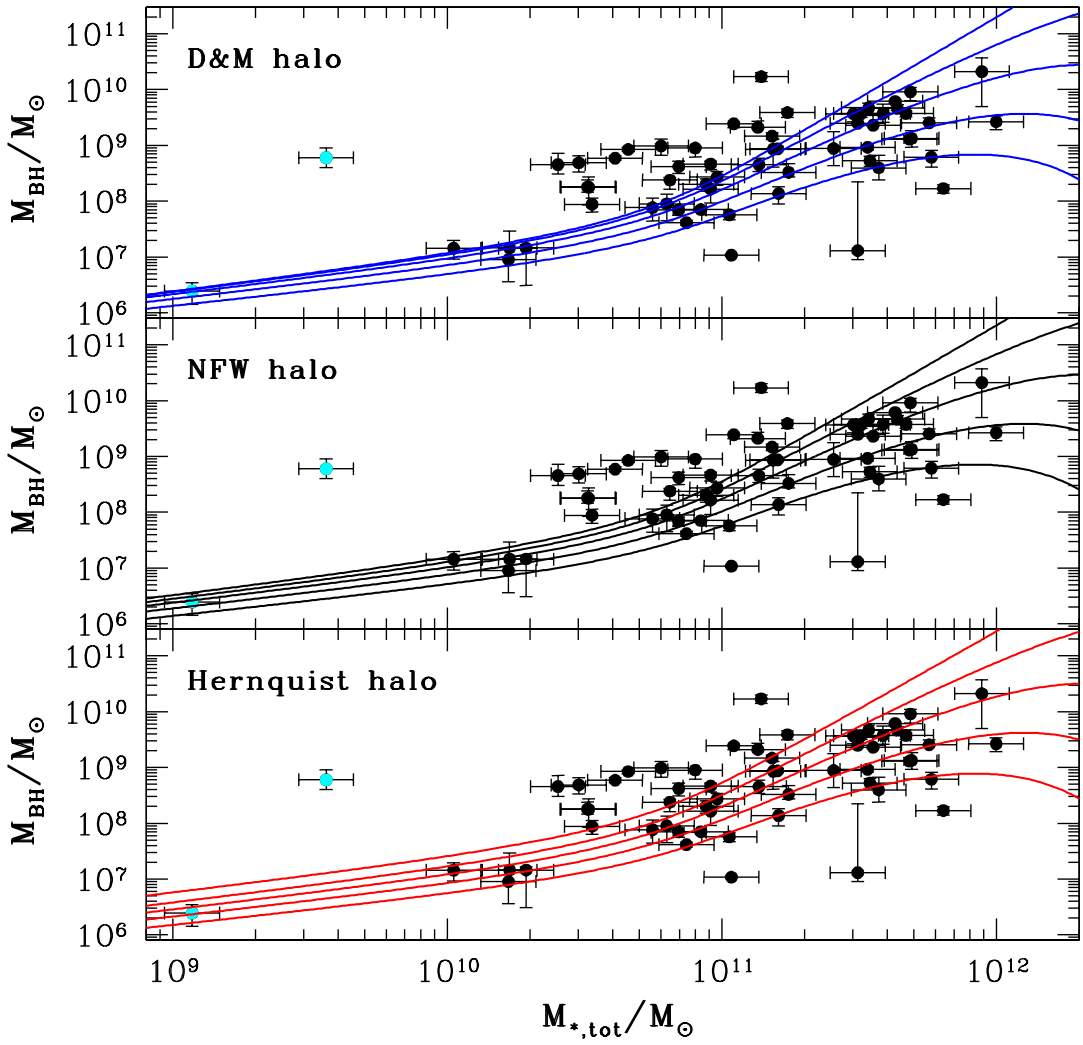

Figure 3.8: SMBH mass versus total stellar mass at $z = 0$. The data points represent galaxies flagged as early types in Kormendy & Ho (2013). The cyan point corresponds to NGC 4886B, a satellite of M87 (the giant elliptical at the centre of the Virgo A cluster). *Top panel:* The solid blue curves are the models for $M_{\rm BH}$ versus $M_{*,\rm tot}$ at $z = 0$, assuming a relation $M_{\rm BH} \propto V_{\rm d,pk}^4$ was established by accretion-driven feedback, according to equation (3.1), at redshift $z_{\rm qso} = 0, 1, 2, 3$ or 4. These curves all assume a Dehnen & McLaughlin halo for the dark matter density profile, and a spatially constant gas-to-dark matter mass ratio $f_0 = 0.18$ in the protogalaxies. Again, they do not include any SMBH growth between $0 < z < z_{\rm qso}$. *Middle panel:* Same as above, but for an NFW halo for the dark matter (black curves). *Bottom panel:* Equivalent to the top two, with a Hernquist halo for the dark matter (red curves).

possible explanation (Kormendy & Ho 2013) is that it could have been been tidally stripped of stellar mass as it orbits M87. However, this is unlikely to fully explain the deviation seen in Figure 3.8. NGC 4486B has a stellar mass approximately 1–2 orders of magnitude smaller than systems with similar $M_{\rm BH}$ values. This suggests it has lost $\sim$ 90–99% of its original stellar mass through tidal stripping. The location of this system in the $M_{\rm BH}$–M_* plane is not yet fully understood, particularly given that the other compact elliptical in this sample, M32, is consistent with the curves. As mentioned, neither M32 nor NGC 4486B appear unusual in the $M_{\rm BH}$-$\sigma_{\rm ap}(R_e)$ plane.

As for the M–σ relation, the curves in Figure 3.8 are very much non-linear, with a sharp upward bend around $M_{*,\rm tot} \simeq 4\times10^{10}M_\odot$. This can again be traced back to the non-linear $f_{*,\rm vir}$–$M_{*,\rm tot}$ relation. The flattening of the curves at $M_{*,\rm tot} \geq 5\times10^{11}M_\odot$ is a reflection of the fact that larger systems were formed more recently. The arguments in §3.3.2 regarding gas-poor mergers scattering $M_{\rm BH}$ masses upwards with respect to the curves applies here as well.

Broadly speaking, the curves are in good agreement with the data. At the higher mass end, with $M_{*,\rm tot} \geq 2\times10^{11}M_\odot$, the curves with $z_{\rm qso} = 1$–4 bracket the majority of the $M_{\rm BH}$–M_* data. In the range $10^{10}M_\odot \lesssim M_{*,\rm tot} \lesssim 10^{11}M_\odot$, there are a handful of data points that lie above the curve. This could, in part, be due to the imperfect connection between $\sigma_{\rm ap}(R_e)$ and $M_{*,\rm tot}$. The intrinsic scatter around the $z_{\rm qso} = 3$ model curve is $\simeq 0.7$ dex, more than double the value from the Kormendy & Ho (2013) linear best-fit (although again, the Kormendy & Ho value includes classical bulges). However, the $z_{\rm qso} = 3$ curve is for a physical model, whereas Kormendy & Ho (2013) were looking for a linear best-fit that minimized the intrinsic scatter. Again, the value of $z_{\rm qso}$ itself could contribute to the scatter, but without a more detailed analysis, it is unclear how much.

3.3.4 Relating SMBHs to halo masses

As discussed, the critical SMBH mass obtained by McQuillin & McLaughlin (2012) relates $M_{\rm BH}$ to $V_{\rm d,pk}$ at the time of quasar-mode blow-out. It is therefore the dark

matter, dominating the potential well that the gas must escape from, that is significant in determining this critical SMBH mass. In this scenario, the observed correlations at $z = 0$ between $M_{\rm BH}$ and the *stellar* properties simply reflect this more fundamental relation. A more accurate reflection of the $M_{\rm BH}$–$V_{\rm d,pk}$ relation at $z_{\rm qso}$ may be provided if the SMBH mass can be directly related to global properties of the dark matter halo at $z = 0$.

The connection between the total (stars and dark matter) circular speed at (or close to) the effective radius, $V_c(R_e)$, and the aperture velocity dispersion, $\sigma_{\rm ap}(R_e)$, is commonly used in the literature as a starting point to connect $M_{\rm BH}$ and $M_{\rm d,vir}$ or $M_{\rm d,200}$ (e.g., Ferrarese 2002, Croton et al. 2009, Bandara et al. 2009, Dutton et al. 2010). In short, the observed circular speed, $V_c(R_e)$, is transformed to $V_c(r_{\rm vir})$ [or $V_c(r_{200})$] and combined with the overdensity definition [$M_{\rm d,vir} \propto r_{\rm vir}^3$], giving a relation between $\sigma_{\rm ap}$ and $M_{\rm d,vir}$ (or $M_{\rm d,200}$). By folding in a best fitting power-law relation for $M_{\rm BH}$–σ from the literature (observational), the authors are then able to ultimately derive an $M_{\rm BH}$–$M_{\rm d,200}$ relation.

Observational and theoretical studies of the $M_{\rm BH}$–$M_{\rm d,200}$ relation generally imply a single power-law relation, with a slope of ~ 1.4–1.8 (Ferrarese 2002; Bandara, Crampton & Simard 2009; Croton 2009; Bogdán & Goulding 2015). However, such a result relies on the simplifying assumption that the observed circular-speed is proportional to the circular-speed at the virial radius, independent of $M_{*,\rm tot}$: $V_{\rm opt} = \gamma V_{200}$ [a singular isothermal sphere corresponds to $\gamma = 1$]. However, this is not true in general (cf. §2.2.8.2). Ferrarese (2002) did point out that assuming $V_{\rm opt} \sim V_{200}$ is only good as a zeroth order approximation. However, she did not account for the halo mass dependence of the global stellar-to-dark matter mass ratio (a $M_{\rm d,vir}$–$M_{*,\rm tot}$ relation) or the halo progenitor evolution with redshift. Both of these contribute to relations between the SMBH and bulge properties being highly non-linear. Therefore, a linear $M_{\rm BH}$–$M_{\rm d,200}$ relation is obtained by Ferrarese (and others), primarily because $M_{\rm BH}$–σ is taken to be a single power-law and $M_{\rm d,vir}$–$M_{*,\rm tot}$ is taken to be linear in their calculations.

In this subsection, the dark matter halo mass at r_{200} is used instead of $M_{\rm d,vir}$. This is so that a direct comparison can be made between the calculations here and a

similar analysis by Dutton et al. (2010). For a given dark matter halo model, the ratio $M_{d,200}/M_{\rm d,vir}$ is calculated by evaluating the mass profile at r_{200} and $r_{\rm vir}$, combined with the overdensity definitions, $M_{\rm d,vir} \propto \Delta_{\rm vir} r_{\rm vir}^3$ and $M_{\rm d,200} \propto 200 r_{200}^3$. For a given $M_{*,\rm tot}$, the value of $f_{*,\rm vir}$ fixes the virial halo mass. This in turn fixes both $r_{\rm vir}$ and r_{-2} through the concentration relation with $M_{\rm d,vir}$. The mass profiles can then be manipulated to solve for r_{200}, and hence $M_{\rm d,200}/M_{\rm d,vir}$. For a Dehnen & McLaughlin halo, $M_{\rm d,200}/M_{\rm d,vir} \simeq 0.8$, with a very weak dependence on $M_{*,\rm tot}$.

Figure 3.9 shows the $M_{\rm BH}(z)$–$M_{\rm d,200}(0)$ relation. The data points represent the early-type galaxies (E and S0) in the Kormendy & Ho (2013) sample. $M_{\rm d,200}$ values are calculated for each galaxy by taking the tabulated $\sigma_{\rm ap}(R_e)$ from Kormendy & Ho (2013) and taking the dark matter virial mass implied by the $\sigma_{\rm ap}(R_e)$–$M_{\rm d,vir}$ average trend line at $z = 0$. The halo mass at r_{200} is then calculated by using the $M_{\rm d,200}$– $M_{\rm d,vir}$ relation. The solid blue curves assume a relation $M_{\rm BH} \propto V_{\rm d,pk}^4$ was established by accretion-driven feedback, according to equation (3.1), at redshift $z_{\rm qso} = 0, 1, 2, 3$ or 4. These curves all assume a Dehnen & McLaughlin halo for the dark matter density profile, and a spatially constant gas-to-dark matter mass ratio $f_0 = 0.18$ in the protogalaxies. The red line segments correspond to $M_{\rm BH} \propto M_{\rm d,200}^{1.4}$ and $M_{\rm BH} \propto M_{\rm d,200}^{0.65}$. These are the approximate slopes suggested by Dutton et al. (2010) for their $M_{\rm BH}$–$M_{\rm d,200}$ relation (see below). Given that the $M_{\rm d,200}$ values for each galaxy are obtained through the trend line for $\sigma_{\rm ap}(R_e)$–$M_{\rm d,vir}$, the intrinsic scatter around individual curves is the same as for the $M_{\rm BH}$–$\sigma_{\rm ap}(R_e)$ relation. For the $z_{\rm qso} = 3$ curve, the intrinsic scatter is $\simeq 0.39$.

The overall shape of these predictions is again noteworthy, with the upward bend seen in the $M_{\rm BH}$–σ curves no longer present. This is because the stars do not affect a relation between the SMBH mass and the mass of the dark matter halo measured on a global scale (the global stellar-to-dark matter mass ratio, $f_{*,\rm vir}$ or $f_{*,200}$, is always $\lesssim 5\%$). The flattening seen toward larger halo masses for higher $z_{\rm qso}$ values reflects the generic feature of hierarchical merging: the largest halos formed most recently. Approximating the $z_{\rm qso} = 3$ curve from Figure 3.9 with a double power-law yields slopes of ~ 1.1 for lower mass halos and ~ 0.6 for higher masses. These are similar to the slopes suggested by Dutton et al. (2010), shown by the red lines.

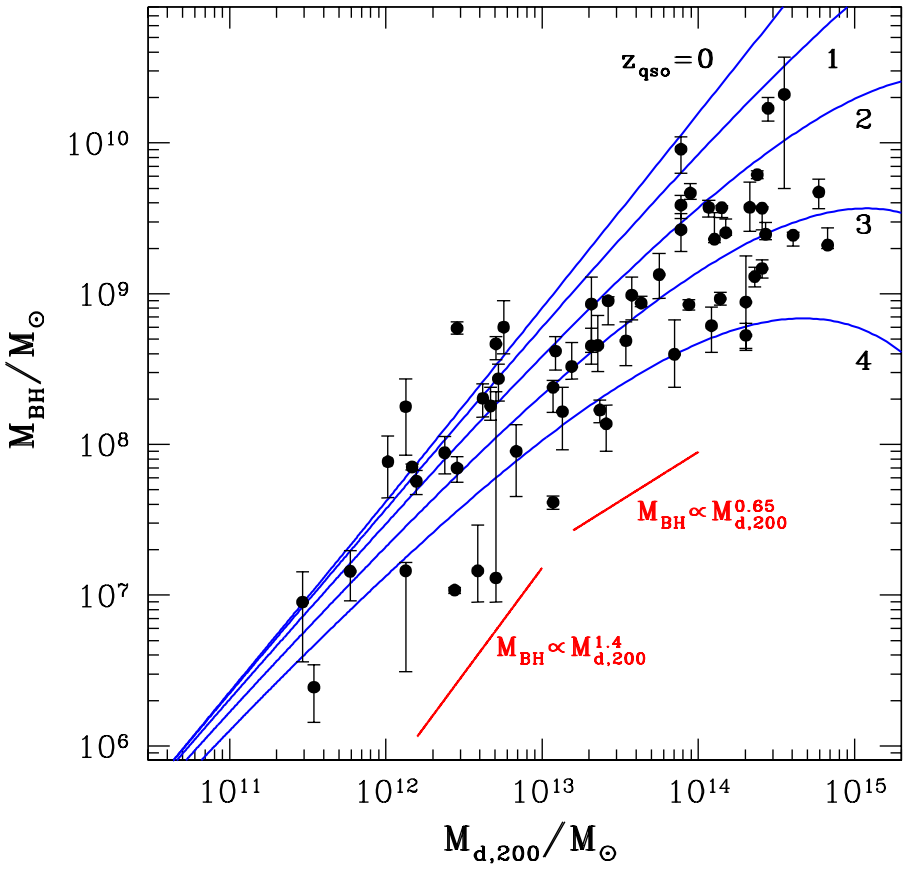

Figure 3.9: SMBH mass versus dark matter halo mass inside the r_{200} radius, $M_{\rm d,200}$, at $z = 0$. The data points represent galaxies flagged as early-types by Kormendy & Ho (2013). To calculate an $M_{\rm d,200}$ value for each galaxy the tabulated $\sigma_{\rm ap}(R_e)$ values have been folded through the scaling relations. The solid blue curves are the models for $M_{\rm BH}$ versus $M_{\rm d,200}$ at $z = 0$, assuming a relation $M_{\rm BH} \propto V_{\rm d,pk}^4$ was established by accretion-driven feedback, according to equation (3.1), at redshift $z_{\rm qso} = 0, 1, 2, 3$ or 4. These curves all assume a Dehnen & McLaughlin halo for the dark matter density profile, and a spatially constant gas-to-dark matter mass ratio $f_0 = 0.18$ in the protogalaxies. Red line segments are for $M_{\rm BH} \propto M_{\rm d,200}^{1.4}$ and $M_{\rm BH} \propto M_{\rm d,200}^{0.65}$.

Figure 3.10 is taken from Dutton et al. (2010). The solid black line shows their derived $M_{\rm BH}$–$M_{\rm d,200}$ relation. This curve was obtained by combining their $V_c(R_e)$–V_{200} relation (cf. §2.2.8.3), which accounts for the halo mass dependence of $f_{*,200}$, with the best-fit $M_{\rm BH}$–σ relation from Gültekin et al. (2009):

$$\log\left(\frac{M_{\rm BH}}{M_\odot}\right) = (8.12 \pm 0.08) + (4.24 \pm 0.41)\log\left(\frac{\sigma}{200\,{\rm km\,s^{-1}}}\right). \tag{3.9}$$

The shaded region shows their 2σ uncertainties. The similarity between the curves calculated here with $z_{\rm qso} > 0$ and the Dutton et al. (2010) results is encouraging. Correcting for the h^{-1} in the halo mass unit, the $z_{\rm qso} = 3$ curve in Figure 3.9 differs by no more than $\sim 20\%$ from the Dutton et al. relation at any given halo mass, well within their 2σ uncertainties.

Dutton et al. (2010) suggest that the change in slope of the $M_{\rm BH}$–$M_{\rm d,200}$ relation could be indicative of different growth mechanisms for the SMBHs at different halo masses. However, by accounting for the redshift evolution of the dark matter halos, a single black hole growth mechanism — gaseous accretion until a critical SMBH mass is reached and expels the surrounding ambient medium via momentum-driven feedback, at some redshift $z_{\rm qso} > 0$ — leads to an $M_{\rm BH}$–$M_{\rm d,200}$ relation that shows a very similar change in slope. The fact that the $M_{\rm BH}$–$M_{\rm d,200}$ relation is non-linear does not mean it is less fundamental than any other relation, as suggested by Dutton et al. (2010) and Kormendy & Ho (2013). The calculations here, based on a physical model, yield $M_{\rm BH}$–$M_{*,\rm tot}$ and $M_{\rm BH}$–$\sigma_{\rm ap}(R_e)$ relations that are also distinctly non-linear. Dutton et al. argue that the relation between SMBH mass and stellar mass may be more fundamental, because of a single power law best-fit to the data. However, there is no reason to expect any of the SMBH correlations to be linear when considering a physical model, as demonstrated here.

Using self-consistent cosmological simulations for the co-evolution of SMBHs and host galaxies, Booth & Schaye (2010) argue that SMBH masses are determined by the masses of the host dark matter halos. Their recipe for regulating the growth of the black hole involved implementing energy feedback by allowing the SMBHs to inject a fixed fraction of the rest mass energy of the gas they accrete into the surrounding

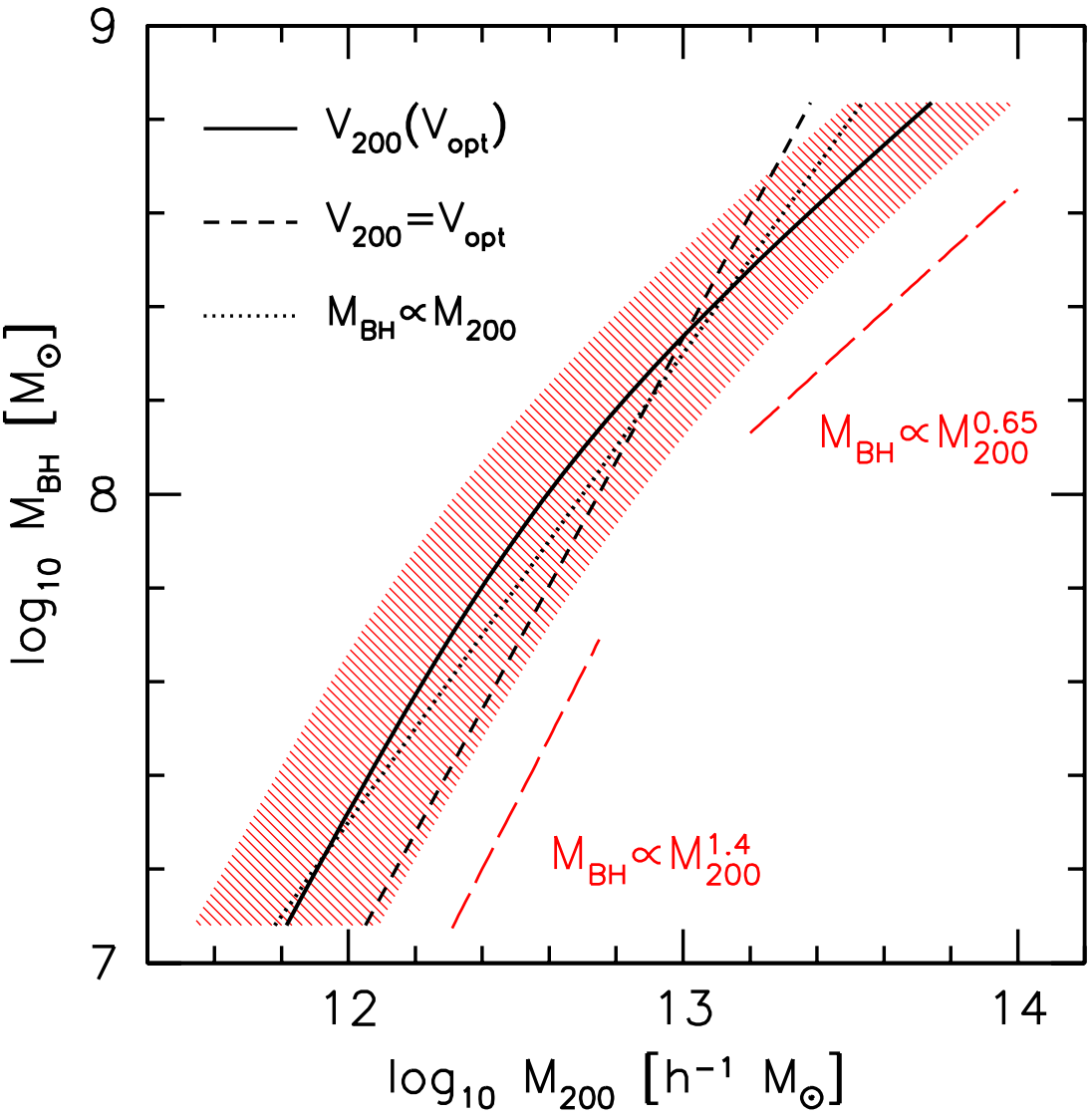

Figure 3.10: SMBH mass, $M_{\rm BH}$, as a function of halo mass, $M_{\rm d,200}$, according to Dutton et al. (2010). The solid black line shows the relation derived by Dutton et al. assuming their relation between $V_{\rm opt}$ and V_{200} for early-types, along with the $M_{\rm BH}$–σ relation from Gültekin et al. (2009). The red shaded region corresponds to the 2σ uncertainties in the relation. As the dashed red lines indicate, the Dutton et al. relation has a slope of $\simeq 0.65$ at high halo masses and $\simeq 1.4$ at low masses. The short-dashed black line shows the $M_{\rm BH}$–$M_{\rm d,200}$ relation derived assuming $V_{200} = V_{\rm opt} = 1.65\sigma$, with a slope of $\simeq 1.32$. For reference only, the dotted line shows a linear relation between $M_{\rm BH}$ and $M_{\rm d,200}$.

medium. This results in a connection between $M_{\rm BH}$ and $M_{\rm d,200}$, both evaluated at $z_{\rm qso}$. This relation can be looked at directly by combining the $V_{\rm d,pk}(z)$–$M_{\rm d,vir}(z)$ and $M_{\rm d,vir}(z)$–$M_{\rm d,200}(z)$ relations with the critical SMBH mass prediction. The $V_{\rm d,pk}(z)$–$M_{\rm d,vir}(z)$ relation is given by the approximation to the van den Bosch et al. (2014a) simulations of the redshift evolution of the halo potential well.

The blue curves in Figure 3.11 show the $M_{\rm BH}(z)$–$M_{\rm d,200}(z)$ relation at $z_{\rm qso} = 0, 1$ and 2, assuming a Dehnen & McLaughlin model halo. The resulting relation in Figure 3.11 is linear since both $M_{\rm BH}$ and $M_{\rm d,200}$ are evaluated at $z_{\rm qso}$. This is different to Figures 3.9 and 3.10, where there is a non-linear relation between $M_{\rm BH}(z_{\rm qso})$ and $M_{\rm d,200}(0)$ — the halo mass at $z = 0$. The red line segment corresponds to $M_{\rm BH} \propto M_{\rm d,200}^{1.55}$, the slope obtained by Booth & Schaye (2010) in their simulations — the slopes of the blue curves are all $\simeq 1.3$. The difference in these slopes is rooted in assumptions made about the mechanisms of the SMBH feedback.

If the energy injected by a black hole is proportional to the halo gravitational binding energy, then for isothermal models, $M_{\rm BH} \propto M_{\rm d,200}^{5/3}$ (Silk & Rees 1998). This is because for energy-driven feedback in an SIS, $M_{\rm BH} \propto \sigma^5$. Combining the virial theorem with the overdensity definition leads to $M_{\rm d,200} \propto V_{200}^3 \propto \sigma^3$, and hence the relation between SMBH mass and halo mass. Extending this to an NFW density profile, Booth & Schaye (2010) find a slope of ~ 1.5–1.6, consistent with their simulations. The analysis here involves the assumption of momentum-driven feedback halting the growth of SMBHs — $M_{\rm BH} \propto V_{\rm d,pk}^4$. This dependence on the velocity scale leads to an expected slope in the $M_{\rm BH}$–$M_{\rm d,200}$ relation of $\simeq 1.33$, again for isothermal models (Bandara et al. 2009). The slopes of the blue curves in Figure 3.11 are consistent with this simple expectation.

3.3.5 Bivariate correlations

Hopkins et al. (2007a,b) proposed a bivariate dependence of $M_{\rm BH}$ on a combination of bulge properties at $z = 0$. Hopkins et al. (2007a) call this the Black Hole Fundamental Plane (BHFP), and suggest that such combinations can significantly reduce

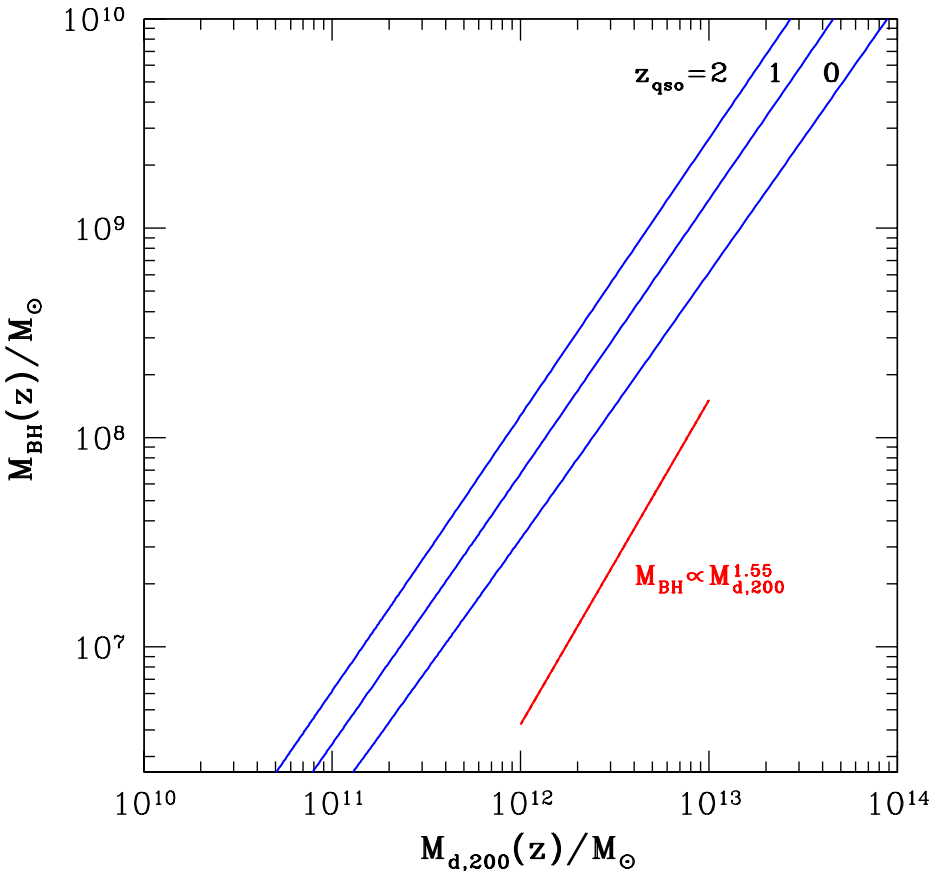

Figure 3.11: SMBH mass, $M_{\rm BH}$, as a function of halo mass, $M_{\rm d,200}$, both evaluated at $z_{\rm qso}$. The three curves correspond to $z_{\rm qso} = 0, 1$ and 2 respectively, assuming a Dehnen & McLaughlin halo and that $M_{\rm BH} \propto V_{\rm d,pk}^4$ was established by momentum-driven feedback, according to equation (3.1). For all values of $z_{\rm qso}$, the slope of the $M_{\rm BH}(z_{\rm qso})$–$M_{\rm d,200}(z_{\rm qso})$ relation is $\simeq 1.3$. The red line is for $M_{\rm BH} \propto M_{\rm d,200}^{1.55}$, the slope found by Booth & Schaye (2010) in their simulations, implementing energy-driven feedback.

the scatter around a linear best-fit, compared to any of the single SMBH–bulge property relations. The scaling relations developed here allow comparisons between the McQuillin & McLaughlin (2012) critical $M_{\rm BH}$ [equation (3.1)] and this version of the data as well.

Considering a bivariate dependence of $M_{\rm BH}$ on a combination of $\sigma_{\rm ap}$ and R_e or $\sigma_{\rm ap}$ and $M_{*,\rm tot}$ actually pre-dates the Hopkins et al. (2007a,b) work. When considering the SMBH mass – bulge mass relation, Marconi & Hunt (2003) work with a *dynamical* bulge mass. They calculated this dynamical mass, $M_{\rm dyn} = k\sigma^2 R_e/G$, assuming homology (i.e. k is constant). Marconi & Hunt (2003) were considering a bivariate dependence of SMBH mass, with $M_{\rm BH} \propto \sigma_{\rm ap}^2 R_e$. More recently, the ATLAS team (Cappellari et al. 2011; Cappellari et al. 2013b; Cappellari et al. 2013a) found that this combination of $\sigma_{\rm ap}$ and R_e produced the best linear fit (for their 258 galaxies) for the fundamental plane of ellipticals: $M_{*,\rm tot} \propto \sigma_{\rm ap}^2 R_e$.

The main goal for the Hopkins et al. (2007a,b) study was to reduce scatter around best fits for the SMBH – bulge relations at $z = 0$. Combining $\sigma_{\rm ap}$ and R_e, they find the scatter reduces to ~ 0.2 dex for $M_{\rm BH} \propto \sigma_{\rm ap}^3 R_e^{0.43}$. Given that $\sigma_{\rm ap}^3 R_e^{0.43} \sim [\sigma_{\rm ap}^2 R_e^{0.3}]^{3/2}$, connecting $M_{\rm BH}$ to $\sigma_{\rm ap}^2 R_e^{0.3}$ results in the same intrinsic scatter around a linear best fit as the Hopkins et al. (2007a) result. This form is more convenient to compare to $\sigma_{\rm ap}^2 R_e$. In what follows, the bivariate dependence of $M_{*,\rm tot}$ at $z = 0$ and $M_{\rm BH}(z)$ on both combinations of $\sigma_{\rm ap}$ and R_e [$\sigma_{\rm ap}^2 R_e$ and $\sigma_{\rm ap}^2 R_e^{0.3}$] at $z = 0$ are considered.

3.3.5.1 Data

Unfortunately, Kormendy & Ho (2013) do not give effective radii for their data sample. R_e values are tabulated in the Harris, Poole & Harris (1977) compilation [along with K-band magnitudes and $\sigma_{\rm ap}(R_e)$], so this compilation is used for the purposes of this Section. Only E and S0 galaxies in Harris et al. (2014) that are also in Kormendy & Ho (2013) are considered, of which there are 35. It is worth noting that the $M_{\rm BH}$ and $\sigma_{\rm ap}(R_e)$ values are the same in Harris et al. and Kormendy & Ho (although the K-band magnitudes are not). Before considering any bivariate dependences, the ATLAS and

Harris et al. data need to be self-consistently compared.

In total, there are 14 galaxies in common between ATLAS, Kormendy & Ho (2013) and Harris et al (2014). Figure 3.12 shows $\sigma_{\rm ap}(R_e)$ (top panel) and R_e (bottom panel) versus $M_{*,\rm tot}$, all at $z = 0$. As in previous Figures, the green squares are for galaxies in ATLAS and magenta triangles are from ACSVCS. The black points are from the Harris et al (2014) data sample, with red points from ATLAS that also appear in Harris et al. The curve in the top panel from the Jeans modelling in §2.2.6, assumes a Dehnen & McLaughlin dark matter halo and a stellar ejecta mass fraction, $F_{\rm ej}$, that depends on $M_{*,\rm tot}$ (cf. §2.2.6.4). The curve in the bottom panel corresponds to the parametrisation of R_e:

$$\frac{R_e}{\rm kpc} = 1.5 \left(\frac{M_{*,\rm tot}}{2 \times 10^{10}\, M_\odot} \right)^{0.1} \left[1 + \left(\frac{M_{*,\rm tot}}{2 \times 10^{10}\, M_\odot} \right)^{5} \right]^{0.1} . \tag{3.10}$$

The top panel of Figure 3.12 again appears to show the selection bias in the $M_{\rm BH}$–$\sigma_{\rm ap}(R_e)$ data, discussed in §3.3.1. For a fixed stellar mass, the velocity dispersions are systematically larger than average for galaxies with measured SMBH masses. Since $\sigma_{\rm ap}(R_e)$ values are the same in Harris et al. and Kormendy & Ho, the ATLAS values are again smaller. Therefore, if the ATLAS velocity dispersions are used where possible for galaxies with $M_{\rm BH}$ (red points), there is no obvious selection bias.

The anti-correlated scatter in $\sigma_{\rm ap}$ and R_e versus stellar mass (or luminosity), related to the fundamental plane of ellipticals (cf. §1.2.3), is reflected in the bottom panel of Figure 3.12. This shows that if $M_{*,\rm tot}$ is fixed, then the effective radius is systematically *lower* than the mean trend for galaxies in the $M_{\rm BH}$–σ data sample. These opposite systematic deviations from the average trends encourages looking at combinations of $\sigma_{\rm ap}$ and R_e, as a function of $M_{*,\rm tot}$. For galaxies in common, the ATLAS values for R_e are larger than those tabulated by Harris et al. As for the $\sigma_{\rm ap}(R_e)$–$M_{*,\rm tot}$ relation, if the ATLAS R_e values are used for galaxies with $M_{\rm BH}$, there is a less obvious selection bias (although this is a small sample of only 14 galaxies).

Figure 3.13 shows the ratios (Harris et al. to ATLAS) of effective radii (top panels), stellar masses (middle panels) and aperture dispersions (bottom panels), as

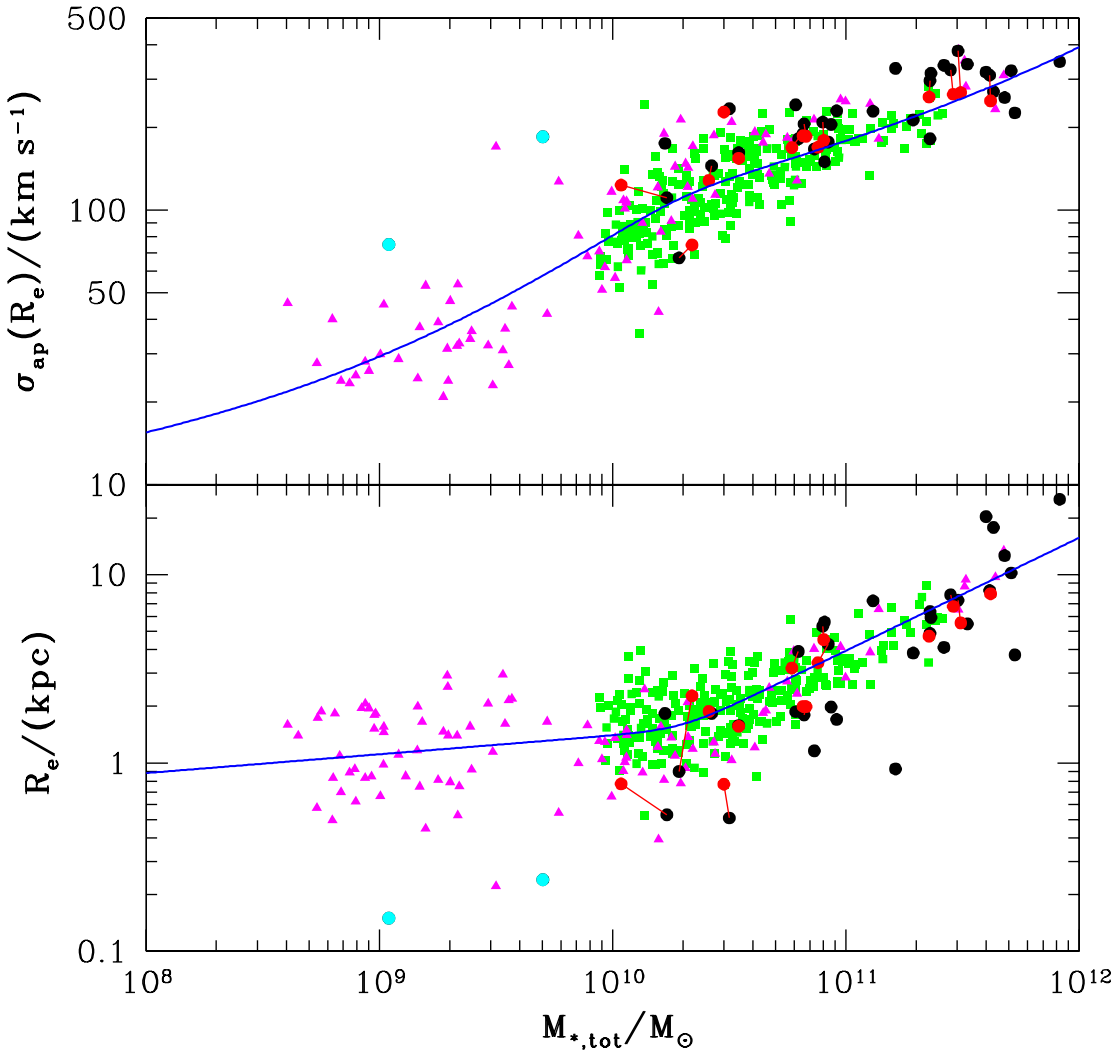

Figure 3.12: Stellar velocity dispersion (top panel) and stellar effective radius (bottom panel), both at $z = 0$, versus total stellar mass, also at $z = 0$. The green squares are from the ATLAS data sample and the magenta triangles are from ACSVCS. Black circles are galaxies from Harris et al. (2014) and red points are ATLAS galaxies that are also in Harris et al. and Kormendy & Ho. *Top panel:* The blue curves are from the Jeans modelling to calculate aperture velocity dispersions. They assume a Dehnen & McLaughlin dark matter halo, as well as the ad-hoc $F_{\rm ej}$–$M_{*,\rm tot}$ relation. *Bottom panel:* Solid blue curve shows the parametrisation of R_e–$M_{*,\rm tot}$ [see equation (3.10)].

functions of $\sigma_{\rm ap}(R_e)$ (left) and $M_{*,\rm tot}$ (right) from ATLAS. Typical error bars are shown in the top left corner of each panel. The horizontal error bars are calculated as before, by taking the typical errors from ATLAS (5% for velocity dispersions and $\sim 20\%$ for stellar masses) and calculating an average error for the 14 galaxies in the plot. The error bars for the ratios are obtained by combining the errors from Harris et al. (2014) and ATLAS for each data point, and an rms scatter is then calculated. Harris et al. give error bars for the K-band magnitudes and velocity dispersions for individual galaxies, and give typical errors of $\sim 10\%$ for R_e, as do ATLAS for effective radii.

The σ ratio plots are the same as the bottom panels of Figure 3.6, with fewer points [since $\sigma({\rm KH}) \equiv \sigma({\rm Harris})$]. The average difference in the velocity dispersions is given by $\langle \log[\sigma({\rm Harris})/\sigma({\rm AT})] \rangle \simeq 0.04$, the same as before. For the stellar masses, the difference is significantly smaller, with $\langle \log[M_*({\rm Harris})/M_*({\rm AT})] \rangle \simeq 0.015$ (for the Kormendy & Ho comparison, this value was $\simeq 0.05$). For the effective radii, the average difference is again reasonably small, but in the opposite direction: $\langle \log[R_e({\rm Harris})/R_e({\rm AT})] \rangle \simeq -0.025$. This is again a reflection of the anti-correlated scatter between velocity dispersion and effective radius.

3.3.5.2 Combinations of stellar velocity dispersion and effective radius

The top panel of Figure 3.14 shows $\sigma_{\rm ap}^2 R_e$ versus total stellar mass at $z = 0$. Point types and colours correspond to the same data samples as the previous Figure. The curve is the predicted mean trend for a Dehnen & McLaughlin dark matter halo and an ad-hoc $F_{\rm ej}$–$M_{*,\rm tot}$ relation. The trend line appears much straighter than in other relations, unsurprising given that $M_{\rm dyn} \propto \sigma_{\rm ap}^2 R_e$. The apparent selection bias for the M–σ data (black points), seen in the $\sigma_{\rm ap}$–$M_{*,\rm tot}$ relation when using the Harris et al. (2014) velocity dispersions, is no longer seen in this bivariate relation. This is in part because the combination of $\sigma_{\rm ap}$ and R_e significantly cancels out the anti-correlated scatter between the two properties.

The bottom panel of Figure 3.14 shows $\sigma_{\rm ap}^2 R_e^{0.3}$ as a function of total stellar mass. The curve is again for a Dehnen & McLaughlin halo and an assumed $F_{\rm ej}$–$M_{*,\rm tot}$ relation.

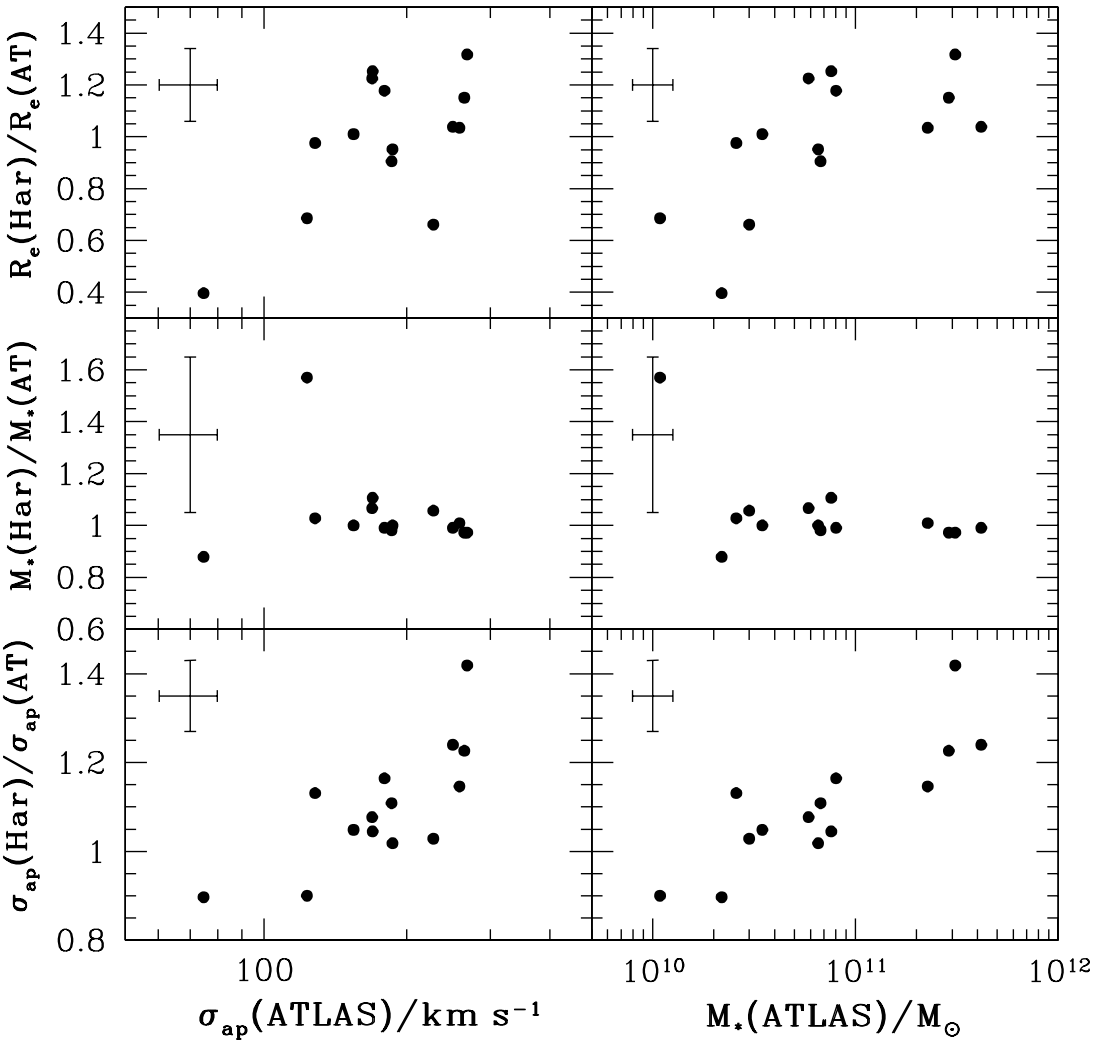

Figure 3.13: Data comparison for the 14 galaxies in common between Harris et al. (2014) and ATLAS^{3D}. Typical error bars are shown in the top left of each panel. *Top panels:* Ratio of effective radius in Harris et al. to effective radius in ATLAS, versus $\sigma_{\rm ap}(R_e)$ (left panel) and stellar mass (right panel), both from ATLAS. *Middle panels:* Ratio of total stellar mass in Harris et al. to stellar mass in ATLAS, as a function of ATLAS stellar velocity dispersion (left panel) and ATLAS $M_{*,\rm tot}$ (right panel). *Bottom panels:* Ratio of stellar velocity dispersion (measured within R_e) in Harris et al. to that in ATLAS, versus $\sigma_{\rm ap}$ (left) and $M_{*,\rm tot}$ (right; both from ATLAS).

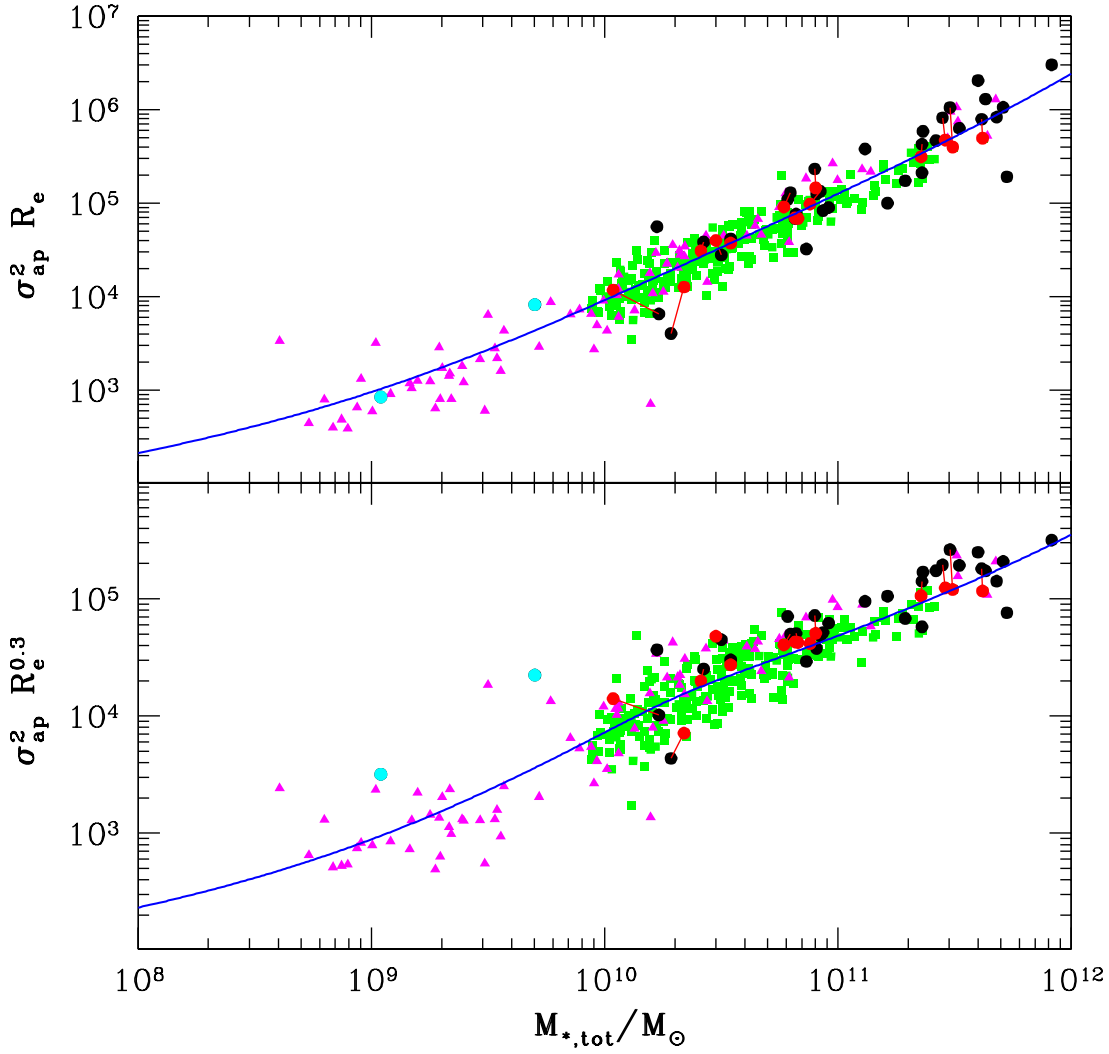

Figure 3.14: *Top panel:* The combination $\sigma^2_{\rm ap}R_e$ at $z = 0$, as a function of total stellar mass, also at $z = 0$. Magenta triangles are for galaxies in the ACSVCS sample, with green squares from ATLAS. Black points are from the Harris et al. (2014) compilation of SMBH data, and the two cyan points are the compact ellipticals M32 and NGC N4486B. The red points are galaxies in common between ATLAS, Kormendy & Ho and Harris et al. (2014), and represent the ATLAS values for $\sigma_{\rm ap}$, R_e and $M_{*,\rm tot}$. These are connected to the corresponding galaxies in Harris et al. by red lines. The blue curves are the calculated mean trends, assuming a Dehnen & McLaughlin halo, with a mass dependent $F_{\rm ej}$. *Bottom panel:* Same as the top panel, but for the combination $\sigma^2_{\rm ap}R_e^{0.3}$ at $z = 0$ versus $M_{*,\rm tot}$ at $z = 0$.

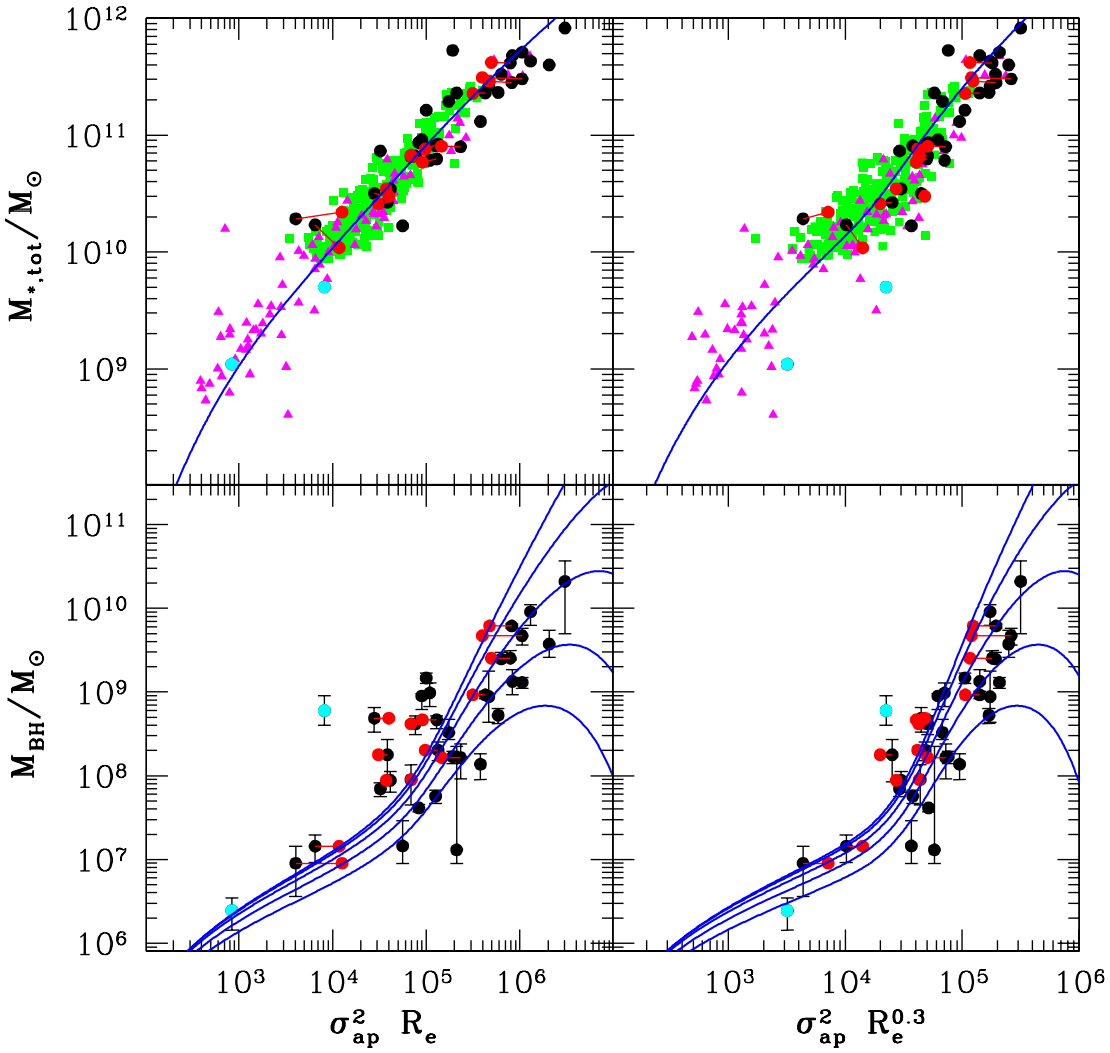

Figure 3.15: *Top panels:* Total stellar mass at $z = 0$ versus $\sigma^2_{\rm ap} R_e$ (left) and $\sigma^2_{\rm ap} R_e^{0.3}$ (right), evaluated at $z = 0$. Point type and colours are the same as for the previous Figure. The blue curves are trend lines for a Dehnen & McLaughlin dark matter halo, assuming an ad-hoc $F_{\rm ej} = -M_{*,\rm tot}$ relation. *Bottom panels:* $M_{\rm BH}(z_{\rm qso})$ as a function of $\sigma^2_{\rm ap} R_e$ (left) and $\sigma^2_{\rm ap} R_e^{0.3}$ (right), evaluated at $z = 0$. The black points are from Harris et al. (2014) and the red points are ATLAS galaxies also appearing in Harris et al. The curves are for a critical SMBH mass calculated using equation (3.1), assuming $f_0 = 0.18$, with $V_{\rm d,pk}$ evaluated at (from top to bottom) $z_{\rm qso} = 0, 1, 2, 3$ and 4.

The shape of the curve is similar to the $\sigma_{\rm ap}$ versus $M_{*,\rm tot}$ average trend, due to the smaller power of R_e, compared to the top panel (0.3 instead of 1). This combination of $\sigma_{\rm ap}$ and R_e still appears to shows a selection bias for the M–σ data, when using the Harris et al. velocity dispersions. However, as for the $\sigma_{\rm ap}$–$M_{*,\rm tot}$ relation, if the ATLAS velocity dispersions are used for these galaxies (where possible), there is again no obvious selection bias.

The top two panels of Figure 3.15 show $M_{*,\rm tot}$ at $z = 0$ as a function of $\sigma^2_{\rm ap}R_e$ (left panel) and $\sigma^2_{\rm ap}R_e^{0.3}$ (right panel). These are equivalent to the panels in Figure 3.14. The bottom two panels show $M_{\rm BH}(z)$ versus $\sigma^2_{\rm ap}R_e$ at $z = 0$ (left panel) and $\sigma^2_{\rm ap}R_e^{0.3}$ at $z = 0$ (right panel). The black points are galaxies from Harris et al. (2014) and the red points are systems that also appear in ATLAS and Kormendy & Ho. The two cyan points are the compact ellipticals M32 and NGC 4486B (M32 has the lower $M_{*,\rm tot}$ and $M_{\rm BH}$ of the two). The blue curves are obtained by combining the bivariate dependencies on $M_{*,\rm tot}$ with the $V_{\rm d,pk}$–$M_{*,\rm tot}$ relation and the critical SMBH mass prediction — $M_{\rm BH}(z) \propto V^4_{\rm d,pk}(z)$. A Dehnen & McLaughlin dark matter halo is assumed, with $f_0 = 0.18$ and $z_{\rm qso} = 0, 1, 2, 3$ and 4. In both panels, the curves are generally in good agreement with the data. As for the other SMBH correlations, the upward inflection traces back to the peak in $f_{*,\rm vir}$ at around $M_{*,\rm tot} \simeq 3.4 \times 10^{10} M_\odot$. The flattening seen in the curves [setting in at $\sigma^2_{\rm ap}R_e \sim 10^6$ in the left panel and $\sigma^2_{\rm ap}R_e^{0.3} \sim 3 \times 10^5$ in the right panel] is again a reflection of the generic feature of structure formation by hierarchical merging — the largest structures formed most recently.

As for the other SMBH relations considered here, the intrinsic scatter around the model curves has been calculated. Although this doesn't give details of the source of the scatter, it gives an idea about which of the correlations are perhaps more fundamental according to the physical model considered. For the $z_{\rm qso} = 3$ curve, the intrinsic scatter is $\simeq 0.67$ dex for $M_{\rm BH} \propto \sigma^2_{\rm ap}R_e$ and $\simeq 0.45$ dex for $M_{\rm BH} \propto \sigma^2_{\rm ap}R_e^{0.3}$. These compare to values from Hopkins et al. (2007a) for scatter around a linear best-fit of $\simeq 0.43$ dex for $M_{\rm BH} \propto \sigma^2_{\rm ap}R_e$ and $\simeq 0.21$ dex for $M_{\rm BH} \propto \sigma^2_{\rm ap}R_e^{0.3}$. For the physical model then, the scatter around the $z_{\rm qso} = 3$ curve is *less* for the $M_{\rm BH}$–$\sigma_{\rm ap}(R_e)$ relation than either of the bi-variate relations considered here.

An important question to ask is whether it is meaningful to try and reduce the scatter around these mean trends. Doing so could hide real, physical scatter in the data that is expected to be present. For example the redshift $z_{\rm qso}$, marking the end of SMBH growth via rapid accretion, is expected to be different for each galaxy. This accounts for some of the scatter in the SMBH correlations, and is seen by the clear separation of the curves in Figures 3.7 and 3.8 showing the $M_{\rm BH}$–σ and $M_{\rm BH}$–$M_{*,\rm tot}$ relations. However, both the bottom panels in Figure 3.15 have curves that are much closer together, showing little dependence in the scatter on $z_{\rm qso}$. It is possible that combining $\sigma_{\rm ap}$ and R_e in this way has just removed a physically interesting result, namely the scatter due to different $z_{\rm qso}$ for galaxies of similar sizes. The key point is, the scatter still needs to be understood, by considering the intrinsic scatter around the trend lines for the $z = 0$ relations, as well as the scatter associated with the SMBH correlations.

3.3.6 Summary

The average trends between stellar and halo properties at $z = 0$ from Chapter 2 have been combined with approximations for the redshift evolution of halo progenitors. This allowed for $V_{\rm d,pk}$ and $M_{\rm d,vir}$ at any redshift to be connected to the stellar properties at $z = 0$. Folding in a relationship of the form $M_{\rm BH} \propto V_{\rm d,pk}^4$ at a range of redshifts $z_{\rm qso} > 0$, model predictions for the SMBH–galaxy property relations have been made. Despite this linear (in log–log space) relation estimating the critical SMBH mass required for gas blow-out, the model predictions that are inferred are highly non-linear. Nevertheless, the resulting curves do describe the data for local early-types if the redshift of quasar-mode blow-out was $z_{\rm qso} \approx 2$–4. This range is reassuringly similar to the epoch of peak quasar density and SMBH accretion rate in the Universe.

This lends support to the notion that the empirical SMBH relations fundamentally reflect some close connection due to accretion feedback between SMBH masses in galactic nuclei and the *dark matter* in their host protogalaxies. It also demonstrates that the true physical relationships between $M_{\rm BH}$ and stellar properties [$\sigma_{\rm ap}(R_e)$, $M_{*,\rm tot}$

and combinations of velocity dispersion and R_e] are not necessarily pure power laws. The model predictions obtained do not include any growth of the SMBH itself at redshifts $z < z_{\rm qso}$, which can occur by coalescences in gas-poor mergers at the centre of a halo (cf. §3.3.2.1). However, this is distinct from the growth of the halo as a whole; many sub-halos can be accreted at low redshift that do not sink to the bottom of the potential well and thus do not grow the central SMBH. The effects of such mergers on halo masses and circular speeds (and hence stellar velocity dispersions at $z = 0$) are fully accounted for.

For each of the SMBH correlations considered, the intrinsic scatter around the model curve for $z_{\rm qso} = 3$ has been calculated. The values range from $\simeq 0.39$ dex for $M_{\rm BH}$–$\sigma_{\rm ap}$ and $M_{\rm BH}$–$M_{\rm d,200}$, to $\simeq 0.7$ dex for $M_{\rm BH}$–$M_{*,\rm tot}$. The bivariate correlations have intrinsic scatter in between these two values. This suggests that in terms of the physical model used here, the intrinsic scatter around the model predictions for the SMBH relations is not necessarily reduced by combining the stellar properties in the ways shown here. It also hints at the connection between $M_{\rm BH}$ and $\sigma_{\rm ap}(R_e)$ (or $M_{\rm d,200}$) perhaps being a more accurate reflection of the fundamental $M_{\rm BH}$–$V_{\rm d,pk}$ relation at $z = z_{\rm qso}$, underpinning all the model curves.

The specific form of the initial $M_{\rm BH}$–$V_{\rm d,pk}$ used in this Chapter comes from a simplified theoretical analysis of momentum-conserving SMBH feedback. This is assumed to occur in isolated protogalaxies containing no stars, with the gas tracing the dark matter. Hence, there are several simplifying assumptions involved that need to be relaxed. The work presented in the next Chapter looks at the implications of relaxing the assumptions of having no stars and a virialised gas.

4 A new critical SMBH mass prediction

The work presented in Chapter 3 demonstrated how a prediction relating SMBH mass, $M_{\rm BH}$, to the potential well depth of a host protogalaxy when quasar-mode blow out occurred, at redshift $z_{\rm qso} > 0$, can be compared to observed correlations between $M_{\rm BH}$ and galaxy properties at $z = 0$. To make such comparisons, the scaling relations obtained in Chapter 2, relating various properties of stars and dark matter in $z = 0$ systems, have also been used. The methods developed up to this point are readily adaptable for other predictions involving the SMBH mass required for blow out.

The prediction used in Chapter 3 related $M_{\rm BH}$ to the peak of the dark matter circular speed, $V_{\rm d,pk}$. This result was obtained by McQuillin & McLaughlin (2012) and is given by:

$$\frac{M_{\rm BH}}{M_\odot} = 1.14 \times 10^8 \left(\frac{f_0}{0.2}\right) \left(\frac{V_{\rm d,pk}}{200\,{\rm km\,s^{-1}}}\right)^4 . \tag{4.1}$$

In this equation, f_0 is the gas-to-dark matter mass fraction in the protogalaxy, assumed to be spatially constant. As discussed, this prediction has several limitations. The force balance behind it assumes that the protogalactic outflows driven by SMBH winds are momentum-driven. The equation also assumes a wind moving into a static ambient medium, where the gas traces the dark matter, making no account for in-falling gas. It also neglects the presence of any stars in the protogalaxy, which could contribute both to the feedback driving the gaseous outflows and to the gravity containing them. It is unclear in detail how correcting for any of these caveats will affect either the normalisation and/or the scaling.

Analytical predictions in the literature based on the assumption that the outflows are energy-driven (e.g. Silk & Rees 1998; McQuillin & McLaughlin 2013) also assume dark matter halos that are distributed isothermally (SIS models) and a virialised gaseous medium. McQuillin & McLaughlin (2013) find that an energy-driven outflow leads to a different functional dependence of $M_{\rm BH}$ on the velocity scale (in this case σ_0, the velocity dispersion of the dark matter halo) — $M_{\rm BH} v_w \propto \sigma_0^5$, where v_w is the wind velocity. On the other hand, Zubovas & Nayakshin (2014) argue that

assumptions about the thermal physics behind the outflows do not affect the SMBH mass required for blow out in a significant way.

Costa et al. (2014) found that the large scale outflows, driven by AGN, are indeed energy-driven in full cosmological simulations. They also suggest that a larger momentum input rate is required to drive efficient outflows, due to infalling gas. Their simulated energy-driven outflows can reach momentum fluxes of up to $10L_{\rm Edd}/c$. The effects of allowing for a non-virialised gas have only briefly been looked at. Ishibashi & Fabian (2012) consider an initial gas distribution with a density profile $\rho_g(r) \propto r^{-2}$, inside a Hernquist dark matter halo. They suggest that the critical SMBH mass required for a gas shell to escape from such a protogalaxy via momentum-driven feedback is the same as for the case of gas tracing dark matter, since the shell will still accelerate at large radii. The contribution from stars to the gravity trying to contain the outflow have not been considered.

In this Chapter, a new prediction relating $M_{\rm BH}$ to the potential well depth of the protogalaxy is derived. This new prediction allows for the presence of stars in the protogalaxy that can contribute to the gravitational force containing the outflow *and* for the gas not to be tracing the dark matter (or indeed the stars). The contributions to the feedback from stellar winds and supernovae (Murray et al. 2005; Power et al. 2011) are not considered here. Allowing for stars contributing to the gravity and a non-virialised gas requires setting up three-component protogalaxies with (potentially) different distributions for each component. Spherical symmetry is assumed for all components, with the wind moving into an initially static ambient medium and that the outflow is purely momentum-driven. It is also assumed that $M_{\rm BH}$ remains constant throughout the process, corresponding to a steady wind. Clearly then, the new prediction still has caveats. However, it is necessary to keep certain assumptions the same to investigate how correcting for other limitations affects the final result (in this case, the critical SMBH mass required for quasar-mode blow out). As mentioned above, it is unclear which of the limitations of equation (4.1) is the most significant.

To derive this new critical SMBH mass, the method from McQuillin & McLaughlin (2012), outlined in §1.4.5, is followed closely. The feedback is modelled as a spherical

radiative shell, driven outwards by an SMBH wind with momentum flux equal to the Eddington value ($dp_{\rm wind}/dt = L_{\rm Edd}/c$ with no pre-factor, King & Pounds 2003). Allowing for stars and non-virialised gas in the protogalaxy potentially has implications for the $M_{\rm BH}$ that is required for quasar-mode feedback to clear the gas from a galaxy. The new result is compared to equation (4.1) to see how the critical SMBH is affected. It will also be compared to the empirical $M_{\rm BH}$–$\sigma_{\rm ap}(R_e)$ relation in $z = 0$ galaxies, making use of the scaling relations developed in Chapter 2 and the methods outlined in Chapter 3.

4.1 Equation of motion

The equation of motion of a momentum-conserving shell, in a protogalaxy consisting of stars, gas and dark matter is given by

$$\frac{d[M_g(r)v(r)]}{dt} = \frac{L_{\rm Edd}}{c} - \frac{GM_g(r)}{r^2}\Big[M_{\rm BH} + M_{\rm con}(r)\Big]. \tag{4.2}$$

Here, r is the instantaneous radius of the shell, $v = dr/dt$ is the velocity of the shell, $M_{\rm con}(r)$ is the sum of the dark matter mass and stellar mass inside r — i.e., the "confining" mass. $M_g(r)$ is the ambient gas mass *originally* inside radius r. The first term on the right hand side, is the assumed outward force on the shell of swept up gas, $L_{\rm Edd}/c = 4\pi GM_{\rm BH}/\kappa$ (King & Pounds 2003). The subtracted term on the right hand side is the gravitational confining force acting on the shell from the black hole, dark matter and stars.

If the gravity from the black hole is negligible, which is true at large radii, then the gravitational confining force has a maximum at a radius, $r_{\rm f}$, provided at least one of the gas, stellar and dark matter distributions are non-isothermal. With $M_{\rm BH}$ removed and given that $V^2(r) = GM(r)/r$, the gravitational force term is

$$\frac{GM_g(r)M_{\rm con}(r)}{r^2} \propto V_g^2(r)V_{\rm con}^2(r). \tag{4.3}$$

The radius $r_{\rm f}$ therefore corresponds to where the product of the gas circular speed, $V_g^2(r) \equiv GM_g(r)/r$, and the circular speed of the "confining" mass, $V_{\rm con}^2(r) \equiv GM_{\rm con}(r)/r$,

peaks. It is at this radius that a gas shell will begin to accelerate, if it is able to get there in the first place. The value of the force at $r_{\rm f}$ therefore determines the critical SMBH mass [if $L_{\rm Edd}/c \geq GM_g(r_{\rm f})M_{\rm con}(r_{\rm f})/r_{\rm f}^2$, then the gas is blown out of the galaxy], assuming that the gas shell is able to overcome the gravity of the black hole at small radii.

To solve for the velocity fields, $v^2(r)$, it is more convenient to write the equation of motion as a derivative with respect to r:

$$\frac{d[M_g^2(r)v^2(r)]}{dr} = \frac{8\pi G}{\kappa} M_{\rm BH}\, M_g(r) \;-\; \frac{GM_g^2(r)}{r^2}\Big[M_{\rm BH} + M_d(r) + M_*(r)\Big]. \qquad (4.4)$$

Following McQuillin & McLaughlin (2012), characteristic mass and radius scales, M_σ and r_σ are defined, in order to write equation (4.4) in dimensionless form. These are given in terms of a characteristic velocity scale,

$$V_{\rm con}^2(r_{\rm f}) \equiv \frac{GM_{\rm con}(r_{\rm f})}{r_{\rm f}} = V_{\rm f}^2. \qquad (4.5)$$

By definition, this is the value of $V_{\rm con}^2(r)$ at the radius at which the gravitational force is a maximum, $r_{\rm f}$. This is *not* necessarily the maximum of $V_{\rm con}^2(r)$. Denoting $f_{\rm g}(r_{\rm f}) \equiv M_{\rm g}(r_{\rm f})/M_{\rm d}(r_{\rm f})$ and $f_*(r_{\rm f}) \equiv M_*(r_{\rm f})/M_{\rm d}(r_{\rm f})$, and defining $f(r_{\rm f}) = f_{\rm g}(r_{\rm f})/[1 + f_*(r_{\rm f})]$, the mass and radius scales are then given by

$$M_\sigma \equiv \frac{f(r_{\rm f})\,\kappa V_{\rm m}^4}{4\pi G^2} \simeq 1.14\times 10^8 \left[\frac{f(r_{\rm f})}{0.2}\right] \left(\frac{V_{\rm f}}{200\,{\rm km\,s^{-1}}}\right)^4 M_\odot$$

and

$$r_\sigma \equiv \frac{GM_\sigma}{V_{\rm m}^2/2}. \qquad (4.6)$$

For the case of no stars [$f_*(r_{\rm f}) = 0$] and gas tracing dark matter [$f(r_{\rm f}) = f_{\rm g}(r_{\rm f}) \equiv f_0$ and $V_{\rm f} = V_{\rm d,pk}$], these units are identical to the ones used by McQuillin & McLaughlin (2012).

In order to express the equation of motion in dimensionless form, the following dimensionless quantities are defined:

$$\widetilde{M} = \frac{M}{M_\sigma} \qquad \widetilde{r} = \frac{r}{r_\sigma} \qquad \widetilde{v} = \frac{v}{V_{\rm m}/\sqrt{2}} \qquad \text{and} \qquad x = \frac{r}{r_{\rm f}}, \qquad (4.7)$$

along with

$$\widetilde{M}_{\rm f} = \widetilde{M}_{\rm con}(\widetilde{r}_{\rm f}) \qquad \text{and} \qquad m(x) = \frac{\widetilde{M}(x)}{\widetilde{M}_{\rm f}}. \tag{4.8}$$

Defining the gas-to-confining mass ratio normalised to $f(r_{\rm f})$ as

$$h(x) \equiv \frac{f(x)}{f(r_{\rm f})} = \frac{m_g(x)/m_{\rm con}(x)}{f(r_{\rm f})}, \tag{4.9}$$

and noting that $\widetilde{M}_{\rm f} = 2\widetilde{r}_{\rm f}$, the dimensionless equation of motion is

$$\begin{aligned}\frac{d}{dx}\left[h^2(x)m_{\rm con}^2(x)\widetilde{v}^2(x)\right] &= 4\widetilde{M}_{\rm BH}h(x)m_{\rm con}(x) \\ &- 4\frac{\widetilde{M}_{\rm BH}}{\widetilde{M}_{\rm f}}\frac{h^2(x)m_{\rm con}^2(x)}{x^2} - 4\frac{h^2(x)m_{\rm con}^3(x)}{x^2}.\end{aligned} \tag{4.10}$$

For the case of no stars [$m_{\rm con}(x) = m_d(x)$] and gas tracing dark matter [$h(x) = 1$ everywhere and $\widetilde{M}_{\rm f} \equiv \widetilde{M}_d(\widetilde{r}_{\rm d,pk})$], equation (4.10) reduces to the equation of motion obtained by McQuillin & McLaughlin (2012). The formal solution to equation (4.10) is

$$\begin{aligned}h^2(x)m_{\rm con}^2(x)\widetilde{v}^2(x) = C &+ 4\widetilde{M}_{\rm BH}\int_0^x h(u)m_{\rm con}(u)du \\ &- 4\frac{\widetilde{M}_{\rm BH}}{\widetilde{M}_{\rm f}}\int_0^x \frac{h^2(u)m_{\rm con}^2(u)}{u^2}du - 4\int_0^x \frac{h^2(u)m_{\rm con}^3(u)}{u^2}du,\end{aligned} \tag{4.11}$$

where C is a constant of integration, related to the initial momentum. By fully specifying profiles for the gas, stars and dark matter, along with values for C and $\widetilde{M}_{\rm BH}$ (the remaining unknown, $\widetilde{M}_{\rm f}$, is determined once the profiles are chosen), equation (4.11) has a unique solution for the velocity field of a particular gas shell.

4.1.1 Condition for shell escape

McQuillin & McLaughlin (2012) used the fact that there is a large class of solutions that have local minima in $v^2(x)$ to derive a critical SMBH mass required for blow-out. This method involves finding the minimum of the shell's velocity fields, v^2, with the

critical case corresponding to $v^2_{\rm min} = 0$ at $r = r_{\rm crit}$. This gives the black hole mass that is necessary to expel a gas shell with particular initial conditions (i.e., a specific value for C) from the protogalaxy. The sufficient condition for *any* shell (i.e., any value of C) is then found by calculating the maximum of the corresponding black hole mass for the radius $r = r_{\rm max}$, at which the shell begins to accelerate, giving $M_{\rm crit}$.

If a local minimum in $\widetilde{v}^2(x)$ exists, the radius where it occurs is denoted as $x_{\rm min}$ and the value at $x_{\rm min}$ is $\widetilde{v}^2_{\rm min}$. Given that $d\widetilde{v}^2/dx = 0$ at $x_{\rm min}$, equation (4.10) gives

$$\widetilde{v}^2_{\rm min}\frac{d\ln[h^2(x_{\rm min})m^2_{\rm con}(x_{\rm min})]}{d\ln x_{\rm min}} \;=\; 4\,\frac{\widetilde{M}_{\rm BH}}{h(x_{\rm min})}\frac{x_{\rm min}}{m_{\rm con}(x_{\rm min})} \;-\; 4\,\frac{\widetilde{M}_{\rm BH}}{\widetilde{M}_{\rm f}}\frac{1}{x_{\rm min}} - 4\,\frac{m_{\rm con}(x_{\rm min})}{x_{\rm min}}. \tag{4.12}$$

If a shell with a given initial momentum (value of C) is to escape, then $\widetilde{v}^2_{\rm min} \geq 0$ is required, so the shell doesn't stall. If $\widetilde{v}^2_{\rm min} < 0$, then the gas shell stalls and re-collapses *if* $M_{\rm BH}$ is assumed to be constant (a steady wind). Taking $\widetilde{v}^2_{\rm min} = 0$ as the critical case, and denoting the corresponding values of $\widetilde{M}_{\rm BH}$ and $x_{\rm min}$ as $\widetilde{M}_{\rm crit}$ and $x_{\rm crit}$. Equation (4.12) then leads to

$$\widetilde{M}_{\rm crit} \;=\; \frac{m^2_{\rm con}(x_{\rm crit})h(x_{\rm crit})}{x^2_{\rm crit}}\left[1 - \frac{h(x_{\rm crit})}{\widetilde{M}_{\rm m}}\frac{m_{\rm con}(x_{\rm crit})}{x^2_{\rm crit}}\right]^{-1}. \tag{4.13}$$

Further to this, setting $x = x_{\rm crit}$, $\widetilde{v}^2 = 0$ and $\widetilde{M}_{\rm BH} = \widetilde{M}_{\rm crit}$ in the formal solution to the equation of motion [equation (4.11)], combined with equation (4.13) yields

$$\widetilde{M}_{\rm crit} = \frac{\dfrac{C}{4} + \displaystyle\int_0^{x_{\rm crit}}\left[\frac{h(u)m_{\rm con}(u)}{u}\right]^2\Big\{m_{\rm con}(x_{\rm crit}) - m_{\rm con}(u)\Big\}du}{\displaystyle\int_0^{x_{\rm crit}}\left[\frac{h(u)m_{\rm con}(u)}{u}\right]^2\left\{\frac{x^2_{\rm crit}}{h(x_{\rm crit})m_{\rm con}(x_{\rm crit})} - \frac{u^2}{h(u)m_{\rm con}(u)}\right\}du}. \tag{4.14}$$

Equating the right-hand sides of equations (4.13) and (4.14), $x_{\rm crit}$ and then $M_{\rm crit}$ can be found in terms of C (providing profiles have been chosen for the gas, stars and dark matter). The necessary condition for the escape of a purely momentum-driven shell with a particular value of C is just $\widetilde{M}_{\rm BH} \geq \widetilde{M}_{\rm crit}$.

Shells with different initial conditions will have different values of $\widetilde{M}_{\rm crit}$ and $x_{\rm crit}$, given by equations (4.13) and (4.14). To compare these, McQuillin & McLaughlin

(2012) differentiate $\widetilde{M}_{\rm crit}$ [equation (4.13)] with respect to $x_{\rm crit}$, for a fixed value of $\widetilde{M}_{\rm m}$:

$$\frac{d\widetilde{M}_{\rm crit}}{dx_{\rm crit}} = \frac{2m_{\rm con}^2(x_{\rm crit})x_{\rm crit}}{h(x_{\rm crit})} \frac{1}{\left[x_{\rm crit}^2/h(x_{\rm crit}) - m_{\rm con}(x_{\rm crit})/\widetilde{M}_{\rm m}\right]^2} \times\Bigg\{ \left[\frac{d\ln m_{\rm con}(x_{\rm crit})}{d\ln x_{\rm crit}} - 1\right] + \frac{1}{2}\left[\frac{d\ln h(x_{\rm crit})}{d\ln x_{\rm crit}}\right] - \frac{h(x_{\rm crit})m_{\rm con}(x_{\rm crit})}{2\widetilde{M}_{\rm f}x_{\rm crit}^2}\left[\frac{d\ln m_{\rm con}(x_{\rm crit})}{d\ln x_{\rm crit}}\right]\Bigg\}. \quad (4.15)$$

Using the definition of $h(x)$, this can be re-written as

$$\frac{d\widetilde{M}_{\rm crit}}{dx_{\rm crit}} = \frac{2m_{\rm con}^2(x_{\rm crit})x_{\rm crit}}{h(x_{\rm crit})} \frac{1}{\left[x_{\rm crit}^2/h(x_{\rm crit}) - m_{\rm con}(x_{\rm crit})/\widetilde{M}_{\rm m}\right]^2} \times\Bigg\{ \left[\frac{1}{2}\left(\frac{d\ln m_{\rm con}(x_{\rm crit})}{d\ln x_{\rm crit}} + \frac{d\ln m_{\rm g}(x_{\rm crit})}{d\ln x_{\rm crit}}\right) - 1\right] - \frac{h(x_{\rm crit})m_{\rm con}(x_{\rm crit})}{2\widetilde{M}_{\rm f}x_{\rm crit}^2}\left[\frac{d\ln m_{\rm con}(x_{\rm crit})}{d\ln x_{\rm crit}}\right]\Bigg\}. \quad (4.16)$$

By definition, $d\ln m_{\rm con}/d\ln x - 1 = d\ln V_{\rm con}^2/d\ln x$, and $d\ln m_{\rm g}/d\ln x - 1 = d\ln V_{\rm g}^2/d\ln x$. Therefore, the term in the square bracket is

$$\frac{1}{2}\left(\frac{d\ln m_{\rm con}(x_{\rm crit})}{d\ln x_{\rm crit}} + \frac{d\ln m_{\rm g}(x_{\rm crit})}{d\ln x_{\rm crit}}\right) - 1 = \frac{d\ln[V_g(x_{\rm crit})\,V_{\rm con}(x_{\rm crit})]}{d\ln x_{\rm crit}}. \quad (4.17)$$

Since $x = 1$ corresponds to $r = r_{\rm f}$, the radius at which the gravitational confining force is a maximum and (equivalently) where the product $V_g(x)\,V_{\rm con}(x)$ peaks, equation (4.17) is positive for $x < 1$ and negative for $x > 1$. Hence, $d\widetilde{M}_{\rm crit}/dx_{\rm crit} > 0$ for shells with sufficiently small $x_{\rm crit}$, and $d\widetilde{M}_{\rm crit}/dx_{\rm crit} < 0$ for shells with sufficiently large $x_{\rm crit}$. Setting $d\widetilde{M}_{\rm c}/dx_{\rm crit} = 0$ for given dark matter, gas and stellar distributions, and a fixed $\widetilde{M}_{\rm m}$, therefore identifies the *largest* critical SMBH mass required for the momentum-driven shell to escape, $\widetilde{M}_{\rm crit}^{\rm max}$.

Defining $x_{\rm crit} = x_{\rm max}$ when $d\widetilde{M}_{\rm crit}/dx_{\rm crit} = 0$, equation (4.16) becomes

$$\left\{\frac{d\ln[m_g\,m_{\rm con}]}{d\ln x}\right\}_{x=x_{\rm max}} - 2 - \frac{1}{\widetilde{M}_{\rm m}}\frac{h(x_{\rm max})m_{\rm con}(x_{\rm max})}{x_{\rm max}^2}\left\{\frac{d\ln m_{\rm con}}{d\ln x}\right\}_{x=x_{\rm max}} = 0. \quad (4.18)$$

Substituting $x_{\rm crit} = x_{\rm max}$ into equation (4.13), the dimensionless critical mass is given by

$$\widetilde{M}_{\rm crit}^{\rm max} = \left\{ \frac{h(x_{\rm max}) m_{\rm con}^2(x_{\rm max})}{x_{\rm max}} \right\} \times \left[1 - \frac{h(x_{\rm max}) m_{\rm con}(x_{\rm max})}{\widetilde{M}_{\rm f}\ x_{\rm max}^2} \right]^{-1}. \tag{4.19}$$

In general, equation (4.18) is solved numerically for $x_{\rm max}$ (for given gas, stellar and dark matter profile shapes and a fixed $\widetilde{M}_{\rm f}$), with the corresponding $\widetilde{M}_{\rm crit}^{\rm max}$ calculated through equation (4.19). In the limit that $\widetilde{M}_{\rm f} \gg h(x_{\rm max}) m_{\rm con}(x_{\rm max})/x_{\rm max}^2$, the final term on the left-hand side of equation (4.18) is negligible [the logarithmic slope of $m_{\rm con}(x)$ is a well behaved function, with a value of order unity at any value of x]. This is only strictly true in the limit of very large dark matter halos. With this limit applied, and making use of the definition $d\ln m/d\ln x - 1 = d\ln V_c^2/d\ln x$, equation (4.18) leads to

$$\left\{ \frac{d\ln[V_{\rm g}^2 V_{\rm con}^2]}{d\ln x} \right\}_{x=x_{\rm max}} \longrightarrow 0. \tag{4.20}$$

Equation (4.20) has a single root in this limiting case, with $x_{\rm max} \rightarrow 1$, namely the location where the product of $V_{\rm g}$ and $V_{\rm con}$ peaks.

Setting $x_{\rm max} = 1$ in equation (4.19), and assuming $\widetilde{M}_{\rm f} \gg h(x_{\rm max}) m_{\rm con}(x_{\rm max})/x_{\rm max}^2$, the *sufficient* SMBH mass is given by

$$\widetilde{M}_{\rm BH} \geq \widetilde{M}_{\rm crit} = 1. \tag{4.21}$$

Combining this with the definition of M_σ, the critical SMBH mass required for a momentum-driven gas shell to escape a galaxy is

$$\begin{aligned} M_{\rm crit} &\longrightarrow \frac{f(r_{\rm f}) \kappa V_{\rm f}^4}{4\pi G^2} \\ &\simeq\ 1.14 \times 10^8 M_\odot \left[\frac{f(r_{\rm f})}{0.2} \right] \left(\frac{V_{\rm f}}{200\,{\rm km\,s^{-1}}} \right)^4, \end{aligned} \tag{4.22}$$

where denoting the radius at which the gravitational force is a maximum as $r_{\rm f}$,

$$f(r_{\rm f}) \equiv \frac{f_{\rm g}(r_{\rm f})}{1 + f_*(r_{\rm f})} \qquad \text{and} \qquad V_{\rm f}^2 \equiv \frac{G[M_*(r_{\rm f}) + M_{\rm d}(r_{\rm f})]}{r_{\rm f}}. \tag{4.23}$$

Again, this is the critical SMBH mass required for gas blow-out, and assumes the gas shell is able to get to the radius where it begins to accelerate, which corresponds to $r_{\rm f}$ in

the limit that $\widetilde{M}_{\rm f} \gg h(x_{\rm max})m_{\rm con}(x_{\rm max})/x_{\rm max}^2$. Whether a gas shell is able to reach $r_{\rm f}$, or stalls before this radius ($\widetilde{v}^2 = 0$), depends on the initial conditions, and in particular the value of C. For the examples in §4.3, it is assumed that the gas shells with $C \geq 0$ do not stall if $M_{\rm BH} \geq M_{\rm crit}$, and they are able to reach $r_{\rm f}$, and hence equation (4.22) can be applied.

4.2 Comparison to previous results

Equation (4.22) is an extension of that obtained by McQuillin & McLaughlin (2012), allowing for a non-virialised gaseous distribution and for the presence of stars in the protogalaxy. A comparison of this new prediction to the "old" one yields

$$\frac{M_{\rm crit,new}}{M_{\rm crit,old}} = \left(\frac{f(r_{\rm f})}{f_0}\right)\left[\frac{V_{\rm f}}{V_{\rm d}(r_{\rm d,pk})}\right]^4, \tag{4.24}$$

where again $r_{\rm f}$ denotes the radius at which the gravitational confining force is a maximum, if the gravity of the SMBH is negligible. For the case of no stars and gas tracing dark matter, $r_{\rm f} \equiv r_{\rm d,pk}$, $V_{\rm f}^4 \equiv V_{\rm d}^4(r_{\rm d,pk})$ and $f(r_{\rm f}) = f_0$, and hence equation (4.24) reduces to 1.

Throughout the rest of this Chapter, comparisons will be made between the new result to the original prediction from McQuillin & McLaughlin (2012). The only differences between the two predictions are the (possible) presence of stars in the protogalaxy and the gas initially being non-virialised (not tracing the dark matter). This will therefore allow for a detailed investigation of how the critical SMBH mass is altered by relaxing these two assumptions. The suggestion by Ishibashi & Fabian (2012), that allowing the gas to have an r^{-2} density profile inside a non-isothermal halo has little effect on the SMBH mass required for blow-out, can be looked at in closer detail. Ishibashi & Fabian (2012) are the only authors that have considered any kind of non-virialised gas, and the contribution from the stars to the gravitational potential has not been looked at before.

In what follows, a general method is outlined for using the new prediction, in

terms of fully specifying profiles for the gas, stellar and dark matter distributions. Ultimately, the new prediction will be compared to the $M_{\rm BH}$–bulge relations observed at $z = 0$, using the methods applied in Chapter 3. A few representative examples to illustrate the key results will be used, but this will not be an exhaustive set of possible combinations of the different distributions.

4.2.1 Three-component protogalaxies

As mentioned above, the new result presented here allows for protogalaxies composed of three components: stars, gas and dark matter. In what follows, it is more convenient to think about the critical SMBH mass prediction [equation (4.22)] in terms of gas- and stellar-to-dark matter mass ratios [$f_g(r) \equiv M_g(r)/M_d(r)$ and $f_*(r) \equiv M_*(r)/M_d(r)$]:

$$M_{\rm crit} \simeq 1.14 \times 10^8 \, M_\odot \left(\frac{f_{\rm g,vir}}{0.2}\right) \left[\frac{f_g(r_{\rm f})}{f_g(r_{\rm vir})}\right] \left(1 + f_{*,\rm vir} \left[\frac{f_*(r_{\rm f})}{f_*(r_{\rm vir})}\right]\right) \left[\frac{V_d(r_{\rm f})}{200\,{\rm km\,s^{-1}}}\right]^4 . \tag{4.25}$$

Here, $f_{\rm g,vir}$ and $f_{*,\rm vir}$ are global mass ratios (to dark matter) for the gas and stars respectively. These are constrained as functions of redshift and/or dark matter virial mass, $M_{\rm d,vir}$, by various studies in the literature (cf. §4.2.1.2 and §4.2.1.3). The ratios in the square brackets in equation (4.25), along with the value of $r_{\rm f}$, are dependent on how the three components are distributed with respect to one another.

The three individual components are determined by a scale radius, $r_{-2,\rm i}$, and the mass within that scale radius, $M_i(r_{-2,\rm i})$. There are therefore six free parameters that need to be chosen for a three-component protogalaxy (and hence a critical SMBH mass) to be fully specified. However, as for the two-component galaxies in Chapter 2, there are interdependencies between these parameters, along with constraints on dark matter mass and radius scales. Results from the literature allow the number of free parameters to be reduced to two (compared to one for Chapters 2 and 3, $M_{*,\rm tot}$), chosen here to be the halo mass at $z = 0$, $M_{\rm d,vir}(0)$ and the gas-to-dark matter concentration, $r_{-2,\rm g}/r_{-2,\rm d}$.

The redshift corresponding to the quasar-mode blow-out, $z_{\rm qso} \geq 0$ needs to be

specified as well. The model galaxies being set up here correspond to systems where there has been no SMBH feedback, so they are essentially at $z = z_{\rm qso}$. This will ultimately lead to connections between $M_{\rm BH}$ and $M_{\rm d,vir}(z_{\rm qso})$ and $V_{\rm d,pk}(z_{\rm qso})$. In §4.3, these connections are considered for some specific examples, and are combined with the average trends from Chapters 2 and 3 to compare to the empirical $M_{\rm BH}$–$\sigma_{\rm ap}(R_e)$ correlation in $z = 0$ quiescent galaxies.

4.2.1.1 Specifying the profiles

The shape for the density profiles of the gas, stars and dark matter can be specified using the (α, β, γ) models from Zhao (1995):

$$\rho_i(r) \propto \left(\frac{r}{a_i}\right)^{-\gamma_i} \left[1 + \left(\frac{r}{a_i}\right)^{1/\alpha_i}\right]^{(\gamma_i-\beta_i)\alpha_i} . \tag{4.26}$$

Here, i =g, $*$ or d, depending on the component being considered, and a_i is a scale radius. Once α, β and γ have been specified, the ratios $r_{-2,i}/a_i$ and $r_{\rm i,pk}/a_i$ are known for each profile. $r_{-2,i}$ is the radius at which the density profile has a logarithmic slope of -2, and $r_{\rm i,pk}$ corresponds to the maximum circular speed. The mass inside radius r is given by

$$M_i(r) \propto \int_0^{r/a_i} u^{2-\gamma_i}(1 + u^{1/\alpha_i})^{(\gamma_i-\beta_i)\alpha_i} du, \tag{4.27}$$

leading to the circular-speed profiles

$$V_i^2(r) = \frac{GM_i(r)}{r}. \tag{4.28}$$

The three cuspy dark matter halos used in Chapters 2 and 3 are all special cases of an (α, β, γ) model. The Hernquist (1990) profile corresponds to $(\alpha, \beta, \gamma) = (1, 4, 1)$, with an NFW (1996, 1997) model defined by $(\alpha, \beta, \gamma) = (1, 3, 1)$ and the Dehnen & McLaughlin (2005) model by $(\alpha, \beta, \gamma) = (9/4, 31/9, 7/9)$. An SIS model is also an example, with $(\alpha, \beta, \gamma) = (1, 2, 2)$.

4.2.1.2 Stellar-to-dark matter mass ratio

In Chapter 2, the Moster et al. (2010) parametrisation of the $f_{*,\mathrm{vir}}$–$M_{\mathrm{d,vir}}$ relation at $z = 0$ was used as one of the constraints, shown by the green curve in Figure 4.1. Moster et al. (2013) again use the abundance matching technique to obtain the stellar-to-dark matter mass ratio as a function of redshift (in the range $0 \lesssim z \lesssim 4$) and $M_{\mathrm{d,vir}}$:

$$f_{*,\mathrm{vir}}(z) \equiv \frac{M_{*,\mathrm{vir}}}{M_{\mathrm{d,vir}}}(z) = 2 f_{*,0}(z) \left[\left(\frac{M_{\mathrm{d,vir}}}{M_1(z)} \right)^{-\beta(z)} + \left(\frac{M_{\mathrm{d,vir}}}{M_1(z)} \right)^{\gamma(z)} \right]^{-1}. \tag{4.29}$$

The four parameters, $f_{*,0}, M_1, \beta$ and γ are functions of redshift given by

$$\begin{aligned} f_{*,0}(z) &= 0.0282 - 0.0247 \frac{z}{z+1} \\ \log M_1(z) &= 11.884 + 1.195 \frac{z}{z+1} \\ \beta(z) &= 1.06 - 0.826 \frac{z}{z+1} \\ \gamma(z) &= 0.556 + 0.329 \frac{z}{z+1}, \end{aligned} \tag{4.30}$$

constrained by Moster et al. (2013) by fitting their model to stellar mass functions at different redshifts. Again, $M_{\mathrm{d,vir}}$ is the dark matter halo mass at the specified redshift.

4.2.1.3 Gas-to-dark matter mass ratio

As well as the stellar mass fraction, it is also possible to constrain the gas-to-dark matter mass fraction within the virial radius. If the total baryon fraction at the virial radius, $f_{\mathrm{b,vir}} \equiv M_{\mathrm{b,vir}}/M_{\mathrm{d,vir}}$, is for gas and stars, then the gas fraction is given by

$$f_{\mathrm{g,vir}} \equiv \frac{M_{\mathrm{g,vir}}}{M_{\mathrm{d,vir}}} = f_{\mathrm{b,vir}} - f_{*,\mathrm{vir}}. \tag{4.31}$$

The solid black curve in Figure 4.1 shows the baryon-to-dark matter mass fraction, $f_{\mathrm{b,vir}}$, as a function of $M_{\mathrm{d,vir}}$ at $z = 0$, discussed in §2.2.3. This is based on the observational result obtained by Giodini et al. (2009), who consider the baryon fraction inside the r_{500} radius for 118 groups and clusters, and from this, $f_{\mathrm{b,vir}}$ was calculated. It has been suggested that the decrease in the baryon fraction for smaller halo masses

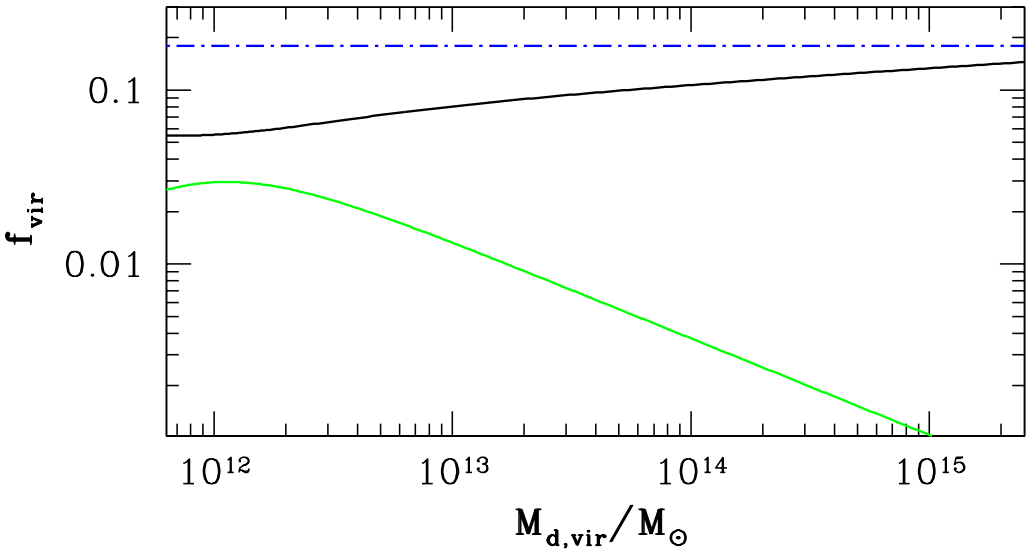

Figure 4.1: The baryon (black curve) and stellar (green curve) mass fraction at the virial radius, $r_{\rm vir}$, as a function of the halo virial mass, $M_{\rm d,vir}$. The broken blue line again corresponds to the cosmic average. $f_{*,\rm vir}$ is from the Moster et al. (2010) parametrisation. The broken blue line corresponds to the cosmic average baryon fraction, $f_0 \simeq 0.18$ (Planck collaboration 2014).

at $z = 0$, is primarily due to AGN or supernovae feedback (Giodini et al. 2009; Lagana et al. 2011; Gonzalez et al. 2013). However, for the model galaxies in this Chapter, a global baryon fraction *before* any AGN feedback has taken place is required, as a function of both redshift and halo mass at that z. For this, it is necessary to turn to results from cosmological simulations that have considered the baryon fraction *without* any radiative effects from AGN and/or supernova feedback.

For halo masses in the range $10^{10} M_{\odot} \lesssim M_{\rm d,vir} \lesssim 10^{15} M_{\odot}$, Crain et al. (2007) investigate the baryon-to-total mass fraction ($M_{\rm b,200}/M_{\rm T,200}$) in dark matter halos formed in non-radiative gas-dynamical simulations, at $z = 0$ and $z = 1$. They find that $M_{\rm b,200}/M_{200}$ is approximately 90% of the cosmic average, $\Omega_{\rm b}/\Omega_{\rm m} \simeq 0.16$, independent of both red shift and halo mass. Crain et al. also perform simulations including a feedback mechanism associated with the energetic photons that re-ionized the Universe at high redshifts. This has the potential to inhibit galaxy formation in low-mass halos (Bullock, Kravtsov & Weinber 2000; Benson et al. 2002), and needs to be accounted for in the context of the models here.

Crain et al. (2007) account for this feedback by including a simple photo-heating model (with a minimum gas temperature of $T \sim 2 \times 10^4$ K imposed from $z = 11$). They again consider halo masses in the range $10^{10} M_{\odot} \lesssim M_{\rm d,vir} \lesssim 10^{15} M_{\odot}$, for $z = 0$ only. In this case, they find that the baryon fraction is again approximately 90% for halo masses $\gtrsim 10^{11} M_{\odot}$, but decreases towards smaller systems. For halo masses $5 \times 10^9 M_{\odot} \lesssim M_{\rm d,200} \lesssim 10^{11} M_{\odot}$, Crain et al. (2007) find their photo-heated simulations are well approximated by

$$\frac{M_{\rm b,200}}{M_{200}} = \frac{\Omega_{\rm b,0}}{\Omega_{\rm m,0}} \left[1 + \left(\frac{M_{\rm d,200}}{1.7 \times 10^9 \, h_0^{-1} \, M_{\odot}} \right)^{-1} \right]^{-3} . \tag{4.32}$$

Equivalently, this can be expressed as a baryon-to-dark matter mass ratio, by multiplying through by $\Omega_{\rm m,0}/\Omega_{\rm d,0}$. Dividing through by $f_0 \equiv \Omega_{\rm b,0}/\Omega_{\rm d,0}$, equation (4.32) becomes:

$$\frac{f_{\rm b,200}}{f_0} \equiv \frac{M_{\rm b,200}/M_{\rm d,200}}{\Omega_{\rm b,0}/\Omega_{\rm d,0}} = \left[1 + \left(\frac{M_{\rm d,200}}{1.7 \times 10^9 \, h_0^{-1} \, M_{\odot}} \right)^{-1} \right]^{-3} . \tag{4.33}$$

Planelles et al. (2013) have analysed a set of hydrodynamical simulations of galaxy

clusters and groups, with the aim of constraining the baryon-to-total mass fraction in clusters, for masses in the range $10^{13} M_{\odot} \lesssim M_{\rm d,vir} \lesssim 10^{15} M_{\odot}$. They consider the redshift evolution (between $0 \leq z \leq 1$) of the baryon fraction inside various overdensity radii (the actual virial radius, along with $\Delta = 200$ and 500). Planelles et al. (2013) consider non-radiative simulations, as well as those that include supernova feedback (along with star formation), and those that also include AGN feedback. For the non-radiative and supernova feedback simulations, they find very weak mass and redshift dependencies, parametrised by

$$\frac{f_{\rm b,vir}}{f_0} = 0.84(1 + 0.03z) \left(\frac{M_{\rm d,vir}(z)}{5 \times 10^{14} h_0^{-1} \, M_{\odot}} \right)^{0.01} \left(\frac{\Delta_{\rm vir}(z)}{500} \right)^{-0.03} . \tag{4.34}$$

These results are consistent with other simulations with no heating included (Kravtsov, Nagai & Vikhlinin 2003; Ettori et al. 2006; Crain et al. 2007). For the simulation including AGN feedback, they find a slightly stronger mass dependence, with a power of ~ 0.03. Planelles et al. (2013) point out that this is consistent with the *trends* displayed by the observational samples (Giodini et al. 2009; Laganá et al. 2011), although with a significantly weaker dependence on mass.

To constrain the virial baryon-to-dark matter mass ratio for the models here, as a function of both redshift and halo mass, it is necessary to combine the results of Crain et al. (2007) and Planelles et al. (2013). Doing so allows $f_{\rm b,vir}$ to be constrained for a larger mass range, and accounts for the weak mass dependence from Planelles et al. (2013) and the effects of feedback associated with energetic photons at high redshift from Crain et al. (2007). Combining the two results, a parametrisation of $f_{\rm b,vir}$ is given by

$$\frac{f_{\rm b,vir}}{f_0} = 0.84 \left(\frac{M_{\rm d,vir}(z)}{5 \times 10^{14} h_0^{-1} M_{\odot}} \right)^{0.01} \left[1 + \left(\frac{M_{\rm d,vir}(z)}{1.7 \times 10^{9} h_0^{-1} M_{\odot}} \right)^{-1} \right]^{-3} \times \left(\frac{\Delta(z)}{500} \right)^{-0.03} (1 + 0.03z). \tag{4.35}$$

Strictly speaking, this only holds for $z = 0$, since the redshift evolution for the photo-heating model is not considered by Crain et al. (2007). However, for their non-radiative

simulation, Crain et al. (2007) find no evolution between $z = 0$ and $z = 1$, consistent with the weak dependence found by Planelles et al. (2013). It is therefore assumed here that the redshift evolution remains weak when photo-heating is included, and that the z dependence in equation (4.35) extends to higher redshifts.

Figure 4.2 shows $f_{\rm b,vir}(z)$ (dashed lines), $f_{*,\rm vir}(z)$ (solid lines) and $f_{\rm g,vir}(z)$ (dotted lines) as a function of $M_{\rm d,vir}(0)$. The mass fractions are evaluated at redshifts $z = 0$ (black curves), $z = 1$ (blue curves) and $z = 3$ (red curves). The broken green line corresponds to the cosmic average baryon fraction, $f_0 \simeq 0.18$ (Planck collaboration 2014). The halo mass at $z = 0$, $M_{\rm d,vir}(0)$, was calculated by using the exponential function that approximates the halo evolution from van den Bosch et al. (2014a; cf. Chapter 3):

$$\frac{M_{\rm d,vir}(z)}{M_{\rm d,vir}(0)} \;=\; \exp\left[-\frac{z\,\ln(2)}{z_{1/2}}\right] , \tag{4.36}$$

where

$$z_{1/2} \;=\; 2.05\left[\frac{M_{\rm d,vir}(0)}{10^{12}\,h_0^{-1}\,M_\odot}\right]^{-0.055} \;-\; 1\;. \tag{4.37}$$

The $f_{*,\rm vir}$ curves were calculated using equations (4.29) and (4.30). The peak in $f_{*,\rm vir}$ decreases with redshift from ~ 0.03 at $z = 0$ to ~ 0.01 at $z = 3$. As mentioned, Moster et al. consider redshifts up to $z \sim 4$, with the qualitative evolution slowing down as z increases, due to the $z/(1+z)$ dependencies in equation (4.30). However, they warn against taking exact numbers too seriously for $z > 3$, due to large uncertainties surrounding the stellar mass functions at these higher redshifts.

As implied by equation (4.35), the baryon fraction has little dependence on both redshift and mass (over most of the halo mass range considered here). For halos at $z = 0$ with masses $M_{\rm d,vir}(0) \gtrsim 10^{11} M_\odot$, the baryon fraction at $r_{\rm vir}$ is close to the cosmic average, independent of z. This supports the notion that it is indeed AGN feedback that reduces $f_{\rm b,vir}$, and is the reason for the steeper mass dependence in observations, from which $f_{\rm bvir} \sim M_{\rm d,vir}^{0.09}$ is implied (cf. §2.2.3). Given that $f_{*,\rm vir}$ is small (always $< 3\%$), $f_{\rm g,vir} \sim f_{\rm b,vir}$ for all masses and redshifts. The slight exception to this is the dip in $f_{\rm g,vir}$ right at the peak of $f_{*,\rm vir}$. This peak has a smaller value for higher z, so the dip becomes less prominent.

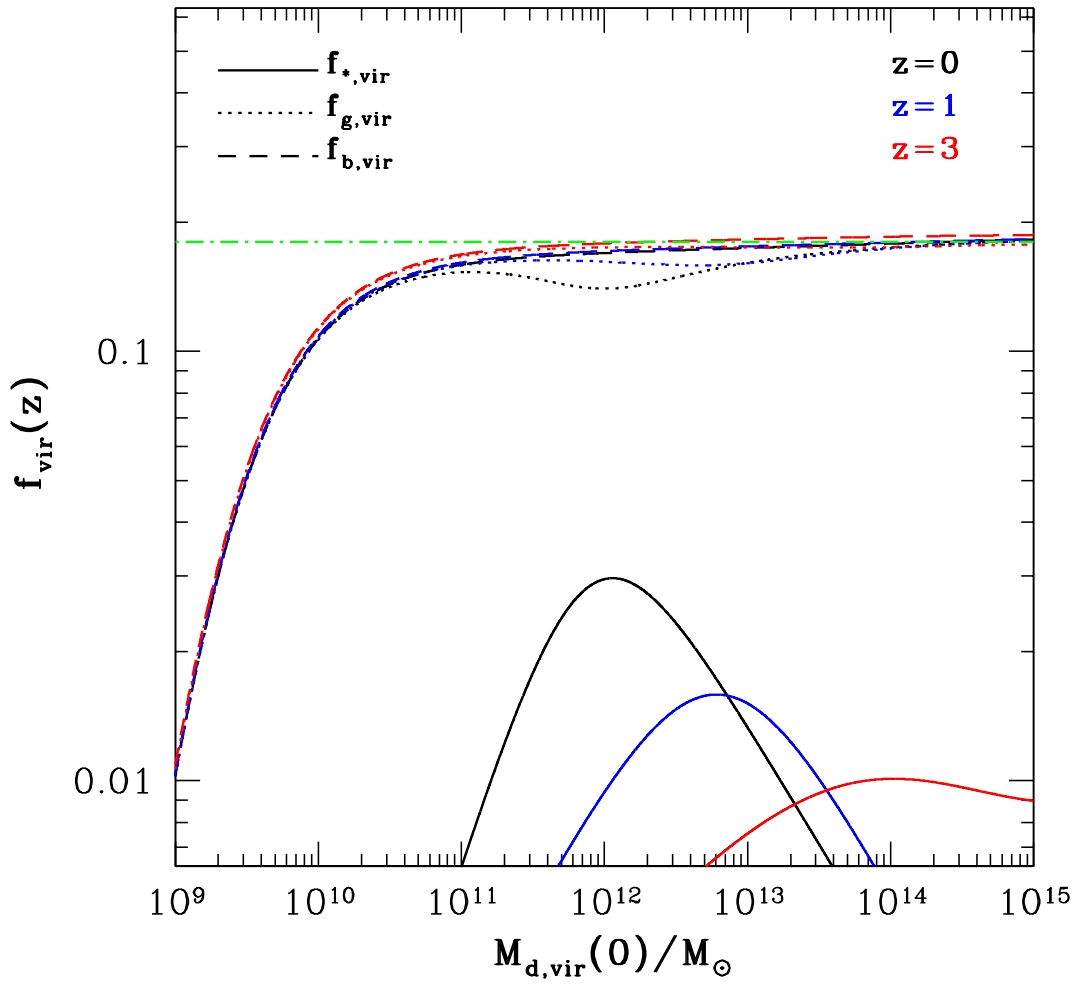

Figure 4.2: Global mass ratios at a specified redshift, z, as a function of dark matter viral mass, $M_{\rm d,vir}$, at $z = 0$. The solid curves correspond to the stellar-to-dark matter mass ratio, given by equations (4.29) and (4.30), taken from Moster et al. (2013). The broken lines are for the baryon-to-dark matter mass ratio, described by equation (4.35). The dotted lines are the gas-to-dark matter mass ratio, $f_{\rm g,vir} = f_{\rm b,vir} - f_{*,\rm vir}$. The three redshifts plotted are $z = 0$ (black curves), $z = 1$ (blue curves) and $z = 3$ (red curves). The solid green line corresponds to the cosmic average, $f_0 = 0.18$.

Specifying $M_{\rm d,vir}(0)$ therefore gives $M_{\rm d,vir}(z)$ $f_{*,\rm vir}(z)$ and $f_{\rm g,vir}(z)$ at $z \geq 0$, and hence the stellar and gas mass inside the virial radius at any given redshift. This in turn fixes the total virial mass, $M_{\rm vir} \equiv M_{\rm d,vir} + M_{\rm g,vir} + M_{*,\rm vir}$. Combining this with the fitting formula for the overdensity of a virialised sphere from Bryan & Norman (1998) and $H(z)/H_0$, the virial radius can be calculated:

$$\frac{r_{\rm vir}}{\rm kpc} = \left\{ 1166.1\, h_0^2\, \frac{\Delta_{\rm vir}(z)}{M_{\rm vir}/M_\odot} \left[\frac{H(z)}{H_0}\right]^2 \right\}^{-1/3}, \tag{4.38}$$

where $h_0 = 0.671$ (Planck Collaboration 2014).

4.2.1.4 Concentration relations

Specifying $M_{\rm d,vir}(0)$, along with a redshift (so $M_{\rm d,vir}(z)$ is known), also fixes the dark matter halo concentration, $r_{\rm vir}/r_{-2,\rm d}$, through the parametrisation given by Dutton & Macció (2014):

$$\log\left[\frac{r_{\rm vir}}{r_{-2}}\right] \simeq a - b \log\left[\frac{M_{\rm d}(r_{\rm vir})}{10^{12}\, h_0^{-1}\, M_\odot}\right] \tag{4.39}$$

with

$$\begin{aligned} a &= 0.537 + 0.488 \exp\left(-0.718\, z^{1.08}\right) \\ b &= 0.097 - 0.024\, z\ . \end{aligned}$$

For a given dark matter halo mass (at a chosen redshift), the virial radius is also known through equation (4.38). Combining this with equation (4.39) therefore gives $r_{-2,\rm d}$, which in turn fixes $r_{\rm d,pk}$ (see discussion in §4.2.1.1). The dark matter component is therefore fully specified by $M_{\rm d,vir}$, assuming the above constraints are used. For the gas and stars, an equivalent parameter is still needed, such as a stellar concentration $r_{\rm vir}/r_{-2,*}$ and gas concentration $r_{\rm vir}/r_{-2,\rm g}$.

The stellar effective radius, R_e, and total stellar mass, $M_{*,\rm tot}$ are related in $z = 0$ early-type galaxies by

$$\frac{R_e}{\rm kpc} = 1.5 \left(\frac{M_{*,\rm tot}}{2\times10^{10}\, M_\odot}\right)^{0.1} \left[1 + \left(\frac{M_{*,\rm tot}}{2\times10^{10}\, M_\odot}\right)^5\right]^{0.1}. \tag{4.40}$$

Once the *shape* parameters for the stellar distribution $(\alpha_*, \beta_*, \gamma_*)$, the ratios R_e/a_* and $a_*/r_{-2,*}$ are known. As an example, a Hernquist profile (used throughout Chapter 2 for the stellar distribution) yields $R_e/a_* \simeq 1.81527$ and $a_*/r_{-2,*} = 2$. Thus, once R_e is known, other radii that are specific to the stellar distribution follow automatically.

Given that the stellar mass profile can be normalised to $M_{*,\mathrm{tot}}$ and the radius normalised to R_e, evaluating $M_*(r)$ at the virial radius gives an equation relating these properties to both $M_{*,\mathrm{vir}}$ and r_{vir}. Again as an example, the Hernquist stellar mass profile evaluated at $r = r_{\mathrm{vir}}$ is

$$M_{*,\mathrm{vir}} = M_{*,\mathrm{tot}} \left[\frac{r_{\mathrm{vir}}/R_e}{r_{\mathrm{vir}}/R_e + a_*/R_e} \right]^2 . \tag{4.41}$$

Since $M_{*,\mathrm{vir}}$ and r_{vir} are set by fixing $M_{\mathrm{d,vir}}$, equations (4.40) and (4.41) can be solved simultaneously to find $M_{*,\mathrm{tot}}$ and R_e. This in turn leads to $r_{-2,*}$ and $r_{*,\mathrm{pk}}$. It is also worth noting that $M_{*,\mathrm{vir}} \gtrsim 0.99 M_{*,\mathrm{tot}}$ for $10^{10}\,M_\odot \lesssim M_{\mathrm{d,vir}} \lesssim 10^{15} M_\odot$, so specifying a dark matter halo mass gives approximate values for $M_{*,\mathrm{tot}}$ and R_e, independent of the choice of stellar density profile.

The R_e–$M_{*,\mathrm{tot}}$ relation in equation (4.40) is for $z = 0$ early-type galaxies only. In order to have the stellar concentration, $r_{\mathrm{vir}}/r_{-2,*}$, constrained for higher redshifts, an equivalent relation is needed for $z > 0$. Observational studies of stellar property scaling relations at higher redshifts have only been done up to $z \sim 1$ (Fernandez Lorenzo et al. 2011; Zahid et al. 2015; Peralta de Arriba et al. 2015). Even at this redshift, corresponding to a look-back time of ~ 8 Gyr, there are limited data, and these are understandably biased toward the high-mass end (Peralta de Arriba et al. 2015).

Various studies have combined observations with hydrodynamical simulations of galaxy mergers to consider the redshift evolution of stellar properties and scaling relations (Hopkins et al. 2009; van Dokkum et al. 2010; Williams et al. 2010; van der Wel et al. 2014). Qualitatively, there is strong agreement in the literature that at a given $M_{*,\mathrm{tot}}$ at $z = 0$, galaxies are more compact at higher redshifts (i.e., stellar effective radii are smaller). This is attributed to a combination of dissipation effects (Hopkins et al. 2009), gas-poor mergers (Williams et al. 2010) and the growth of extended stellar halos (van Dokkum et al. 2010).

For a galaxy with a given $M_{*,\rm tot}$ at $z = 0$ [determined by specifying $M_{\rm d,vir}(0)$], the effective radius at $z > 0$ is

$$R_e(z) = R_e(0)\,[1+z]^{-\alpha}, \tag{4.42}$$

where values of α in the literature range from ~ 0.2–1.5. This large range is due to the specific initial conditions in the individual simulations for merger rates, star formation rates and the significance of dissipation. Both Hopkins et al. (2009) and Williams et al. (2010) find that α depends weakly on stellar mass — the effective radii of higher mass systems evolve more rapidly (larger α). Van der Wel et al. (2014) distinguish between late- and early-type galaxies, and find a significantly different rate of size evolution, with $\alpha = 0.75$ for late-types and $\alpha = 1.48$ for early-types. Peralta de Arriba et al. (2015) consider a small sample of 27 giant ellipticals at $z \sim 1$, and compare to a larger sample of early-type galaxies at $z = 0$ in the R_e–$M_{*,\rm tot}$ plane. Their results are consistent with equation (4.42), with $\alpha = 1.25$. Ultimately, the value of R_e at a given redshift determines the values of $r_{-2,*}$ and $r_{*,\rm pk}$, and hence the location where $V_*(r)$ reaches a maximum.

The gas concentration, $r_{\rm vir}/r_{-2,\rm g}$, is the only unknown once $M_{\rm d,vir}(0)$ has been specified (along with a value for $z_{\rm qso}$). Instead of this, the gas-to-dark matter concentration, $r_{-2,\rm g}/r_{-2,\rm d}$, can be chosen as the second free parameter, and $r_{\rm vir}/r_{-2,\rm g}$ calculated after. Leaving $r_{-2,\rm g}/r_{-2,\rm d}$ unconstrained essentially means that whether the gas is centrally concentrated ($r_{-2,\rm g}/r_{-2,\rm d} < 1$) or spatially extended ($r_{-2,\rm g}/r_{-2,\rm d} > 1$) with respect to the dark matter, is decided beforehand. If $r_{-2,\rm g}/r_{-2,\rm d} = 1$ *and* $(\alpha_g, \beta_g, \gamma_g) = (\alpha_d, \beta_d, \gamma_d)$, then the gas directly traces the dark matter.

4.3 Examples

To demonstrate how the new critical SMBH mass [equation (4.22)] compares to the McQuillin & McLaughlin (2012) result [equation (4.1)], a few representative examples are considered. In what follows, the stellar component is modelled as a Hernquist profile [$(\alpha_*, \beta_*, \gamma_*) = (1, 4, 1)$] and a Dehnen & McLaughlin model [$(\alpha_d, \beta_d, \gamma_d) =$

$(9/4, 31/9, 7/9)]$ is used to describe the dark matter. The baryon fraction inside the virial radius depends on mass and redshift as described by equation (4.35). The effective radius at $z > 0$, $R_e(z)$, is determined through equation (4.42), with $\alpha = 1.25$. Again, for all examples it is assumed that the gas shells with $C \geq 0$ do not stall and reach $r_{\rm f}$ if $M_{\rm BH} \geq M_{\rm crit}$, allowing them to escape from the protogalaxy (i.e., it is assumed that $M_{\rm crit}$ is the sufficient condition for blow-out, independent of the relative distributions of gas, stars and dark matter).

4.3.1 Dehnen & McLaughlin gas profile

For the first example, the gas and dark matter are both assumed to be described by Dehnen & McLaughlin profiles $[(\alpha_d, \beta_d, \gamma_d) = (\alpha_g, \beta_g, \gamma_g) = (9/4, 31/9, 7/9)]$. This does not necessarily mean that the two components trace each other. $r_{\rm vir}/r_{-2,{\rm d}}$ is fixed by the halo virial mass (at a given redshift). The gas will trace the dark matter if the gas-to-dark matter concentration, $r_{-2,{\rm g}}/r_{-2,{\rm d}} = 1$.

Figure 4.3 shows the circular-speed profiles for the dark matter (top panels), mass fractions (middle panels) and density profiles (bottom panels) as functions of $r/r_{\rm vir}$. The columns corresponds to different values of the gas-to-dark matter concentration, with $r_{-2,{\rm g}}/r_{-2,{\rm d}} = 0.1$ (left), 1 (middle), and 2 (right). This final value was chosen as a maximum to ensure that $r_{\rm f}/r_{\rm vir}$, shown by the vertical magenta lines in each panel, does not exceed 1. In the middle row, the red curves are for $f_g(r)/f_{\rm g,vir}$ and the green ones for $f_*(r)/f_{*,{\rm vir}}$. The curves in the bottom row are for the gas (red curves) dark matter (black curves) and stellar (green curves) density profiles, normalised to the value at $r_{\rm vir}$. The solid curves in all panels are for $z_{\rm qso} = 0$ and the broken lines correspond to $z_{\rm qso} = 3$. In all panels, the virial halo mass at $z = 0$ is $M_{\rm d,vir}(0) = 10^{12} M_\odot$, corresponding to a halo mass at $z_{\rm qso} = 3$ of $M_{\rm d,vir}(3) \simeq 1.5 \times 10^{11} M_\odot$.

In terms of the critical SMBH mass, the most important parts of these plots are the values of $V_{\rm d}(r)/V_{\rm d,pk}$, $f_g(r)/f_{\rm g,vir}$ and $f_*(r)/f_{*,{\rm vir}}$ at $r = r_{\rm f}$. Although the stars are extremely centrally concentrated (compared to the gas and dark matter), they have little impact on the final value of $M_{\rm BH}$. This is because the stars enter the new

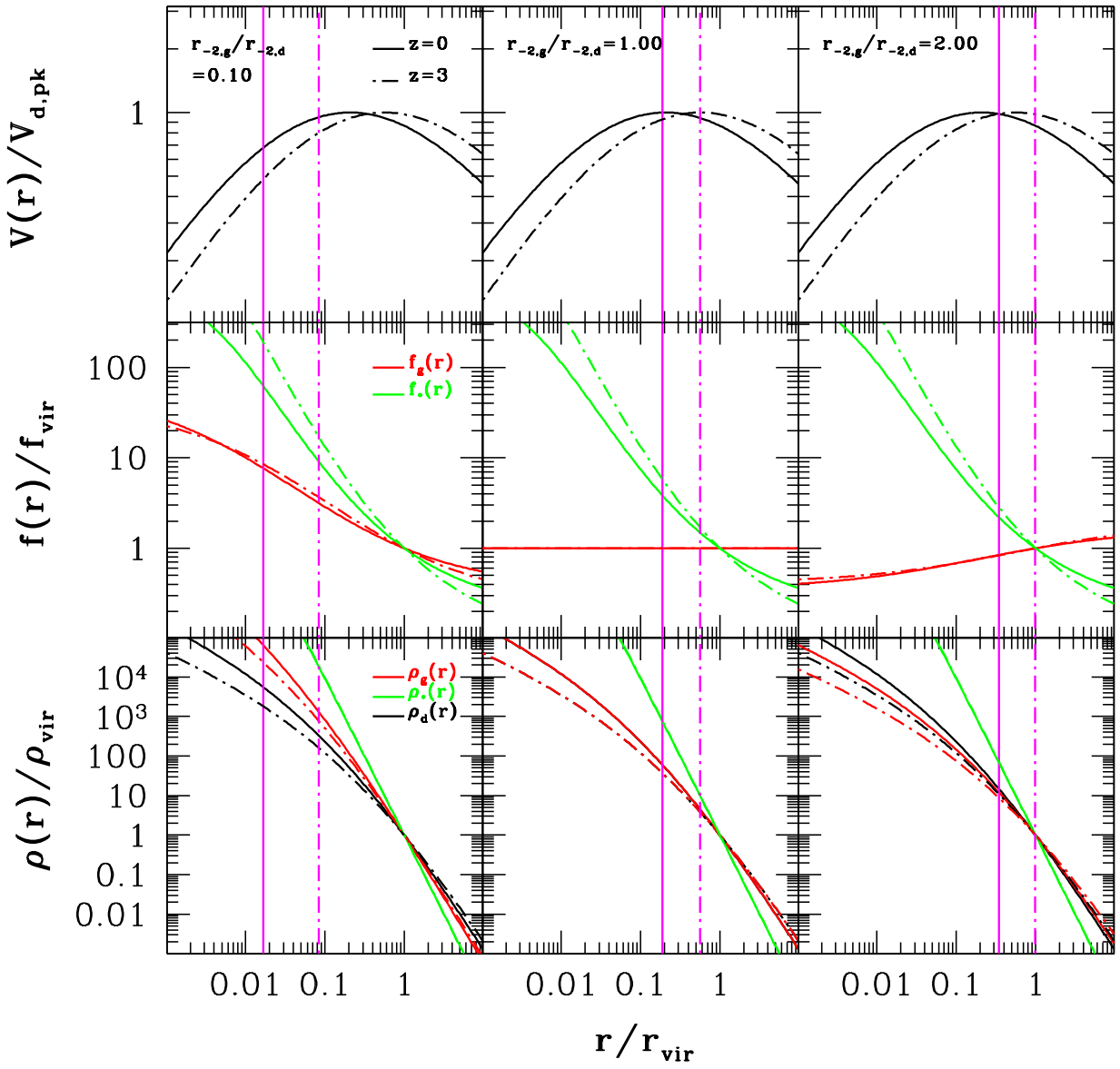

Figure 4.3: Circular-speed profiles for the dark matter (top row), mass fractions (middle row) and density profiles (bottom row) as functions of $r/r_{\rm vir}$. The stellar distribution is a Hernquist profile, with the gas and dark matter described by a Dehnen & McLaughlin model. In all panels, the halo mass at $z = 0$ is $M_{\rm d,vir}(0) = 10^{12} M_\odot$, corresponding to $M_{\rm d,vir}(3) \simeq 1.5 \times 10^{11} M_\odot$. The solid lines correspond to $z_{\rm qso} = 0$ and the broken lines to $z_{\rm qso} = 3$. The vertical magenta lines indicate the value of $r_{\rm f}/r_{\rm vir}$. In the bottom two rows, the red curves represent the gas, black curves the dark matter and green curves are for the stars. Columns are for different gas-to-dark matter concentrations, with $r_{-2,\rm g}/r_{-2,\rm d} = 0.1$ (left), 1 (middle) and 2 (right).

prediction through the term

$$\left[1 + f_{*,\mathrm{vir}} \frac{f_*(r_\mathrm{f})}{f_{*,\mathrm{vir}}}\right].$$

$f_{*,\mathrm{vir}}$ is typically small (always less than 4%), and the value of r_f is driven mainly by the gas-to-dark matter concentration. For the example in Figure 4.3, $r_\mathrm{f}/r_\mathrm{vir} \sim 0.1$–1 for the $z_\mathrm{qso} = 3$ case. Even for the smallest value of $r_\mathrm{f}/r_\mathrm{vir} \simeq 0.1$ [and hence the largest value of $f_*(r_\mathrm{f})/f_{*,\mathrm{vir}}$], the stars contribute very little. For a halo mass at $z = 0$ of $M_\mathrm{d,vir} \simeq 10^{12} M_\odot$, the global stellar-to-dark matter ratio at $z = 3$ is $f_{*,\mathrm{vir}}(z = 3) \sim 0.003$. From Figure 4.3, $f_*(r_\mathrm{f})/f_{*,\mathrm{vir}} \simeq 18$, implying the stars change the value of M_BH by less than 5%.

Figure 4.4 shows the ratio $M_\mathrm{crit,new}/M_\mathrm{crit,old}$ (top row) and the critical SMBH mass, M_BH (bottom row) halo virial mass (left) and $r_{-2,\mathrm{g}}/r_{-2,\mathrm{d}}$ (right) at $z_\mathrm{qso} = 3$. In the left column, three values of the gas-to-dark matter concentration are shown, with $r_{-2,\mathrm{g}}/r_{-2,\mathrm{d}} = 0.1, 1$, and 2. The right column shows curves for $M_\mathrm{d,vir}(3) = 10^{10}, 10^{11}$ and $10^{12} M_\odot$. The solid red curves in the bottom row correspond to the critical SMBH mass calculated using the McQuillin & McLaughlin (2012) result [equation (4.1)].

The overall shape of the curves in the top left panel [$M_\mathrm{crit,new}/M_\mathrm{crit,old}$ versus halo mass] is primarily driven by the $f_\mathrm{b,vir}$–$M_\mathrm{d,vir}$ relation, with the "fall-off" for $M_\mathrm{d,vir} \lesssim 10^{11}$ due to the form of equation (4.35). Even in the most massive halos, the baryon fraction inside the virial radius is approximately 90% of the cosmic average ($f_\mathrm{b,vir} \sim 0.9\, f_0$), according to equation (4.35). McQuillin & McLaughlin (2012) assumed that all of the baryons were gas (and traced the dark matter), and that the baryon fraction was always equal to the cosmic average, independent of mass. This is why even for the case of gas traces dark matter (corresponding to the middle curves in each panel, with $r_{-2,\mathrm{g}}/r_{-2,\mathrm{d}} = 1$), the new prediction is lower than the old critical mass in the top left panel of Figure 4.4, and hence why $M_\mathrm{crit,new}/M_\mathrm{crit,old} < 1$.

The dips in the curves are due to the connection between $f_{*,\mathrm{vir}}(z)$ and $M_\mathrm{d,vir}(z)$ at $z_\mathrm{qso} = 3$. Combining $f_\mathrm{b,vir}(z)$ with the maximum in $f_{*,\mathrm{vir}}(z)$, this corresponds to a dip in the global gas-to-dark matter mass ratio, $f_\mathrm{g,vir}(z)$. This propagates through to the new critical SMBH mass prediction, and hence the ratio, $M_\mathrm{crit,new}/M_\mathrm{crit,old}$. The

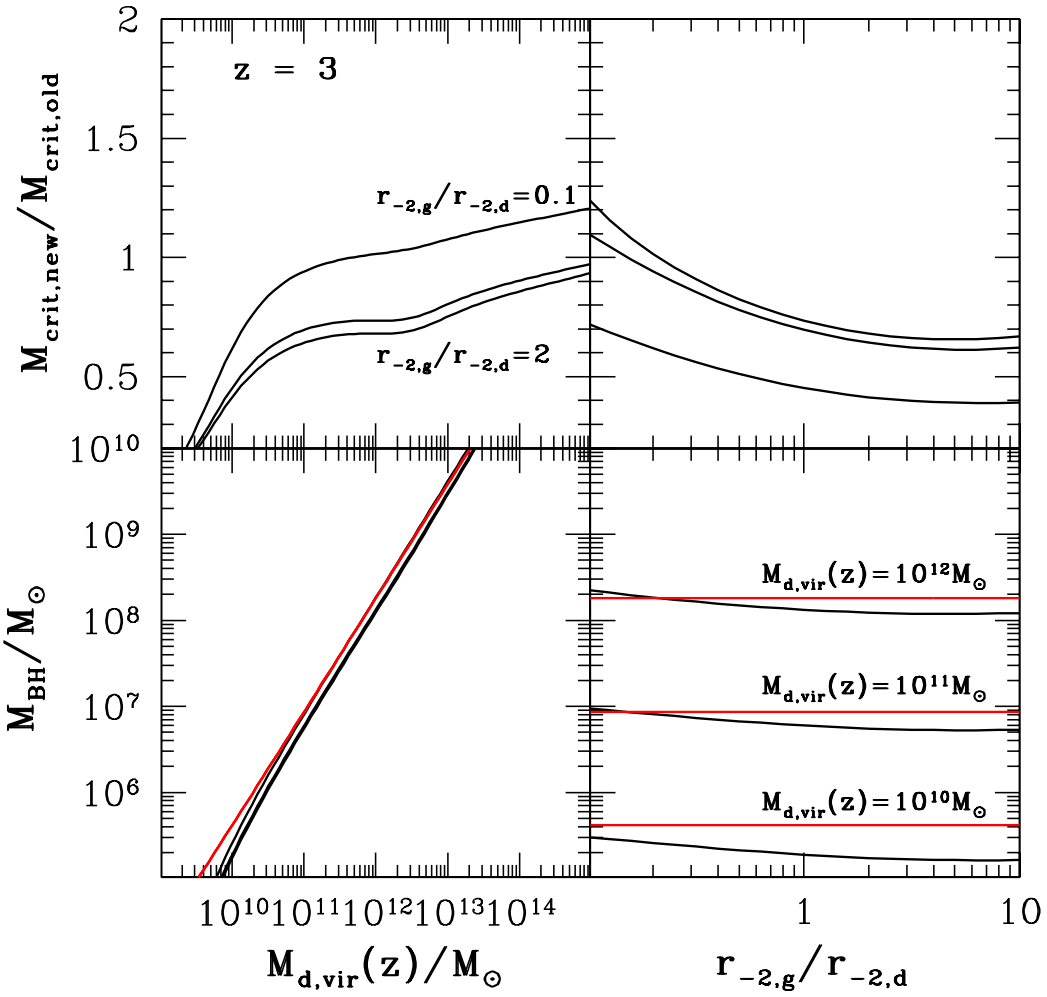

Figure 4.4: The ratio $M_{\rm crit,new}/M_{\rm crit,old}$ (top row) and $M_{\rm BH}$ (bottom row) as functions of $M_{\rm d,vir}(z)$ (left column) and $r_{-2,\rm g}/r_{-2,\rm d}$ (right column), at $z_{\rm qso} = 3$. The red lines in the bottom row correspond to the critical SMBH mass according to McQuillin & McLaughlin (2012). In the left column, the solid black curves from top to bottom correspond to $r_{-2,\rm g}/r_{-2,\rm d} = 0.1, 1$ and 2. For the right column, the curves correspond to halo masses at $z_{\rm qso} = 3$ of $M_{\rm d,vir}(3) = 10^{12}M_\odot$ (top curve), $M_{\rm d,vir}(3) = 10^{11}M_\odot$ (middle curve) $M_{\rm d,vir}(3) = 10^{10}M_\odot$ (bottom curve).

curves in the bottom left panel illustrate that the main difference between the new prediction and the old one is the slight change in the baryon fraction [from the cosmic average to the mass dependent $f_{\rm b,vir}(z)$]. The stars clearly have little impact on the value of the critical SMBH mass as a function of halo mass.

When the gas is centrally concentrated (wrt the dark matter), $r_{-2,\rm g}/r_{-2,\rm d} < 1$, so there is relatively more gas closer to the SMBH. This makes it more difficult for the SMBH wind to push the gas outwards, requiring a larger mass for blow-out (than if gas traced dark matter, with $r_{-2,\rm g}/r_{-2,\rm d} = 1$), so $M_{\rm crit,new}/M_{\rm crit,old}$ increases as $r_{-2,\rm g}/r_{-2,\rm d}$ decreases. On the other hand, a gas distribution that is more extended than the dark matter ($r_{-2,\rm g}/r_{-2,\rm d} > 1$) will be easier to clear for the SMBH, hence $M_{\rm crit,new}$ decreases with increasing $r_{-2,\rm g}/r_{-2,\rm d}$. This is illustrated by the two left panels in Figure 4.4. As alluded to earlier, a value of $r_{-2,\rm g}/r_{-2,\rm d} \gtrsim 2$ implies that $r_{\rm f} \gtrsim r_{\rm vir}$. From the definition of $r_{\rm f}$, this means that the gravitational force pulling against the gas shell has a maximum value outside of the virial radius. Such a model is not physically meaningful, so the behaviour of any quantity for $r_{-2,\rm g}/r_{-2,\rm d} \gtrsim 2$ should not be over-interpreted.

Only when the gas is reasonably centrally concentrated ($r_{-2,\rm g}/r_{-2,\rm d} \lesssim 0.15$), and only for $M_{\rm d,vir}(3) \gtrsim 10^{11} M_{\odot}$, does the ratio $M_{\rm crit,new}/M_{\rm crit,old}$ exceed unity. This limit on $M_{\rm d,vir}$ again reflects the additional constraint of the virial baryon fraction as a function of halo mass that has been used here. For the gas and dark matter having the same profile shapes, it is $f_{\rm b,vir}$ and $r_{-2,\rm g}/r_{-2,\rm d}$ that dominate the differences between the new and old predictions.

Figure 4.5 shows $M_{\rm BH}$ as a function of aperture stellar velocity dispersion at $z = 0$. Data points correspond to the early-type galaxies from the Kormendy & Ho (2013) sample. The blue curves in each panel correspond to the McQuillin & McLaughlin (2012) critical SMBH mass, evaluated with $f_0 = 0.18$ at $z_{\rm qso} = 0$, 1 and 3, so are the same as the curves from §3.3.2. The red curves correspond to the new critical $M_{\rm BH}$ prediction [equation (4.22)], evaluated at the same values of $z_{\rm qso}$, with the baryon fraction given by $f_{\rm b,vir}$ in equation (4.35). Each panel corresponds to a different value for the gas-to-dark matter concentration with $r_{-2,\rm g}/r_{-2,\rm d} \lesssim 0.1$ (top panel), 1 (middle panel) and 2 (bottom panel).

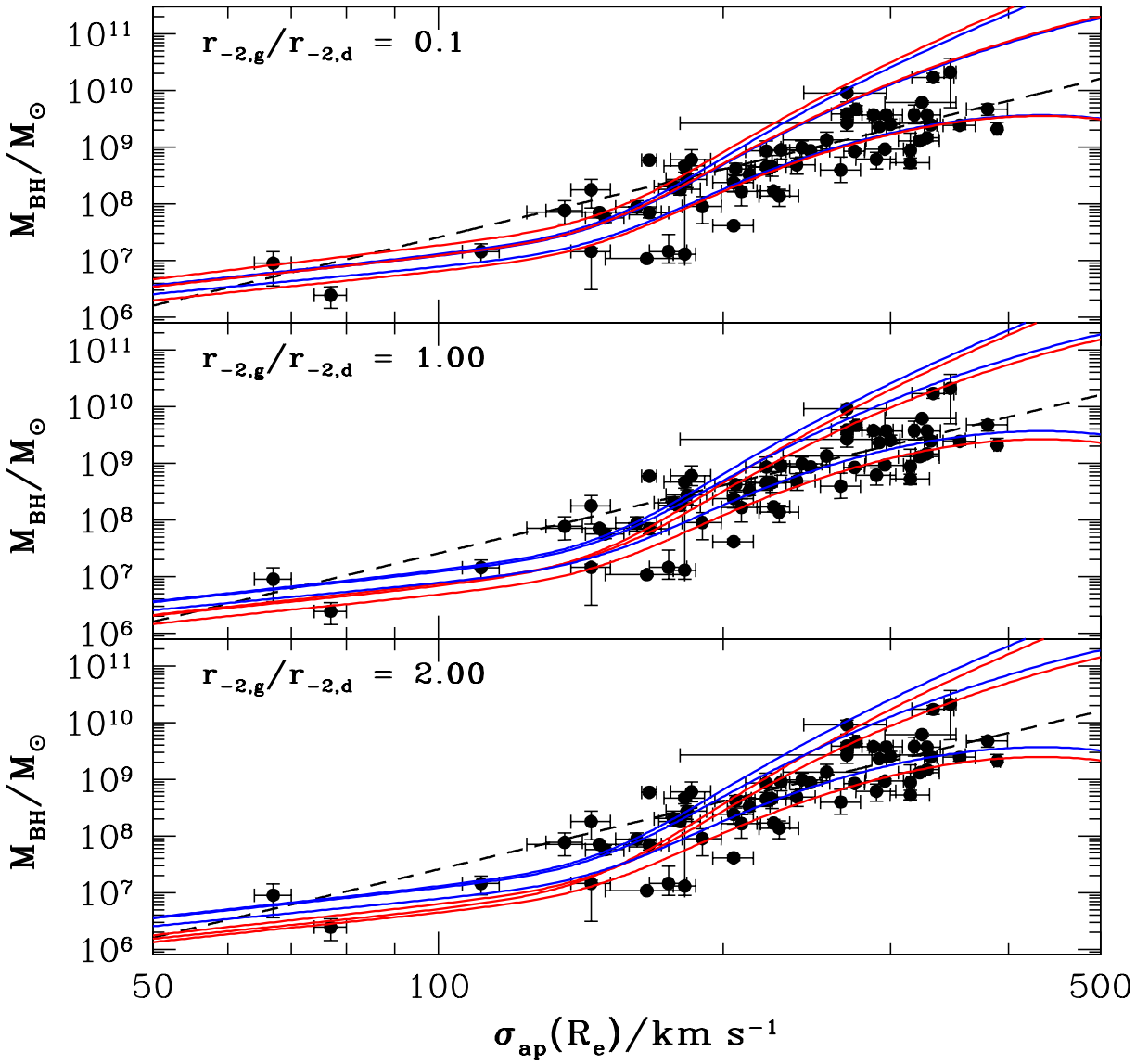

Figure 4.5: SMBH mass as a function of $\sigma_{\rm ap}(R_e)$ at $z = 0$. In all panels, the data points are for the early-type galaxies from the Kormendy & Ho (2013) sample. The blue curves correspond to the McQuillin & McLaughlin (2012) critical SMBH mass, evaluated with $f_0 = 0.18$ at $z_{\rm qso} = 0, 1$ and 3. The red curves are for the new prediction evaluated at the same values of $z_{\rm qso}$, for Hernquist stars and a Dehnen & McLaughlin model for the gas and dark matter. Panels correspond to different values of the gas-to-dark matter concentration, with $r_{-2,\rm g}/r_{-2,\rm d} = 0.1$ (top), 1 (middle) and 2 (bottom).

Ultimately then, the new prediction is not all that different from the McQuillin & McLaughlin (2012) result in this case, even though $M_{\rm crit,new}$ allows for:

- a mass dependent baryon fraction, $f_{\rm b,vir}$;
- the presence of stars in the protogalaxy;
- the gas to be centrally concentrated (top panel) or spatially extended (bottom panel).

For $\sigma_{\rm ap}(R_e) \gtrsim 200\,{\rm km\,s^{-1}}$, all of the red curves differ from the corresponding blue curves (i.e. with the same $z_{\rm qso}$) by no more than $\sim 40\%$. The similarities are a result of the weak dependence of $M_{\rm crit,new}/M_{\rm crit,old}$ on both $M_{\rm d,vir}(z)$ and $r_{-2,{\rm g}}/r_{-2,{\rm d}}$. The gas and dark matter both have the same profile *shape* in this example, so a critical SMBH mass similar to if gas traces dark matter is perhaps to be expected.

4.3.2 r^{-2} gas

For the next example, a gas profile with an r^{-2} density profile is considered, corresponding to $(\alpha_g, \beta_g, \gamma_g) = (1, 2, 2)$. The dark matter halo is still assumed to be a Dehnen & McLaughlin model. In the previous example, it was shown that the stars do not significantly influence the new critical SMBH mass. This is because the stars contribute only a small fraction of the overall mass of the system. Stars are therefore discarded for this example, so the protogalaxy consists of gas and dark matter only. This is comparable to the set-up in Ishibashi & Fabian (2012), who considered an r^{-2} gas profile inside a Hernquist dark matter halo. For a direct comparison, $f_{\rm b,vir} \equiv f_0$, independent of $M_{\rm d,vir}$ is assumed for this example only.

Given that the gas density is $\rho_{\rm g}(r) \propto r^{-2}$, then $d\ln\rho_g/d\ln r \equiv -2$ for all radii. The gas-to-dark matter concentration, $r_{-2,{\rm g}}/r_{-2,{\rm d}}$, is therefore not defined for this example. The gas mass profile is $M_{\rm g}(r) \propto r$, leading to $V_{\rm g}^2(r) = $ constant. Since there are no stars in this example, the radius at which the gravitational force (i.e., the

product $V_{\rm g}^2 V_{\rm d}^2$) is a maximum, is exactly where the dark matter circular speed peaks: $r_{\rm f} \equiv r_{\rm pk}$. This is always the case, independent of redshift.

Figure 4.6 shows $V_d(r)/V_{\rm d,pk}$ (top row), $f_g(r)/f_{\rm g,vir}$ (middle row) and $\rho(r)/\rho_{\rm vir}$ (bottom row) as functions of radius, at $z_{\rm qso} = 3$. All panels correspond to a halo mass of $M_{\rm d,vir}(3) \simeq 1.5 \times 10^{11} M_{\odot}$. The vertical magenta line indicates the value of $r_{\rm f}/r_{\rm vir} \equiv r_{\rm pk}/r_{\rm vir}$, at which $V_d(r)/V_{\rm d,pk} = 1$. Given the shape of the gas density and mass profiles relative to the dark matter, both $f_{\rm g}(r)$ and $\rho_{\rm g}(r)/\rho_{\rm d}(r)$ tend to infinity as $r \longrightarrow 0$ and $r \longrightarrow \infty$.

Figure 4.7 shows SMBH mass (top panel) and $M_{\rm crit,new}/M_{\rm crit,old}$ (bottom panel) as functions of $M_{\rm d,vir}(z)$ at $z_{\rm qso} = 0$ and $z_{\rm qso} = 3$. In the top panel, the red curves correspond to the McQuillin & McLaughlin (2012) critical SMBH mass. For this example, the ratio $M_{\rm crit,new}/M_{\rm crit,old}$ is given by

$$\frac{M_{\rm crit,new}}{M_{\rm crit,old}} = \frac{f_{\rm g}(r_{\rm f})}{f_{\rm g,vir}} = \frac{f_{\rm g}(r_{\rm pk})}{f_0}. \tag{4.43}$$

This depends on the halo mass at a given redshift, due to the $M_{\rm d,vir}$ dependence of $r_{\rm pk}$. For a given $M_{\rm d,vir}$ (and redshift), the virial radius and halo concentration, $r_{\rm vir}/r_{-2,\rm d}$, are both fixed, thus fixing r_{-2}. For a chosen dark matter density profile, the ratio $r_{\rm pk}/r_{-2,\rm d}$ is known (for Dehnen & McLaughlin, $r_{\rm pk}/r_{-2,\rm d} \simeq 2.28732$), and therefore specifying the halo mass determines $r_{\rm pk}$. The fact that the $M_{\rm d,vir}$ dependence of $M_{\rm crit,new}/M_{\rm crit,old}$ is weaker for higher redshifts reflects the redshift dependence of the halo concentration.

For $z_{\rm qso} = 3$, the ratio of new-to-old critical SMBH masses is $M_{\rm crit,new}/M_{\rm crit,old} \gtrsim 0.95$. This is consistent with the results of Ishibashi & Fabian (2012). They suggest that the SMBH mass required for a particular gas shell to escape is essentially the same for gas tracing the dark matter and gas having $\rho_{\rm g}(r) \propto r^{-2}$. For this example, the new prediction is therefore very close to the original result from McQuillin & McLaughlin (2012), as shown by the similarity between the red curve and black curve in the top panel for $z_{\rm qso} = 3$.

Figure 4.8 shows SMBH mass versus $\sigma_{\rm ap}(R_e)$ at $z = 0$, for early-type galaxies from Kormendy & Ho (2013). The blue curves are again the same as from §3.3.2, corresponding to the critical SMBH mass prediction from McQuillin & McLaughlin

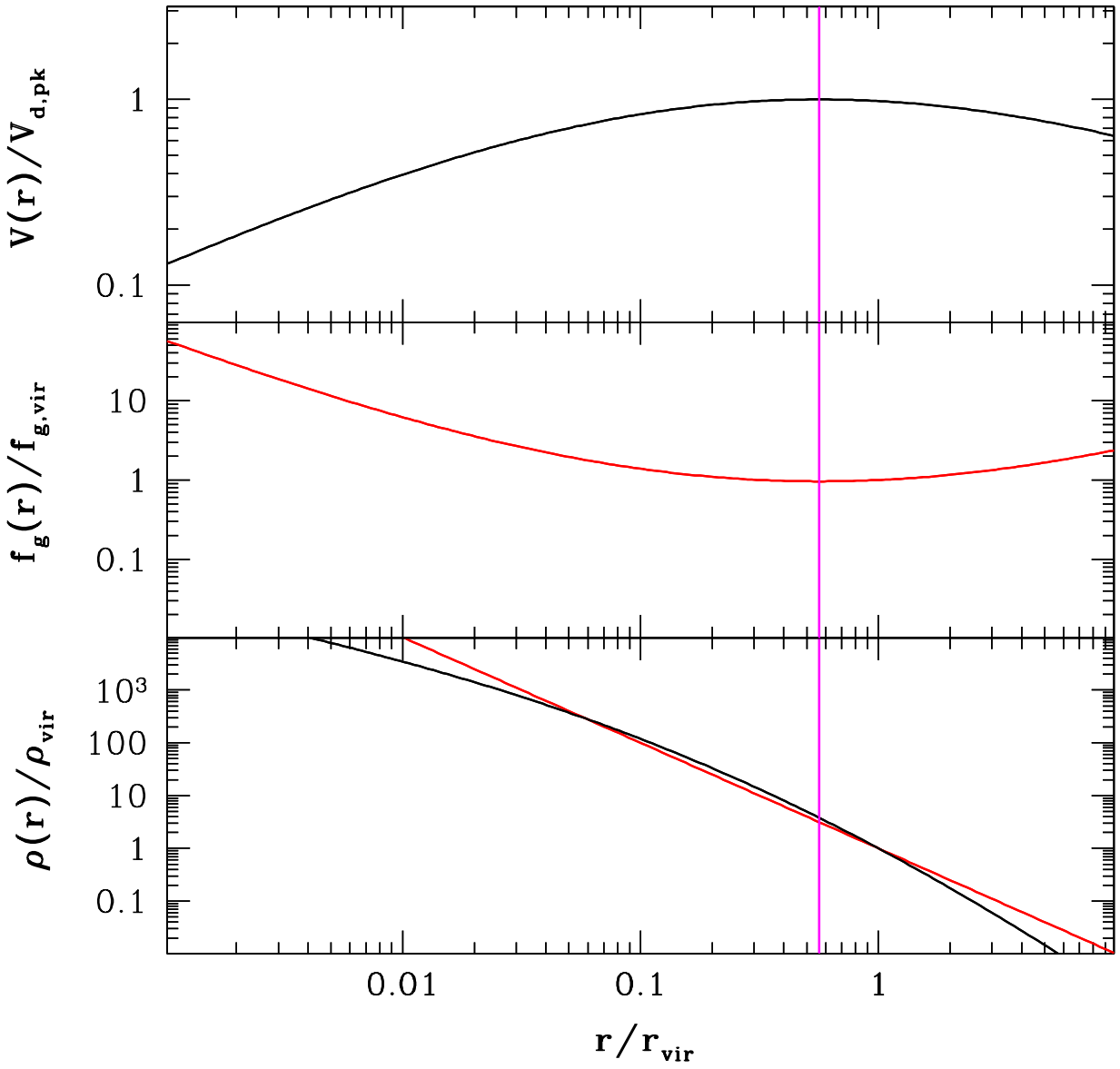

Figure 4.6: Circular-speed profiles for the dark matter (top row), mass fractions (middle row) and density profile ratios (bottom row) as functions of $r/r_{\rm vir}$, at $z = 3$. The dark matter is modelled by a Dehnen & McLaughlin halo and the gas is described by $(\alpha_g, \beta_g, \gamma_g) = (1, 2, 2)$, i.e., $\rho_g \propto r^{-2}$. The stars are left out of this model, and the virial gas fraction is set to the cosmic average: $f_{\rm g,vir} \equiv f_0$. In all panels, the halo mass at $z = 0$ is $M_{\rm d,vir}(0) = 10^{12} M_\odot$, corresponding to $M_{\rm d,vir}(3) \simeq 1.5 \times 10^{11} M_\odot$. The vertical magenta lines indicate the value of $r_{\rm f}/r_{\rm vir}$. Columns are for different gas-to-dark matter concentrations, with $r_{-2,\rm g}/r_{-2,\rm d} = 0.1$ (left), and 1 (right).

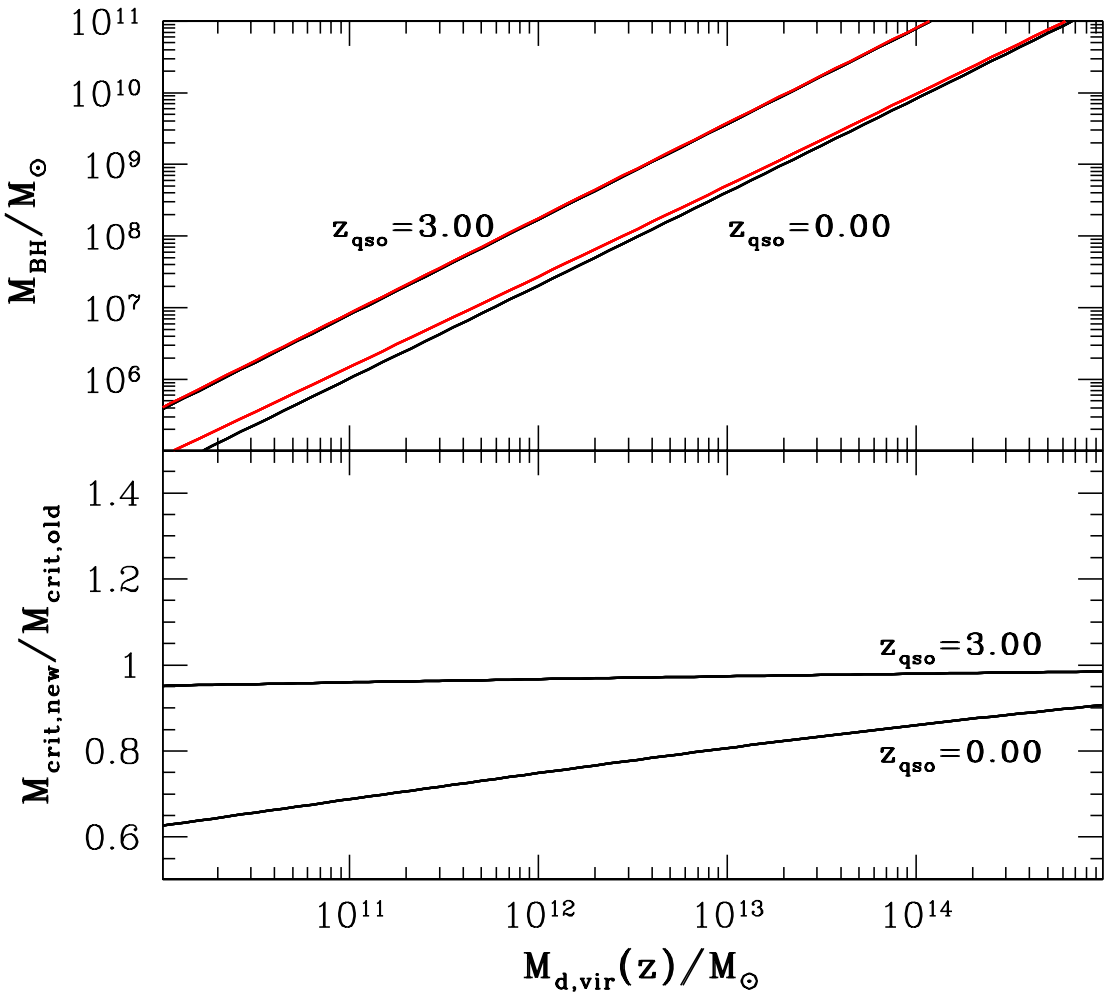

Figure 4.7: $M_{\rm BH}$ (top row) and the ratio $M_{\rm crit,new}/M_{\rm crit,old}$ (bottom row) as functions of $M_{\rm d,vir}(z)$ at $z = 3$ and $z = 0$. The red lines in the top row correspond to the critical SMBH mass according to McQuillin & McLaughlin (2012).

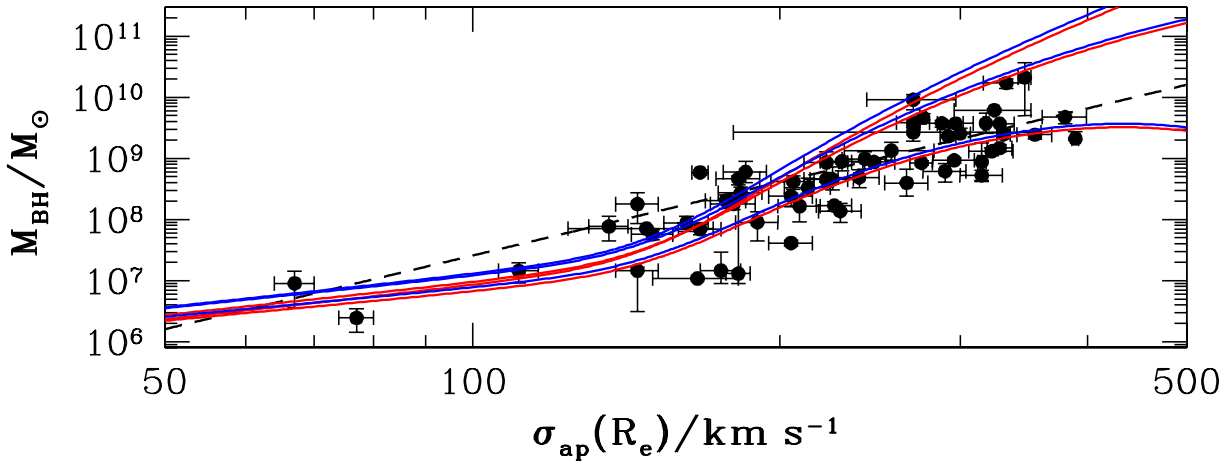

Figure 4.8: SMBH mass as a function of $\sigma_{\rm ap}(R_e)$ at $z = 0$. The data points are for the early-type galaxies from the Kormendy & Ho (2013) sample. The blue curves correspond to the McQuillin & McLaughlin (2012) critical SMBH mass, evaluated with $f_0 = 0.18$ at $z_{\rm qso} = 0, 1$ and 3. The red curves are for the new prediction evaluated at the same values of $z_{\rm qso}$, for a Dehnen & McLaughlin model for the dark matter and a gas profile described by $(\alpha_g, \beta_g, \gamma_g) = (1, 2, 2)$.

(2012), evaluated with $f_0 = 0.18$ at $z_{\rm qso} = 0, 1$ and 3 for a Dehnen & McLaughlin dark matter halo. The dashed black line, shown for reference only, corresponds to the same prediction with $V_{\rm d,pk} = \sqrt{2}\sigma_{\rm ap}(R_e)$. The red curves are from the new critical SMBH mass, evaluated at the same $z_{\rm qso}$ values. For this example, there are no stars [$f_{*,\rm vir} = 0$], and the baryon fraction is taken to be the cosmic average, $f_{\rm b,vir} = f_{\rm g,vir} = f_0$. The dark matter is described by a Dehnen & McLaughlin model, and the gas has a r^{-2} profile.

This again illustrates the fact that whether the gas has a density profile $\rho_g(r) \propto r^{-2}$, or the gas traces the dark matter, does not ultimately matter for the model $M_{\rm BH}$–$\sigma_{\rm ap}(R_e)$ prediction (and other SMBH relations), if the gas is able to escape. For the $z_{\rm qso} = 3$ curves, the new prediction is always within 5% of the original one. For $\sigma_{\rm ap}(R_e) \gtrsim 200\,{\rm km\,s^{-1}}$, the $z = 0$ curves differ by no more than 20%. The similarity

lends support to the idea that it is the dark matter, and the depth of the protogalactic potential well at the point of blow-out, that are fundamental in determining the critical $M_{\rm BH}$. The maximum gravitational force occurs where the dark matter circular speed peaks, which probes the protogalaxy on global scales. Therefore $f_{\rm g}(r_{\rm pk})/f_{\rm g,vir}$ of order unity is to be expected in this case, and so $M_{\rm crit,new}/M_{\rm crit,old} \sim 1$ is not surprising.

4.3.3 Extreme gas distributions

The two previous examples suggest that, assuming gas shells with $C \geq 0$ do not stall if $M_{\rm BH} \geq M_{\rm crit}$, the details of the initial gas distribution in the protogalaxy might not be significant in the context of a critical SMBH mass required for blow-out. For both examples, it was perhaps expected to be the case, given the choice of gas distributions used. However, it is worth checking this more generally, to see how significant the gas distribution is. This final example considers two physically extreme gas distributions inside a Dehnen & McLaughlin dark matter halo, with stars again neglected. The first of these is a highly centrally concentrated gas (relative to the dark matter), described by $(\alpha_g, \beta_g, \gamma_g) = (1, 4, 2)$, with $r_{-2,\rm g}/r_{-2,\rm d} = 0.01$. Such a gas distribution could be possible if the gas has a way of cooling rapidly before SMBH feedback begins, falling towards the centre as it does so. The second distribution is a spatially extended (again relative to the dark matter) gas, with the maximum gravitational force at $r_{\rm f} \sim r_{\rm vir}$. A spatially extended gas can be described by $(\alpha_g, \beta_g, \gamma_g) = (1, 4, 0)$ with $r_{-2,\rm g}/r_{-2,\rm d} = 2.5$, and is possible if the gas is able to be heated somehow (again before SMBH feedback), perhaps from supernova or photo-heating from energetic photons at high z in low mass galaxies.

Figure 4.9 shows the circular-speed profiles of the dark matter (top panels), gas-to-dark matter mass ratios (middle panels) and gas-to-dark matter density ratios (bottom panels) as functions of $r/r_{\rm vir}$ at $z_{\rm qso} = 3$. The left column is for the centrally concentrated gas distribution and the right for the spatially extended gas. The magenta lines again indicate the value of $r_{\rm f}/r_{\rm pk}$. In each panel, the halo mass at $z = 0$ is $M_{\rm d,vir}(0) \simeq 10^{12} M_\odot$ corresponding to $M_{\rm d,vir}(3) \simeq 1.5 \times 10^{11} M_\odot$.

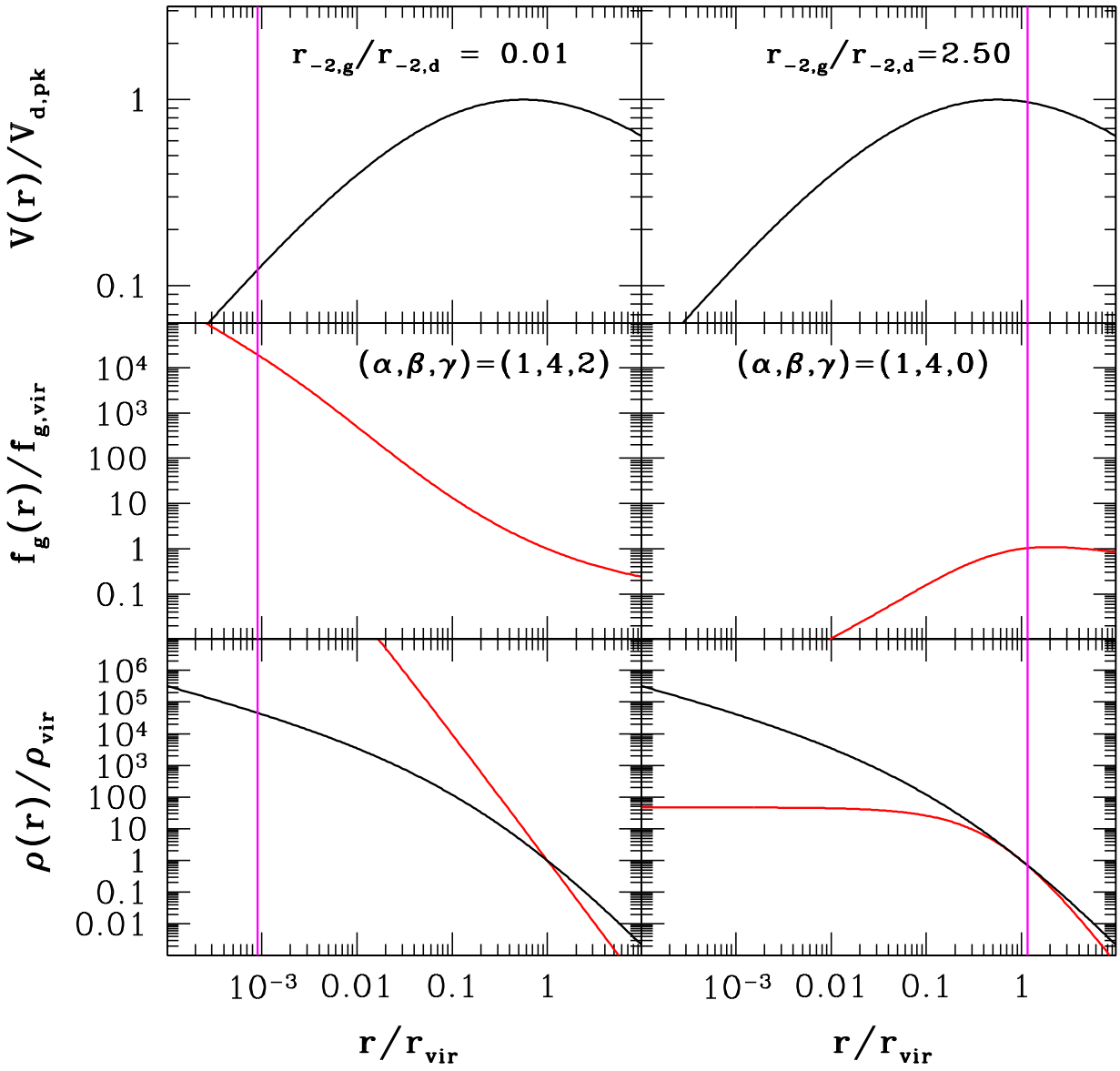

Figure 4.9: Circular-speed profiles for the dark matter (top row), mass fractions (middle row) and density profile ratios (bottom row) as functions of $r/r_{\rm vir}$, at $z_{\rm qso} = 3$. The dark matter is modelled by a Dehnen & McLaughlin halo and the gas is described by $(\alpha_g, \beta_g, \gamma_g) = (1, 4, 2)$ with $r_{-2,\rm g}/r_{-2,\rm d} = 0.01$ [left column] and $(\alpha_g, \beta_g, \gamma_g) = (1, 4, 0)$ with $r_{-2,\rm g}/r_{-2,\rm d} = 2.5$ [right column]. In all panels, the halo mass at $z = 3$ is $M_{\rm d,vir}(3) \simeq 1.5 \times 10^{11} M_\odot$. The vertical magenta lines indicate the value of $r_{\rm f}/r_{\rm vir}$. gas-to-dark matter concentrations, with $r_{-2,\rm g}/r_{-2,\rm d} = 0.01$ (left), and 1 (right).

For the centrally concentrated gas, $f_g(r) \longrightarrow \infty$ as $r \longrightarrow 0$. The radius for which the gravitational force is a maximum is $r_{\rm f}/r_{\rm vir} \simeq 10^{-3}$, at which $f_{\rm g}(r_{\rm f})/f_{\rm g,vir} \simeq 10^4$. This is a very large value, reflecting the excessive amounts of gas at such small radii. Given the form of the new critical SMBH prediction, it could be naively assumed that this would imply an extremely large $M_{\rm crit,new}$. However at $r_{\rm f}/r_{\rm vir} \simeq 10^{-3}$, the ratio $V_d(r_{\rm f})/V_{\rm d,pk} \simeq 0.1$. This ratio enters the prediction to the $4^{\rm th}$ power, and hence there is a "cancelling" effect between $f_{\rm g}$ and $V_{\rm d}$ at $r_{\rm f}$. As $f_{\rm g}(r_{\rm f})$ increases, the value of $[V_d(r_{\rm f})/V_{\rm d,pk}]^4$ decreases by a similar amount, so the product of the two remains approximately the same. For the spatially extended gas, $f_g(r) \longrightarrow 0$ as $r \longrightarrow 0$ and $r_{\rm f} \simeq r_{\rm vir}$, so most of the gas is already out at the virial radius. At $r_{\rm f} \simeq r_{\rm vir}$, both $f_{\rm g}(r_{\rm f})/f_{\rm g,vir}$ and $V_d(r_{\rm f})/V_{\rm d,pk}$ are of order unity, so $M_{\rm crit,new} \sim M_{\rm crit,old}$.

Figure 4.10 shows SMBH mass as a function of $\sigma_{\rm ap}(R_e)$ at $z = 0$. The data are again for E and S0 galaxies from Kormendy & Ho (2013). The blue curves represent the McQuillin & McLaughlin (2012) critical SMBH mass prediction for a Dehnen & McLaughlin halo and $f_0 = 0.18$, evaluated at $z_{\rm qso} = 0, 1$ and 3. The red curves are for the new prediction evaluated at the same $z_{\rm qso}$ values, for a Dehnen & McLaughlin model for the dark matter and a baryon fraction from the $f_{\rm b,vir}$–$M_{\rm d,vir}$ relation. The top panel is for the extremely centrally concentrated gas, described by $(\alpha_g, \beta_g, \gamma_g) = (1, 4, 2)$, with $r_{-2,{\rm g}}/r_{-2,{\rm d}} = 0.01$. The middle panel corresponds to a gas profile described by a Dehnen & McLaughlin density profile with $r_{-2,{\rm g}}/r_{-2,{\rm d}} = 1$ — i.e. the gas traces the dark matter. The bottom panel is for the spatially extended gas, described by $(\alpha_g, \beta_g, \gamma_g) = (1, 4, 0)$, with $r_{-2,{\rm g}}/r_{-2,{\rm d}} = 2.5$.

For the centrally concentrated gas, the ratio of $M_{\rm crit,new}/M_{\rm crit,old} \sim 3$–4, with a slight dependence on redshift. This is a relatively small change given the extreme differences in the gas distributions in the two predictions. Intuitively, a more centrally concentrated gas should lead to a higher SMBH mass, with $M_{\rm BH}$ increasing for lower values of the gas-to-dark matter concentration. However, if the gas is more centrally concentrated, then the value of $r_{\rm f}/r_{\rm vir}$ decreases. There is therefore less dark matter inside $r_{\rm f}$, and hence the gravitational force pulling against the outflow is smaller. These two effects cancel each other out to some extent, leading to very similar critical SMBH

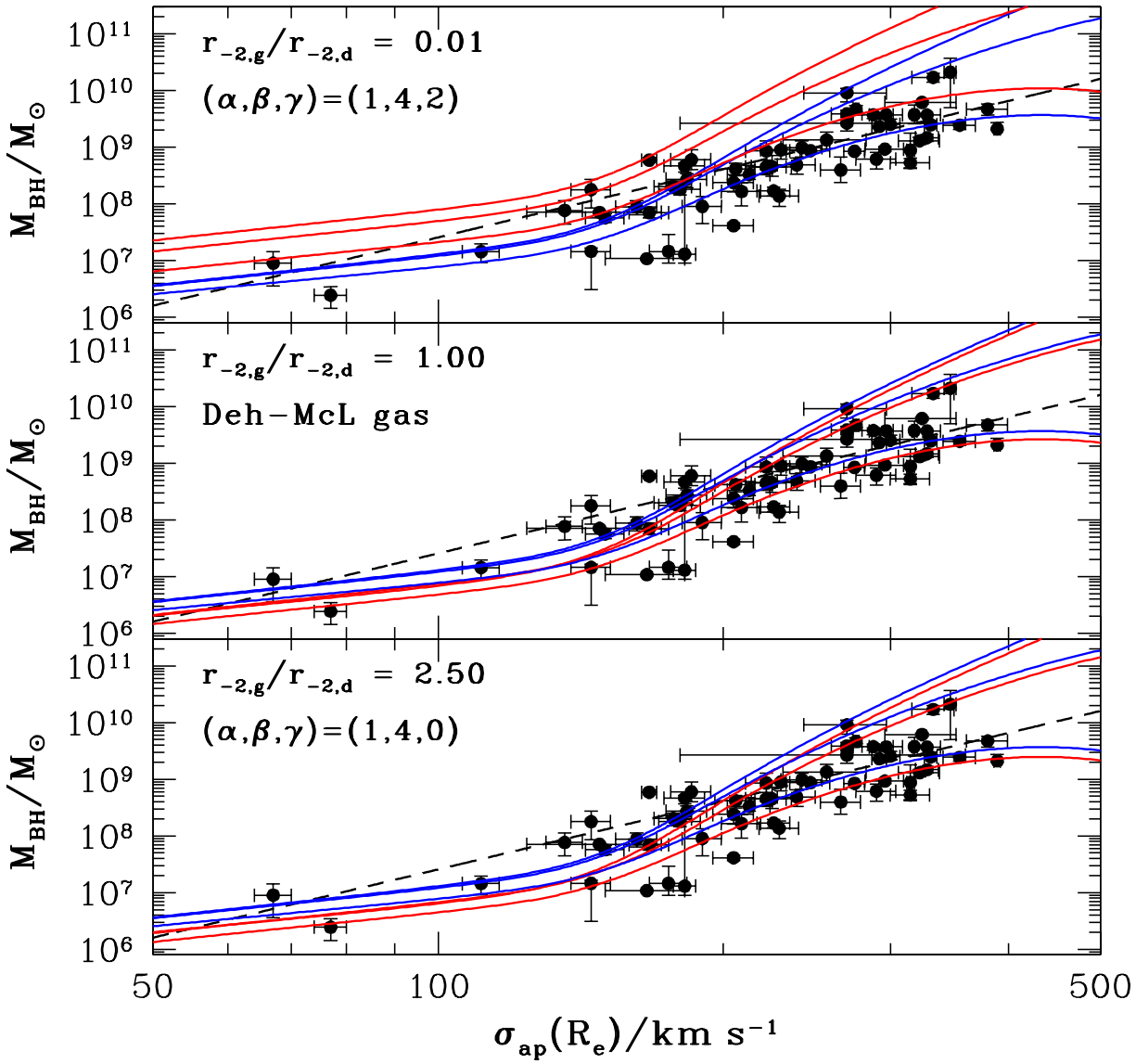

Figure 4.10: SMBH mass as a function of $\sigma_{\rm ap}(R_e)$ at $z = 0$. In all panels, the data points are for the early-type galaxies from the Kormendy & Ho (2013) sample. The blue curves correspond to the McQuillin & McLaughlin (2012) critical SMBH mass, evaluated with $f_0 = 0.18$ at $z_{\rm qso} = 0, 1$ and 3. The red curves are for the new prediction evaluated at the same values of $z_{\rm qso}$, for a Dehnen & McLaughlin model for the dark matter. In the top panel, the gas profile is described by $(\alpha_g, \beta_g, \gamma_g) = (1, 4, 2)$ with $r_{-2,\rm g}/r_{-2,\rm d} = 0.01$. The middle panel is for a Dehnen & McLaughlin gas profile, with $r_{-2,\rm g}/r_{-2,\rm d} = 1$. The bottom panel is for a gas profile described by $(\alpha_g, \beta_g, \gamma_g) = (1, 4, 0)$ with $r_{-2,\rm g}/r_{-2,\rm d} = 2.5$.

masses for extremely different gas distributions. For the gas tracing the dark matter (middle panel) and spatially extended gas (bottom panel), the difference between the two predictions is $\lesssim 40\%$ for $\sigma_{\rm ap}(R_e) \gtrsim 200\,{\rm km\,s^{-1}}$.

Ultimately then, the $M_{\rm BH}$–$V_{\rm d,pk}$ prediction from McQuillin & McLaughlin (2012) is fairly robust to allowing for stars in the protogalaxies and allowing different initial gas distributions. Given the constraint on $f_{*,\rm vir}$ from Moster et al. (2013), the stars have a negligible effect on the critical SMBH mass, with a $< 5\%$ difference for $M_{\rm BH}$ at $z_{\rm qso} = 3$. The value of $M_{\rm BH}$ is also not overly sensitive to the details of the gas distribution, again with the given constraints on $f_{*,\rm vir}$ and $f_{\rm b,vir}$.

This result is based on the assumption that any shell with $C \geq 0$ escapes from a protogalaxy if $M_{\rm BH} \geq M_{\rm crit}$. However, it could be the case that $M_{\rm crit}$ is no longer sufficient to drive the shells out. For example, for an extremely centrally concentrated gas, it could be required that C be very large to avoid the shells stalling at $r < r_{\rm f}$. This would imply that the sufficient SMBH mass that *guarantees* escape, is somewhat larger than the $M_{\rm crit}$ from equation (4.22). To investigate this requires a detailed analysis of the velocity fields of the gas shells.

For an initial gas distribution that is extremely concentrated, with the maximum gravitational force at a radius of $r_{\rm f} \simeq 10^{-3} r_{\rm vir}$, the critical SMBH mass is only a factor of 3–4 times larger than the McQuillin & McLaughlin (2012) prediction. This again demonstrates that it is the dark matter in the protogalaxy, and the depth of the corresponding potential well, that is fundamental in determining $M_{\rm BH}$. Allowing for stars and a non-virialised gas in the protogalaxy therefore has little impact on the SMBH mass required for quasar-mode blow-out of the gas.

5 Summary & Discussion

5.1 Summary

The observed correlations between the masses of supermassive black holes (SMBH), $M_{\rm BH}$, and properties of the galaxies at $z = 0$, are strong evidence for co-evolution between the SMBH and host. As discussed, this co-evolution likely involved self-regulated feedback. Most of the SMBH mass in the Universe today was grown during a quasar phase of Eddington-rate accretion (Yu & Tremaine 2002). This deposits significant amounts of energy and momentum back into the gaseous medium, possibly leading to a blow-out that stops any further growth of the SMBH. It is therefore the depth of the potential well, from which the SMBH feedback has to expel the protogalactic gas, that determines $M_{\rm BH}$.

The potential wells in question were dominated by dark matter. The main goal of the work presented here was to establish a method for connecting stellar properties at $z = 0$ to dark matter halo properties at $z = 0$ and higher redshifts. This allows for theoretical results connecting $M_{\rm BH}$ to a measure of the potential well depth, to be transformed into model predictions for the observed SMBH correlations at $z = 0$.

One such analytical prediction comes from McQuillin & McLaughlin (2012), who connect $M_{\rm BH}$ to the peak of the dark matter circular-speed curve, $V_{\rm d,pk}$, at the time of blow-out. Their prediction that $M_{\rm BH} \propto V_{\rm d,pk}^4$ assumes that the SMBH feedback is purely-momentum driven, in a gaseous protogalaxy with a static ambient medium that initially traces the dark matter. This critical SMBH mass prediction was used in Chapter 3 to obtain model predictions to compare to the observed SMBH correlations.

A two-component model for spherical galaxies was used as a starting point in Chapter 2 for establishing scaling relations between stellar and dark matter properties at $z = 0$. The stellar properties that are important are the total stellar mass, $M_{*,\rm tot}$, along with other properties at (or averaged inside of) the effective radius: R_e, $\sigma_{\rm ap}(R_e)$ and $f_*(R_e)$. Hernquist (1990) density profiles were therefore used for the stars inside

any galaxy. The consequences of this assumption on the scaling relations are considered by comparing the stellar properties for a Hernquist profile to those for more general Sérsic (1968) profiles, with variable Sérsic index, n. It is the dark matter halos that are key to determining SMBH mass in the feedback scenario focussed on in Chapter 3. Four different halo density profiles are therefore considered for the scalings in Chapter 2: those of Navarro et al. (1996, 1997; NFW), Hernquist (1990), Dehnen & McLaughlin (2005) and Burkert (1995).

These model galaxies were constrained by various results from the literature. Cosmological simulations relate dark matter virial masses to the halo concentrations, $r_{\rm vir}/r_{-2}$ (Dutton & Macció 2014), and stellar masses, $M_{*,\rm tot}$ (Moster et al. 2010). Data samples of early-type galaxies at $z = 0$ relate $M_{*,\rm tot}$ to the effective radii, R_e (Cappellari et al. 2011, 2013a,b). All of these together allowed the model galaxies to be put in terms of single independent parameter, which was chosen here to be $M_{*,\rm tot}$. Establishing trend lines in terms of one parameter leads to inevitable scatter around them, but the focus of the work here was to obtain the "correct" trends.

The R_e–$M_{*,\rm tot}$ relation was obtained by considering three data samples for local, early-type galaxies: 258 systems from the ATLAS^{3D} survey (Cappellari et al. 2011, 2013a,b), 100 from the ACSVCS (Chen et al. 2010) and summary data for $\sim 16,000$ galaxies in the SDSS (Graves et al. 2009a,b). In each case, effective radii and integrated luminosities were tabulated by the authors. Total stellar masses were estimated by combining these luminosities with mass-to-light ratios calculated from the single burst population synthesis models of Maraston (1998, 2005), assuming mean stellar ages of 9 Gyr and a Kroupa (2001) IMF. A mean stellar age of 9 Gyr corresponds to $z \sim 1.3$ (assuming Planck 2013 cosmology), and was chosen as an intermediate value for "typical" early-type galaxies with ages 7–11 Gyr, corresponding to $0.8 \lesssim z \lesssim 2.5$. A parametrisation of the average R_e–$M_{*,\rm tot}$ relation was then chosen such that equal numbers of ATLAS^{3D} & ACSVCS data points lie above and below the trend line. This relation does not depend on the choice of stellar or dark matter distribution.

The virial properties ($M_{\rm d,vir}$, $r_{\rm vir}$, and $f_{*,\rm vir}$) were then connected to $M_{*,\rm tot}$ by combining the $f_{*,\rm vir}$–$M_{\rm d,vir}$ relation from Moster et al. (2010) with the Hernquist mass

profile (evaluated at $r_{\rm vir}$) and the overdensity definition ($M_{\rm vir} \propto r_{\rm vir}^3$). These are independent of any assumptions about the density profiles of the halos. The shape of the $f_{*,\rm vir}$–$M_{*,\rm tot}$ relation is a direct result of the Moster et al. (2010) parametrisation, reflecting the inefficiency of star formation in the smallest and largest systems. This emphasises that halos around central galaxies with $M_{*,\rm tot} \gtrsim 10^{11} M_\odot$ encompass entire groups and clusters. The effects of "extra" baryons not associated with the central galaxy were also considered, and were found to change $r_{\rm vir}$ by $< 5\%$ and have little impact on the values of $M_{\rm d,vir}$. It was also found that the relations involving the virial properties are insensitive to the choice of stellar density profile, so long as $M_*(r)$ converges within $r \lesssim 100 R_e$.

With $r_{\rm vir}$ and $M_{\rm d,vir}$ known as functions of $M_{*,\rm tot}$, the scale radius r_{-2} followed from the concentration–halo mass relation of Dutton & Macció 2014. The location of the peak of the dark matter circular-speed curve, $r_{\rm pk}$, was then obtained for each halo as a function of total stellar mass. The model halo dependence of $r_{\rm pk}$ versus $M_{*,\rm tot}$ was found to be weak, due to $r_{\rm pk}/r_{-2} \sim 2$ for all these halos (and it was assumed that $r_{\rm vir}/r_{-2}$ versus $M_{\rm d,vir}$ is always the same). The peak value of the circular-speed, $V_{\rm d,pk}$, was obtained by evaluating the circular-speed profiles for each halo at $r_{\rm pk}$ and $r_{\rm vir}$, and folding in the dependencies of $M_{*,\rm tot}$ on $r_{\rm vir}$ and $M_{\rm d,vir}$. This gave $V_{\rm d,pk}$ for any given stellar mass. The model halo dependence was primarily driven by the differences in the widths of the circular-speed curves between $r_{\rm pk}$ and $r_{\rm vir}$.

The stellar-to-dark matter mass ratio at the effective radius, $f_*(R_e)$, was calculated by evaluating the stellar and dark matter mass profiles at R_e, and combining with $f_{*,\rm vir}$. The average trend for $f_*(R_e)$–$M_{*,\rm tot}$ was then compared to data from Cappellari et al. (2013b), who tabulated dark-to-total mass fractions for the 258 galaxies in the ATLAS sample. For the three cuspy halos (NFW, Hernquist and Dehnen & McLaughlin), the trend lines were found to be broadly consistent with the data. The cored halo (Burkert) was incompatible with these data, due to the much steeper $M_d(r)$ profiles at small radii. The dependence on using a Hernquist profile to describe the distribution of stars was also considered, entering $f_*(R_e)$ through the value $M_*(R_e)/M_{*,\rm tot}$. For Sérsic profiles with $3 \lesssim n \lesssim 7$, corresponding to stellar masses $M_{*,\rm tot} \gtrsim 10^{10} M_\odot$, the

values of $f_*(R_e)$ were altered by less than 5%. For smaller n, the stellar mass fractions were lower than the Hernquist value by no more than 20%. This was a relatively small change compared to the significant scatter around the $f_*(R_e)$–$M_{*,\rm tot}$ trend line.

Stellar velocity dispersions were then calculated using the isotropic Jeans equation, including contributions to the gravitational potential from the dark matter, stars and accumulated stellar ejecta. Initially, the stellar ejecta were assumed to be confined to the central regions, with $M_{\rm ej}(r) \approx F_{\rm ej} M_*(r)$. The value of $F_{\rm ej}$ came from the stellar population synthesis models from Maraston. For a mean stellar age of 9 Gyr and a Kroupa (2001) IMF, $F_{\rm ej} \simeq 0.72$. The value of the ejecta mass fraction was calculated for various star formation histories and was found to be robust, with $F_{\rm ej}$ increasing by $< 2\%$ for extended star formation lasting up to 6 Gyr.

Solving the Jeans equation gave $\sigma_*^2(r)$ profiles for any given stellar mass. The aperture dispersions were then calculated by projecting this along the line of sight, and taking a luminosity-weighted average over a disc of radius R_e. The calculated $\sigma_{\rm ap}(R_e)$–$M_{*,\rm tot}$ scaling relation was then compared against the early-type galaxy data. For stellar masses $10^{10} M_\odot \lesssim M_{*,\rm tot} \lesssim 10^{12} M_\odot$, encompassing the range used to define the $M_{\rm BH}$–galaxy property correlations, the three cuspy halos were consistent with the data. The cored halo over-estimated the value of $\sigma_{\rm ap}(R_e)$ for a given stellar mass. $\sigma_{\rm ap}(R_e)/(GM_{*,\rm tot}/R_e)^{1/2}$ values were also calculated for self-gravitating Sérsic profiles without any dark matter. These differed from the value for Hernquist stars by no more than $\sim 20\%$, with a slight tilt due to the stellar mass dependence of n.

All of the model curves were above the data for $M_{*,\rm tot} \lesssim 10^{10} M_\odot$. One possible reason for this was because $F_{\rm ej} \simeq 0.72$ was assumed for all stellar masses. More realistically, the stellar ejecta mass fraction will be closer to zero in low-mass galaxies, where supernovae driven winds can expel the gas. an ad-hoc relation between $F_{\rm ej}$ and $M_{*,\rm tot}$ was introduced such that $F_{\rm ej} = 0$ for low-mass galaxies and $F_{\rm ej} = 0.72$ for high-mass systems. The resulting trend line for $\sigma_{\rm ap}(R_e)$ was consistent with the early-type galaxy data for $10^8 M_\odot \lesssim M_{*,\rm tot} \lesssim 10^{12} M_\odot$. The effects on the velocity dispersions of including intracluster baryons were found to be an increase of $< 5\%$, similar to the effect on the virial properties.

The average trends connecting $M_{\rm d,vir}$, $V_{\rm d,pk}$ and $\sigma_{\rm ap}(R_e)$ to $M_{*,\rm tot}$ were then combined to obtain $M_{\rm d,vir}$ and $V_{\rm d,pk}$ as functions of aperture velocity dispersion. This demonstrated that in the most massive galaxies, the maximum of the dark matter circular speed far exceeds the aperture velocity dispersions at R_e. At this stage, the average trends were checked by comparing various numbers extracted from them to relevant data in the literature for the Milky Way, M87, M49 and NGC 4889. It was particularly notable that, starting with just the galaxies' total stellar masses, the scalings imply detailed properties of the cluster-sized dark matter halos around each of M87, M49 and NGC 4889, which were in reasonable agreement with the literature values.

Total (stars and dark matter) circular speed profiles, $V_c(r)$ were obtained by combining the stellar and dark matter mass profiles. Each of these was fixed by specifying $M_{*,\rm tot}$, and hence so was $V_c(r)$. In general, the total circular-speed curves were not flat, an assumption made in the literature when investigating relations between SMBH mass and halo mass. The relation between $V_c(R_e)$ and $\sigma_{\rm ap}(R_e)$ was calculated and was found to be broadly consistent with results from the literature. The connection between $V_c(R_e)$ and $V_c(r_{200})$, and how it varies with stellar mass, was also calculated. The trend lines obtained here compared well to results from Dutton et al. (2010), suggesting that distinguishing between late- and early-type galaxies, and the differences in how $f_{*,\rm vir}$ is defined, are not significant in this context. It should be noted that all the average trends are largely untested against dwarf galaxies with $\sigma_{\rm ap} \lesssim 60$–$70\,{\rm km\,s^{-1}}$ (corresponding to $M_{*,\rm tot} \lesssim$ several $\times 10^9 M_\odot$). More comprehensive modelling is required to be confident of how these kinds of average trends extrapolate to lower stellar masses.

With scaling relations between stellar and dark matter properties at $z = 0$ established, the halo evolution was considered in Chapter 3. This was ultimately so the $z = 0$ properties could be related to the halo properties at $z > 0$, which are connected to the SMBH masses required for gas blow-out. The simulation and merger tree results from van den Bosch et al. (2014a) were approximated by an exponential function describing $M_{\rm d,vir}(z)/M_{\rm d,vir}(0)$ and estimating the $z_{1/2}$ redshift [the redshift at which the

most massive progenitor had a virial mass $M_{\rm d,vir}(z_{1/2}) = M_{\rm d,vir}(0)$]. $V_{\rm d,pk}(z)/V_{\rm d,pk}(0)$ was then approximated for the three cuspy dark matter halo models, through a dependence on $M_{\rm d,vir}(z)/M_{\rm d,vir}(0)$. The relation $M_{\rm d,vir}(z)$ versus $M_{\rm d,vir}(0)$ showed gradual flattening towards higher masses, which set in at more modest halo masses for higher redshifts. This reflects a generic feature of structure formation by hierarchical merging — the most massive systems have formed more recently — and ultimately has significant implications for the $M_{\rm BH}$–galaxy property correlations.

The approximations for $M_{\rm d,vir}(z)/M_{\rm d,vir}(0)$ and $V_{\rm d,pk}(z)/V_{\rm d,pk}(0)$ were then combined with the average scalings from Chapter 2 to obtain connections between $z > 0$ halo properties [$V_{\rm d,pk}(z)$ and $M_{\rm d,vir}(z)$] and $z = 0$ stellar properties [$M_{*,\rm tot}$ and $\sigma_{\rm ap}(R_e)$]. These again showed the flattening towards higher masses in the dependence of $M_{\rm d,vir}(z)$ on $M_{\rm d,vir}(0)$. Folding in the $M_{\rm BH} \propto V_{\rm d,pk}^4$ prediction form McQuillin & McLaughlin (2012), model predictions for $M_{\rm BH}$ versus $\sigma_{\rm ap}(R_e)$ at $z = 0$ and $M_{*,\rm tot}$ at $z = 0$ were obtained.

Before comparing these model predictions for the SMBH correlations to data, it was necessary to make comparisons between the ATLAS and SMBH data. The ATLAS data were used to construct the trend lines in Chapter 2, so ideally would've been used here to compare to model predictions. however, there were only 22 galaxies in the ATLAS sample with confirmed $M_{\rm BH}$ values, so a larger sample was required. This was provided by the Kormendy & Ho (2013) compilation. In the $\sigma_{\rm ap}(R_e)$–$M_{*,\rm tot}$ plane, the Kormendy & Ho (2013) compilation lie systematically above the trend line, implying a selection bias in the SMBH data. However, for galaxies in common between ATLAS and Kormendy & Ho, if the $\sigma_{\rm ap}(R_e)$ and $M_{*,\rm tot}$ values from ATLAS were used instead, there was no obvious selection bias or systematic offset. The ATLAS velocity dispersions and stellar masses were lower than those cited by Kormendy & Ho (2013) by, on average, 10%. For the same galaxies, the ATLAS data points therefore lie to the left of the "usual" SMBH data in the $M_{\rm BH}$–$\sigma_{\rm ap}(R_e)$ and $M_{\rm BH}$–$M_{*,\rm tot}$ planes. However, for $\sigma_{\rm ap}(R_e) \gtrsim 200\,{\rm km\,s^{-1}}$ (or $M_{*,\rm tot} \gtrsim 10^{11} M_\odot$), where the majority of the current SMBH data lie, there were less than ten galaxies in common, so there was no way to check the majority of the cited values in Kormendy & Ho (2013).

The model predictions connecting $M_{\rm BH}$ to $\sigma_{\rm ap}(R_e)$ and $M_{*,\rm tot}$ at $z = 0$ were compared to the SMBH data. The predictions were calculated at a range of redshifts, $z_{\rm qso}$, defined as the redshift at which gas-blow out due to quasar phase accretion occurred. The specific form of this $M_{\rm BH}$–$V_{\rm d,pk}$ relation comes from a simplified analysis of momentum-conserving SMBH feedback in isolated and virialised gaseous protogalaxies with non-isothermal dark matter halos. This yielded model predictions for the $M_{\rm BH}$–$\sigma_{\rm ap}(R_e)$ and $M_{\rm BH}$–$M_{*,\rm tot}$ relations that were highly non-linear in log–log space. The shape of these predictions was driven by the non-monotonic shape of $f_{*,\rm vir}$ as a function of $M_{*,\rm tot}$ (resulting in an upward inflection) and, more fundamentally, the flattening in the curves due to the largest objects forming most recently.

As discussed, SMBH growth via gas-poor mergers at $z < z_{\rm qso}$ was not accounted for. The simulations by Volonteri & Ciotti (2013) suggest that low-redshift merging has a significant effect on the SMBH masses in systems with large $\sigma_{\rm ap}(R_e) \gtrsim 300$–$350\,{\rm km\,s^{-1}}$ at $z = 0$, increasing $M_{\rm BH}$ by a wide range of factors, $f_{\rm co} \equiv M_{\rm BH}(0)/M_{\rm BH}(z_{\rm qso}) \simeq 1$–$30$. Nevertheless, the model predictions describe the data reasonably well if the redshift of quasar-mode blow-out was $z_{\rm qso} \sim 2$–4. This range is reassuringly similar to the epoch of peak quasar density and SMBH accretion rate in the Universe (Richards et al. 2006; Hopkins, Richards & Hernquist 2007; Delvecchio et al. 2014). This lends support to the notion that the empirical SMBH correlations fundamentally reflect *some* close connection due to accretion feedback between SMBH masses in galactic nuclei and the dark matter in their host protogalaxies. It also demonstrates how the true physical relationship between SMBH mass and stellar velocity dispersion at $z = 0$ is not necessarily a power-law.

The relation between SMBH mass, fixed at $z_{\rm qso}$, and halo mass at $z = 0$ was also considered. As for the other model predictions, this was found to be non-linear. However, the contribution from the stars is insignificant on global scales, so there was no upward inflection. The $M_{\rm BH}$–$M_{\rm d,200}$ relation was compared to a similar study from Dutton et al. (2010). The model prediction calculated here showed a similar change in slope, without requiring a different SMBH growth mechanism (as suggested by Dutton et al. 2010).

The model prediction for $M_{\rm BH}(z_{\rm qso})$–$M_{\rm d,200}(z_{\rm qso})$ calculated here yielded a slope of ~ 1.3. This was found to be linear because both $M_{\rm BH}$ and $M_{\rm d,200}$ were evaluated at $z_{\rm qso}$, unlike the Dutton et al. (2010) study that considered $M_{\rm d,200}$ at $z = 0$. Booth & Schaye (2010) also considered a $M_{\rm BH}(z_{\rm qso})$–$M_{\rm d,200}(z_{\rm qso})$ relation, and found a slope of $\simeq 1.55$. The differences in the slopes between this study and Booth & Schaye (2010) are due to different assumptions regarding the driving mechanisms behind the feedback. Booth & Schaye (2010) assumed an energy-driven outflow, whereas the theoretical prediction used here is based on a momentum-driven analysis.

The final version of the SMBH data considered was the bivariate dependence of $M_{\rm BH}$ on a combination of bulge properties at $z = 0$. Two different combinations of $\sigma_{\rm ap}$ and R_e were considered — $\sigma_{\rm ap}^2 R_e$ and $\sigma_{\rm ap}^2 R_e^{0.3}$ — and connected to $M_{*,\rm tot}$ at $z = 0$ and transformed to model predictions for $M_{\rm BH}$. These model curves were again highly non-linear, and were broadly consistent with the data for $z_{\rm qso} \sim 2$–4. This once again supports the idea that the key connection is between $M_{\rm BH}$ and the dark matter halo of the protogalaxy when quasar-mode blow-out occurred. Any of the observed SMBH correlations at $z = 0$ are a reflection of this fundamental relation.

For all of the SMBH correlations at $z = 0$, a calculation was made for the intrinsic scatter around the model predictions for a fixed $z_{\rm qso}$. For the model curve corresponding to $z_{\rm qso} = 3$, the intrinsic scatter ranged from 0.39 dex for the $M_{\rm BH}$–$\sigma_{\rm ap}(R_e)$ and $M_{\rm BH}$–$M_{\rm d,200}$ relations up to 0.7 dex for the $M_{\rm BH}$–$M_{*,\rm tot}$ relation. The bivariate correlations yielded intrinsic scatter (again around the $z_{\rm qso} = 3$ curve) of 0.67 dex for $\sigma_{\rm ap}^2 R_e$ and 0.45 dex for $\sigma_{\rm ap}^2 R_e^{0.3}$. This suggests that connecting $M_{\rm BH}$ to $\sigma_{\rm ap}(R_e)$ or $M_{\rm d,200}$ at $z = 0$ leads to a more accurate reflection of the fundamental relation between $M_{\rm BH}$ and $V_{\rm d,pk}$ at $z = z_{\rm qso}$.

The theoretical relation $M_{\rm BH} \propto V_{\rm d,pk}^4$, used to obtain model predictions for the SMBH correlations in Chapter 3, has several caveats associated with it. Chapter 4 focussed on relaxing two of these simplifying assumptions: allowing for the presence of stars contributing to the confining gravity and allowing for a non-virialised gas. A full mathematical derivation was given, following the methods from McQuillin &

McLaughlin (2012). This new prediction was given by

$$M_{\rm crit} \simeq 1.14 \times 10^8 \, M_\odot \left(\frac{f(r_{\rm f})}{0.2} \right) \left(\frac{V_{\rm f}}{200 \, {\rm km \, s^{-1}}} \right)^4 , \tag{5.1}$$

where

$$f(r_{\rm f}) = \frac{f_{\rm g}(r_{\rm f})}{1 + f_*(r_{\rm f})} \qquad \text{and} \qquad V_{\rm f}^2 = \frac{G[M_*(r_{\rm f}) + M_{\rm d}(r_{\rm f})]}{r_{\rm f}}. \tag{5.2}$$

It was trivial to show that this reduces to the McQuillin & McLaughlin (2012) result in the case where there are no stars [$f_*(r_{\rm f}) = 0$] gas traces the dark matter [$f_{\rm new} = f_0$ and $V_{\rm m} = V_{\rm d,pk}$].

A general method was set up for making use of this new result by specifying profile shapes for the density distributions of the stars, gas and dark matter. These three-component models were constrained in a similar way to the model galaxies in Chapter 2. Cosmological simulations gave stellar (Moster et al. 2013) and baryon (Crain et al. 2007; Planelles et al. 2013) mass fractions as functions of both redshift, z, and halo mass at that redshift, $M_{\rm d,vir}(z)$. The halo mass at $z = 0$ determined $M_{\rm d,vir}(z)$ itself through the approximations of $M_{\rm d,vir}(z)/M_{\rm d,vir}(0)$ and $z_{1/2}$ from Chapter 3. The dark matter concentration was also constrained (Dutton & Macció 2014), as was the stellar concentration (through the R_e–$M_{*,\rm tot}$ relation and $R_e(z)/R_e(0)$). The relative concentration of gas-to-dark matter, $r_{-2,\rm g}/r_{-2,\rm d}$, was left as a free parameter.

A few representative examples were considered to demonstrate how the new prediction compared to the McQuillin & McLaughlin (2012) result. For each of these, it was assumed that if $C \geq 0$ (related to the initial momentum) in the formal solution for the velocity fields, then the gas shells were guaranteed to escape for $M_{\rm BH} \geq M_{\rm crit}$ (i.e., it was assumed that $M_{\rm crit}$ was sufficient for blow-out, independent of the relative distributions of gas, stars and dark matter). It was first of all found that, given the constraint on $f_{*,\rm vir}$, the presence of stars did not contribute to the gravity, and therefore to the critical SMBH mass, in a significant way. Stars were therefore only considered in the first example, assuming a Hernquist (1990) distribution. In this example, both the dark matter and gas were assumed to have Dehnen & McLaughlin (2005) density profiles, with $r_{-2,\rm g}/r_{-2,\rm d}$ allowed to vary. It was found that if the gas is more centrally

concentrated than the dark matter ($r_{-2,\mathrm{g}}/r_{-2,\mathrm{d}} < 1$), the critical SMBH mass required for blow-out was higher, but not by much.

The second example considered a gas distribution described by an $\rho(r) \propto r^{-2}$ profile inside a Dehnen & McLaughlin halo. It was found from this example that the gravitational force has maximum at the same location of the peak of the dark matter circular speed, $r_{\mathrm{f}} \equiv r_{\mathrm{pk}}$. The critical SMBH mass was found to have a slight dependence on $f_{\mathrm{g}}(r_{\mathrm{pk}})/f_{\mathrm{g,vir}}$, which was smaller for lower $M_{\mathrm{d,vir}}$. This result also showed that in this case, the critical SMBH mass is approximately the same as the McQuillin & McLaughlin (2012) result, consistent with the findings of Ishibashi & Fabian (2012).

Finally, the robustness of the new result was tested by considering two extreme cases for the gas distribution. The first was a highly centrally concentrated gas (relative to the dark matter), with an r^{-2} profile in the central regions. The second was a spatially extended gas (relative to the dark matter), with a central density core. It was found that the details of the gas distribution are not hugely significant to the critical SMBH mass. However, if is unclear how much of an issue the assumption of gas shells always escaping for $C \geq 0$ and $M_{\mathrm{BH}} \geq M_{\mathrm{crit}}$ could be. Nevertheless, for the extreme physical examples considered, the new M_{crit} only differed from the McQuillin & McLaughlin (2012) results by factors of 3–4. This lends yet more support to the idea that it is the dark matter in the protogalaxies, and more specifically their depth of the potential wells, that determines the SMBH mass required for gas blow-out during quasar-mode feedback.

5.2 Open questions and future work

The work presented here has demonstrated how an analytical prediction for the SMBH mass required for gas blow-out in a quasar-phase of a protogalaxy can be compared to the observed M_{BH}–galaxy property correlations at $z = 0$. A theoretical relation based on an analysis of momentum-driven feedback — $M_{\mathrm{BH}} \propto V_{\mathrm{d,pk}}^4$ (McQuillin & McLaughlin 2012) — was shown to ultimately yield model predictions that are consistent with

the observed relations for current SMBH data. It was also shown that these model predictions are not overly sensitive to the details of the initial gas distribution in the protogalaxies (assuming the gas shells *always* escape), just before quasar-mode blow-out. Despite these successes, there are many open questions remaining and several areas for improvement in future work.

5.2.1 Scatter

As mentioned at the start of Chapter 2, all of the average trends that have been established have intrinsic scatter around them. This is inevitable given the results from cosmological simulations (stellar-to-dark matter mass fractions, halo concentrations) and observations (R_e–$M_{*,\mathrm{tot}}$ relation, related to the fundamental plane for early-type galaxies at $z = 0$) used as a starting point. These all have significant scatter, and are combined in various ways to obtain other trend lines. The scatter around these average trends is important and can contain physical information (such as the anti-correlated scatter between R_e and $\sigma_{\mathrm{ap}}(R_e)$). For the stellar properties at $z = 0$, the trend lines were checked against data to ensure obtaining them from combining other scaling relations had not systematically offset them from the data (due to scatter).

For the model predictions of the SMBH relations, intrinsic scatter is again inevitable. This is partly because of the scatter associated with the average trends for $z = 0$ properties, used in part to obtain the model predictions. Other possible sources of the scatter in the SMBH relations are:

- the value of the quasar-mode blow-out redshift, z_{qso};
- gas-poor mergers at redshifts $z < z_{\mathrm{qso}}$, not accounted for in the model predictions here;
- details of the halo progenitor evolution, more specifically the difference between most massive progenitor and most contributing progenitor.

A very much open question related to this is why is the scatter around the model

predictions for the SMBH relations so small, given all the sources and the scatter in the average trends combined to obtain them.

Now that the "correct" trends for the $z = 0$ properties and the SMBH relations have been established, the *actual* scatter can be calculated for trend lines that can be compared to data. The intrinsic scatter for the model predictions of $M_{\rm BH}$ versus various galaxy properties at $z = 0$, was calculated in Chapter 3 for fixed $z_{\rm qso}$. However, the value of $z_{\rm qso}$ itself could well be the dominant source of the scatter in the observed SMBH correlations. For a range of $z_{\rm qso}$ values, the model curves appear to cover the majority of the data in the $M_{\rm BH}$–$\sigma_{\rm ap}(R_e)$ plots.

Estimating the scatter around the trend lines established in Chapter 2 is no trivial task. The scatter in the concentration (Dutton & Maccio 2014) and stellar mass fraction (Moster et al. 2010; Behroozi et al. 2013) relations have been quantified in the literature and the rms scatter could be calculated for the R_e–$M_{*,\rm tot}$ relation. These were used as the starting point to obtain all the other average trends throughout Chapter 2. Calculating the expected scatter around each trend line requires a thorough statistical investigation. This could involve merger tree algorithms to combine the average trends, keeping track of the scatter along the way.

5.2.2 Improving the prediction

The outflows are expected to switch from momentum-driven to energy-driven at relatively small radii. This motivates the question as to why the momentum-driven prediction used in Chapters 3 and 4 does so well when compared to the data. The energy- versus momentum-driven debate needs to be investigated thoroughly for non-isothermal dark matter halos in the protogalaxy. It could well be the case that these details are not significant, as alluded to by Zubovas & Nayakshin (2014).

Related to this is the issue of time dependence of the SMBH mass. The $M_{\rm BH} \propto V_{\rm d,pk}^4$ prediction, and other analytical results in the literature, always assumes that $M_{\rm BH}$ remains constant during the accretion phase. Realistically, the SMBH mass increases with time, resulting in changes in the forces driving the outflow. If the SMBH is

accreting at a fraction q of the Eddington rate, then during the quasar phase,

$$\dot{M}_{\rm BH}(t) = \frac{qL_{\rm Edd}}{\eta c^2} = \frac{4\pi G q M_{\rm BH}}{\eta \kappa c}, \tag{5.3}$$

where η is the accretion efficiency. Thus

$$M_{\rm BH}(t) = M_{\rm BH}(0) \exp\left[\frac{4\pi q G t}{\eta \kappa c}\right], \tag{5.4}$$

with $M_{\rm BH}(0)$ corresponding to the mass of the black hole just before the quasar-mode accretion begins at $t = 0$. The e-folding time (Salpeter 1964) is therefore

$$t_{\rm s} = \frac{M_{\rm BH}(t)}{\dot{M}_{\rm BH}(t)} = \frac{\eta \kappa c}{4\pi q G t} \simeq 4.7 \times 10^7 \left(\frac{\eta}{0.1}\right)\left(\frac{1}{q}\right) \text{ yr}. \tag{5.5}$$

This time-scale is less than the time taken for an outflow with a constant $M_{\rm BH}$ to be driven out to the scale radii of the non-isothermal halos, with $t \sim 10^8$ yr (McQuillin & McLaughlin 2012). If the SMBH accretes matter at a rate comparable to Eddington, the SMBH mass will approximately double during the time $t_{\rm s}$, which will have a significant effect on the forces driving the outflow.

With a time-dependent $M_{\rm BH}$ included, it is possible to investigate the time evolution of the driving forces behind the outflow, rather than assuming an outflow to be purely momentum- or purely energy-driven. To do this, the nature of the cooling and how it changes with time needs to be better understood. Appropriate cooling functions need to be included in calculations, allowing the cooling time of the shocked wind to be obtained at any given radius. Given this, changes in the structure of the shocked wind and shocked ambient medium over time can be completely specified. The issues of time-dependent cooling and shell structure are non-trivial, and may well be best addressed through simulations.

Another area for future work is to consider the stability of the outflows. The $M_{\rm BH}$–$V_{\rm d,pk}$ prediction assumes the outflow is always spherical and smooth (i.e. stable). Thermal instabilities have been briefly considered in the analysis of energy-driven outflows through the Rayleigh-Taylor instabilities (Costa et al. 2014). However, the shells could be subject to gravitational instabilities during the momentum-driven stage, when

the shocked wind region is thin, causing the outflow to fragment. These instabilities have been considered for supernova remnants and stellar winds (Vishniac 1983; Ryu & Vishniac 1988). In the context of SMBH feedback, such instabilities could trigger star formation in the galaxy, as a fragmented shell will lead to a clumpy outflow.

One possible way to proceed is to use linear perturbation theory. This method assumes that an initial perturbation is small compared to an initial quantity — if the radius r is perturbed by δr, then $\delta r \ll r$. The equation of motion of the gas shell can then be perturbed by evaluating the quantities $[M_g(r),\, M_d(r),\, v(r)]$ at the radius $r + \delta r$. This equation can then be solved to identify under what conditions instability occurs. In typical fluid-instability problems, this involves deriving a dispersion relation and determining when imaginary parts are present. If there are imaginary parts in the dispersion relation, the system is unstable.

The time scales for these instabilities can determine if they are applicable to realistic outflows from SMBH feedback. If the perturbations are violent and grow quickly, then the fragmentation time, $t_{\rm frag}$, is short. If the outflow can be approximated as being purely momentum-driven for a time, $t_{\rm mom}$, and $t_{\rm frag} \gg t_{\rm mom}$, the shell will become energy-driven before it has time to fragment. However, if $t_{\rm frag} < t_{\rm mom}$, then the shell will break up into clumps of gas. These will be dense regions that can themselves become gravitationally unstable and collapse, forming stars (Nayakshin & Zubovas 2012). Otherwise, the clumps are likely to fall toward the centre of the galaxy, refuelling the SMBH.

5.2.3 Improving the scalings and model predictions

For the average trends in Chapter 2, and hence the model predictions in Chapters 3 and 4, more detailed analysis is required for extrapolating down to dwarf galaxies [less than a few $\times 10^9 M_\odot$]. This would involve properly accounting for:

- different dark matter distributions, with cored halos possibly more applicable;
- different stellar density profiles — low-mass early-types are better described

by a Sérsic profile with $n \sim 1$;

- the stellar mass ejecta fraction, $F_{\rm ej}$, and whether it does depend on $M_{*,\rm tot}$.

The dark matter halos are potentially cored due to the SMBH winds changing the central structures (Burkert & Silk 1997; Pontzen & Governato 2012). This effect is likely to become more significant as halo mass decreases. This could imply that the "core" radius [i.e., the radius when $\rho_d(r)$ becomes constant] is a mass dependent quantity, increasing as $M_{*,\rm tot}$ (or $M_{\rm d,vir}$) decreases. The mass dependence of $F_{\rm ej}$ was considered in Chapter 2, but only through an ad-hoc $F_{\rm ej}$–$M_{*,\rm tot}$ relation.

Related to this is the non-homology of stellar structure in early-type galaxies. This is discussed in terms of connecting Sérsic index, n, to the total stellar mass, $M_{*,\rm tot}$. This n–$M_{*,\rm tot}$ relation has not been fully accounted for in the trend lines from Chapters 2 and 3. The effects of using a Hernquist profile instead of the more general Sérsic profiles to describe the stars were considered for connecting $\sigma_{\rm ap}(R_e)$ and $V_{\rm d,pk}$, and were shown to be a second-order concern in this limited context. However, at the same time as considering the extrapolation down to low mass galaxies, it would be a good idea to also include the n–$M_{*,\rm tot}$ relation in establishing the average trends, thus accounting for different stellar density profiles. This relation of course has associated intrinsic scatter, and this ultimately needs to be considered as well.

Cosmological simulations could be used to evaluate the balance between effects that pull the model curves for the SMBH relations upwards (gas-poor mergers) and those pushing them down ($f_{\rm b,vir} < f_0$, prior work done by a growing SMBH etc.). One possible way to do this would be to include a recipe which "switches off" SMBH growth via accretion when the simulated black holes reach, for example, the model prediction for $M_{\rm BH}$–$\sigma_{\rm ap}(R_e)$, at a specified $z_{\rm qso}$ [or folding in a $z_{\rm qso}$–$\sigma_{\rm ap}(R_e)$ relation]. For $z < z_{\rm qso}$, the simulations could then invoke a recipe for gas-poor mergers, and see where the final simulated $M_{\rm BH}$ values lie with respect to the model predictions. If any prior work done by black hole can be quantified (by considering the time dependence of $M_{\rm BH}$) and accounted for as well, this could then be used to interpret the baryon fraction required to make the simulated black holes consistent with the model predictions (and hence

the data).

Another possible line of future work is to look at the potential systematic dependence of the quasar-mode blow-out redshift, $z_{\rm qso}$, on $M_{*,\rm tot}$ or $\sigma_{\rm ap}(R_e)$ at $z = 0$, with $z_{\rm qso}$ decreasing as stellar mass increases. If such a dependence could be quantified, this would lead to single model predictions for the SMBH relations. Presumably a $z_{\rm qso}$–$M_{*,\rm tot}$ or $z_{\rm qso}$–$\sigma_{\rm ap}(R_e)$ relation would again have intrinsic scatter around it. Investigating this would therefore perhaps be best done along side a detailed analysis of the scatter in all of the trend lines from Chapters 2 and 3.

Publications

Refereed

- Larkin A., McLaughlin D. E., 2016, MNRAS, 462, 1864

Bibliography

Arnaud M., Pointecouteau E., Pratt G., 2007, A&A, 474, 37

Ascasibar Y., Yepes G., Gottlober S., Muller V., 2004, MNRAS, 352, 1109

Ashman K., Salucci P., Persic M., 1993, MNRAS, 260, 610

Baes M., Buyle P., George K., Dejonghe H., 2003, MNRAS, 341, 44

Bandara K., Crampton D., Simard L., 2009, ApJ, 704, 1135

Bautista M., Dunn J., Arav N., Korista K., Moe M., Benn C., 2010, ApJ, 713, 25

Behroozi P., Silk J., 2015, ApJ, 799, 32

Behroozi P. ., Conroy C., Wechsler R., 2010, ApJ, 717, 379

Behroozi P., Wechsler R., Conroy C., 2013, ApJ, 770, 57

Beifiori A., Courteau S., Corsini E., Zhu Y., 2012, MNRAS, 419, 2497

Bekki K., 2010, MNRAS, 401, 58

Bender R., Burstein D., Faber S., 1992, ApJ, 399, 462

Bender R., Burstein D., Faber S., 1993, ApJ, 411, 153

Bender R., Kormendy J., Bower G., Green R., Thomas J., Danks A., Gull T., Hutchings J., Joseph C., Kaiser M., Lauer T., Nelson C., Richstone D., Weistrop D., Woodgate B., 2005, ApJ, 631, 280

Bender R., Saglia R., Gerhard O., 1994, MNRAS, 269, 785

Bennett C., Halpern M., Hinshaw G., 2003, ApJS, 148, 1

Benson A., Lacey C., Baugh C., Cole S., Frenk C., 2002, ApJ, 599, 38

Benson A., Bower R., Frenk C., Lacey C., Baugh C., Cole S., 2003, ApJ, 599, 38

Bernardi M., Sheth R., Annis J., Burles S., Finkbeiner D., Lupton R., Schlegel D., Subbarao M., Bahcall N., Blakeslee J., 2003, AJ, 125, 1866

Bernardi M., Sheth R., Tundo E., Hyde J., 2007, ApJ, 660, 267

Binney J., Mamon G., 1982, MNRAS, 200, 361

Binney J., Tremaine S., 2008, Galactic Dynamics, Princeton Series in Astrophysics, Second edition

Blakeslee J., Jordán A., Mei S., Côté P., Ferrarese L., Infante L., Peng E., Tonry J., West M., 2009, ApJ, 694, 556

Blandford R., McKee C., 1982, ApJ, 255, 419

Blumenthal G., Faber S., Primack J., Rees M., 1984, Nature, 311, 517

Blumenthal G., Pagels H., Primack J., 1982, Nature, 299, 37

Bogdán A., Goulding A., 2015, ApJ, 800, 124

Bond J., Cole S., Efstsathiou G., Kaiser N., 1991, ApJ, 379, 440

Bond J., Szalay A., Turner M., 1982, Physics Review Letters, 48, 1636

Booth C., Schaye J., 2010, MNRAS, 405, 1

Bower R., 1991, MNRAS, 248, 322

Bromm V., Loeb A., 2003, ApJ, 596, 34

Bromm V., Coppi P., Larson R., 1999, ApJ, 527, 5

Bromm V., Coppi P., Larson R., 2002, ApJ, 564, 23

Bruzual G., Charlot S., 2003, MNRAS, 344, 1000

Bryan G., Norman M., 1998, ApJ, 495, 280

Bullock J., Kolatt T., Sigad Y., Somerville R., Kravtsov A., Klypin A., Primack J., Dekel A., 2001, MNRAS, 321, 559

Bullock J., Kravtsov A., Weinber D., 2000, ApJ, 539, 517

Burbridge G., Burbridge E., Sandage A., 1963, Review of Modern Physics, 35, 947

Burkert A., Silk J., 1997, ApJ, 488, 55

Burkert A., 1995, ApJ, 447, 25

Burstein D., 1982, ApJ, 253, 539

Caon N., Capaccioli M., D'Onofrio M., 1993, MNRAS, 265, 1013

Cappellari M., bacon R., Bureau M., Damen M., Davies R., de Zeeuw P., Emsellem E., 2006, MNRAS, 366, 1126

Cappellari M., Emsellem E., Krajnoivć D., McDermind R., Scott N., Verdoes Kleijn G., 2011, MNRAS, 413, 813

Cappellari M., McDermid R., Alatalo K., Blitz L., Bois M., Bournaud F., Bureau M., Crocker A., Davies R., Davis T., 2013a, MNRAS, 432, 1862

Cappellari M., Scott N., Alatalo K., Blitz L., Bois M., Bournaud F., Bureau M., Crocker A., Davies R., Davis T., 2013b, MNRAS, 432, 1709

Chabrier G., 2003, PASP, 115, 763

Chartas G., Brandt W., Gallagher S., 2003, ApJ, 595, 85

Chen C., Côté P., West A., Peng E., Ferrarese L., 2010, ApJ, 191, 1

Ciotti L., Bertin G., 1999, A&A, 352, 447

Ciotti L., 1991, A&A, 249, 99

Cole S., Norberg P., Baugh C., Frenk C., Bland-Hawthorn J., Bridges T., 2001, MNRAS, 326, 255

Conroy C., Prada F., Newman J., Croton D., Coli A., Conselice C., Cooper M., Davis M., Faber S., 2007, ApJ, 654, 153

Costa T., Sijacki D., Haehnelt M., 2014, MNRAS, 444, 2355

Côté P., McLaughlin D., Hanes D., Bridges T., Geisler D., Merritt D., Hesser J., Harris G., Lee M., 2001, ApJ, 559, 828

Côté P., McLaughlin D., Cohen J., Blakeslee J., 2003, ApJ, 591, 850

Côté P., Blakeslee J., Ferrarese L., Jordán A., Mei S., Merritt D., Milosavljević M., Peng E., Tonry J., West M., 2004, ApJS, 152, 223

Coupon J., Arnouts S., van Waerbeke L., Moutard T., Ilbert O., van Uitert E., Erben T., Garilli B., Guzzo L., Heymans C., 2015, MNRAS, 449, 1352

Couteau S., McDonald M., Widrow L., Holtzman J., 2007, ApJ, 655, 21

Crain R., Eke V., Frenk C., Jenkins A., McCarthy I., Navarro J., Pearce F., 2007, MNRAS, 377, 41

Croton D., 2009, MNRAS, 394, 1109

de Vaucouleurs G., 1948, Ann. d'Astroph., 11, 247

DeGraf C., Di Matteo T., Khandai N., Croft R., Lopez J., Springel V., 2012, MNRAS, 424, 1892

DeGraf C., Di Matteo T., Treu T., Feng Y., Woo J., Park D., 2015, MNRAS, 454, 913

Dehnen W., McLaughlin D., 2005, MNRAS, 362, 1057

Dehnen W., McLaughlin D., Sachania J., 2006, MNRAS, 362, 1057

Dekel A., Silk J., 1986, ApJ, 303, 39

Delvecchio I., Gruppioni C., Pozzi F., Berta S., Zamorani G., Cimatti A., Lutz D., Scott D., Vignali C., Cresci G., 2014, MNRAS, 439, 2736

Di Matteo T., Colberg J., Springel V., Hernquist L., Sijacki D., 2008, ApJ, 676, 33

Di Matteo T., Springel V., Hernquist L., 2005, Nature, 433, 604

Diemand J., Moore B., Stadel J., 2004, MNRAS, 352, 535

Djorgovski S., Davis M., 1987, ApJ, 313, 59

Djorgovski S., Santiago B., 1993, Structure, Dynamics and Chemical Evolution of Elliptical Galaxies, Danziger, Zeilinger and Kjar, First edition

Dopita M., Sutherland R., 2003, Astrophysics of the Diffuse Universe, Springer, First edition

dos Anjos S., da Silva M., 2013, Memorie della Societa Astronomica Italiana Supplementi, 25, 33

Dressler A., Lynden-Bell D., Burstein D., Davies R., Faber S., Terlevich R., Wegner G., 1987, ApJ, 313, 42

Dubinski J., Carlberg R., 1991, ApJ, 378, 496

Dutton A., Macció A., 2014, MNRAS, 441, 3359

Dutton, A.A. anf Conroy C., van den Bosch F., Prada F., More S., 2010, MNRAS, 407, 2

Einasto J., 1965, Trudy Inst. Astroz. Alma-Ata, 57, 87

Eke V., Navarro J., Steinmetz M., 2001, ApJ, 554, 114

Eliche-Moral M., Gonzalez-Garcia A., Balcells M., 2011, A&A, 533, 104

Emsellem E., Cappellari M., Krajnovic D., van de Ven G., Bacon R., Bureau M., Davies R., de Zeeuw P., 2007, MNRAS, 379, 401

Ettori S., Dolag K., Borgani S., Murante G., 2006, MNRAS, 365, 1021

Faber S., Jackson R., 1976, ApJ, 204, 668

Fabian A., 1999, MNRAS, 308, 39

Fakhouri O., Ma C., Boylan-Kolchin M., 2010, MNRAS, 406, 2267

Faucher-Giguére C., Quataert E., 2012, MNRAS, 425, 605

Fernandez Lorenzo M., Cepa J., Bongiovanni A., Perez-Garcia A., Ederoclite A., Lara-Lopez M., Povic M., Sanchez-Portal M., 2011, A&A, 526, 72

Ferrarese L., Ford H., 2005, SSRv, 116, 523

Ferrarese L., Merritt D., 2000, ApJ, 539, 9

Ferrarese L., 2002, ApJ, 578, 90

Fisher D., Drory N., 2015, ASSL, 418, 41

Freeman K., 1985, IAUS, 106, 113

Gallazzi A., Charlot S., Brinchmann J., White S., 2006, MNRAS, 370, 1106

Gavazzi R., Treue T., Rhodes J., Koopmans L., Bolton A., Burles S., Massey R., Moustakas L., 2007, ApJ, 667, 176

Gebhardt K., Richstone D., Kormendy J., Lauer T., 2000, ApJ, 539, 13

Gebhardt K., Lauer T., Kormendy J., Pinkney J., 2001, AJ, 122, 2469

Gebhardt K., Richstone D., Tremaine S., Lauer T., Bender R., Bower G., Dressler A., Faber S., Filippenko A., Green R., 2003, ApJ, 583, 92

Genzel R., Eisenhauer F., Gillessen S., 2010, RvMP, 82, 3121

Gerhard O., Kronawitter A., Saglia R., Bender R., 2001, AJ, 121, 1936

Ghez A., Salim S., Hornstein S., Tanner A., Lu J., Morris M., Becklin E., 2005, ApJ, 620, 744

Ghez A., Salim S., Weinberg N., Lu J., Do T., Dunn J., Matthews K., Morris M., Yelda S., Becklin E., 2008, ApJ, 689, 1044

Giocoli C., Tormen G., Sheth R., 2012, MNRAS, 422, 185

Giodini S., Pierini D., Finoguenov A., Pratt G., Boehringer H., Leauthaud A., Guzzo L., Aussel H., Bolzonella M., Capak P., 2009, ApJ, 703, 982

Gofford J., Reeves J., Tombesi F., Braito V., Turner T., Miller L., Cappi M., 2013, MNRAS, 430, 60

Gonzalez A., Sivanandam S., Zabludoff A., Zaritsky D., 2013, ApJ, 778, 14

Graham A., Colless M., 1997, MNRAS, 287, 221

Graham A., Driver S., 2007, ApJ, 655, 77

Graham A., Scott N., 2013, ApJ, 764, 151

Graham A., Scott N., 2015, ApJ, 798, 54

Graham A., Lauer T., Colless M., Postman M., 1996, ApJ, 465, 534

Graham A., Merritt D., More B., Diemand J., Terzic T., 2006, AJ, 132, 2711

Graves G., Faber S., Schiavon P., 2009a, ApJ, 693, 486

Graves G., Faber S., Schiavon P., 2009b, ApJ, 698, 1590

Gültekin K., Richstone D., Gebhardt K., Lauer T., 2009, ApJ, 698, 198

Gunn J., Gott J., 1972, ApJ, 176, 1

Gunn J., 1977, ApJ, 218, 592

Guzik, J. Seljak U., 2002, MNRAS, 335, 311

Guzman R., Lucey J., Bower R., 1993, MNRAS, 265, 731

Hansen S., Sheldon E., Wechsler R., Koester B., 2009, ApJ, 699, 1333

Häring N., Rix H., 2004, ApJ, 604, 89

Harris G., Poole G., Harris W., 1977, ApJ, 215, 483

Harrison E., 1970, Phys. Rev. D., 1, 2726

Heitmann K., Higdon D., White M., Habib S., Williams B., Lawrence E., Wagner C., 2009, ApJ, 705, 156

Hernquist L., 1990, ApJ, 356, 359

Hinshaw G., Nolta M., Bennett C., 2007, ApJS, 170, 288

Holt J., Tadhunter C., Morganti R., 2008, MNRAS, 387, 639

Hopkins P., Hernquist L., Cox T., Robertson B., Krause E., 2007a, ApJ, 669, 45

Hopkins P., Hernquist L., Cox T., Robertson B., Krause E., 2007b, ApJ, 669, 67

Hopkins P., Hernquist L., Cox T., Keres D., Wuyts S., 2009, ApJ, 691, 1424

Hopkins P., Richards G., Hernquist L., 2007, ApJ, 654, 731

Hubble E., 1926, ApJ, 64, 321

Hudson M., Gwyn S., Dahle H., Kaiser N., 1998, ApJ, 503, 531

Hudson M., Gllis B., Coupon J., Hildebrandt H., Erben T., Heymans C., Hoekstra H., Kitching T., Mellier Y., Miller L., 2015, MNRAS, 447, 298

Into T., Portinari L., 2013, MNRAS, 430, 2715

Ishibashi W., Fabian A., 2012, MNRAS, 427, 2998

Keselman J., Nusser A., 2012, MNRAS, 424, 1232

King A., Pounds K., 2003, MNRAS, 345, 657

King A., 2003, ApJ, 596, 27

King A., 2005, ApJ, 635, 121

Klypin A., Shandarin S., 1983, MNRAS, 204, 891

Koo B. C., McKee C., 1990, ApJ, 354, 513

Koo B. C., McKee C., 1992, ApJ, 388, 93

Koopmans L., Treu T., Bolton A., Burles S., Moustakas L., 2006, ApJ, 649, 599

Koopmans L., Bolton A., Treu T., Czoske O., Auger M., Barnabe M., Vegetti S., Gavazzi R., Moustakas L., Burles S., 2009, ApJ, 703, 51

Kormendy J., Bender R., 2011, Nature, 469, 377

Kormendy J., Ho L., 2013, Annu. Rev. Astron. Astrophys., 51, 511

Kormendy J., Kennicutt R., 2004, Annu. Rev. Astron. Astrophys., 42, 603

Kormendy J., 2012, ApJS, 198, 2

Kravtsov A., Nagai D., Vikhlinin A., 2003, ApJ, 599, 38

Kronawitter A., Saglia R., Gerhard ., Bender R., 2000, A&AS, 143, 53

Krongold Y., Nicastro F., Elvis M., Brickhouse N., Binette L., Mathur S., Jiménez-Bailón E., 2007, ApJ, 659, 1022

Kroupa P., 2001, MNRAS, 322, 231

Lacey C., Cole S., 1993, MNRAS, 262, 627

Lagana T., Zhang Y., Reiprich T., Schneider P., 2011, ApJ, 743, 13

Lamers H., Cassinelli J., 1999, Introduction to Stellar Winds, Cambridge University Press, First edition

Larkin A., McLaughlin D., 2016, MNRAS, 463, 1864

Li Y., Mo H., van den Bosch F., Lin W., 2007, MNRAS, 379, 689

Lin Y., Mohr J., 2004, ApJ, 617, 879

Lokas E., Mamon G., 2003, MNRAS, 343, 401

Longair M., 2011, High energy astrophysics, Cambridge University Press, First edition

Lynden-Bell D., Rees M., 1971, MNRAS, 152, 461

Lynden-Bell D., 1969, Nature, 223, 690

Macchetto F., Marconi A., Axon D., Capetii A., Sparks W., Crane P., 1997, ApJ, 489, 579

Macció A., Dutton A., van den Bosch F., 2008, MNRAS, 391, 411

Madelbaum R., Seljak U., Kaufmann G., Hirata C., Brinkmann J., 2006, MNRAS, 368, 715

Magorrian J., Tremaine S., Richstone D., Bender R., Bower G., 1998, ApJ, 115, 2285

Makino J., Akiyama K., Sugimoto D., 1990, Publ. Astron. Soc. Japan, 42, 205

Maraston C., 1998, MNRAS, 300, 872

Maraston C., 2005, MNRAS, 362, 799

Marconi A., Hunt L., 2003, ApJ, 589, 21

Maulbetsch C., Avila-Reese V., Colin P., Gottlober S., Khalatyan A., Steinmetz M., 2007, ApJ, 654, 53

McBride J., Fakhouri O., Ma C., 2009, MNRAS, 398, 1858

McConnell N., Ma C., 2013, ApJ, 764, 184

McConnell N., Ma C., Gebhardt K., Wright S., Murhpy J., Lauer T., Graham J., Richstone D., 2011, Nature, 480, 215

McConnell N., Ma C., Murhpy J., Gebhardt K., Lauer T., Graham J., Wright S., D.O. R., 2012, ApJ, 756, 179

McGaugh S., Schombert J., De Blok W., Zagyrsky M., 2010, ApJ, 708, 14

McLaughlin D., 1999, ApJ, 512, 9

McMillan P., 2011, MNRAS, 414, 2446

McQuillin R., McLaughlin D., 2012, MNRAS, 423, 2162

McQuillin R., McLaughlin D., 2013, MNRAS, 434, 1332

Merritt D., 2013, Dyanmics and Evolution of Galactic Nuclei, Princeton, First edition

Meyer L., Ghez A., Schodel R., Yelda S., Boehle A., Lu J., Do T., Morris M., Becklin E., Matthews K., 2012, Science, 338, 84

Miller G., Scalo J., 1979, ApJS, 41, 513

Moster B., Somerville R., Maulbetsch C., van den Bosch F., Maccío A., Naab T., Oser L., 2010, ApJ, 710, 903

Moster B., Naab T., White S., 2013, MNRAS, 428, 3121

Murray N., Quataert E., Thomson T., 2005, ApJ, 618, 569

Nardini E., Reeves J., Gofford J., Harrison F., Risaliti G., Braito V., Costa M., Matzeu G., Walton D., Behar E., 2015, Annu. Rev. Astron. Astrophys., 2, 107

Navarro J., Frenk C., White S., 1996, ApJ, 462, 563

Navarro J., Frenk C., White S., 1997, ApJ, 490, 493

Nayakshin S., Zubovas K., 2012, MNRAS, 424, 666

Netzer H., Peterson B., 1997, Astronomical Time Series, 85, 1

O'Brien P., Reeves J., Simpson C., Ward M., 2005, MNRAS, 360, 25

Oke J., Schmidt M., 1963, AJ, 68, 288

Oke J., 1963, Nature, 197, 1040

Ostriker J., Peebles P., Yahil A., 1974, ApJ, 193, 1

Padmanabhan N., Seljak U., Strauss M., Blanton M., Kauffmann G., Schlegel D., Tremonti C., Bahcall N., Bernardi M., Brinkmann J., Fukugita M., Ivezic Z., 2004, New Astronomy, 9, 329

Peacock J., Dodds S., 1996, MNRAS, 280, 19

Peebles J., 1982, ApJ, 263, 1

Peralta de Arriba L., Balcells M., Trujillo I., Falcon-Barroso J., Tapia T., Cardiel N., Gallego J., Guzman R., Hempel A., Martin-Navarro I., Perez-Gonzalez P., Sanchez-Blaquez P., 2015, MNRAS, 453, 704

Perna M., Brusa M., Cresci G., Comastri A., Lanzuisi G., Lusso E., Marconi A., Salvato M., Zamorani G., Bongiorno, A. Mainieri V., Maiolino R., Mignoli M., 2015, A&A, 574, 82

Pizzella A., Corsini E., Dalla-Bonta E., Sarzi M., Coccato L., Bertola F., 2005, ApJ, 631, 785

Planck-Collaboration, 2014, A&A, 571, 16

Planelles S., Borgani S., Dolag K., Ettori S., Fabjan D., Murante G., Tornatore L., 2013, MNRAS, 431, 1487

Pontzen A., Governato F., 2012, MNRAS, 421, 3464

Pounds K., Reeves J., King A., Page K., O'Brien P., Turner M., 2003, MNRAS, 345, 705

Power C., Zubovas K., Nayakshin S., King A., 2011, MNRAS, 413, 110

Prada F., Vitvitska M., Klypin A., Holtzman J., Schlegel D., Grebel E., Rix H., Brinkmann J., McKay T., Csabai I., 2003, ApJ, 598, 260

Prada F., Klypin A., Cuesta A., Betancort-Rijo J., Primack J., 2012, MNRAS, 423, 3018

Press W., Schechter P., 1974, ApJ, 187, 425

Rasia E., Tormen G., Moscardini L., 2004, MNRAS, 351, 237

Recillas-Cruz E., Carrasco L., Serrano P., Cruz-Gonzales I., 1990, A&A, 229, 64

Rees M., 1978, Phydivs Scripta, 17, 193

Reeves J., O'Brien P., Ward M., 2003, ApJ, 593, 65

Richards G., Strauss M., Fan X., Hall P., Jester S., Schneider D., Vanden Berk D., Stoughton C., Anderson S., 2006, AJ, 131, 2766

Richstone D., Tremaine S., 1985, ApJ, 296, 370

Rubin D., Ford W., Thonnard N., 1980, ApJ, 729, 27

Rupke D., Veilleux S., 2011, ApJ, 238, 471

Ryu D., Vishniac E., 1988, ApJ, 331, 350

Saha K., Martinez-Valpuesta I., Gerhard O., 2012, MNRAS, 421, 333

Salpeter E., 1955, ApJ, 121, 161

Salpeter E., 1964, ApJ, 140, 796

Sandage A., 1963, ApJ, 141, 1560

Sani E., Marconi A., Hunt L., Risaliti G., 2011, MNRAS, 413, 1479

Sargent W., Young P., Boksenberg A., Shortridge K., Lynds C., Hartwick F., 1978, ApJ, 221, 731

Savorgnan G., 2016, ApJ, 821, 88

Savorgnan G., Graham A., Marconi A., Sani E., Hunt L., Vika M., Driver S., 2013, MNRAS, 434, 387

Scalo J., 1986, Fund. of Cosmic Phys., 11, 1

Schmidt M., 1963, Nature, 197, 1040

Schombert J., 1986, ApJS, 60, 603

Schwarzschild M., 1979, ApJ, 232, 236

Seljak U., 2002, MNRAS, 334, 797

Sérsic J., 1968, Atlas de Galaxias Astrales, Observatorio Astronomico, Cordoba, First edition

Shankar F., Lapi A., Salucci P., de Zotti G., Danese L., 2006, ApJ, 643, 14

Shankar F., Bernardi M., Sheth R., Ferrarese L., Graham A., Savorgnan G., Allevato V., Marconi A., Lasker R., Lapi A., 2016, MNRAS, 465, 1

Sheldon E., Johnston D., Frieman J., Scranton R., McKay T., Connolly A., Budayari T., Zehavi I., Bahcall N., Brinkmann J., Fukugita M., 2004, ApJ, 127, 2544

Sijacki D., Springel V., Di Matteo T., Hernquist L., 2007, MNRAS, 380, 877

Sijacki D., Voglesberger M., Genel S., Springel V., Torrey P., Snyder G., Nelson D., Hernquist L., 2015, MNRAS, 452, 575

Silk J., Rees M., 1998, A&A, 331, 1

Smoot G., Bennett C., Kogut A., 1992, ApJ, 396, 1

Soltan A., 1982, MNRAS, 200, 115

Spergel D., Verde L., Peiris H., Komatsu E., Nolta M., Bennett C., Halpern M., Hinshaw G., Jarosik N., Kogut A., 2003, ApJS, 148, 175

Spergel D., Bean R., Dore O., Nolta M., Bennett C., Dunkley J., Hinshaw G., Jarosik N., Komatsu E., Page L., 2007, ApJS, 170, 377

Springel V., Di Matteo T., Hernquist L., 2005, ApJ, 620, 79

Sturm E., González-Alfonso E., Veilleux S., Fischer J., Graciá-Carpio J., Hailey-Dunsheath S., Contursi A., Poglitsch A., Sternberg A., Davies R., 2011, ApJ, 733, 16

Sun M., Voit G., Donahue M., Jones C., Forman W., Vikhlinin A., 2009, ApJ, 693, 1142

Tasitsiomi A., Kravtsov A., Gottlober S., Klypin A., 2004, ApJ, 607, 125

Taylor J., Navarro J., 2001, ApJ, 563, 483

Tombesi F., Cappi M., Reeves J., Palumbo G., Braito V., 2011, ApJ, 742, 44

Tremonti C., Moustakas J., Diamond-Stanic A., 2007, ApJ, 663, 77

Trujillo I., Burkert A., Bell E., 2004, ApJ, 600, 39

Tully R., Fisher J., 1977, A&A, 54, 661

Valiante R., Schneider R., Volonteri M., Omukai K., 2016, MNRAS, 457, 3356

van den Bosch F., 2002, MNRAS, 331, 98

van den Bosch F., Norberg P., Mo H., Yang X., 2004, MNRAS, 352, 1302

van den Bosch F., Jiang F., Hearin A., Campbell D., Watson D., Padmanabhan N., 2014a, MNRAS, 445, 1713

van den Bosch R., Gebhardt K., Gültekin K., Yildrim A., Walsh J., 2014b, ApJ, 218, 10

van der Marel R., 1994, MNRAS, 270, 271

van der Wel A., Franx M., van Dokkum P., Skelton R., Momcheva I., Whitaker K., Brammer G., Bell E., Rix H., Wuyts S., Ferguson H., Holden B., Barro G., Koekemoer A., Chang Y., McGrath E., Haussler B., Dekel A., Behroozi P., Fumagalli M., Leja J., Lundgren B., Maseda M., Nelson E., Wake D., Patel S., Labbe I., Faber S., Grogin N., Kocevski D., 2014, ApJ, 788, 28

van Dokkum P., Whitaker K., Brammer G., Franx M., Kriek M., Labbe I., Marchesini D., Quadri R., Bezanson R., Illingworth G., Muzzin A., Rudnick G., Tal T., Wake D., 2010, ApJ, 709, 1018

Veilleux S., Melendez M., Sturm E., Gracia-Carpo J., Fischer J., Gonzalez-Alfonso E., Contursi A., Lutz D., Poglitsch A., Davies R., 2013, ApJ, 776, 27

Vika M., Driver S., Cameron E., Kelvin L., Robotham A., 2012, MNRAS, 419, 2264

Vikhlinin A., Kravtsov A., Forman W., Jones C., Markevitch M., Murray S., van Speybroeck L., 2006, ApJ, 640, 691

Vishniac E., 1983, ApJ, 274, 152

Volonteri M., Ciotti L., 2013, ApJ, 768, 29

Volonteri M., 2010, A&A, 18, 279

Volonteri M., Natarajan P., Gültekin K., 2011, ApJ, 737, 50

Wechsler R., Bullock J., Primack J., Kravtsov A., Dekel A., 2002, ApJ, 568, 52

White S., Rees M., 1978, MNRAS, 183, 341

Williams M., Bureau M., Cappellari M., 2009, MNRAS, 400, 1665

Williams R., Quadri R., Franx M., van Dokkum P., Toft S., Kriek M., Labbe I., 2010, ApJ, 713, 738

Wolf J., Martinez G., Bullock J., Kaplinghat M., Geha M., Munoz R., Simon J., Avedo F., 2010, MNRAS, 406, 1220

Wyithe S., 2006a, MNRAS, 365, 1082

Wyithe S., 2006b, MNRAS, 371, 1536

Yang X., Mo H., van den Bosch F., Pasquali A., Li C., Barden M., 2007, ApJ, 671, 153

Yoshida N., Omukai K., Hernquist L., Abel T., 2006, ApJ, 652, 6

Young P., Westphal J., Kristian J., Wilson C., Landaure F., 1978, ApJ, 221, 721

Yu Q., Tremaine S., 2002, MNRAS, 335, 965

Zahid H., Damjanov I., Geller M., Chilingarian I., 2015, ApJ, 806, 122

Zaritsky D., White S., 1994, ApJ, 435, 599

Zel'dovich Y., 1972, MNRAS, 160, 1

Zhang Y., Lagana T., Pierini D., Puchwein E., Schneider P., Reiprich T., 2011, A&A, 535, 78

Zhao H., 1995, MNRAS, 278, 488

Zhao D., Jing Y., Mo H. ., Borner G., 2003a, ApJ, 597, 9

Zhao D., Mo H., Jing Y., Borner G., 2003b, MNRAS, 339, 12

Zhao D., Jing Y., Mo H., Borner G., 2009, ApJ, 707, 354

Zubovas K., King A., 2012, MNRAS, 426, 2751

Zubovas K., Nayakshin S., 2014, MNRAS, 440, 2625

Zwicky F., 1933, Helv. Phys. Acta, 6, 110